ULTRASONIC INVESTIGATIONS OF MAGNETIC FIELD INDUCED TEXTURAL CHANGES IN SUPERFLUID ^{3}HE-A

A. D. EASTOP

1986

This thesis has been submitted to the Victoria University of Manchester in partial fulfilment of the requirements for the degree of Doctor of Philosophy in the Faculty of Science.

Alison D Eastop

Minor corrections to thesis

'refrigerator' is mis-spelt throughout.

p.6, penultimate sentence, 'This' → 'The'

p.7, eq. (1.11) and last para., $\rho_L \rightarrow \lambda$

p.11, line 12, 'were fitted' → 'was fitted'

p.18 'crenellated' is mis-spelt

p.27 arrows missing on Fig. 2.9

p.28 pin numbers missing on Fig. 2.10

p.95 eq. (4.6), K^{-1}, → $K^{-1/2}$

p.121, above eq. (5.14) $3Nm/p_F^2 \rightarrow 3Nm^*/p_F^2$

p.123, 'discontinuity' mis-spelt

p.126 eqs.(5.19) and (5.20) $\xi \rightarrow \xi'$ and $\xi' \rightarrow \xi$

ULTRASONIC INVESTIGATIONS OF MAGNETIC FIELD INDUCED TEXTURAL CHANGES IN SUPERFLUID ^{3}HE-A

A. D. EASTOP

1986

This thesis has been submitted to the Victoria University of Manchester in partial fulfilment of the requirements for the degree of Doctor of Philosophy in the Faculty of Science.

Alison D Eastop

Minor corrections to thesis

'refrigerator' is mis-spelt throughout.

p.6, penultimate sentence, 'This' → 'The'

p.7, eq. (1.11) and last para., $\rho_L \rightarrow \lambda$

p.11, line 12, 'were fitted' → 'was fitted'

p.18 'crenellated' is mis-spelt

p.27 arrows missing on Fig. 2.9

p.28 pin numbers missing on Fig. 2.10

p.95 eq. (4.6), K^{-1}, → $K^{-1/2}$

p.121, above eq. (5.14) $3Nm/p_F^2 \rightarrow 3Nm^*/p_F^2$

p.123, 'discontinuity' mis-spelt

p.126 eqs.(5.19) and (5.20) $\xi \rightarrow \xi'$ and $\xi' \rightarrow \xi$

ABSTRACT

A method has been proposed for detecting the inertia associated with a local reorientation of the $\hat{\mathbf{l}}$ vector in superfluid ^{3}He-A and which is characteristic of an intrinsic angular momentum density. A transition is predicted to occur in the behaviour of the orbital angular momentum $\hat{\mathbf{l}}$, for ^{3}He-A contained between two parallel planes, from precessional to oscillatory motion as the frequency of magnetic field precession about an axis normal to the planes is increased. Attempts to observe this transition and to detect the inertia were unsuccessful, possibly since the slab of ^{3}He-A was not infinite in lateral extent as assumed in the calculations.

The Fréedericksz transition has been observed in ^{3}He-A. This consists of an instability of the uniform orbital texture in a perpendicular magnetic field, analogous to that observed in a nematic liquid crystal. The measured transition fields lie below the theoretically predicted threshold fields but do exhibit the same temperature dependence.

All measurements were performed with a ^{3}He pressure of 29.316 bar and the anisotropic propagation of 15.15 MHz ultrasound was used throughout to determine the orientation of $\hat{\mathbf{l}}$ with respect to the sound axis. A disc-shaped slab of ^{3}He of height 2 mm and diameter 10.7 mm defined the experimental region. Sound anisotropy coefficients were determined and found to have the predicted order of magnitude. These describe the dependence of the velocity and attenuation of the sound in terms of the angle made between the $\hat{\mathbf{l}}$ vector and the direction of sound propagation. Their determination relied on theoretical predictions about the distorted $\hat{\mathbf{l}}$ texture above the Fréedericksz transition field.

The work described in this thesis has been carried out with the financial support of the Science and Engineering Research Council in the form of a research studentship.

The design and construction of the ^{3}He melting curve thermometer described in section 3.3 formed the basis of a Diploma in Advanced Scientific Studies (Physics) awarded to me by the Victoria University of Manchester in 1983. No other portion of the work referred to in this thesis has been submitted in support of any application for another degree or qualification in this or any other university or institution of learning.

ACKNOWLEDGEMENTS

I would like to thank my supervisor John Hook, and Henry Hall for their continual advice and assistance throughout my post-graduate studies.

I would also like to thank Gil, Stan and Jeff for providing liquid helium and technical assistance.

Finally, I would like to thank Eser Faraj for his help, encouragement and boundless good humour.

CONTENTS

CHAPTER 1 : INTRODUCTION

1.1 Introduction

In 1972 ^{3}He was found to exhibit superfluid phases stable below 2.72 mK. The phase diagram for ^{3}He is shown in Figure 1.1(1) and shows two superfluid phases, the A phase and the B phase.

^{3}He is a fermion and can display superfluid properties by Cooper pairing of atoms, with nuclear spins of paired atoms aligning parallel to each other. p-wave (L=1) pairing is selected on energetic grounds and the spin triplet state (S=1) then follows from the Pauli exclusion principle since the total wavefunction for the pair must be antisymmetric. The "Cooper pairs" of atoms form bound states with energy less than the Fermi energy by an energy gap Δ. Simple BCS theory predicts that the superfluid B phase is the stable state, although the inclusion of strong coupling effects in the theory explains the stability of the A phase.

The ^{3}He order parameter is often represented by a complex 3×3 matrix, $d_{\alpha i}$, where α specifies the orbital part and i is the spin part. The self-consistent field singles out a particular form of $d_{\alpha i}$ which has the lowest free energy. $d_{\alpha i}$ is normalised

$$\sum_{\alpha i} | d_{\alpha i} |^2 = 3 < | \Delta(\hat{\mathbf{k}}) |^2 >_{AV} \qquad (1.1)$$

where $\Delta(\hat{\mathbf{k}})$ represents the energy gap as a function of the direction $\hat{\mathbf{k}}$ around the Fermi surface (the average is over the directions $\hat{\mathbf{k}}$).

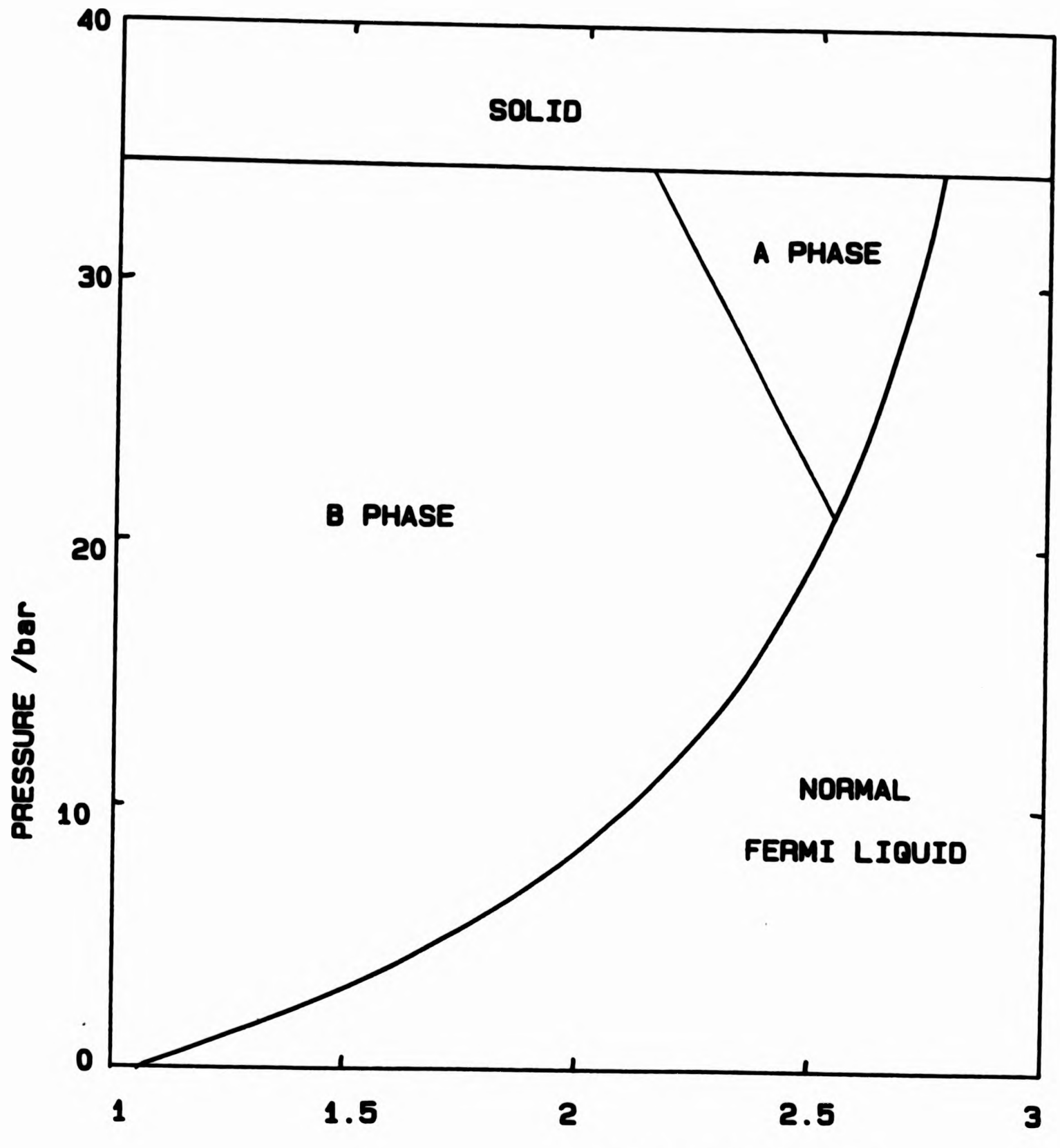

FIG 1.1 : PHASE DIAGRAM OF LIQUID ^{3}HE IN ZERO MAGNETIC FIELD

This work is concerned with the superfluid A phase, and for this bulk phase

$$d_{\alpha i} = (\underline{\Delta}_1 + i \underline{\Delta}_2)_\alpha \hat{d}_i \qquad (1.2)$$

where $\hat{d}$ is a unit vector in spin space along which all the pairs are in the $m_S = 0$ state. $\underline{\Delta}_1$, $\underline{\Delta}_2$ are a pair of real orthogonal vectors of equal magnitude precisely defining the orbital wave function, with

$$\underline{\Delta}_1 \times \underline{\Delta}_2 = \Delta_0^2 \hat{l} \qquad (1.3)$$

where $\hat{l}$ is the direction of orbital angular momentum of all the pairs and Δ_0 is the maximum magnitude of the energy gap. The form $\underline{\Delta}_1 + i \underline{\Delta}_2$ has the angular dependence of the spherical harmonic Y_{11} with respect to the $\hat{l}$ axis. This means that the energy gap has a $\sin\theta$ dependence, resulting in nodes in the energy gap on the Fermi surface in the direction of this axis. Therefore the A phase exhibits anisotropic properties, with $\hat{l}$ defining the anisotropy axis for the gap.

This work is particularly concerned with the effect of static and precessing magnetic fields on the orbital angular momentum $\hat{l}$.

1.2 Orbital Statics and Textures in ^{3}He-A

This section contains a brief discussion of influences on the orientation of $\hat{l}$. Further details are contained in reference 2.

1.2.1 Dipole Energy

The magnetic interaction between nuclear dipole moments $\underline{\sigma}$ in a pair separated by $\underline{r} - \underline{r}'$ may be represented by

$$H_D = \frac{\gamma^2\hbar^2}{2}\int d^3r \int d^3r' \left[\frac{\underline{\sigma}(\underline{r}).\underline{\sigma}(\underline{r}')}{|\underline{r}-\underline{r}'|^3} - \frac{3(\underline{r}-\underline{r}').\underline{\sigma}(\underline{r})\ (\underline{r}-\underline{r}').\underline{\sigma}(\underline{r}')}{|\underline{r}-\underline{r}'|^5} \right] \quad (1.4)$$

where γ is the gyromagnetic ratio. The dipolar coupling energy can be calculated from equation 1.4 and written in the form

$$\Delta E_D = -\ 3/5\ g_D(T)\ (\ \hat{l}.\hat{d}\ )^2 \quad (1.5)$$

where $g_D(T)$ has been introduced by Leggett(3) and is proportional to the mean square gap.

It is apparent that in the absence of other influences the lowest energy state will occur for $\hat{l}$ parallel to $\hat{d}$. This effect is referred to as dipole-locking. For a single pair the strength of this interaction only becomes comparable to k_BT below about 1 μK, but all Cooper pairs must have the same wavefunction in bulk ^{3}He so that the total dipole energy is greater by a factor equal to the number of Cooper pairs.
Leggett has estimated that $g_D(T) \approx 10^{-4}\ (1 - T/T_C)\ Jm^{-3}$ near T_C in the bulk liquid.

1.2.2 Field and Flow Energies

The magnetic susceptibility is anisotropic with anisotropy axis $\hat{d}$. The field orientation energy for a field $\underline{H}$ may be represented by

$$\Delta E_H = 1/2\ \Delta\chi\ (\ \hat{d}.\underline{H}\ )^2 \quad (1.6)$$

where $\Delta\chi = \chi_\perp - \chi_\parallel$ and $\chi_\parallel$, $\chi_\perp$ are the magnetic susceptibilities, with $\chi_\parallel < \chi_\perp$, for $\hat{d}$ parallel and perpendicular to $\underline{H}$ respectively. This energy will be minimised for the orientation of $\hat{d}$ perpendicular to $\underline{H}$. $\Delta\chi$ may be evaluated from microscopic theory to give $\Delta\chi \approx 10\ (1 - T/T_C)\ Jm^{-3}T^{-2}$ near T_C(2).

It should be noted that a field of 30 G provides a susceptibility anisotropy energy of the same order as the dipole energy, close to T_c, so that dipole-locking of the Cooper pairs may be disrupted for external fields with greater magnitude.

The flow orienting effect for an applied counterflow $\underline{v}_s - \underline{v}_n$ and a uniform $\hat{\ell}$ may be represented by

$$\Delta E_F = - 1/2 \, \Delta\rho_s \, [\, \hat{\ell}.(\underline{v}_s - \underline{v}_n) \,]^2 \qquad (1.7)$$

where $\Delta\rho_s = \rho_{s\perp} - \rho_{s\parallel}$ and $\rho_{s\perp}$, $\rho_{s\parallel}$ are the superfluid densities, with $\rho_{s\perp} > \rho_{s\parallel}$, for $\hat{\ell}$ perpendicular and parallel to the direction of counterflow respectively. This energy will be minimised for the orientation of $\hat{\ell}$ parallel to the direction of counterflow $\underline{v}_s - \underline{v}_n$. Near T_c it is found that $\Delta\rho_s \approx 20 \, (1 - T/T_c) \; Js^2m^{-5}$ so that a flow of 2 mms^{-1} gives an energy comparable to the susceptibility anisotropy energy in a field of 30 G.

1.2.3 Bending Energies and Boundary Conditions

Other influences on $\hat{\ell}$ include the presence of container walls which force $\hat{\ell}$ perpendicular at the boundaries(4). This is a strong condition which has never been seen to be violated.

The combined influence of boundaries, magnetic field and flow can cause the $\hat{\ell}$ vectors to form patterns called "textures". Then the existence of a "bending energy", that is an energy resisting spatial variations of the order parameter, is obvious. This energy describes energies of bend, twist and splay of $\hat{\ell}$ which may be represented by

$$\Delta E_b = 1/2 \, K_b \, (\, \hat{\ell} \times \mathrm{curl}\hat{\ell} \,)^2 \qquad (1.8)$$

$$\Delta E_t = 1/2 \, K_t \, (\, \hat{\ell}.\mathrm{curl}\hat{\ell} \,)^2 \qquad (1.9)$$

$$\Delta E_s = 1/2\ K_s\ (\ div\hat{\mathbf{l}}\ )^2 \qquad (1.10)$$

where K_b, K_t and K_s are the elastic constants of bend, twist and splay. These energies are analagous to the Franck energies for distortions of the director $\hat{\mathbf{n}}$ in a nematic liquid crystal.

Provided spatial variation is slow the bending energy terms will be smaller than the dipole locking energy. This leads to the definition of a "dipole-locking length" ξ_d, a characteristic distance in which the system will return to equilibrium under the influence of the dipolar energy if locally disturbed by some other means (e.g. a surface). ξ_d is found to be $\simeq$ 10 μm so that for geometries with dimensions larger than this the dipole-locked limit will be obtained (in the absence of other influences).

1.3 Aims of Experiment

1.3.1 Measurement of Inertia Associated with Intrinsic Angular Momentum Density

In the A phase all the pairs are in an orbital state with the orbital angular momentum aligned along $\hat{\mathbf{l}}$. There should then be an orbital angular momentum $\underline{L} = \hbar\rho_L/2m\ \hat{\mathbf{l}}$ in the equilibrium state. This idea was introduced by Anderson and Morel(5) and ρ_L is called the intrinsic angular momentum density. This angular momentum density that appears as the inertia in the motion of $\hat{\mathbf{l}}$ would govern the low frequency orbital dynamics in the absence of dissipation. However, dissipation is easily included in the hydrodynamic limit and it has been suggested by theoretical work by Cross(6) and experimental work by Paulson et al(7) that this would

dominate the motion. Dissipation arises since a rotation of $\hat{\ell}$, the anisotropy axis of the energy gap, changes the energy of a thermal excitation so that the motion of $\hat{\ell}$ is strongly coupled to the normal fluid of thermal excitations. The time lag between the motion of $\hat{\ell}$ and the motion of the excitation distribution then results in dissipation. Therefore dissipation can be introduced into the equation of motion of $\hat{\ell}$ as a viscous torque on $\hat{\ell}$ opposing its rotation through the normal fluid. So that for a stationary normal fluid

$$\rho_L \frac{d\hat{\ell}}{dt} = - \hat{\ell} \times \left(\frac{\partial f}{\partial \hat{\ell}} \right) - \mu \hat{\ell} \times \frac{d\hat{\ell}}{dt} \qquad (1.11)$$

where f is the free energy giving the reactive torques and μ is the orbital viscosity coefficient.

The magnitude of the intrinsic angular momentum associated with the $\hat{\ell}$ vector has become a subject of considerable controversy(8) and Hall and Hook(9) have suggested that three different types of experiment which might be used to measure the intrinsic angular momentum would lead to different answers.

The main aim of the experiment described in this thesis was the measurement of the inertia associated with a local re-orientation of $\hat{\ell}$ i.e. a measurement of ρ_L. According to Hall and Hook the inertia should be characteristic of an intrinsic angular momentum density $(2C - C_o)\,\hat{\ell}$, where the coefficients C and C_o may be represented by $C_\perp$ and $C_\perp - C_\parallel$ respectively, with

$$C_\parallel = \frac{- 1/2\ \rho^o_{s\parallel}\ \hbar/2m}{1 + 1/3\ F^s_1\ \rho^o_{n\parallel}/\rho} \qquad (1.12)$$

$$C_\perp = \frac{1/2\ \rho^o_{s\parallel}\ \hbar/2m}{1 + 1/3\ F_1^s\ \rho^o_{n\perp}/\rho} \qquad (1.13)$$

(see reference 2)

ρ, ρ_s^o, ρ_n^o represent the total density, superfluid density and normal fluid density respectively (in the absence of Fermi liquid corrections), and F_1^s is one of the Fermi liquid parameters.

Under these circumstances, the equation of motion of $\hat{\ell}$ becomes

$$\mu \frac{\partial \hat{\ell}}{\partial t} - (2C - C_o)\ \hat{\ell} \times \frac{\partial \hat{\ell}}{\partial t} = \hat{\ell} \times \{ \hat{\ell} \times \left[\frac{\delta f}{\delta \hat{\ell}} \right]_\Phi \} \qquad (1.14)$$

where the variational derivative of the free energy density f is at constant phase Φ.

Although $(2C - C_o)/\mu$ is predicted to be very small in the absence of Fermi liquid corrections(2) the existence of these corrections should lead to a value for this quantity of a few percent at the A-B transition. This has been estimated as follows:-

From equations 1.12 and 1.13 $2C-C_o$ can be written

$$2C-C_o = 1/2\ \rho^o_{s\parallel}\ \hbar/2m\ \{(m^*/m - F_1^s\ \rho^o_{s\perp}/3\rho)^{-1} - (m^*/m - F_1^s\ \rho^o_{s\parallel}/3\rho)^{-1}\} \qquad (1.15)$$

where the effective mass $m^* = m\ (1 + F_1^s/3)$ and

$$\rho^o_{s\parallel} + \rho^o_{n\parallel} = \rho^o_{s\perp} + \rho^o_{n\perp} = \rho \qquad (1.16)$$

Expanding binomially for small $\rho^o_{s\perp}/\rho$, $\rho^o_{s\parallel}/\rho$ and with $\rho^o_{s\parallel} = \rho^o_{s\perp}/2$ then

$$(2C-C_o)/\mu \simeq 1/6\ (\ \rho^o_{s\parallel}/\rho\ )^2\ F_1^s\ (\ m/m^*\ )^2\ \hbar\rho/2m\mu \simeq 0.05 \text{ i.e. } 5\% \qquad (1.17)$$

For this rough estimation the following were assumed : $\rho^o_{s\parallel} = \rho_{s\parallel}\ (m^*/m)$ where the superscript o indicates that Fermi liquid corrections have been neglected. At 29 bar and $T/T_C = 0.85$, $\rho_{s\parallel}/\rho = 0.025(10)$; $F_1^s = 13.08(11)$;

$m = 5.009\times10^{-27}$ kg(12); $\rho = 115$ kgm^{-3}(12); $\mu = 3.4\times10^{-8}$ Nm^{-2}s(10).

It was assumed that if $\hat{\mathbf{l}}$ were caused to lie at an angle to the z axis by applying a suitably directed magnetic field (small enough for the dipole-locked limit to be considered), then rotation of the field about the z axis at a frequency ω_0 would cause $\hat{\mathbf{l}}$ to precess about the z axis at the same rate. The effect of the inertial term would then be to cause the angle θ between $\hat{\mathbf{l}}$ and z to depend on the direction of rotation. In fact it was found that this precessional solution for $\hat{\mathbf{l}}$ did not occur in the bulk liquid but could be obtained for ^{3}He-A in a restricted geometry, under certain circumstances.

Chapter 6 contains a discussion of the solution of the equation of motion of $\hat{\mathbf{l}}$ for this situation and experimental attempts to observe the predicted behaviour and hence the inertia associated with the angular momentum density.

1.3.2 Measurement of a Fréedericksz Transition in ^{3}He-A

The Fréedericksz transition(13) in a nematic liquid crystal was first observed over fifty years ago. The orientation of a nematic liquid crystal can be described by a unit vector $\hat{\mathbf{n}}$, known as the director. Container boundaries may be specially treated to provide preferred orientations of $\hat{\mathbf{n}}$ and in addition $\hat{\mathbf{n}}$ can be aligned by magnetic fields because of the diamagnetic properties of the aromatic rings which form part of the molecule. If a magnetic field is applied to a nematic single liquid crystal of spatially uniform texture in a direction such that the alignment favoured by the field is perpendicular to that preferred by the

boundaries, the $\hat{\mathbf{n}}$ texture will start to distort at a certain value of the applied field. This value is called the Fréedericksz transition field and represents the field at which this 2nd order phase transition occurs.

The $\hat{\mathbf{l}}$ vector of superfluid ^{3}He-A can be influenced by magnetic fields and container boundaries in an analogous manner (see section 1.2). This suggests that a similar transition should occur in the orbital texture of dipole-locked ^{3}He-A, contained between two parallel plane surfaces, when a magnetic field is applied perpendicular to the surfaces. One aim of this work was to observe this transition in ^{3}He-A and to measure a critical threshold field. The Fréedericksz transition had not previously been observed in superfluid ^{3}He.

Chapter 5 contains a discussion of these observations, together with the theory of the transition.

1.3.3 Measurement of Velocity and Attenuation of Ultrasound in ^{3}He-A

The transmission of ultrasound through ^{3}He-A can be used as a probe since the dependence of the received sound signal on the direction of $\hat{\mathbf{l}}$ is so large that it serves as a means for detecting the orientation of the $\hat{\mathbf{l}}$ field. Thus the velocity and attenuation of sound are characterised by the angle made between the $\hat{\mathbf{l}}$ vector and the direction of sound propagation. This relationship is described by characteristic coefficients, known as sound anisotropy coefficients. Another aim of this experiment was the determination of these coefficients and this depended on theoretical predictions about the distorted $\hat{\mathbf{l}}$ texture.

Chapter 4 describes the velocity and attenuation of sound in normal and superfluid ^{3}He in the absence of a magnetic field, and chapter 5 discusses the determination of the anisotropy coefficients.

1.4 Experimental Arrangement

In all measurements discussed in this thesis the anisotropic propagation of ultrasound through ^{3}He-A was used to determine the orientation of $\hat{\mathbf{l}}$ with respect to the sound axis.

A disc-shaped slab of ^{3}He of height 2 mm and diameter 10.7 mm defined the experimental region, with the circular slab boundaries provided by two quartz transducers. These were used to transmit 15 MHz sound from one transducer to the other through the liquid helium. A system of magnetic field coils were fitted around the experimental cell. This had the capability of providing magnetic fields along any direction with respect to the sound axis, thus enabling the statics and dynamics of the $\hat{\mathbf{l}}$ texture to be investigated. Throughout this work the magnetic fields applied were $\ll$ 30 G so that the superfluid was in the dipole-locked regime. All the measurements discussed here were performed with a helium pressure of 29.316 bar.

Chapter 2 describes the experimental arrangement in detail, and chapter 3 discusses the thermometry employed.

CHAPTER 2 : EXPERIMENTAL

2.1 Introduction

This chapter contains a discussion of the experimental arrangement used to achieve the results presented in this work.

A sample of ^3He was cooled into its superfluid A phase using the cryogenic system referred to in section 2.2. The design and construction of the experimental cell are discussed in section 2.3. The system of coils which was capable of providing magnetic fields in any direction with respect to the cell axis is discussed in section 2.4, and the Mu metal shield used for screening the experimental cell is discussed in section 2.5. Finally, the system of data handling and storage is described in section 2.6.

2.2 The Cryogenic system

A schematic diagram of the cryostat used for cooling ^3He into its superfluid phases is given in Figure 2.1. The low millikelvin temperatures required were achieved by using a dilution refridgerator for precooling and adiabatic demagnetisation of copper for the final stage of cooling. The entire apparatus was housed in a shielded enclosure, which was grounded at one point, in order to prevent heating by electrical interference from outside equipment. The design of this cyostat has been well documented by D. C. Carless(14) and therefore it is not proposed to discuss this

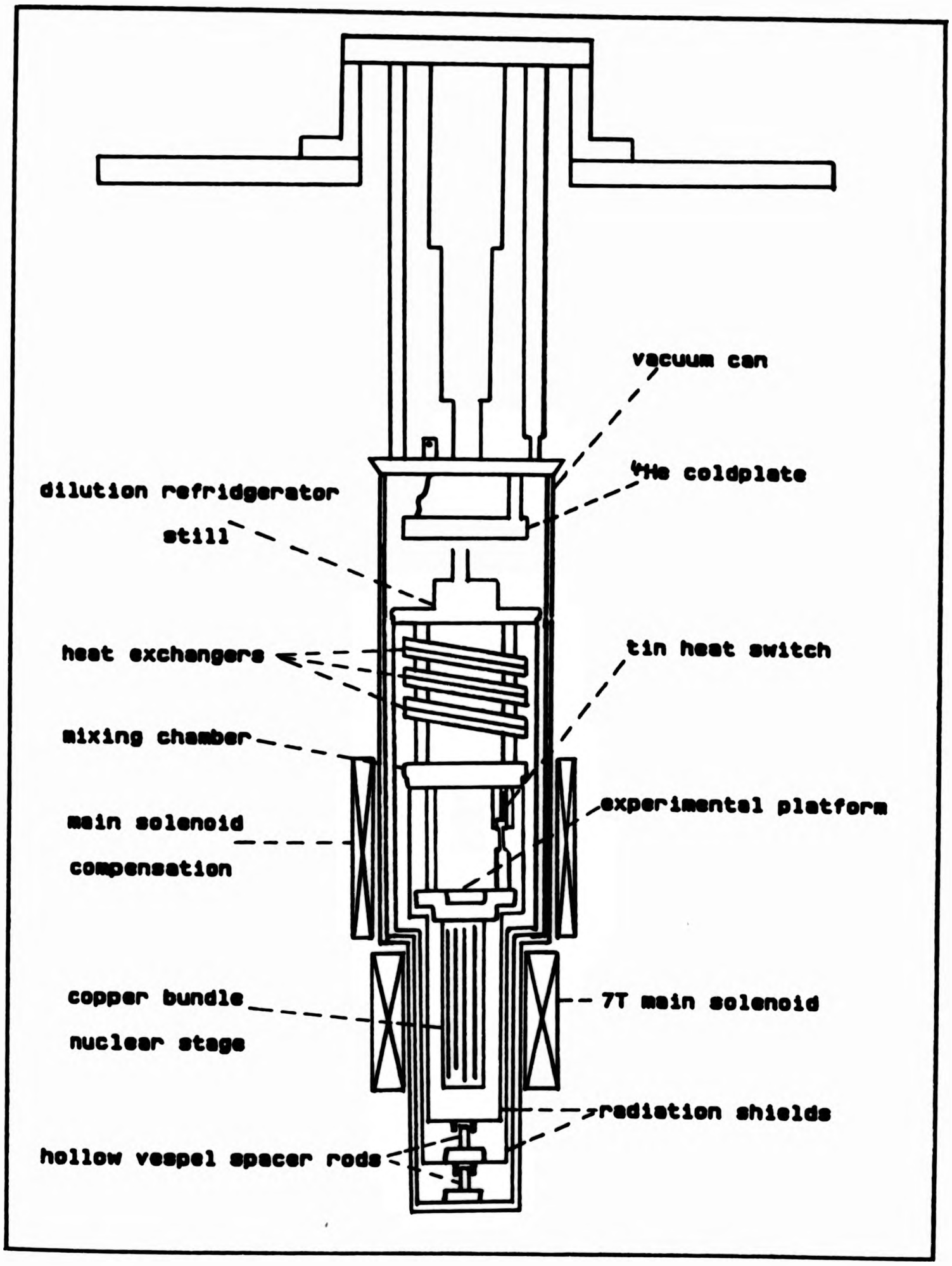

FIG 2.1 : Schematic diagram of cryostat insert

apparatus in any further detail here.

Some changes made to the system are described by R. Mitchell(15). To summarise these: the tin heat switch was remade in 1983 and a 4.2K trap added into the dilution refridgerator condensing line to reduce the incidence of blocking.

The author has constructed a ^{3}He melting curve thermometer(16) which bolted onto the experimental platform and was used in the establishment of a Manchester temperature scale. Further details of this and the other thermometry employed are contained in chapter 3.

While cooling the experimental apparatus from ambient temperatures to 4.2K a cylindrical "Mu metal" shield(17) was positioned around the superinsulating dewar. This was done to prevent flux due to the earth's magnetic field being trapped by the superconducting components of the system and possibly producing a magnetic field in the ^{3}He cell region. An improvement in SQUID behaviour was observed from the previous experimental cool-down. The increase in signal to noise ratio may have been a result of either the presence of the Mu metal shield or an addition in the lead shielding of the SQUID probe itself.

The dilution refridgerator typically precooled the experimental region to 16.6 mK. The longest nuclear demagnetisation performed held the liquid ^{3}He in the superfluid A phase for a period of 10 days at the end of which time there remained 11.6% main solenoid field applied to the copper demagnetisation stage. This indicated that the residual heat leak to the ^{3}He was small, and the rate of warming of the ^{3}He this produced was observed to be about 30 μK/day.

2.3 The Experimental Cell

A schematic diagram of the experimental cell is shown in Figure 2.2. A sound signal at ultrasonic frequencies was transmitted through the liquid helium from one piezoelectric quartz crystal to another along a path defined by an annular fused quartz spacer.

2.3.1 Design and Construction

The two parts of the cell body were machined from stycast 1266 epoxy resin(18). No part of the experimental cell could be made out of copper since the eddy currents induced by a rotating magnetic field would produce too much heating. Since the cell was required to contain pressure of up to 30 bar a rough estimate of the stycast wall thickness needed was made(see refs 18 & 19). Neglecting stresses associated with corners of the body and any deflections due to shear a minimum value for the wall thickness of approximately 1.6 mm was obtained. The cell walls were actually made approximately 3 mm thick.

The brass cell-support tube was glued into the lower part of the cell body with stycast 1266 to form a pressure tight seal. This tube served both as a helium fill line for the cell and as a means of mounting the cell in the experimental region of the cryostat using an indium 'o' ring seal. A circular brass flange which bolted around the tube was used to support the magnetic coil system and Mu metal shield of section 2.5. Figure 2.3 shows this arrangement schematically.

Two BeCu springs were used to hold the crystals in place. BeCu

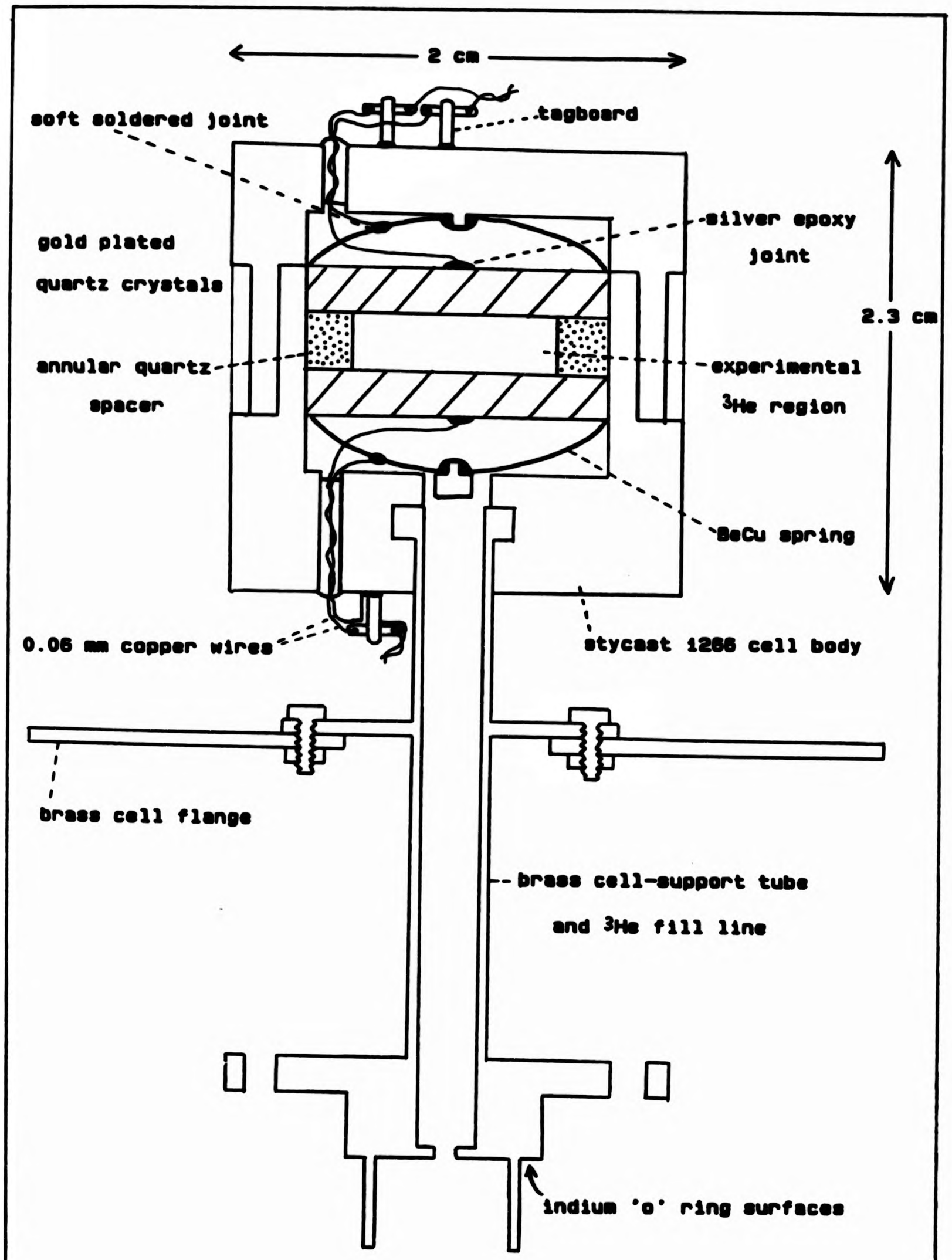

FIG 2.2 : Schematic diagram of experimental cell

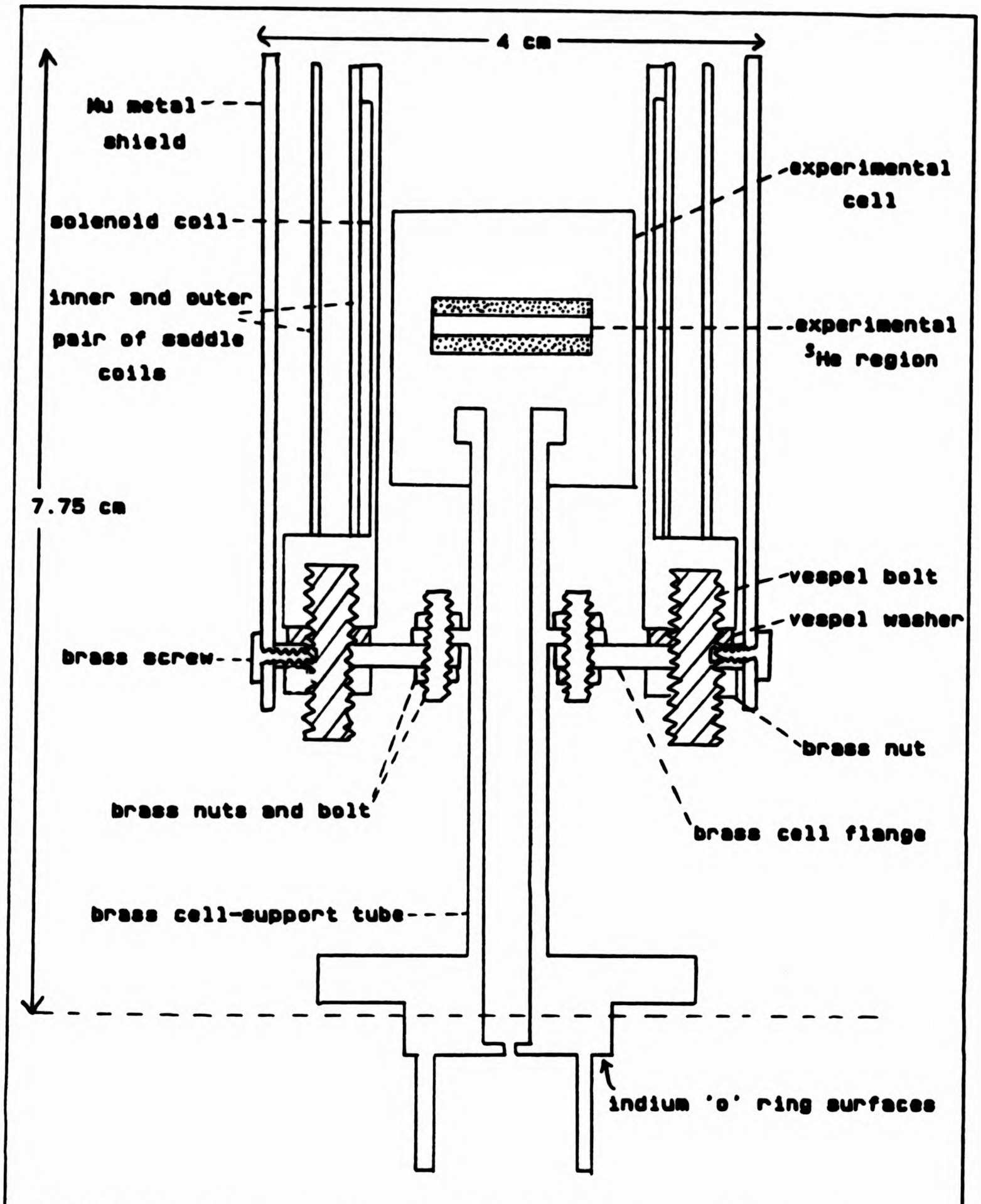

FIG 2.3 : Schematic diagram showing mounting of magnet coil system and Mu metal shield around the experimental cell

was chosen since it is hard and springy and eddy current heating would be negligible. Each spring was clipped out of 0.25 mm thick foil and bent into shape (see Figure 2.4). The earth connection to each crystal was made via the pressed BeCu spring contact. In each case a 0.06 mm diameter copper wire was wrapped several times around one of the legs of the spring and soldered in place to provide good electrical contact. The springs were located inside either part of the cell body by fitting the hole punched at the centre of each one over a small stycast pip.

The piezoelectric crystals used were 5 MHz 0° X-cut quartz crystals, ground optically flat and coaxially gold plated(20). Their resonant frequencies were matched to better than 1/4 %. A 0.06 mm diameter copper wire was attached to the centre electrode of each crystal with a dab of silver epoxy(21) and these joints were cured at 80°C for approximately 60 minutes.

Each pair of copper leads providing electrical contact to each crystal was threaded through a narrow channel in either the top or bottom part of the cell body. These channels were then filled with stycast 1266 to form a pressure tight seal. All four fine wires were soldered to tagboards stuck to the outside of the cell body as a precaution against lead breakage.

The crystals were pressed either side of an annular quartz spacer(20), the ends of which were ground optically flat to minimise phase cancellation of the sound wavefront. The ends of the spacer were also crenelated in antiphase in order to minimise spurious transmission of sound through the spacer. Figure 2.5 shows the spacer schematically. The BeCu

springs provided the mechanical pressure, each with its 3 prongs orientated so as to apply pressure to the crystal at the 3 raised regions of the spacer.

With the crystals held in place as described above the two halves of the cell body were gently pushed together and held with a clamp while stycast 1266 was used to make a seal. The cell was found to be pressure tight up to pressures of at least 42 bar at 77 K.

The fused quartz spacer with an outer diameter of 1.27 cm, an inner diameter of 1.07 cm and a height of 2 mm defined the path of the sound through the ^{3}He. In deciding on a crystal separation, d, of 2 mm several factors were taken into account. The presence of the boundaries becomes a dominant influence on the $\hat{\mathbf{l}}$ texture of superfluid ^{3}He-A for very small separations and thus a relatively large magnetic field would need to be applied to alter the texture. (See chapter 1 for details of the influence of boundaries and fields on the orientation of the $\hat{\mathbf{l}}$ vector). As the crystal separation d is made larger, however, the influence of these two becomes comparable with the applied magnetic field eventually producing the greater effect on the texture in the centre of the channel. Also, since changes in the attenuation, α, of the sound transmitted through the ^{3}He are being used to monitor changes in its $\hat{\mathbf{l}}$ texture it might seem sensible to make d of order $1/\alpha$ which is approximately 5-10 mm for 15 MHz sound in the superfluid A phase. Considering all the above, a value for d of 2 mm was chosen such that the effect of the boundaries on the $\hat{\mathbf{l}}$ texture is not negligible compared to the effect of magnetic fields of order 1 G. The limit on the diameter of the helium disc region was the amount of space available on the experimental platform of the cryostat. These slab

dimensions provided a diameter to height ratio of approximately 5:1 so that edge effects should not be too important.

The fundamental resonance of each quartz crystal was measured after mounting these in the cell containing air at ambient temperatures and using the circuit shown in Figure 2.6. The inclusion of the resistors in this circuit was found to be necessary since each crystal had an estimated capacitance of 3.4 pF suggesting an off resonance impedance of order 10 kΩ at 3 MHz for example. The crystal resonances measured are shown in Figures 2.7 and 2.8. For the top crystal in the cell a quality factor Q of 470 was estimated with a resonant peak at 5.010 MHz and a bandwidth of approximately 11 kHz. For the bottom crystal a quality factor Q of 430 was estimated with a resonant peak at about 5.005 MHz and a bandwidth of approximately 11 kHz. The bottom crystal also displayed several secondary resonant peaks.

With the cell mounted on the experimental platform of the cryostat the four copper leads from the crystals were twisted in pairs and each soldered to the inner conductor of four CuNi matrix, multifilamentary, superconducting coaxes with stainless steel outers of diameter 0.6 mm(22). These superconducting coaxes were led from the experimental platform up to the vacuum can flange with heat sinks to the dilution refridgerator mixing chamber, 4th heat exchanger and still, and to the 1K cold plate. These heat sinks were made by gently squeezing approximately 3 cm lengths of the coax between clean OFHC copper plates. Four coaxial cables took the crystal leads out of the cryostat and to the transmission and detection electronics. The capacitance measured between each quartz crystal's pair of leads outside the cryostat insert was about 14 pF.

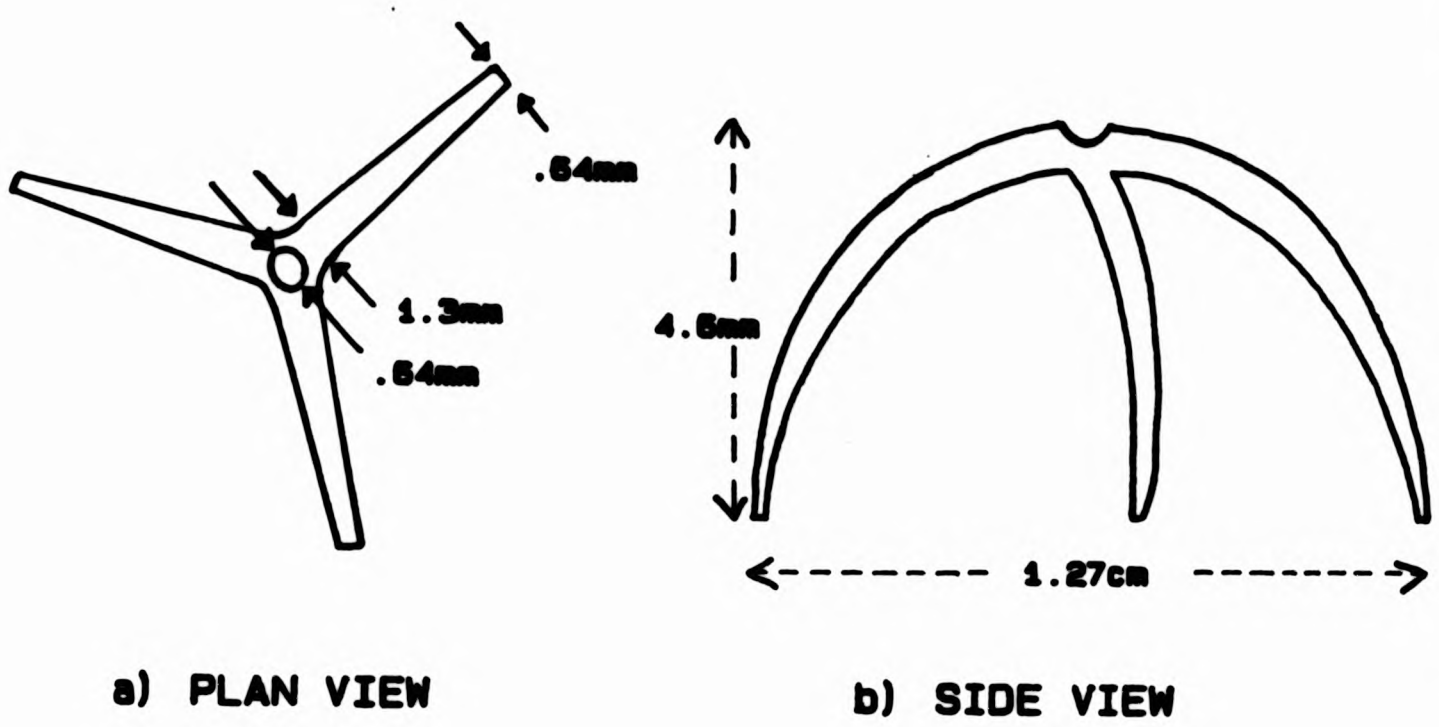

a) PLAN VIEW

b) SIDE VIEW

FIG 2.4: BeCu SPRING

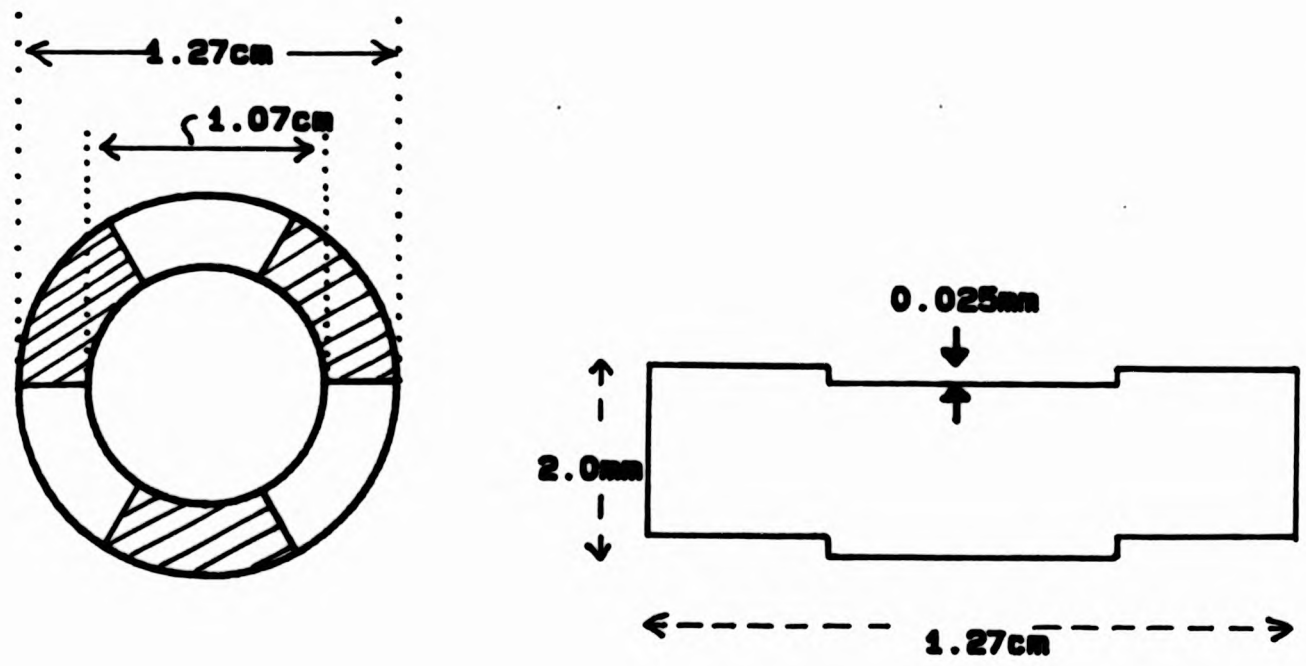

a) PLAN VIEW

b) SIDE VIEW

FIG 2.5: FUSED QUARTZ SPACER

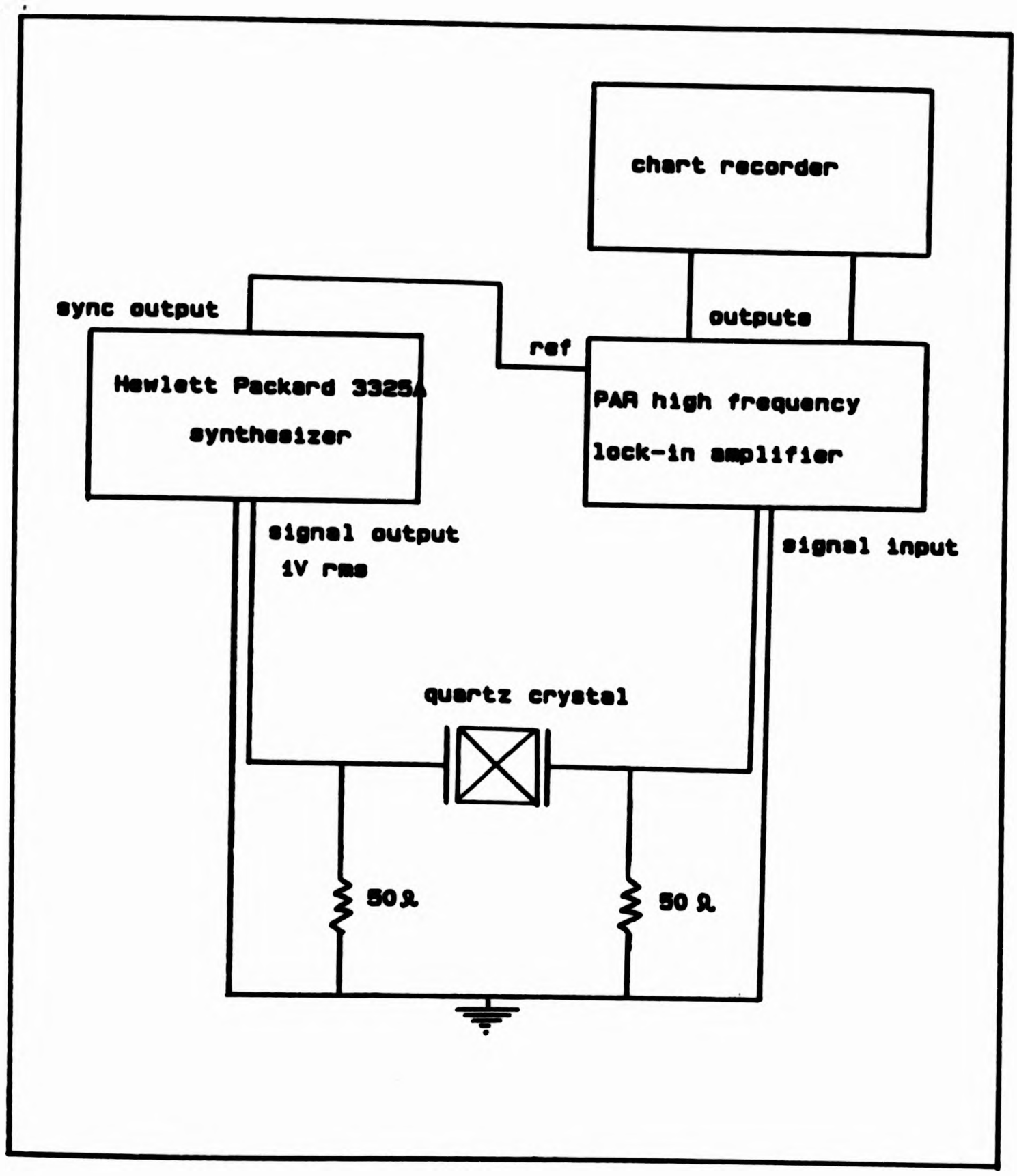

FIG 2.6 : CIRCUIT USED TO MEASURE QUARTZ CRYSTAL RESONANCES

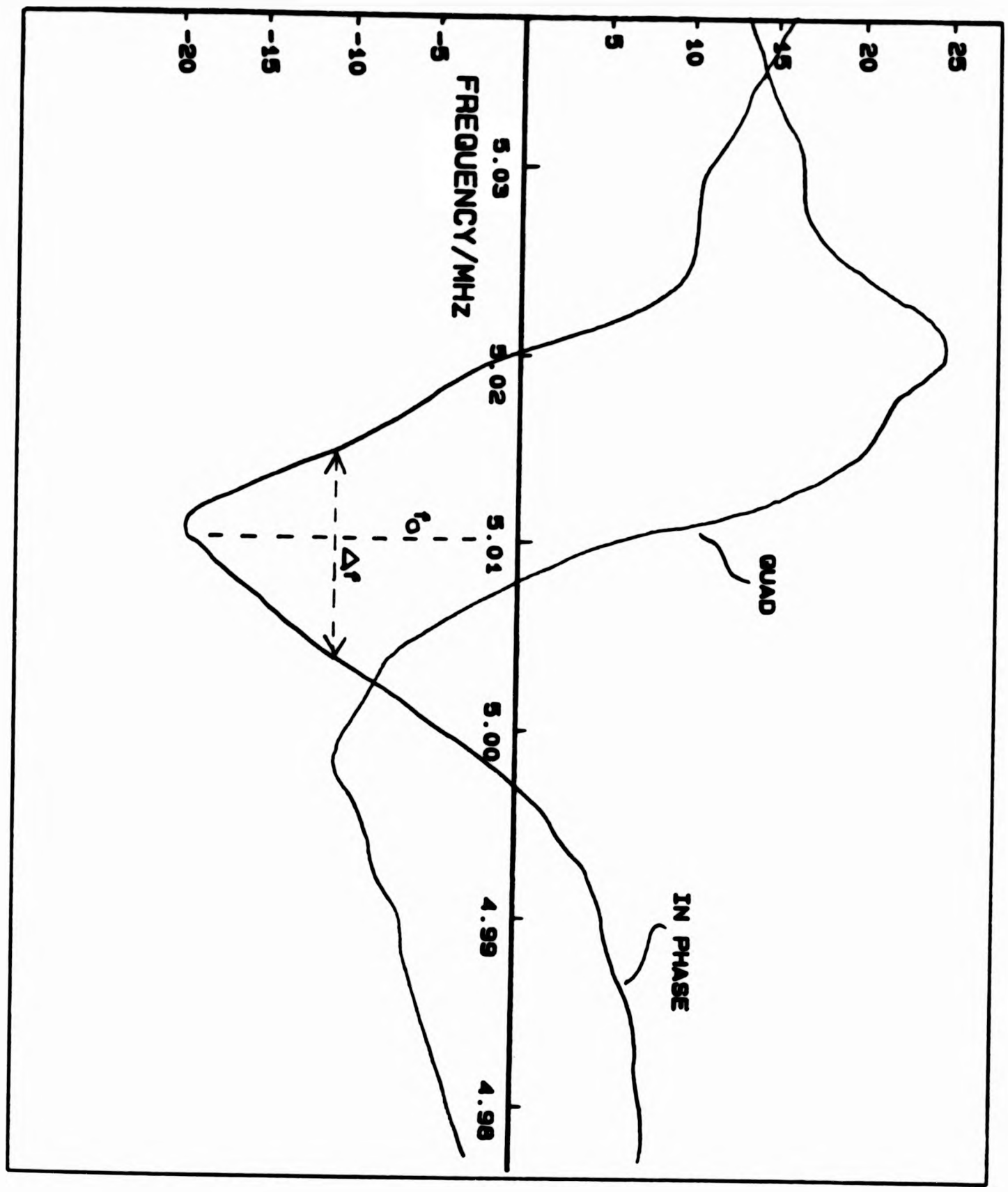

FIG 2.7 : Fundamental resonance of top quartz crystal (i.e. transmitter) measured when mounted in cell containing air at ambient temperatures. $f_o = 5.01MHz$, $\Delta f \approx 11kHz$ and $Q \approx 470$.

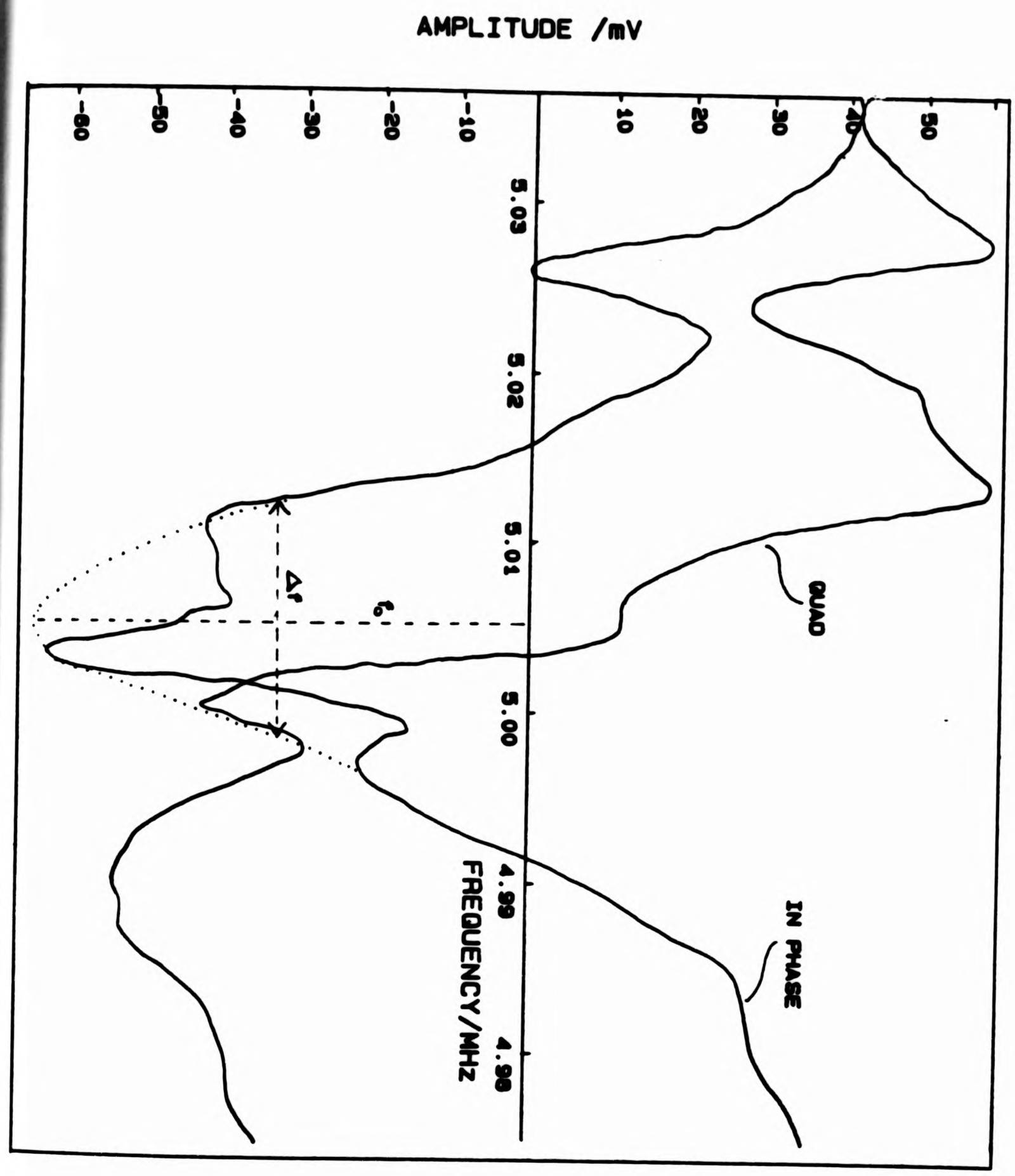

FIG 2.8 : Fundamental resonance of bottom quartz crystal (i.e. receiver) measured when mounted in cell containing air at ambient temperatures. f_o = 5.005MHz, $\Delta f \approx 11$kHz and $Q \approx 430$.

2.3.2 Sound Circuitry

Figure 2.9 shows a block diagram of the sound transmission and detection electronics. Throughout the experiment pulsed ultrasound of approximately 15.15 MHz was transmitted from the top crystal to the bottom crystal through the liquid helium. The 15 MHz resonance (1st harmonic) was used because sound of this frequency was attenuated by the superfluid ^3He to a greater extent than sound at the crystal's fundamental resonant frequency of 5 MHz. Although 25 MHz sound would have been absorbed to a yet greater extent, practically this was not as easy to use.

During preliminary attempts at observing sound transmission through the ^3He it rapidly became apparent that this was masked by a signal similar in behaviour to a "crystal ringing". This signal was believed to be a result of leading the earth connections to each crystal out of the cryostat separately instead of joining them together as close to the crystals as possible. (Since earlier test measurements performed with superfluid ^4He at 1K, with a total of 3 rather than 4 coaxial leads to the crystals and with the crystal earths joined nearer the cell, were not subject to this extra "nuisance" signal to any noticeable extent). However, because of a technical problem it was decided not to warm the cryostat insert back to room temperature. Instead, therefore, the cables leading from the crystals' earth faces were extended to approximate $\lambda/2$ at 15 MHz lengths and connected together to simulate connecting the earths at the cell. This involved the addition of 9.05 m of coaxial cable outside the cryostat insert, with the approximate midpoint of this arrangement earthed via a 1 MΩ resistor. In practice, of course, this was not a perfect solution so that some of the unwanted signal remained, henceforth

2.3.2 Sound Circuitry

Figure 2.9 shows a block diagram of the sound transmission and detection electronics. Throughout the experiment pulsed ultrasound of approximately 15.15 MHz was transmitted from the top crystal to the bottom crystal through the liquid helium. The 15 MHz resonance (1st harmonic) was used because sound of this frequency was attenuated by the superfluid ^{3}He to a greater extent than sound at the crystal's fundamental resonant frequency of 5 MHz. Although 25 MHz sound would have been absorbed to a yet greater extent, practically this was not as easy to use.

During preliminary attempts at observing sound transmission through the ^{3}He it rapidly became apparent that this was masked by a signal similar in behaviour to a "crystal ringing". This signal was believed to be a result of leading the earth connections to each crystal out of the cryostat separately instead of joining them together as close to the crystals as possible. (Since earlier test measurements performed with superfluid ^{4}He at 1K, with a total of 3 rather than 4 coaxial leads to the crystals and with the crystal earths joined nearer the cell, were not subject to this extra "nuisance" signal to any noticeable extent). However, because of a technical problem it was decided not to warm the cryostat insert back to room temperature. Instead, therefore, the cables leading from the crystals' earth faces were extended to approximate $\lambda/2$ at 15 MHz lengths and connected together to simulate connecting the earths at the cell. This involved the addition of 9.05 m of coaxial cable outside the cryostat insert, with the approximate midpoint of this arrangement earthed via a 1 MΩ resistor. In practice, of course, this was not a perfect solution so that some of the unwanted signal remained, henceforth

referred to as the "nuisance" signal. Pulsed ultrasound was used in preference to cw because the nuisance signal problem was found to be more severe in the case of the latter. Pulses of 2.8 μs width with a typical repetition rate of 5 Hz were provided by a Matec 305 broadband gated amplifier(23) driven by a 1 V_{p-p} cw signal at 15.154 MHz from a Hewlett-Packard 3325A synthesizer(24). These pulses were typically attenuated by 26 dB provided by a switchable attenuator(25), so that pulses of amplitude 2.5 V_{p-p} were fed to the driving crystal. The peak to peak output level of the received signal was of order 100 μV. This signal was amplified by an Avantek ×1000 amplifier(26), passed through a double balanced mixer operating as a phase sensitive detector and integrated, typically over the period from 15-25 μs after the pulse input to the transmitter crystal. This period was chosen for the integration for an optimisation of the transmitted sound signal in comparison to the nuisance signal. The time constant of the detection electronics was chosen to be 1-10 s depending on the measurement being performed.

The PSD and integration circuitry are shown in Figures 2.10 and 2.11. The PSD/integration circuitry was operating in its linear region for the signals with magnitudes of order 100 mV it was detecting. Figure 2.12 indicates this by showing the PSD/integration circuitry response for a range of different magnitude input signals. A nominal $\lambda/4$ at 15 MHz coaxial cable length was inserted between the Hewlett-Packard drive and the PSD reference for some of the measurements. This produced a signal that was found to be 91°± 1° (1.59 radians) out of phase with the original 15.154 MHz signal, and thus enabled a complete sound record to be collected. The inclusion or not of this extra cable length was found to have no measurable effect on the drive signal sent to the experimental

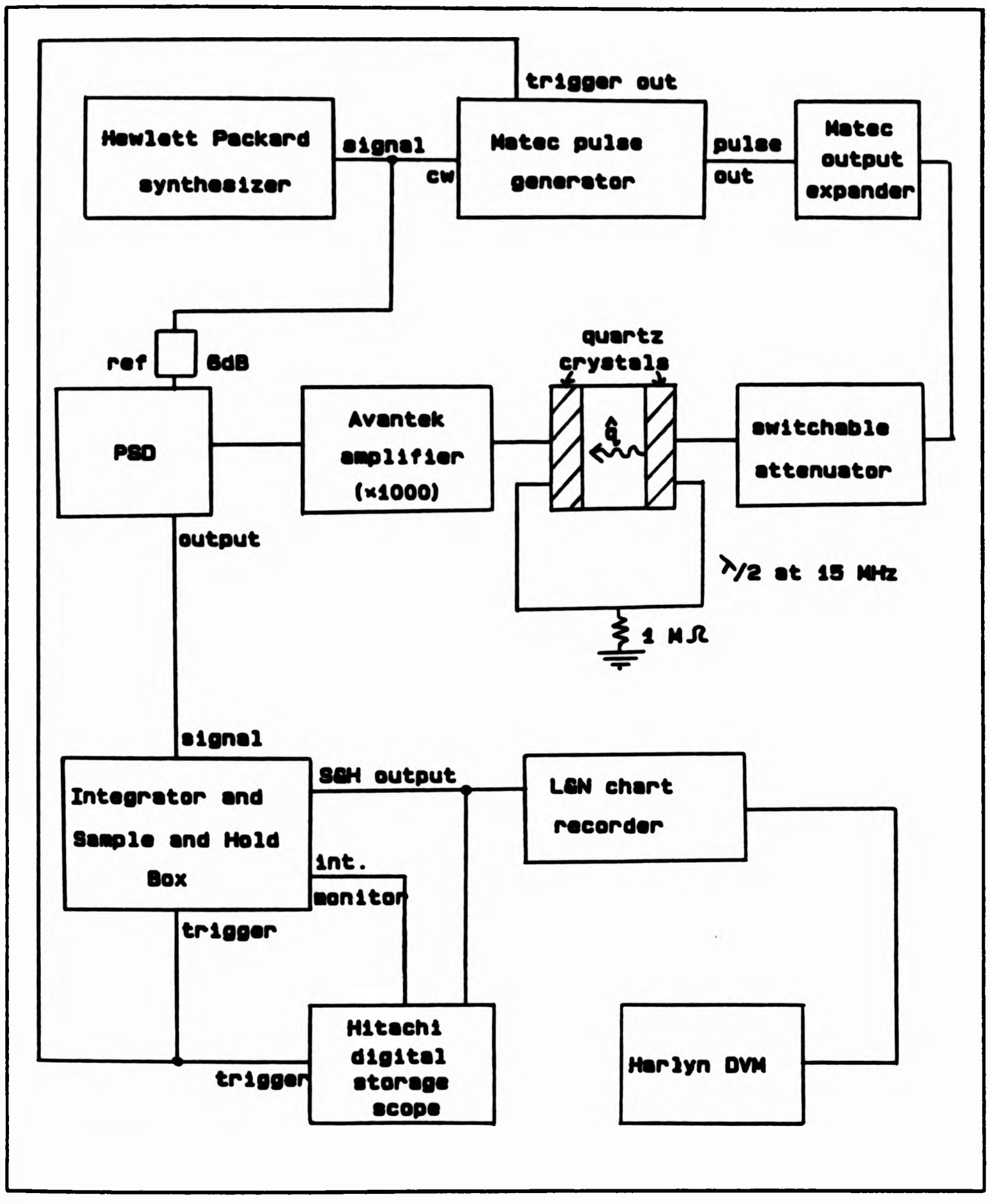

FIG 2.9 : Block diagram of sound transmission and detection electronics

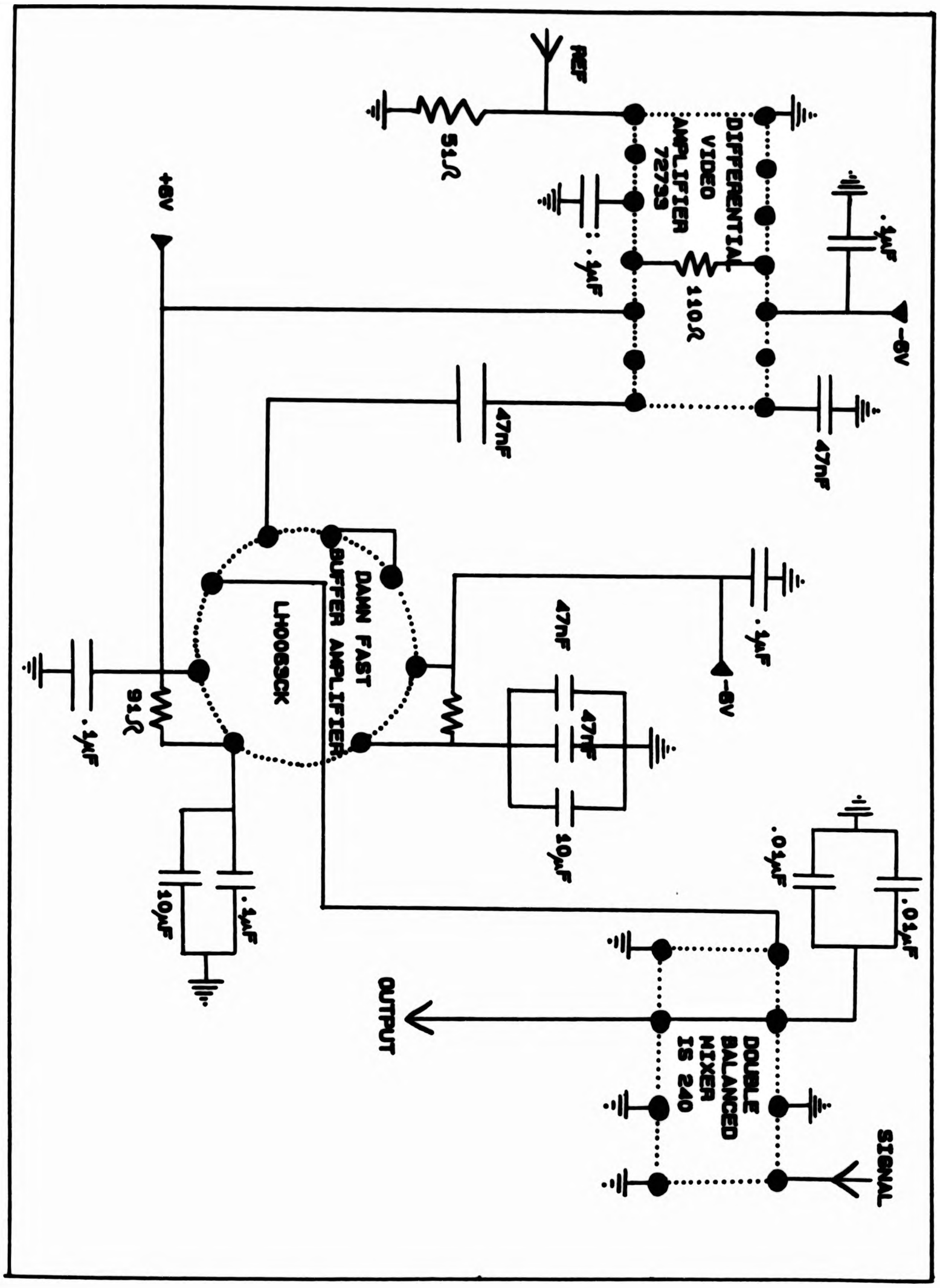

FIG 2.10 : Circuit diagram for double balanced mixer acting as a phase sensitive detector

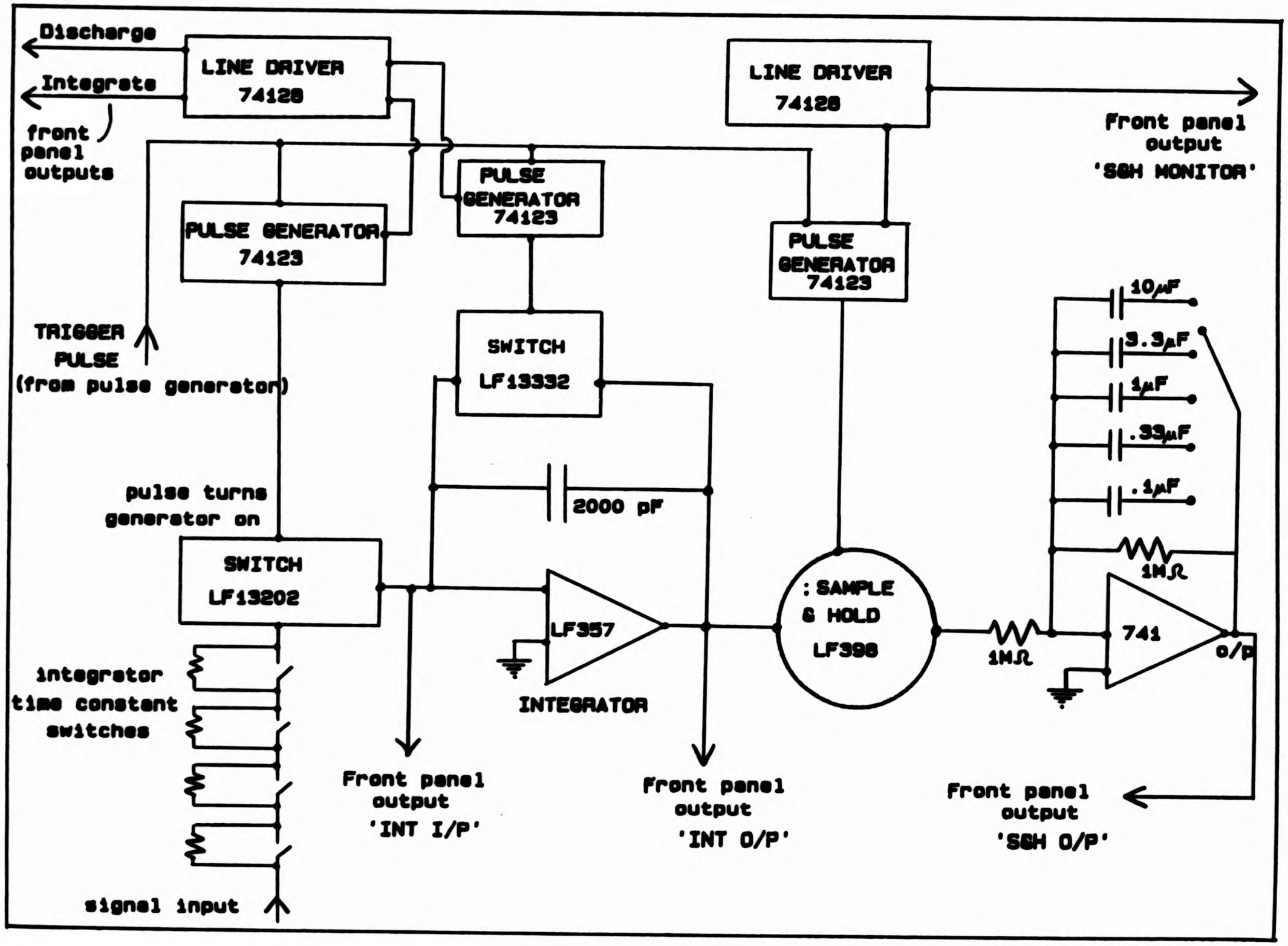

FIG 2.11 : Block diagram of integration circuitry

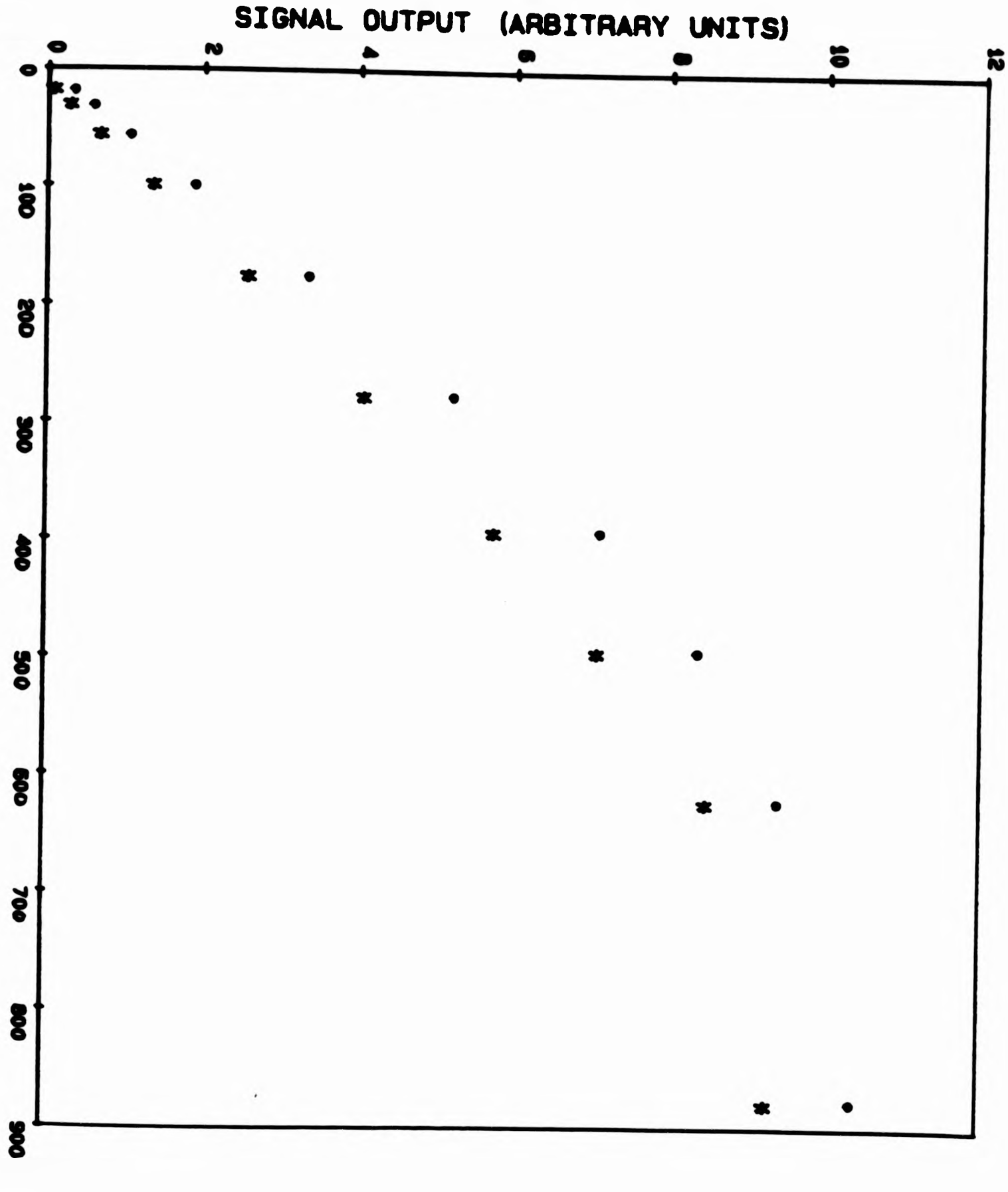

FIG 2.12 : Phase sensitive detector/integration circuitry response for different magnitude input signals. * at 5.05MHz, ● at 15.154MHz. For signals of order 100mV input during course of experiment PSD/integration circuitry was operating in its linear region.

cell. Henceforth the signal measured without this cable present will be referred to as "in phase" and that measured with this cable in the PSD reference as "quadrature".

The integrated signal was displayed on a Leeds & Northrup Speedomax 250 multichannel chart recorder(27). An Hitachi digital storage oscilloscope(28) was used for diagnostics.

2.4 The Magnetic Coil System

A schematic diagram of the magnetic coil system, and its positioning with respect to the experimental cell and the Mu metal shield used for screening the cell from external fluxes, is shown in Figure 2.3. A solenoid and two sets of saddle coils were constructed allowing the application of a magnetic field to the ^3He in any direction and providing the facility for a rotating field to be applied about any axis.

2.4.1 Construction

The wire used for each of the coils was insulated single filament NbTi copper clad superconducting wire with an outer diameter of 0.1 mm(29).

The solenoid coil was wound on a cylindrical former made from stycast 1266 with a wall thickness of 0.25 mm and a diameter of 2.3 cm. The former had a lip at the top, and a wider base with which the coil could be bolted down onto the brass cell flange. The coil windings were lightly painted with stycast 1266 to hold them in place more securely. Lengths of approximately 2 cm of the lead at either end of the coil were stripped of

insulating varnish, wrapped a few times around a 0.9 mm thick stripped "Niomax"(30) post and soldered in place. The Niomax post was then stuck onto the top of the former with stycast 1266. This was done for each of the 5 coils wound as a back-up measure in case of fine lead breakage.

Each of the inner pair of saddle coils was wound separately around 4 stycast 1266 posts stuck onto a stycast 1266 cylindrical former of approximately 2.5 cm diameter and 0.25 mm thick. Figure 2.13 illustrates the shape of the coil obtained in this way. The four leads were attached to niomax posts as described above. The coil former was slipped over the solenoid coil and held in position with a few dabs of vacuum grease(31) at its base.

The pair of outer saddle coils were wound in a similar manner on a cylindrical stycast 1266 former of approximately 2.8 cm diameter and 0.25 mm thick. The coil former was slipped over the inner saddle pair and orientated by eye in an attempt to produce a $\pi/2$ difference in the direction of the magnetic field produced by each pair. This former was also held in position with a few dabs of vacuum grease at its base.

The entire coil system had an inner diameter of 2.2 cm, an outer diameter of about 3.6 cm and a height of about 5 cm.

2.4.2 The Solenoid Coil

For a solenoid which is long compared to its diameter the magnetic field on-axis at its centre is given by $B = \mu_0 ni$ where n is the number of turns/unit length, i is the current flowing through the wire and μ_0 is the

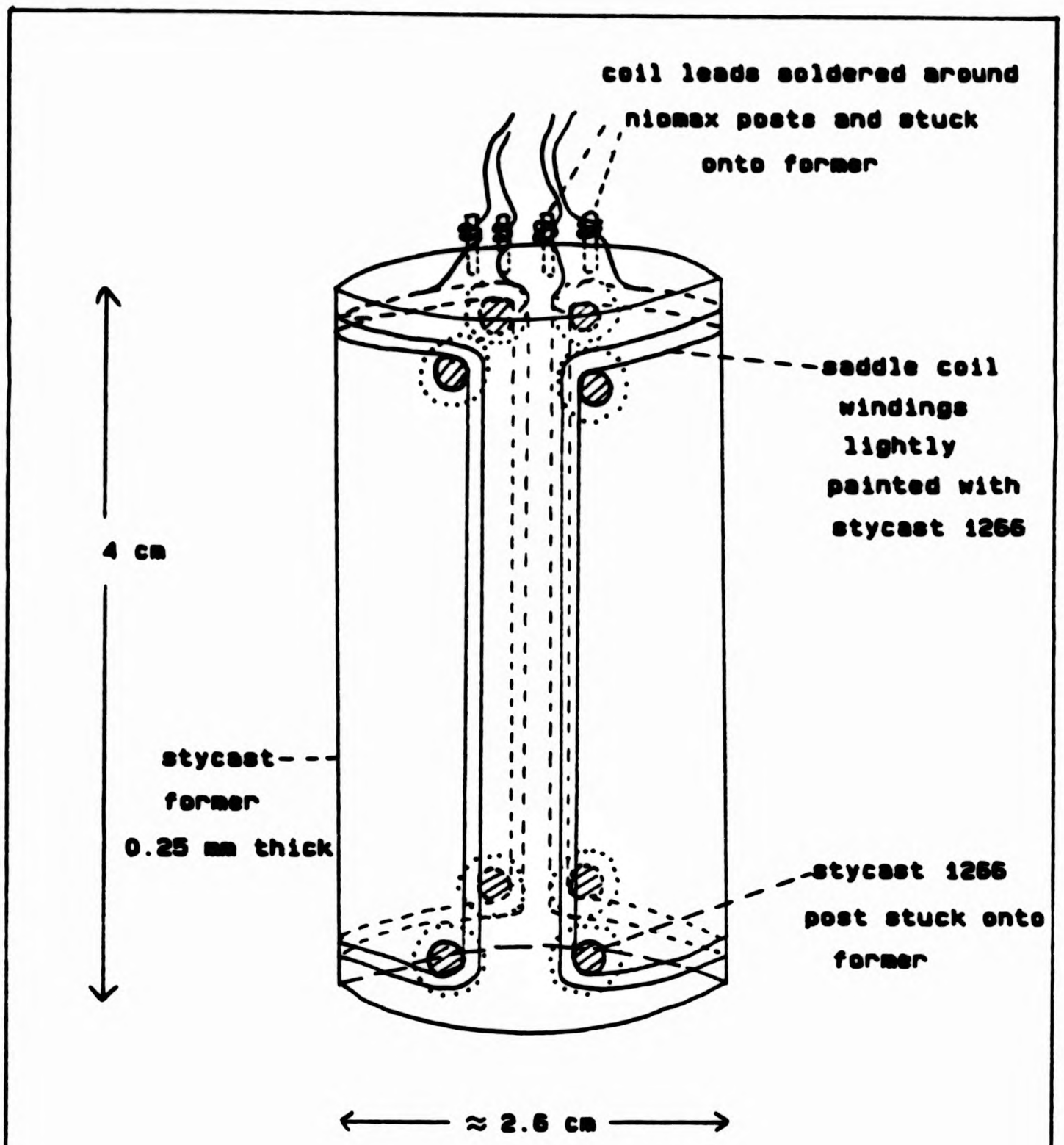

FIG 2.13 : Schematic diagram showing ' bent rectangular' pair of saddle coils.

permeability of free space. 323 turns were wound onto the solenoid coil former in one layer, corresponding to a calculated magnetic field constant of 114 G/A.

The field profile and field constant of the solenoid were measured using a planar search coil which had 30 turns of 0.06 mm diameter high conductivity copper and a cross-sectional area of 2.03×10^{-5} m^2 ($\pm$ 1%). An a.c. method was used since a search coil voltage of a few μV produced by a few mA flowing in the solenoid coil could be easily detected using a lock-in amplifier, thus enabling the room temperature current through the superconducting wire to be limited. The field profile of the solenoid was measured both along its central axis and across a horizontal slice at a vertical height corresponding to the approximate position of the cell ^{3}He. Figures 2.14 and 2.15 show these profiles. The field was observed to change by < 1% along the coil axis over the vertical region occupied by the cell ^{3}He, and by 1-2% across the horizontal region it occupied. The field constant of the coil at a position corresponding to the centre of the experimental ^{3}He region was measured by recording the voltage induced in the search coil for several different a.c. currents flowing through the solenoid, and for several different frequency sine waves. Using $B_o = V_{rms}/NA\omega$ where N is the number of turns on the search coil, A is its cross-sectional area and V_{rms} is the search coil signal which would be obtained with 1 A flowing through the solenoid, this measurement gave a value of 111 G/A ($\pm$ 3%). A value of 117 G/A ($\pm$ 3%) was measured with the solenoid placed in position inside the Mu metal shield.

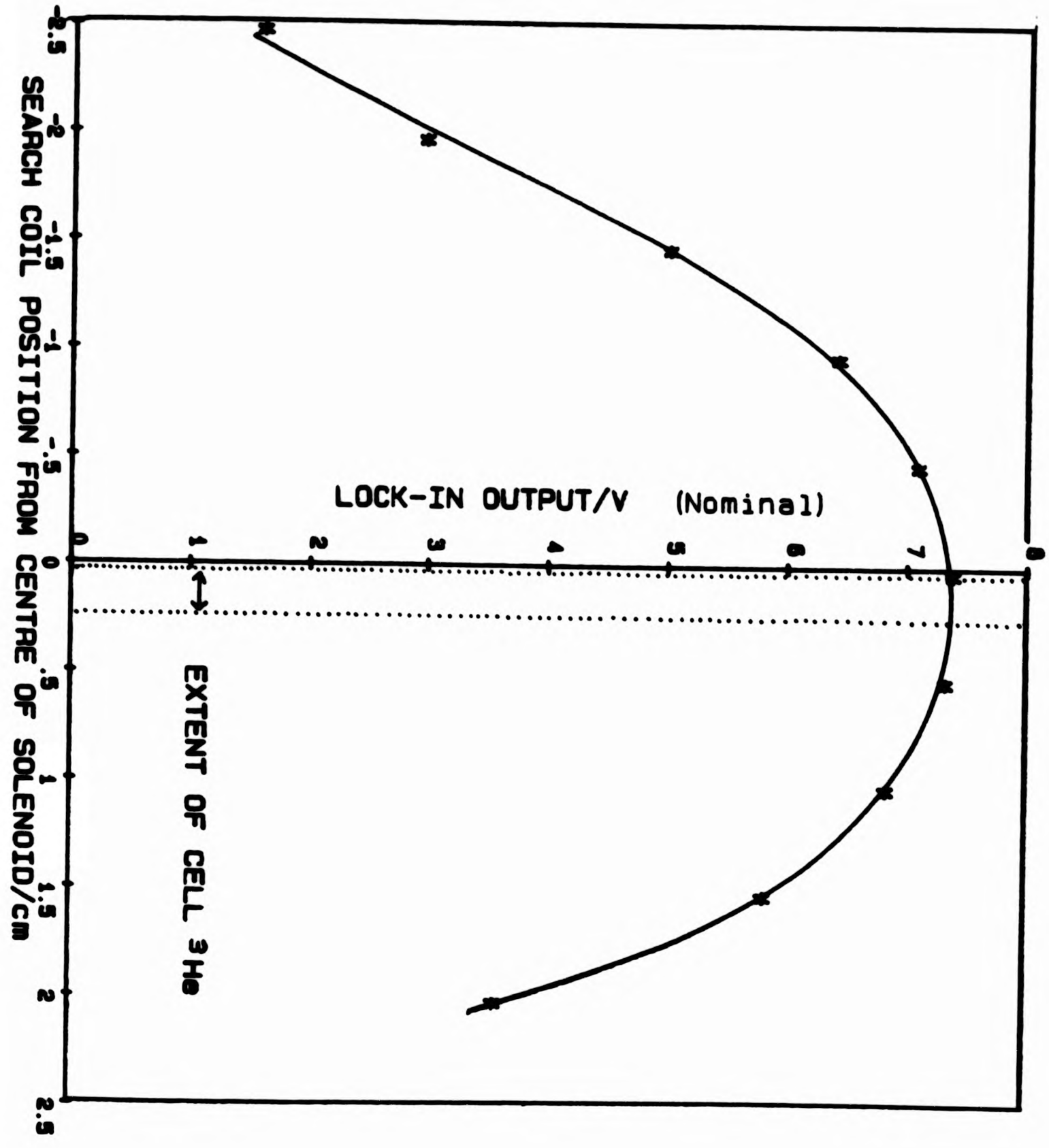

FIG 2.14 : Solenoid coil field profile measured along central axis. Field changes by <1% over vertical region occupied by cell ^{3}He. The solid line acts as a guide to the eye.

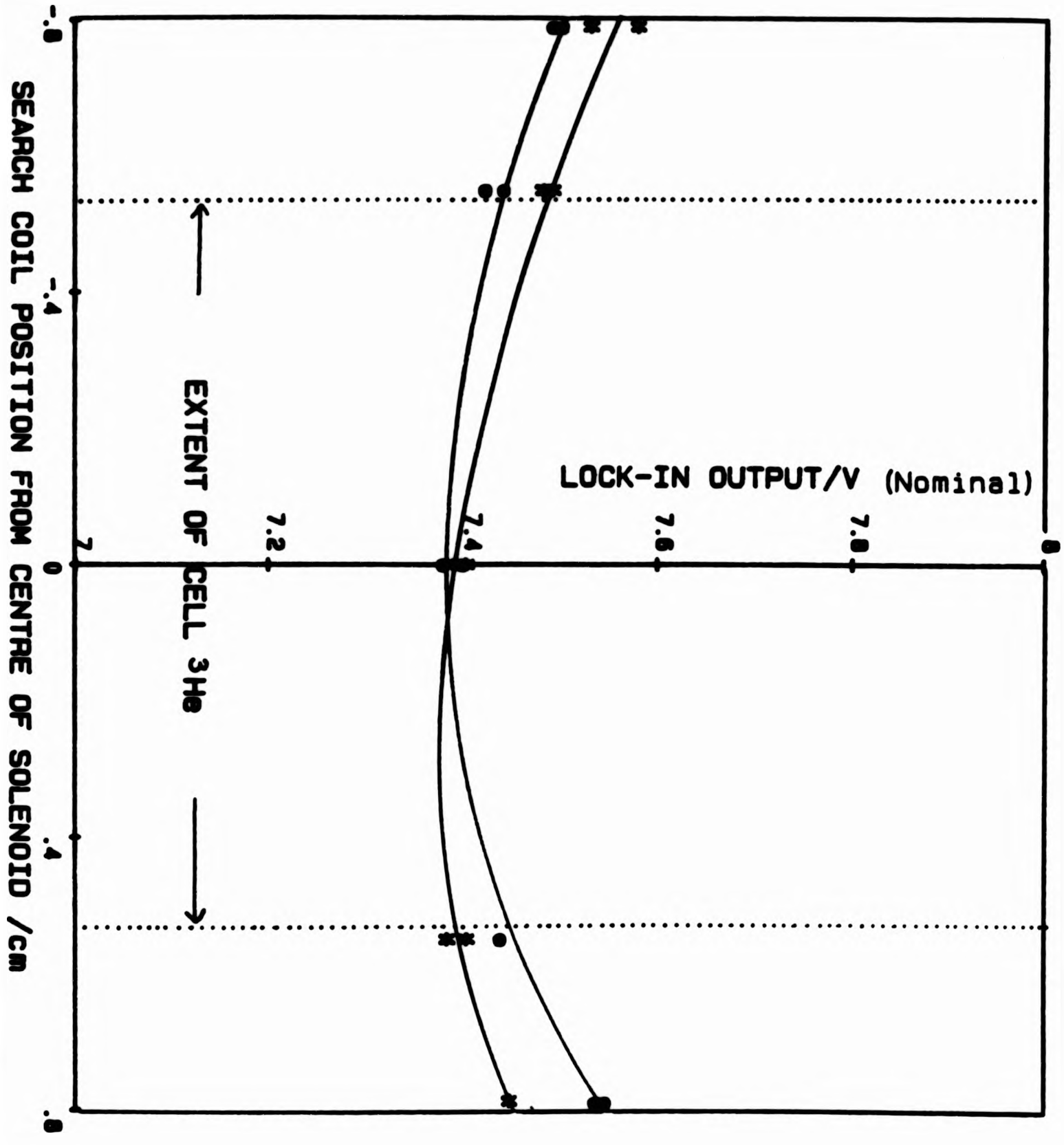

FIG 2.15 : Solenoid coil field profile measured across a horizontal slice at a vertical height corresponding to approx. position of cell ^3He .Profile was measured along 2 perpendicular axes. Field changes by 1-2% over horizontal region occupied by cell ^3He. The solid lines act as guides to the eye.

2.4.3 The Saddle Coils

Ideally the two sets of saddle coils should have been made as Helmholtz pairs in order to maximise the field homogeneity. In pratice this was not possible because of the limited space available coupled with construction difficulties. Therefore each coil of each pair was wound around posts on a cylindrical former producing a "bent rectangular" shape for the windings as illustrated in Figure 2.13. A set of calculations was executed to find expressions for the variation in the off-axis field, with respect to the field at the centre, for a set of saddle coils with this shape. These expressions were minimised by suitable choice of design parameters, before construction of each saddle pair. Details of these calculations are contained in Appendix A.

Comparison of the calculated magnetic field at the centre of a Helmholtz pair system and at the centre of the system described above shows similar expressions

$$B_{Helmholtz} = \frac{8}{\sqrt{125}} \frac{\mu_o N i}{r} \qquad (2.1)$$

where N is the number of turns on each coil and r is the coil radius which is also 1/2 the coil separation.

$$B_{bent\ rect} = \frac{3 \sin\Phi}{\sqrt{2}\ \pi} \frac{\mu_o N i}{R} \qquad (2.2)$$

where 2Φ is the angular extent of the curved sections, N is the number of turns on each coil and R is the radius of the curved sections (which has been equated with 1/2 the separation of the curved sections of the same coil for this equation). All other symbols have their usual meanings.

For each of the inner saddle pair 106 turns were wound onto the cylindrical former as described in section 2.4.1, with an estimated R = 1.27 cm, d (1/2 the coil height) = 1.9 cm and Φ = 61°, chosen with reference to the calculations discussed in Appendix A. This gave a calculated field constant of 63 G/A for the pair. For each coil of the outer saddle pair 118 turns were wound onto the cylindrical former with an estimated R = 1.42 cm, d = 1.9 cm and Φ = 59°, chosen with reference to the calculations discussed in Appendix A. This gave a calculated field constant of 62 G/A for the pair.

The field profile of each set of saddle coils separately was measured, both along the central axis of the former and across a horiontal slice at a vertical height corresponding to the experimental ^3He region, using the search coil as described in section 2.4.2. Figures 2.16-2.19 show the profiles measured. The field was found to vary by < 1% and 1-2% for fields produced by the inner and outer saddle coils respectively along the solenoid coil axis over the vertical region occupied by the cell ^3He. Across the horizontal region occupied by the ^3He the field was found to change by about 3% and 3-5% along and perpendicular to the saddle coil axis for each of the inner and outer pairs respectively. For these and all the remaining measurements described in this section the two coils of each pair were soldered together in series. The field constant for each set of saddle coils was measured at the same vertical height in a similar manner to that described in section 2.4.2. Values of 80 G/A (± 3%) and 66 G/A (± 3%) were obtained without the Mu metal shield in postion for the inner and outer pairs respectively. The most probable reason for the difference of these measured field constants from the theoretical estimates is that the coils wound in practice did not have the exact shape indicated in Figure

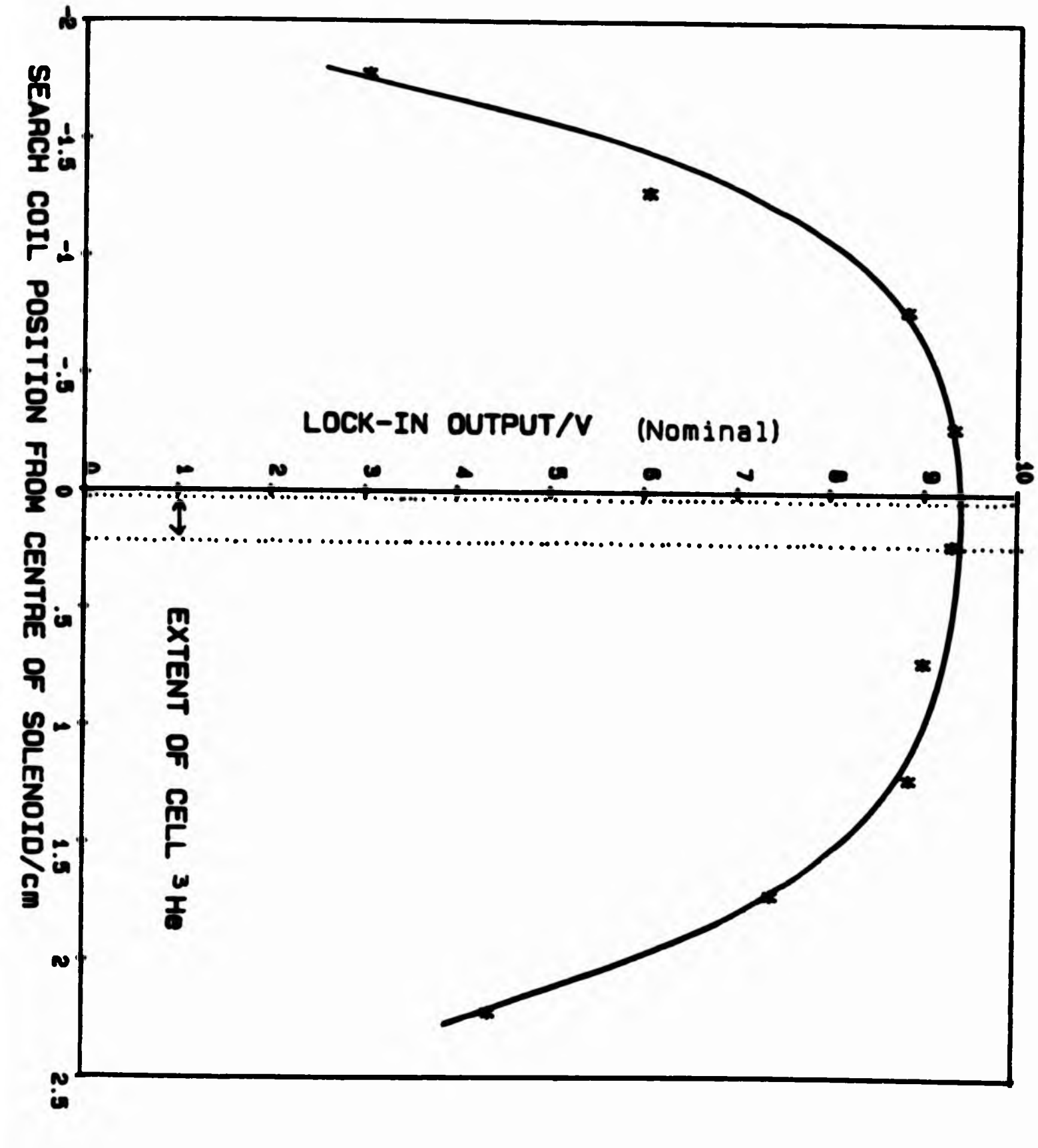

FIG 2.16 : Inner saddle coils field profile measured along central axis of solenoid coil. Field changes by <1% over vertical region occupied by cell ^{3}He. The solid line acts as a guide to the eye.

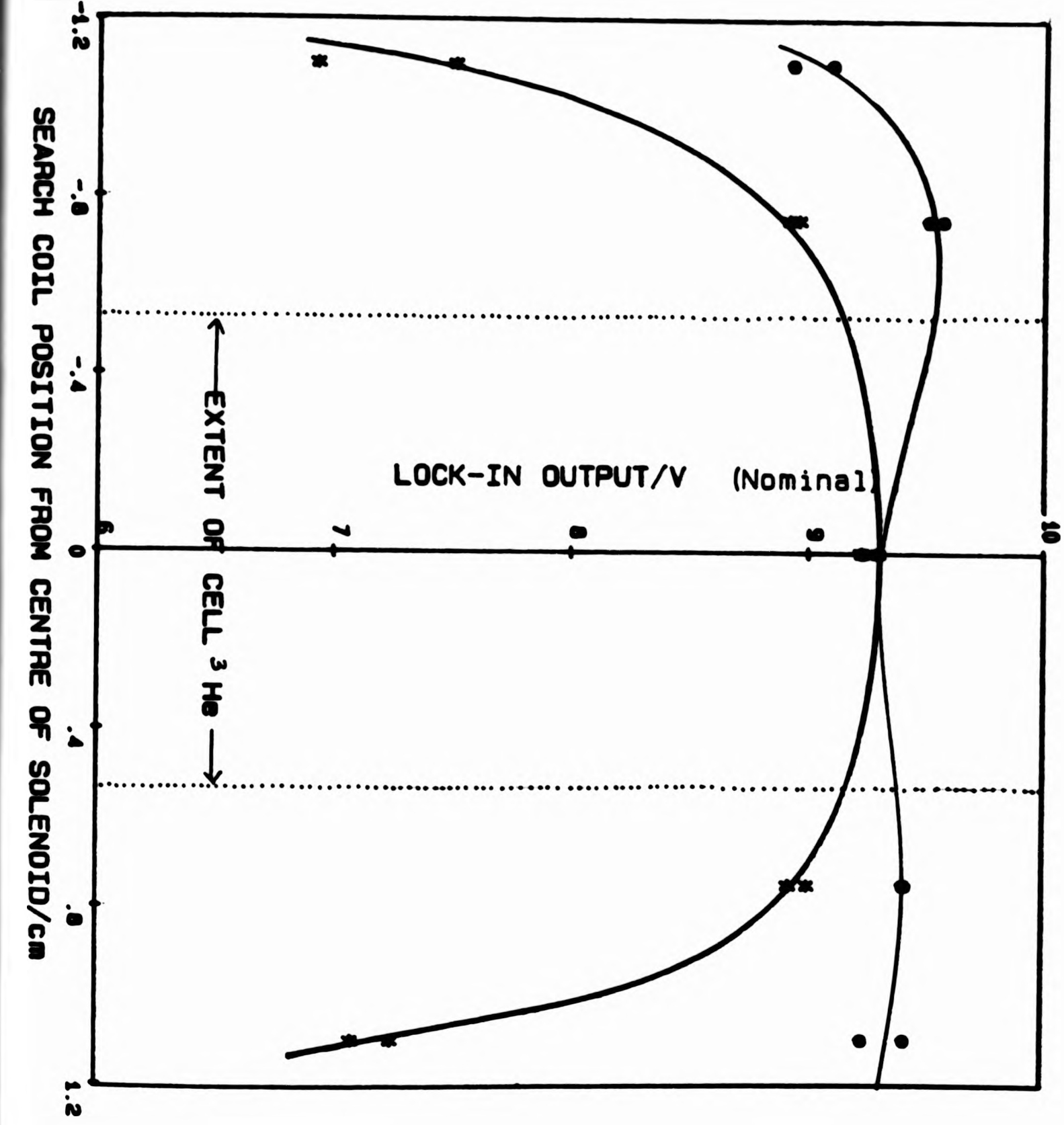

FIG 2.17 : Inner saddle coils field profile measured across a horizontal slice at a vertical height corresponding to approx. position of cell ^{3}He. Profile was measured along 2 perpendicular axes. Field changes by 3% over horizontal region occupied by cell ^{3}He. The solid lines act as guides to the eye.

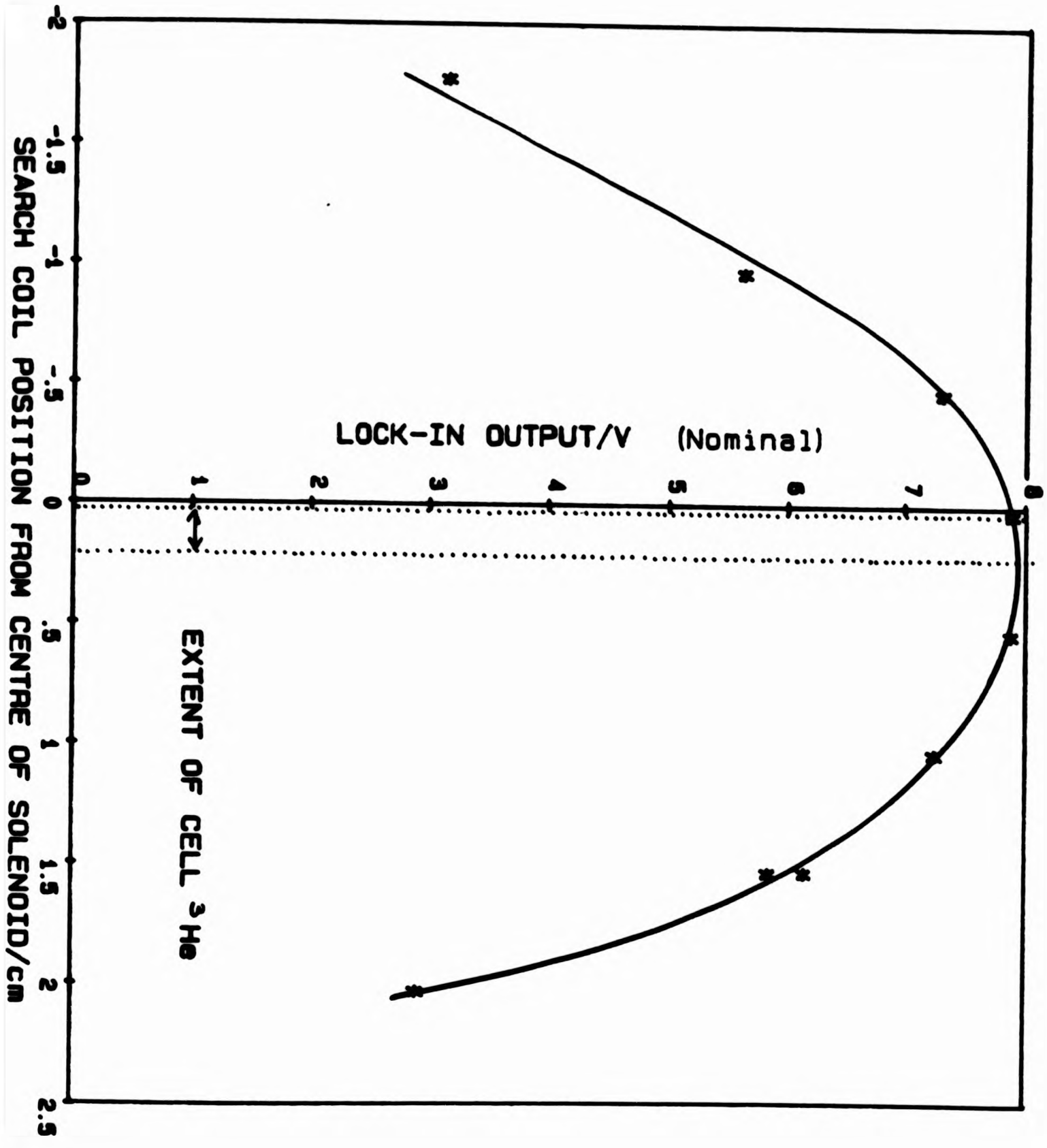

FIG 2.18 : Outer saddle coils field profile measured along central axis of solenoid coil. Field changes by 1-2% over vertical region occupied by cell ^{3}He. The solid line acts as a guide to the eye.

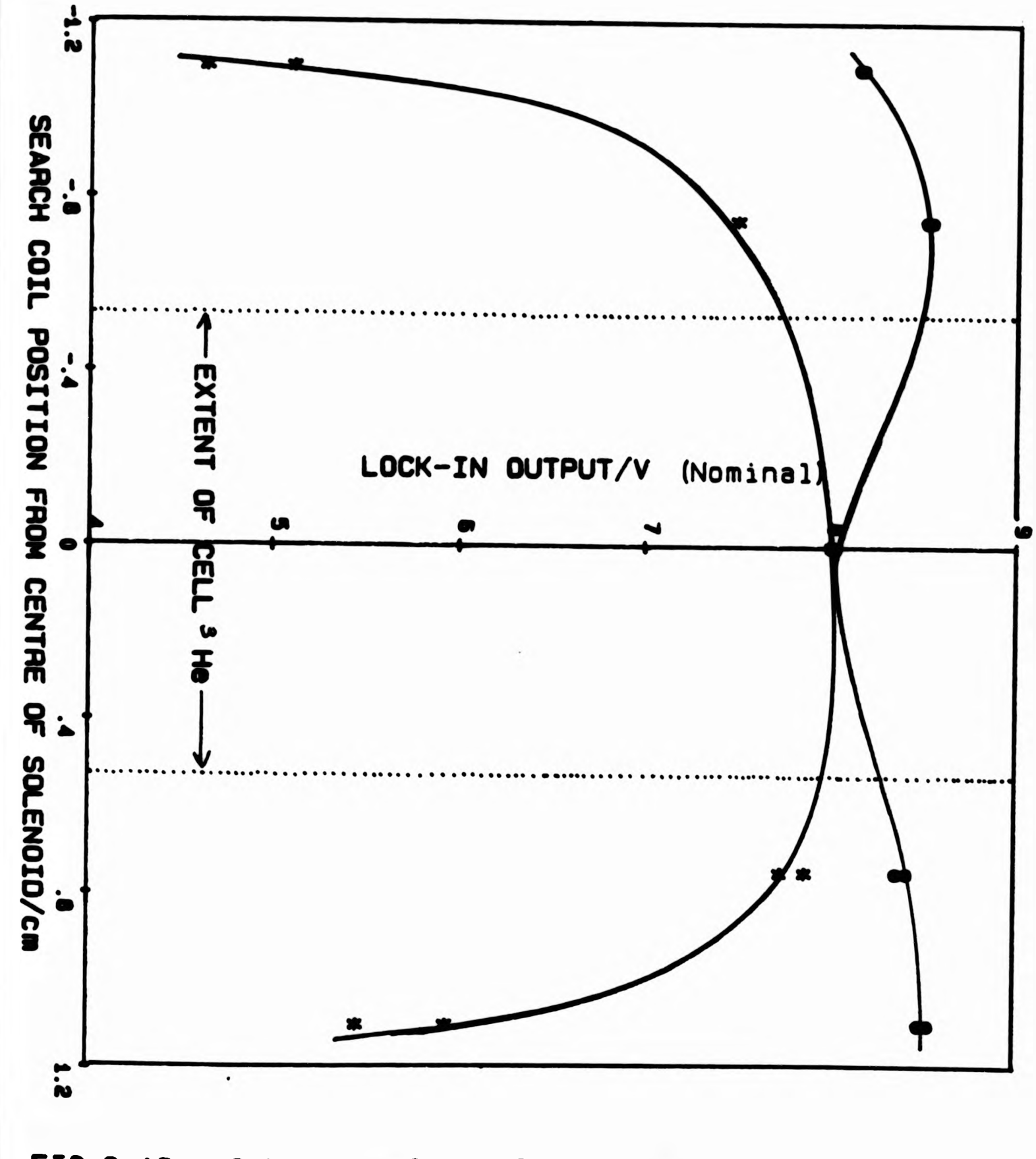

FIG 2.19 : Outer saddle coils field profile measured across a horizontal slice at a vertical height corresponding to approx. position of cell ^{3}He. Profile was measured along 2 perpendicular axes. Field changes by 3-5% over horizontal region occupied by cell ^{3}He. The solid lines act as guides to the eye.

2.13, but, for example, had rounded corners.

The entire coil system was positioned within the Mu metal shield and the saddle coil field constants were remeasured to be 98 G/A (± 3%) and 90 G/A (± 3%) for the inner and outer sets of coils respectively. The angular position of the maximum field for each set of coils was measured, and an angular difference in the maxima of 89.5° ± 0.5° was found. Table 1 gives a summary of the magnetic field constants for all three sets of coils.

2.4.4 Coil Leads and Power Supplies

All the magnetic field coils were wound from superconducting wire which had a copper matrix. The conductive heat leak to the cell along this matrix would be too great if the windings were in thermal contact with the cell. Therefore the coil system was thermally attached to the mixing chamber of the dilution refridgerator (by the wire itself) and bolted onto the cell flange using thermally insulating vespel SP22(32) washers and bolts. Appendix B contains an estimation of the conductive heat leak to the cell with this arrangement.

The 10 magnet leads were led away from the coils as 5 twisted pairs, each varnished together with G.E. varnish(33) and threaded through a 0.8 mm diameter teflon tube for thermal insulation from the cell region. All 5 pairs were heat sunk at the dilution refridgerator mixing chamber by wrapping a few cm length several times around an OFHC copper post which screwed into the mixing chamber and varnishing down with G.E. varnish. The two members of each of the inner and outer saddle coils were joined in

series using a "crimped joint" at the mixing chamber. (To make a "crimped joint" between two wires their insulating varnish was removed, the copper matrix of the superconducting wire was dissolved away with a solution of 50% nitric acid in 50% water, and the NbTi conductor was cleaned with a mixture of 25% HF acid, 25% nitric acid and 50% water. The inside of a narrow niobium tube was cleaned with the same mixture and the wires were threaded into either end of the tube. This was then crushed flat, securing the wires in place. This joint should be superconducting at low temperatures thus eliminating the Joule heating associated with currents flowing through soldered joints.) The three remaining pairs of magnet leads were joined to 0.06 mm diameter niomax wire(30) using crimped joints, and led up and out of the vacuum can with a heat sink at the refridgerator 6th heat exchanger. Three twisted pairs of copper leads were used to extend the coil leads from the cryostat vacuum can to the coil power supplies.

Each set of coils could be attached to any of the three supplies as required by the measurement being performed. One of the power supplies consisted of a current ramp source capable of delivering 350 mA in a maximum of 60 minutes. An Oxford Instruments voltage ramp(33) and a Feedback 2-channel oscillator(34) were also used as coil power supplies by converting their outputs into currents using a 759 power operational amplifier in each case. Figure 2.20 shows the circuit used. Great care was taken to ensure that this operational amplifier circuit remained stable with the coil inductive load attached, since the change in phase this produced in the feedback loop was otherwise enough to set up voltage oscillations in the feedback loop resulting in severe warming of the liquid helium. The dilution refridgerator's performance was found to be

series using a "crimped joint" at the mixing chamber. (To make a "crimped joint" between two wires their insulating varnish was removed, the copper matrix of the superconducting wire was dissolved away with a solution of 50% nitric acid in 50% water, and the NbTi conductor was cleaned with a mixture of 25% HF acid, 25% nitric acid and 50% water. The inside of a narrow niobium tube was cleaned with the same mixture and the wires were threaded into either end of the tube. This was then crushed flat, securing the wires in place. This joint should be superconducting at low temperatures thus eliminating the Joule heating associated with currents flowing through soldered joints.) The three remaining pairs of magnet leads were joined to 0.06 mm diameter niomax wire(30) using crimped joints, and led up and out of the vacuum can with a heat sink at the refridgerator 6th heat exchanger. Three twisted pairs of copper leads were used to extend the coil leads from the cryostat vacuum can to the coil power supplies.

Each set of coils could be attached to any of the three supplies as required by the measurement being performed. One of the power supplies consisted of a current ramp source capable of delivering 350 mA in a maximum of 60 minutes. An Oxford Instruments voltage ramp(33) and a Feedback 2-channel oscillator(34) were also used as coil power supplies by converting their outputs into currents using a 759 power operational amplifier in each case. Figure 2.20 shows the circuit used. Great care was taken to ensure that this operational amplifier circuit remained stable with the coil inductive load attached, since the change in phase this produced in the feedback loop was otherwise enough to set up voltage oscillations in the feedback loop resulting in severe warming of the liquid helium. The dilution refridgerator's performance was found to be

unaffected by the input of up to 50-60 mA current into each set of coils simultaneously, which produced a magnetic field of approximately 10 G across the ^{3}He slab.

TABLE 1 : FIELD CONSTANTS FOR EXPERIMENTAL COILS

COIL	FIELD CONSTANT (G/A) (±3%) measured without Mu metal shield	FIELD CONSTANT (G/A) (±3%) measured in position inside Mu metal shield
SOLENOID	111	117
INNER SADDLE PAIR	80	98
OUTER SADDLE PAIR	66	90

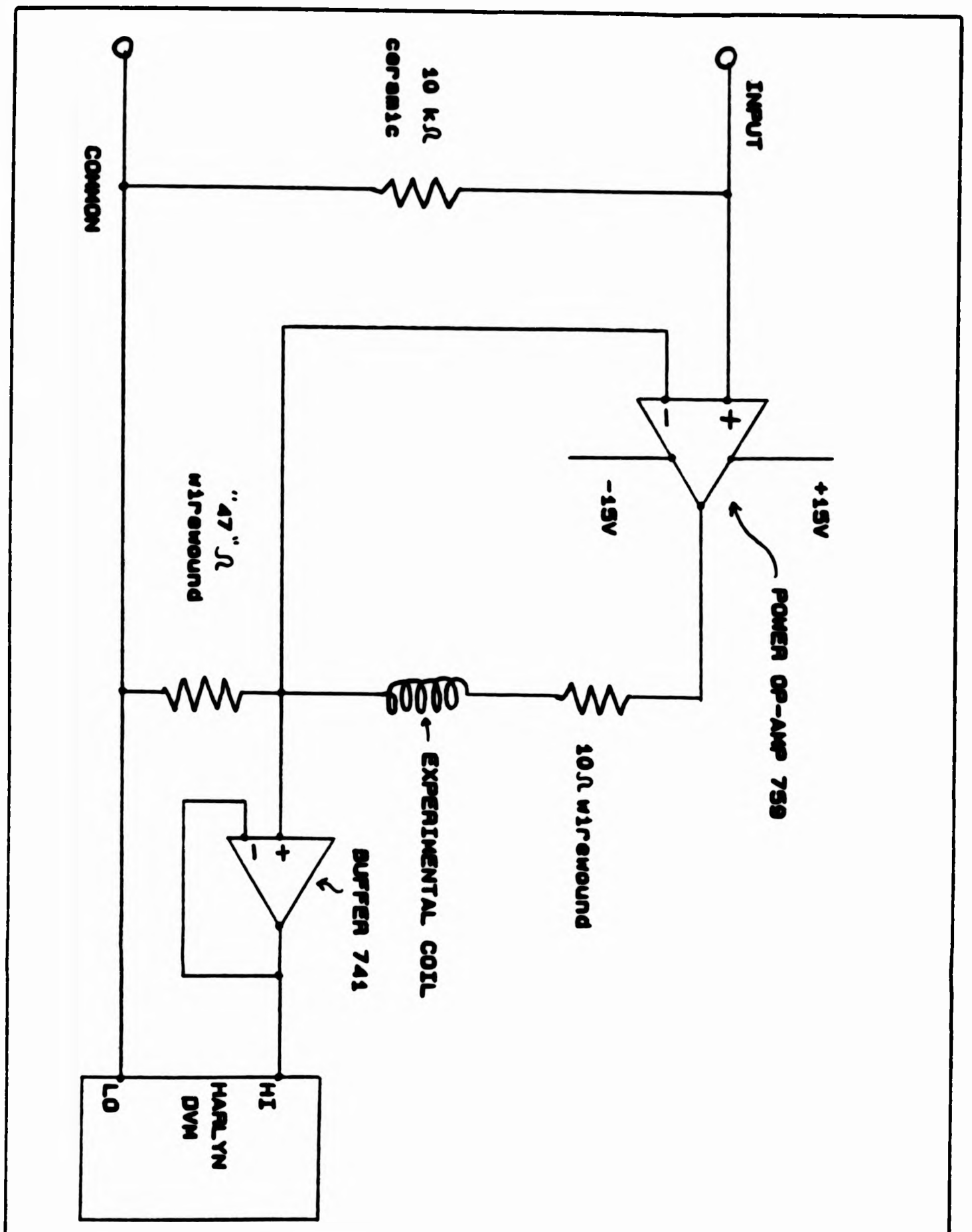

FIG 2.20 : One of two identical power operational amplifier circuits used to convert voltages into currents flowing in an experimental coil.

2.5 The Mu Metal Shield

This was used to shield the cell/coil system from fields external to the experiment. "Mu metal" is a Ni-Fe alloy with a large permeability and very little hysteresis so that any external flux is trapped out. It has to be specially treated for low temperature use since hysteresis depends on movement of domain walls. A superconducting shield could not be used for this purpose since flux created by thermal emfs would be trapped as the metal cooled.

The "Cryoperm 10/4.2" used was supplied by "Vacuumschmelze"(17) in a 1 mm thick annealed sheet form. The metal was rolled into a cylinder, with an outer diameter of 4 cm and height of 5.5 cm, and butt welded using an argon torch. The prepared cylinder was sent back to "Vacuumschmelze" for heat treatment to restore the metal's shielding properties.

The shield was slipped over the magnetic field coils and attached to the cell brass flange with 6 × 10BA brass screws through holes which had been drilled in the metal shield. It was therefore in thermal contact with the cell but not with the magnetic field coils.

The shield was designed with intention to maximise its magnetic shielding capabilities within the limited experimental space available. Appendix C contains the calculations that were performed for this purpose.

2.6 The Microcomputer Interface

Throughout the course of the experiment an analogue record of both the integrated sound signal and the signal from the LCMN-SQUID thermometry electronics (see chapter 3) was obtained using a multichannel recorder. However, in addition to this the sound signal could be digitised, averaged as required, and stored on cassette. This proved particularly useful when the magnetic field applied to the helium was being altered since a voltage proportional to this field could be stored in addition to the sound signal.

This data handling system is shown schematically in Figure 2.21. The sound and field voltages were fed to a Harlyn multichannel analogue to digital interface module(35), then along an IEEE-488 interface bus to a Nascom II microcomputer(36). The interfacing was performed using circuitry based on a Texas TMS9914 interface chip with the timing of the data management handled by a real time clock microchip. The computer was positioned outside the shielded enclosure to avoid warming of the cryostat by the rf radiation it generated. Hard wire contact between the two sides of the shielded enclosure was avoided by using a custom built opto-isolator interface(37) on the IEEE-488 bus.

A listing of the data handling program used is given in Appendix D.

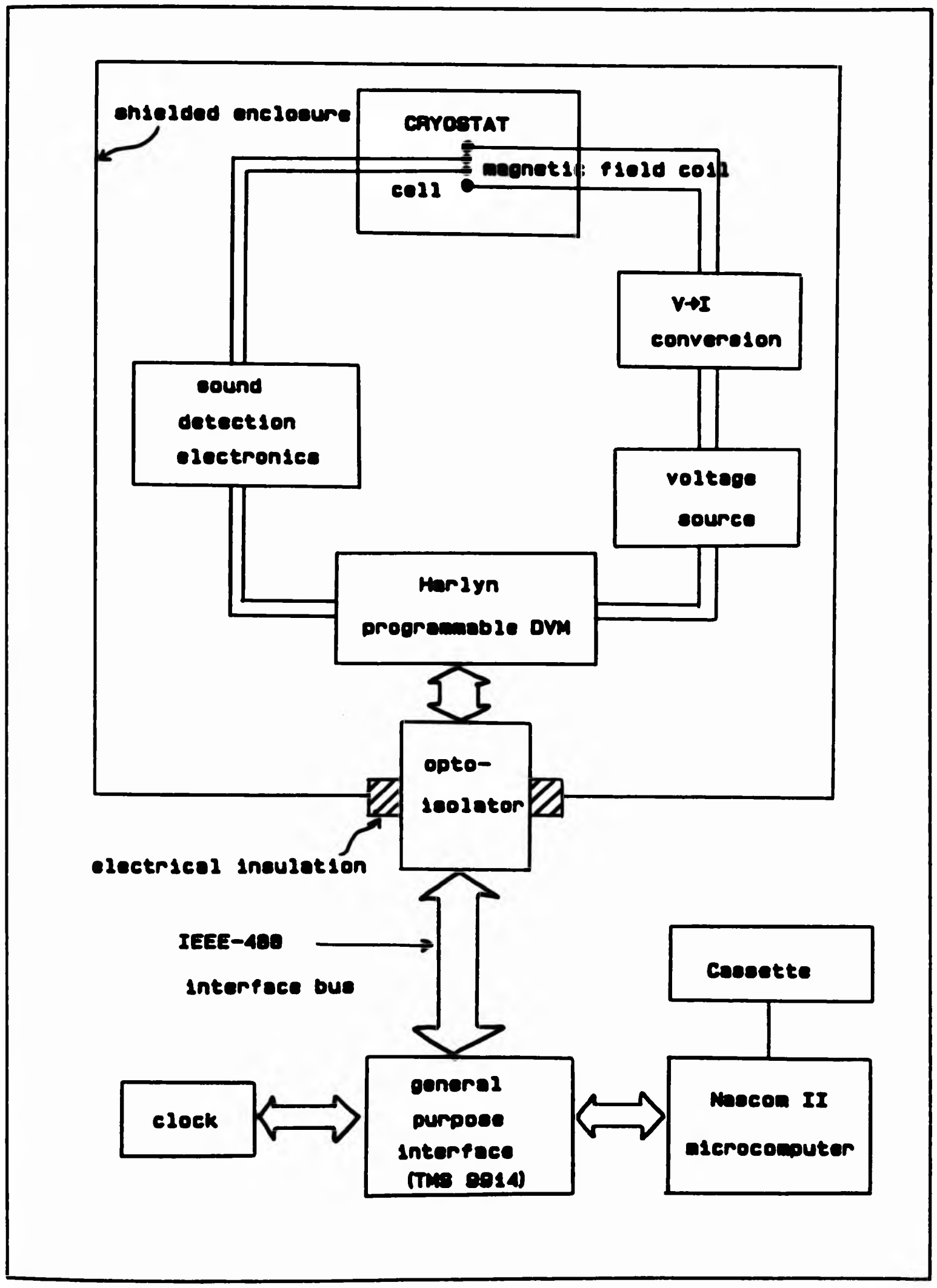

FIG 2.21 : DATA HANDLING SYSTEM

CHAPTER 3: THERMOMETRY

3.1 Introduction

In any experiment carried out in the millikelvin temperature range unreliable thermometry is a potential problem. In an attempt to overcome this a Manchester temperature scale has been established using a ^{3}He melting curve thermometer and a platinum NMR thermometer to calibrate an LCMN thermometer in the range 1 to 22 mK. Section 3.3 contains a description of the melting curve thermometer and a brief discussion of this process.

Different valued carbon Speer resistors(38) were used to monitor the performance of the cryostat in cooling to approximately 16 mK. Resistance measurements were made with an ac bridge circuit and good reproducibilty was observed for all demagnetisation cycles. Below 16 mK, the temperature of the ^{3}He was measured using an LCMN thermometer. This also provided a sensitive determination of the superfluid transition temperature by indicating the change in heat capacity associated with the 2nd. order phase transition. The LCMN thermometer is discussed in section 3.2 with calibration details contained in section 3.4. The sound signal received from the experimental cell also clearly indicated the ^{3}He superfluid transition.

There was some evidence for believing that the temperature of the ^{3}He in the experimental cell was greater than that in the main ^{3}He reservoir in which the LCMN thermometer was situated. Discussion of this

and the calibration of the temperature of the ^3He in the experimental cell are contained in section 3.5.

3.2 The LCMN Thermometer

This thermometer expoits the temperature dependence of the magnetic susceptibily of paramagnetic cerium ions contained in a sample of LCMN. It was constructed by Peter Alexander.

Changes in susceptibilty were determined at 60 Hz by a bridge using a flux locked loop rf SQUID system as null detector. Doping with diamagnetic lanthanum magnesium nitrate was necessary to lower the Curie temperature so that magnetic ordering did not occur for T>0.5 mK. Hydrated cerium magnesium nitrate contributed approximately 10% by volume to the right cylindrical pill which had a mass of 0.17g and an 80% packing fraction.

Figure 3.1 shows schematically the LCMN tower which bolted onto the experimental platform using an indium 'o' ring to produce a leak tight seal. The LCMN pill was situated at the base of the tower and was therefore in thermal contact with the liquid helium in the main reservoir.

The thermometer ac mutual inductance bridge circuit is shown in Figure 3.2. Changes in magnetic susceptibility of the LCMN produced a voltage inbalance between the coils of the astatic pair thus generating an alternating current in the primary of the flux transformer at the bridge driving frequency. The current flowing in the SQUID input coil which produced a change in flux linking the SQUID was balanced by the signal

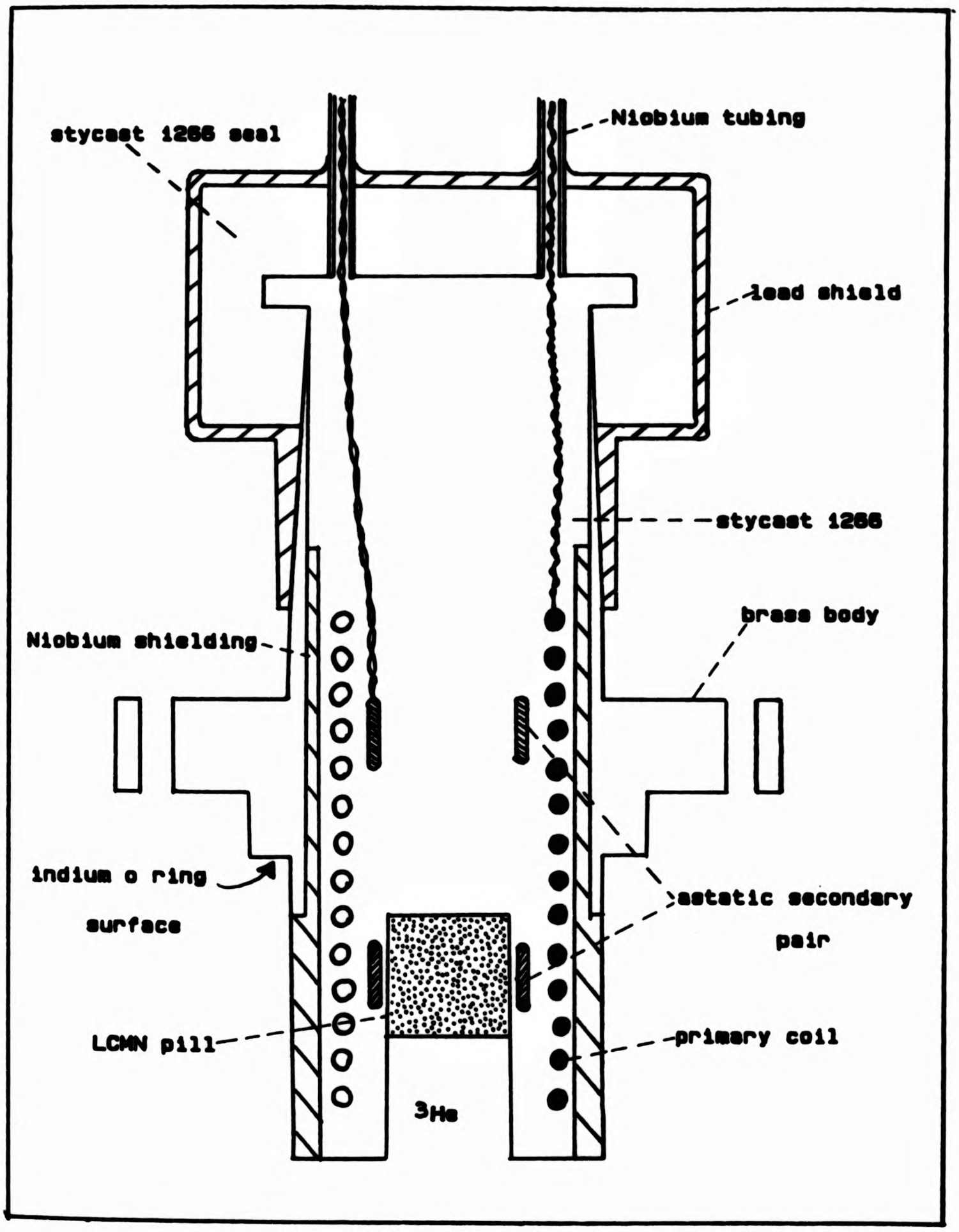

FIG 3.1 : Schematic diagram of LCMN thermometer tower

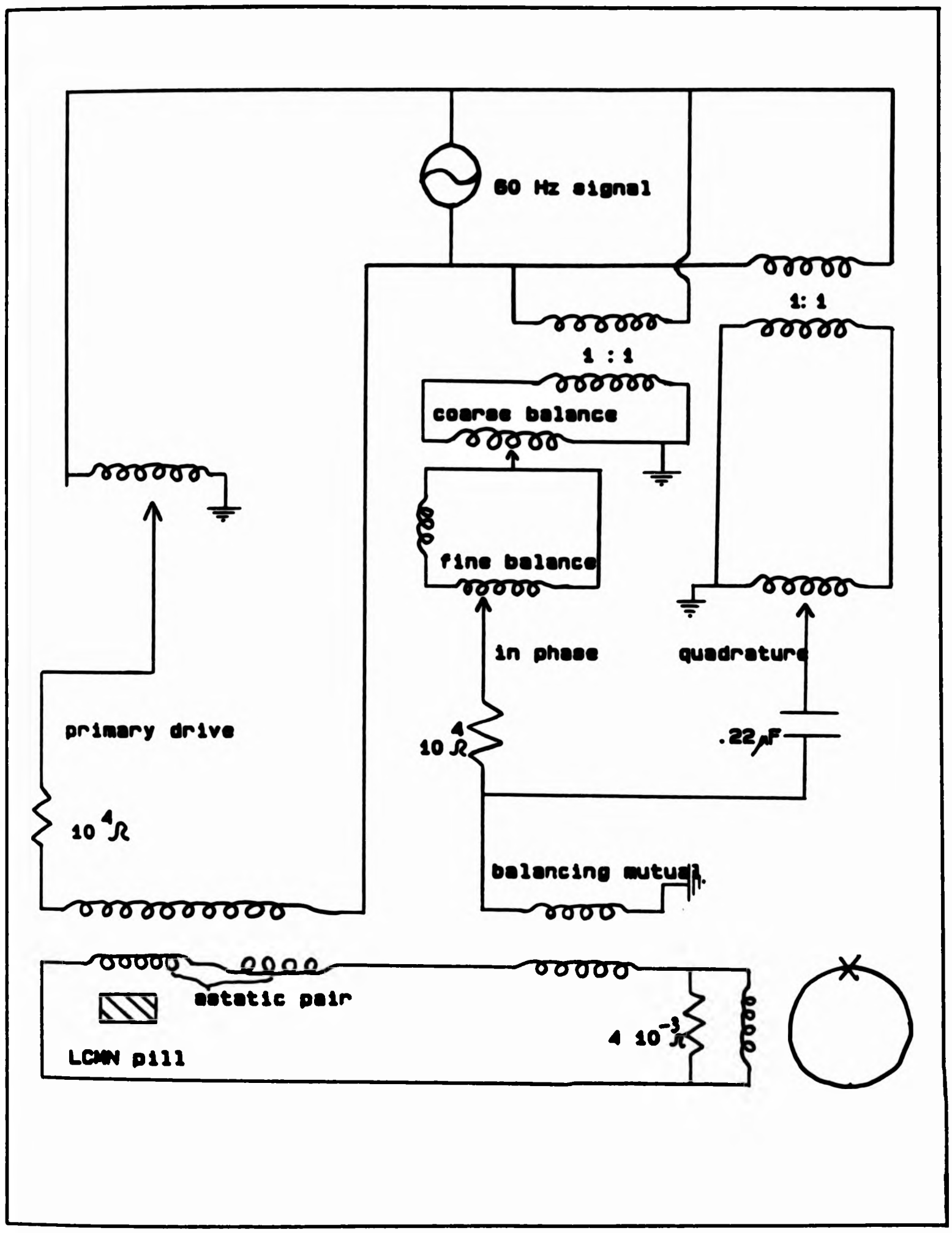

FIG 3.2 : LCMN THERMOMETER ac MUTUAL INDUCTANCE BRIDGE

generated by the balancing mutual. The out of balance signal was detected using a 5205 EG&G Brookdeal lock in amplifier(39) to monitor the SQUID output. Changes in the SQUID output associated with temperature changes of around 1 μK could be detected above the noise in the low millikelvin region. The SQUID probe and SCU300 detection circuitry were supplied by Cryogenic Consultants Ltd.(40). A General Radio audio oscillator provided the bridge drive. Further details about the LCMN thermometer are contained in reference 15.

3.3 The Melting Curve Thermometer

A ^{3}He melting curve thermometer was constructed to help establish a Manchester temperature scale. This thermometer was not used directly in the measurements described here but was necessary to produce the superfluid transition temperature scale shown in Figure 3.3, which was used in the calibration of the LCMN thermometer.

The melting curve of ^{3}He at low temperatures is shown in Figure 3.4(41). The curve possesses a well defined minimum at T_{min}= 318 mK and P_{min}= 29.316 bar(42). An experimental consequence of this is that a tube filled with ^{3}He and passing from a temperature $T<T_{min}$ to $T>T_{min}$ will become blocked with solid as soon as the pressure is increased above P_{min}. This property can be used to seal a fixed number of moles of ^{3}He into a chamber and if the pressure to do this is suitably chosen a mixture of liquid and solid ^{3}He in equilibrium will be present. As the chamber temperature changes the chamber pressure will vary such that the melting curve is followed. Because of the blocked capillary an in situ measurement of the pressure is necessary. This is achieved by making one wall of the chamber

containing the ^{3}He mixture flexible and monitoring changes in deflection of this using a capacitative method.

Figure 3.5 shows the melting curve thermometer schematically. Constructed with a design similar to that described by Greywall and Busch(42), it was bolted to the copper platform on which the experimental cell and LCMN thermometer were mounted. 0.3g of copper powder of nominal size 40 nm was sintered into the chamber of the thermometer to give a surface area of 0.45 m^2 for thermal contact to the 0.11 cm^3 of ^{3}He inside it. Further details about the construction of this thermometer are contained in reference 16.

The operation of this thermometer is described briefly as follows. At around 1K different ^{3}He gas pressures were used to make a pressure vs. capacitance calibration of the thermometer. This is shown in Figure 3.6. Figure 3.7 is from Greywall(42) and shows the density of liquid and solid ^{3}He along the melting curve which can be used to determine the amount of solid in the cell as a function of temperature and starting pressure. The starting pressure here is defined as the constant pressure at which the ^{3}He is cooled through T_{min}. By reference to this Figure, 36 bar was chosen for the starting pressure to ensure a liquid/solid mixture throughout the low mK range, and at around 1K the melting curve thermometer was pressurised up to this value. The dilution refridgerator was started up more slowly than usual, taking care that the mixing chamber was always the coolest part. This ensured that the solid plug of ^{3}He was formed in the thermometer fill line near the mixing chamber rather than further away from the thermometer, in an attempt to eliminate the incidence of plug slippage. The thermometer fill line was well thermally anchored to the mixing chamber, 4th. heat exchanger, still and 1K cold plate.

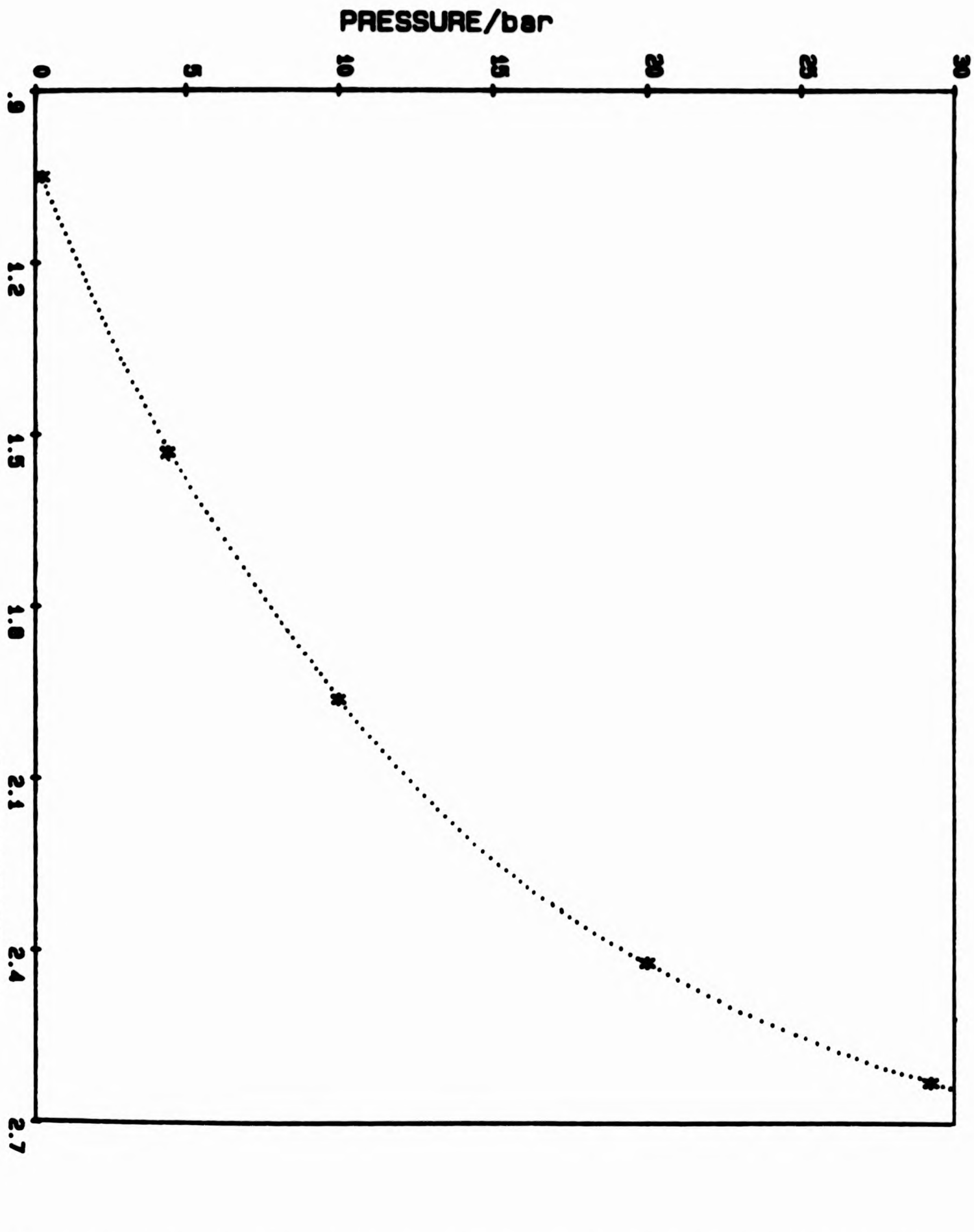

FIG 3.3 : Superfluid transition temperature scale (47), used in calibration of LCMN thermometer. The dotted line acts as a guide to the eye.

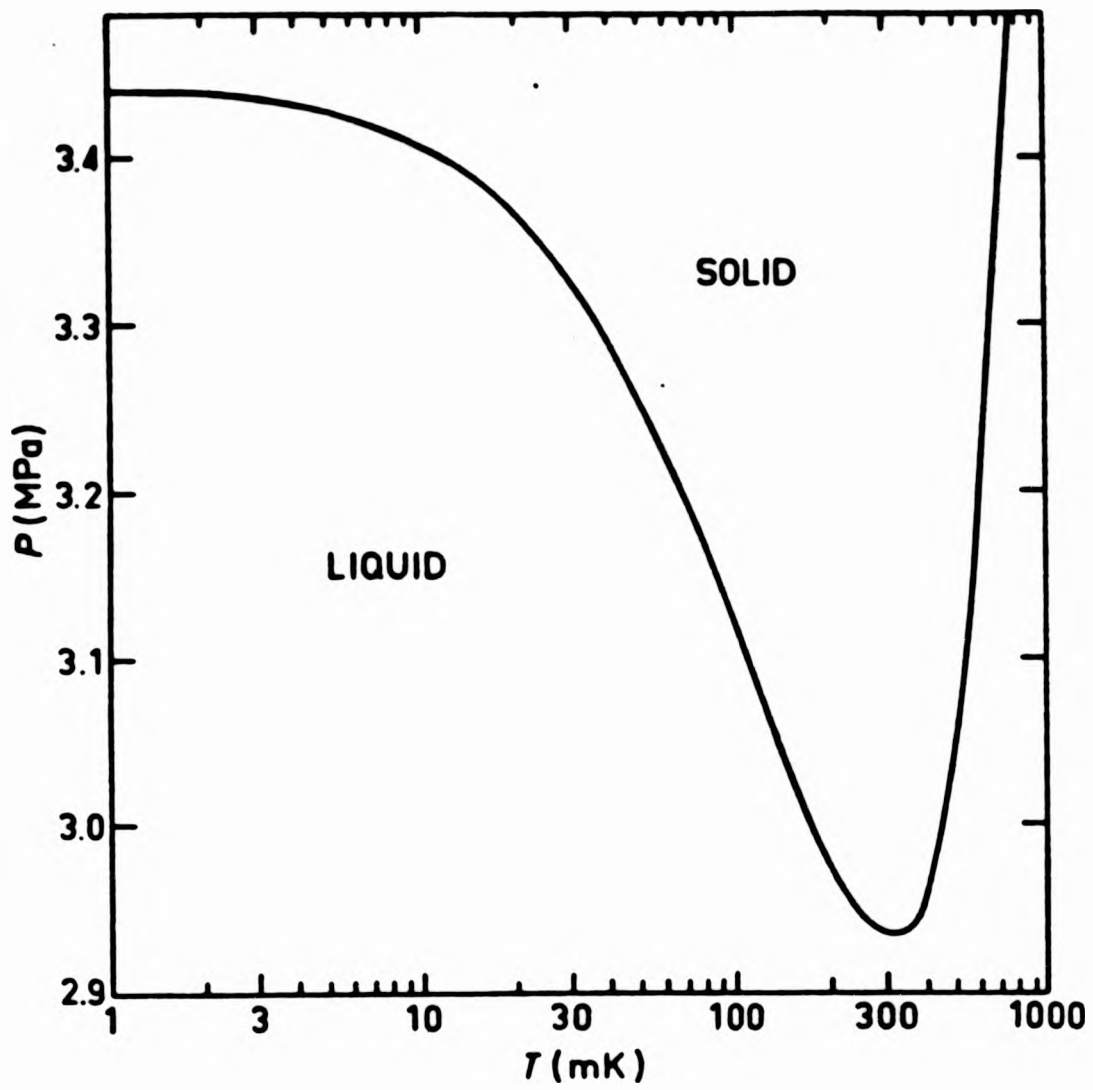

FIG 3.4 : The melting curve of ^3He at low temperatures (41)

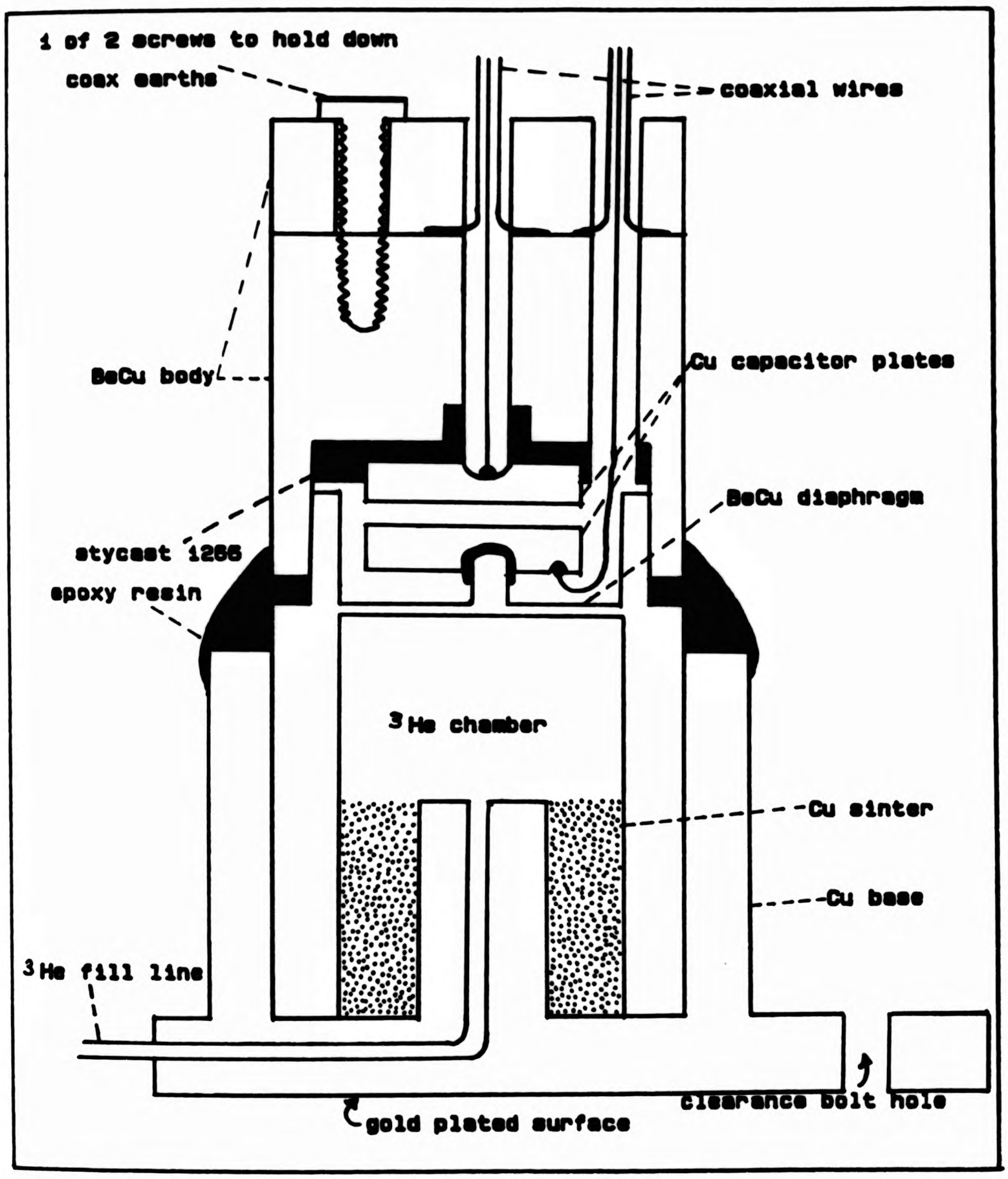

FIG 3.5 : Schematic diagram of melting curve thermometer

(total height approx. 2 cm)

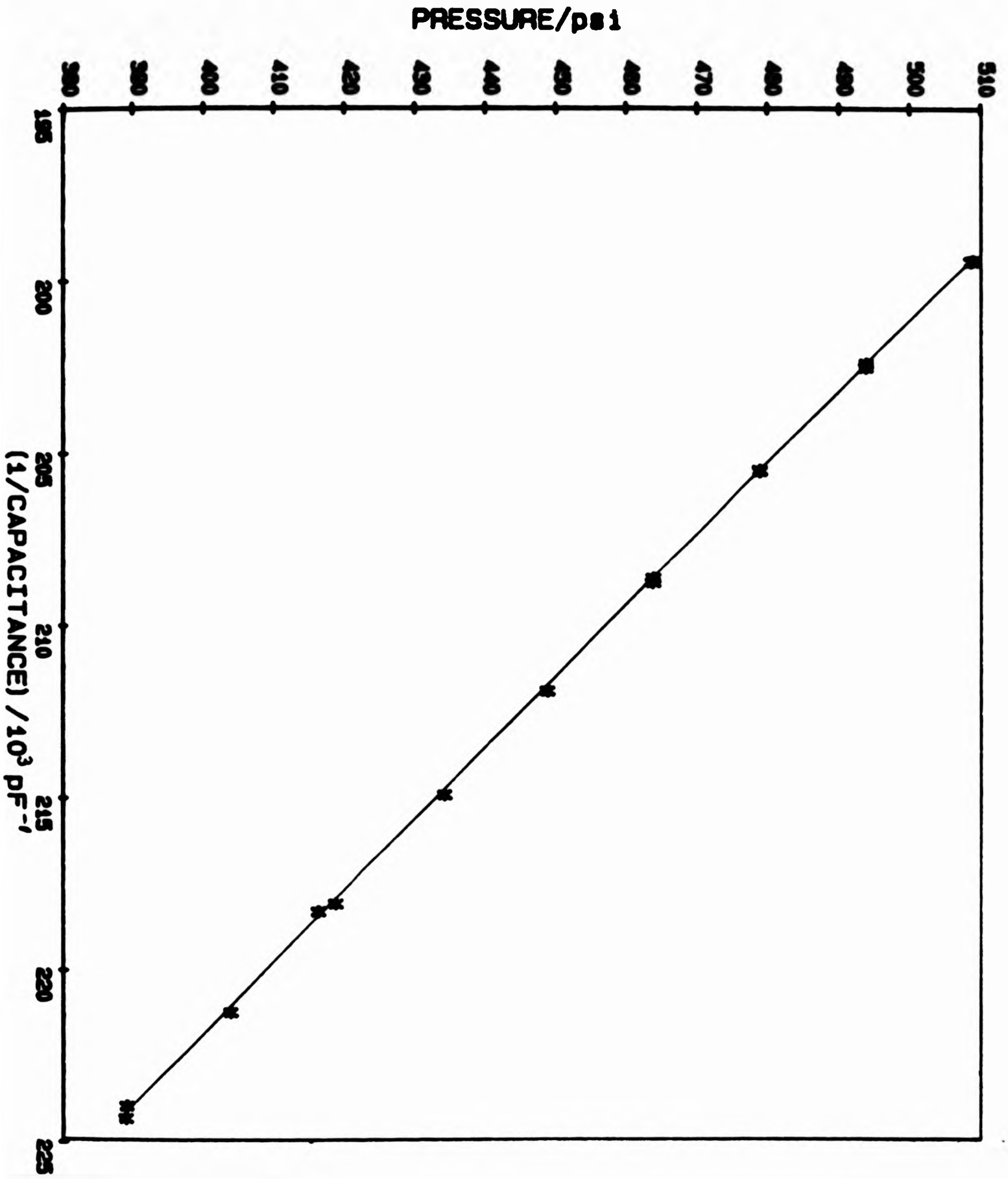

FIG 3.6 : Pressure vs. capacitance calibration of ^{3}He melting curve thermometer at 1K.

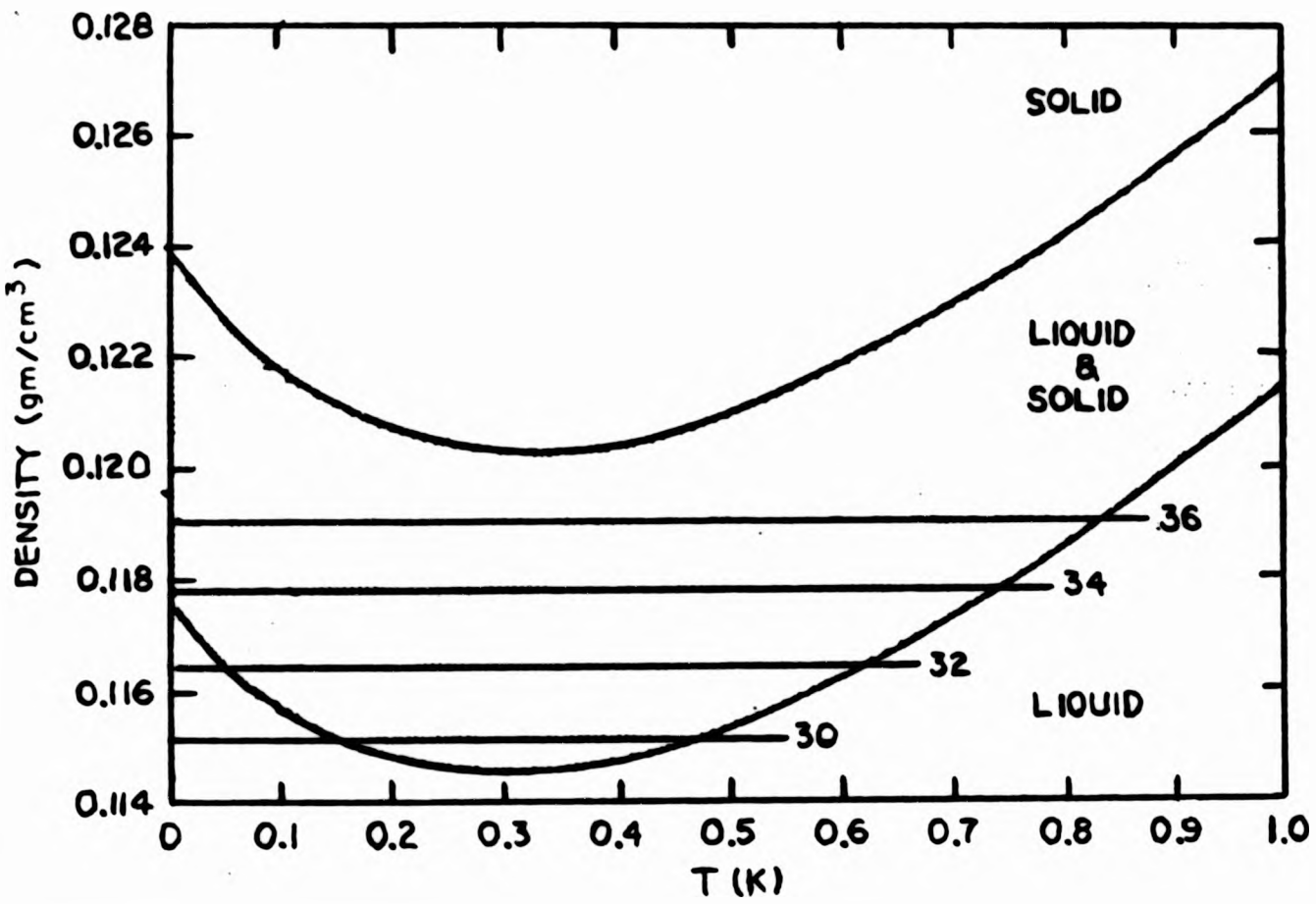

FIG 3.7 : The density of liquid and solid ^{3}He along the melting curve (42)

The capacitance could be measured to about 1 part in 10^5 using a General Radio capacitance bridge(43)(a low temperature reference capacitor was not used) and as a result the melting pressure could be measured to better than 1 mbar. This corresponds to a sensitivity for temperature measurement of about 0.02 mK in the temperature range 5-22 mK in which this thermometer was used for calibration purposes.

The ^{3}He melting curve thermometer was used in an earlier set of measurements to establish a temperature scale, together with the LCMN thermometer described in section 3.2 and a platinum NMR thermometer consisting of 0.76g of 2 μm platinum powder with a packing fraction of 25% used with an IT PLM-3 system(44). Briefly, the melting curve of Greywall(45) was used in conjunction with this melting curve thermometer to calibrate the other two thermometers. The Korringa law states that T_1T = K, where T_1 is the spin lattice relaxation time and K a temperature and pressure independent Korringa constant. The value for K = 29.8 $\pm$ 0.2 s mK found for platinum from this data was in good agreement with that measured by Ahonen et al.(46) and thus provided confirmation of the Pt NMR temperature scale for T>2.8 mK, the lowest temperature at which T_1 was measured. This gave independent justification for the temperature scale established in the above manner. Reference 47 contains further details about this process.

3.4 Calibration of LCMN thermometer

At sufficiently high temperatures the susceptibility of the LCMN is given by the Curie Weiss law and therefore the signal x required to balance the inductance bridge can be described by

$$x - x_\infty = \frac{C}{T + \Delta} \qquad (3.1)$$

where x_∞, C and Δ are all calibration constants. x_∞ represents the signal required to balance the bridge at infinite temperature.

The Curie Weiss law has been found to provide a good fit to the data for T>2.6 mK and with a value for the constant Δ of order zero(47). x_∞ was given by a plot of x vs. 1/T over the approximate temperature range 16-60 mK. Figure 3.8 shows this plot. The temperature T for this process was measured using a carbon Speer resistor which had been calibrated against a nuclear orientation thermometer on a previous occasion and which was situated on the copper experimental platform. The value found for x_∞ was consistent with the value found by a similar method on a previous experimental cool down(15). The constant C was found as the gradient of Figure 3.8. When the x measured at the superfluid transition at 29.316 bar was used together with these constants a value for the transition temperature of 2.63 mK was found which was consistent with Figure 3.3.

In summary, the LCMN thermometer has been calibrated to fit the Curie Weiss law for T>2.6 mK and with

$$x_\infty = 5094 \pm 15$$

$$C = -4579 \pm 15$$

$$\Delta = 0$$

Systematic departures for fits to the Curie Weiss law were observed below this temperature and this may be because the Curie Weiss law breaks down for the 10% LCMN used here(47). Departures from this law at the superfluid transition for three different pressures and at the B-A transition at 29.316 bar, where the reduced temperature was provided by both Greywall(11) and Alvesalo et al(48)(agreeing to within .5%), suggest a correction to the magnetic temperature T^* of the form

$$T = T^* + \Delta T_m$$

where $\Delta T_m = -0.11(T^*-2.63)^2$

with an error for ΔT_m of around 5%, partly contributed by the estimated 2% error in T_c.

3.5 Temperature Calibration of the Experimental Cell

On each occasion of a superfluid transition a time delay was observed between the transition as indicated by the sound signal from the experimental cell and by the LCMN thermometer. In each case, whether while warming or cooling through the transition, the sound cell indicated a higher temperature than the LCMN. Figure 3.9 shows a portion of the chart recorder record for a typical cooling through the transition.

If $\dot{q}$ represents the power input to the helium in the cell by the ultrasound and any residual heat input then the cell temperature T_1 for ^3He in the normal state may be represented by

$$\dot{q} - \frac{k A}{\ell} \ln \frac{T_1}{T_2} = \beta T_1 \frac{\partial T_1}{\partial t} \qquad (3.2)$$

where T_2 represents the temperature of helium in the main bath, $C = \beta T$ and $K = k/T$ the heat capacity and thermal conductivity for ^3He in the normal state.

For a small temperature difference ΔT this can be approximated to

$$\Delta T = \frac{\ell}{kA} \dot{q} T - \frac{\beta \ell T^2}{k A} \frac{dT}{dt} \qquad (3.3)$$

indicating that the temperature difference depends on the rate of cooling or warming and the heat input to the cell. Experimental evidence suggested some contribution to ΔT from both terms.

First consider the normal state. By assuming the thermal diffusivity term was the dominant one a time constant could be estimated for a system consisting of a volume of liquid helium representing the experimental cell separated from the main bath by a thermal resistance provided by the helium in the stem of the cell tower. This time constant was estimated to be 36 minutes. An estimate of ΔT was made by looking at the change in sound signal between the superfluid transitions indicated by the LCMN thermometer and the cell, with the latter in the normal state. Using $\Delta T = \Delta T_0 \pm 36\ dT/dt$ a value for ΔT_0 of 0.07 mK (±50%) was found corresponding to a value of q of around 0.2 nW for the usual sound settings. The q contribution to ΔT was thus determined to be 2% of T (±1%) at all temperatures greater than T_c.

Now consider the superfluid state. An estimate of ΔT was made for $T<T_c$ by looking at the change in x, indicated by the LCMN thermometer in the superfluid state, between the transitions indicated by this thermometer and the cell. Again, a value of 36 minutes for the time constant and a corresponding ΔT_0 of 0.07 mK (±50%) seemed reasonable estimates. The q contribution to ΔT was thus determined to be 2% of T (±1%) at all temperatures less than T_c.

For all measurements discussed here, made in both the normal and superfluid states, the cell and LCMN thermometer were believed to have reached steady state conditions so that the thermal diffusivity term contribution to ΔT vanishes. Therefore the sound cell temperature was adjusted by +2% (±1%) throughout the temperature range of interest.

i.e. $T_{cell} = 102\%\ T_{LCMN}$ (±1%)

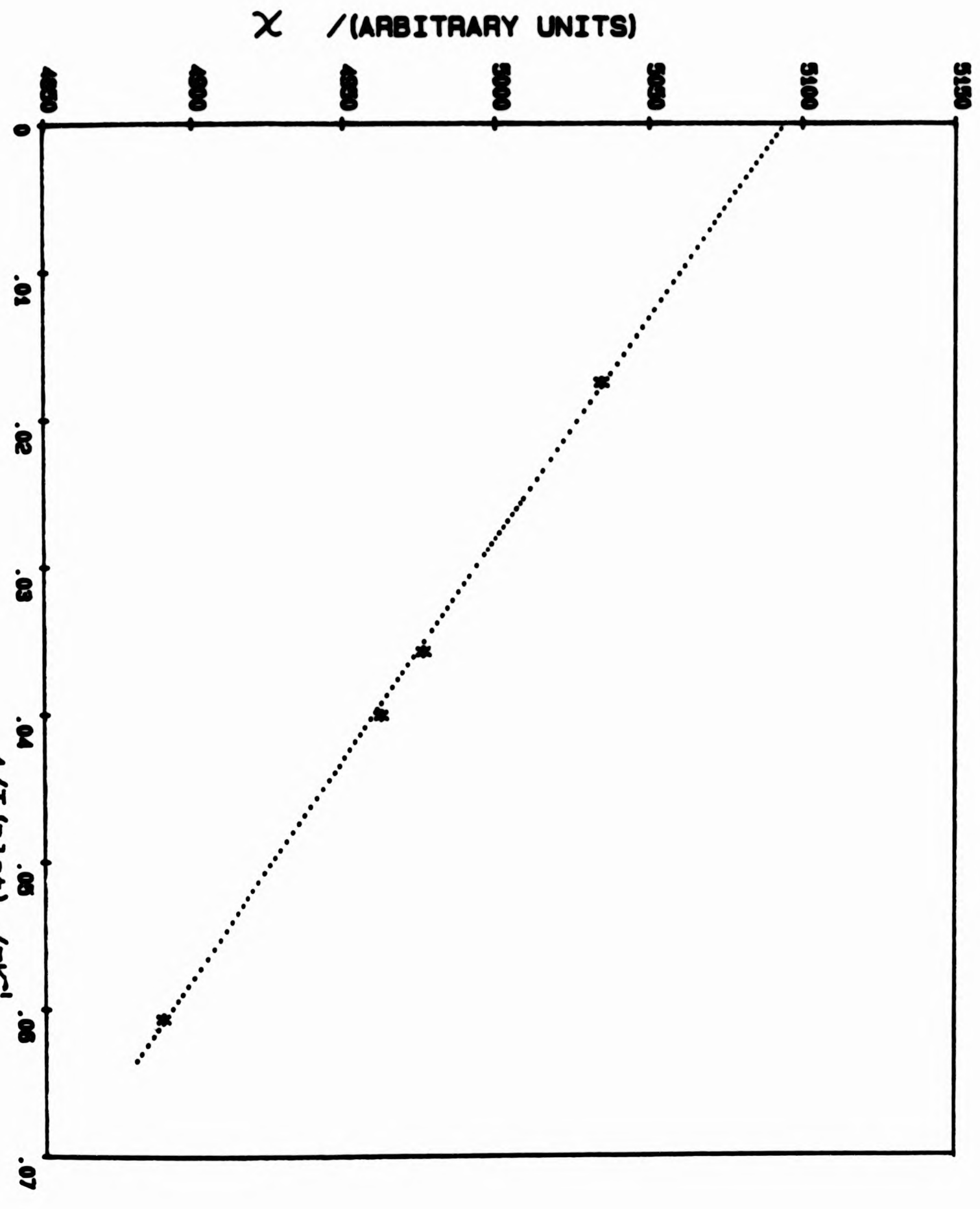

FIG 3.8 : Plot of LCMN χ vs. 1/T for 16-60 mK, used in the determination of the Curie-Weiss coefficients χ_o and C. A least squares line fit to the data is shown as a dotted line.

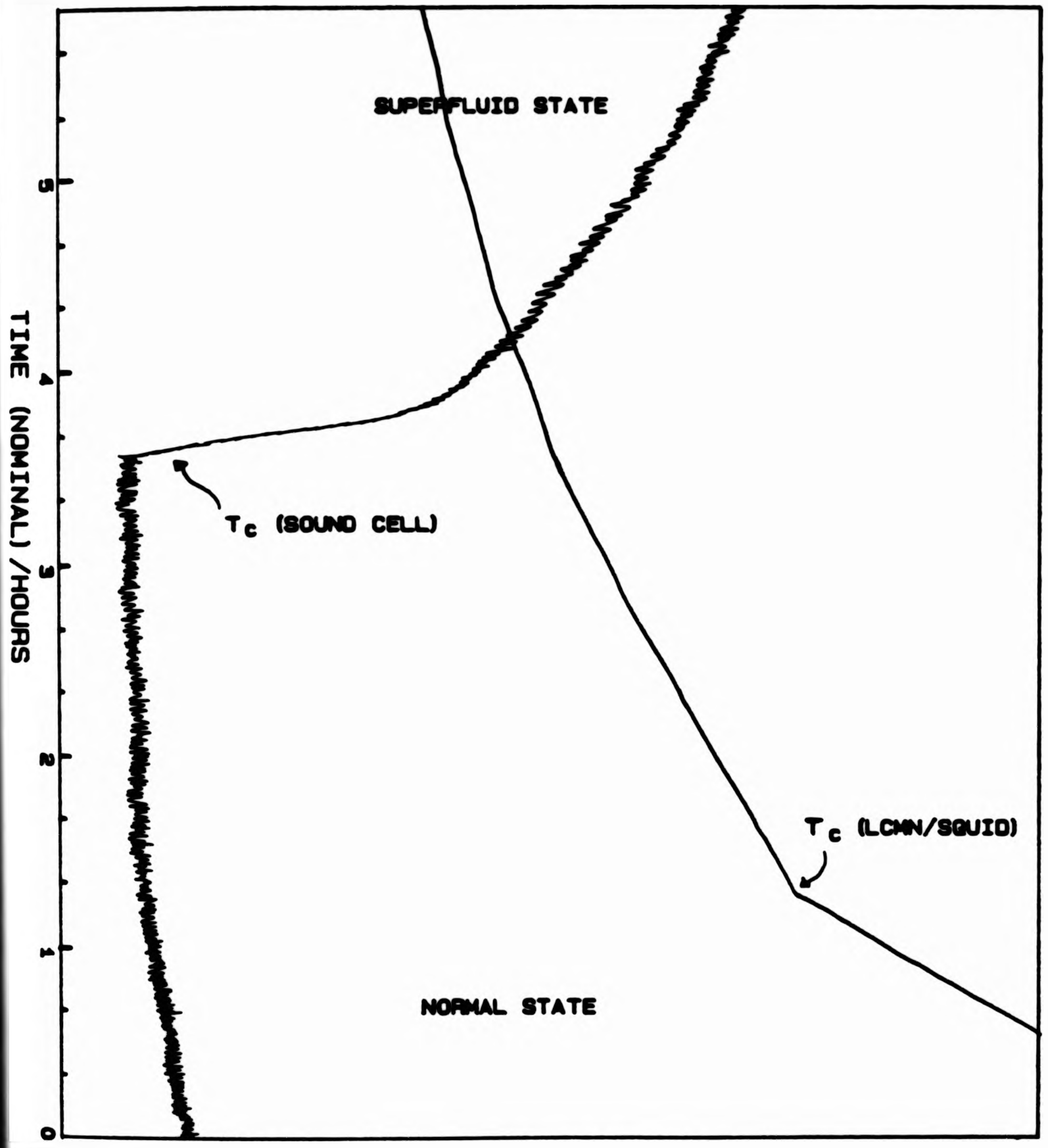

FIG 3.9 : Portion of chart recorder record showing 15.154MHz sound signal and LCMN-SQUID output for a typical cooling through the superfluid transition

CHAPTER 4 : SOUND IN ^{3}HE

4.1 Introduction

This chapter contains a discussion of the transmission of sound through normal state ^{3}He (section 4.3) and 15.154 MHz sound through ^{3}He in the superfluid state (section 4.4). Sound measurements were made in the temperature range 20.4 to 2.18 mK for a ^{3}He pressure of 29.316 bar. By fitting the normal state data to values for sound velocity and attenuation provided by Wölfle(52) and Ketterson(53) it was possible to extract the signal due to sound transmission through the experimental cell from the nuisance signal discussed in section 2.3.2. This enabled values for the velocity and attenuation of 15.154 MHz sound in ^{3}He-A to be deduced from the superfluid data.

4.2 Method of Measurement and Composition of Signal

At each of 14 temperatures in the normal state and 11 temperatures in the superfluid state a frequency sweep measurement was performed once the cell and main ^{3}He bath had attained steady state conditions. Each set of data consisted of two frequency sweeps, one of the "in phase" signal and the other of the "quadrature" signal (a definition of these has been given in section 2.3.2). In the superfluid state this was supplemented by additional sound data recorded at a frequency of 15.154 MHz. The range of frequency 14.88 MHz to 15.44 MHz encompassed the resonant response of the system, centred at around 15.15 MHz, and was swept at a rate of 0.92 kHz/s.

The block diagram of the circuit used to perform the sweeps is shown in Figure 2.9 and a data collection program similar to that listed in Appendix D was used to sample the digitised sound signal every 2s together with the time at which the measurement was made. The detection electronics time constant was set to 1s. The standard pulse duty cycle of 5s was inappropriate for the sweeps and so was changed to 0.5s. This would have produced more heating of the cell ^{3}He than tolerable so the switchable attenuator shown in Figure 2.9 was set to 31 dB rather than the more usual 26 dB.

Figures 4.1 and 4.2 show some typical sweep data, collected at 16.66 mK. The composition of the detected signal is described as follows. It should be noted that not all of the signal measured was due to transmission of sound through the ^{3}He but that some nuisance signal was also present. A brief discussion of this has been given in section 2.3.2. Also it is apparent from Figures 4.1 and 4.2 that the sound signal measured off resonance is not centred on 0 mV as might be expected. An offset was observed for all sound measurements and corresponds to the signal output by the detection electronics for zero signal input. (The detection electronics are shown in Figure 2.11). In an attempt to keep this as constant as possible over the 11 weeks of the experimental run the integrator chip zero was checked daily and the integrator offset voltage adjusted if necessary to reset this. Nevertheless, the offset was observed to vary slowly with time as a reflection of electronics drift. This was not a problem since the offset could be deduced from every frequency sweep performed by measuring the off resonance sound signal at the extremes of the frequency range swept. In most of the discussion that follows this offset value has been subtracted from each sound reading. Figure 4.2

would appear to indicate an offset that varies with frequency for the quadrature signal. This behaviour was observed for all quadrature signal frequency sweeps and for the purpose of analysis a value for the offset was taken as the mean value of the off resonance signal.

For a sound velocity of order 400 ms^{-1} in liquid ^3He at 29 bar, and a crystal separation of 2 mm, the leading edge of the pulse input to the driving crystal and then transmitted through the ^3He would be expected to reach the receiver crystal after about 5 μs. Some of this pulse will be reflected at the receiver crystal and again at the transmitter crystal, traversing the liquid three times in total, before its leading edge reaches the receiver crystal again about 15 μs after input of the initial drive pulse. Both of these signals, referred to henceforth as "1st echo" and "3rd echo" respectively, would take at least the time width of the pulse (2.8 μs) to build up to a maximum before decaying exponentially. The 1st echo would of course be expected to have the greater amplitude since this has not undergone any reflections and has been attenuated by travelling through 2 mm of liquid ^3He as compared to 6 mm for the 3rd echo. The sound signal was integrated over the period from 15-25 μs after the pulse input to the driving crystal (the reason for selecting this time window for the integration is discussed in section 2.3.2). From the above it might be expected that the sound signal detected and integrated would contain contributions from both the 1st and 3rd echo signals. Initial attempts to fit the sound signal to "1st echo" only and then to "3rd echo" only did suggest a contribution from both of these with the former making the greater contribution.

To summarise :-

sound signal measured	=	offset	+	nuisance	+	1st echo contribution	+	3rd echo contribution

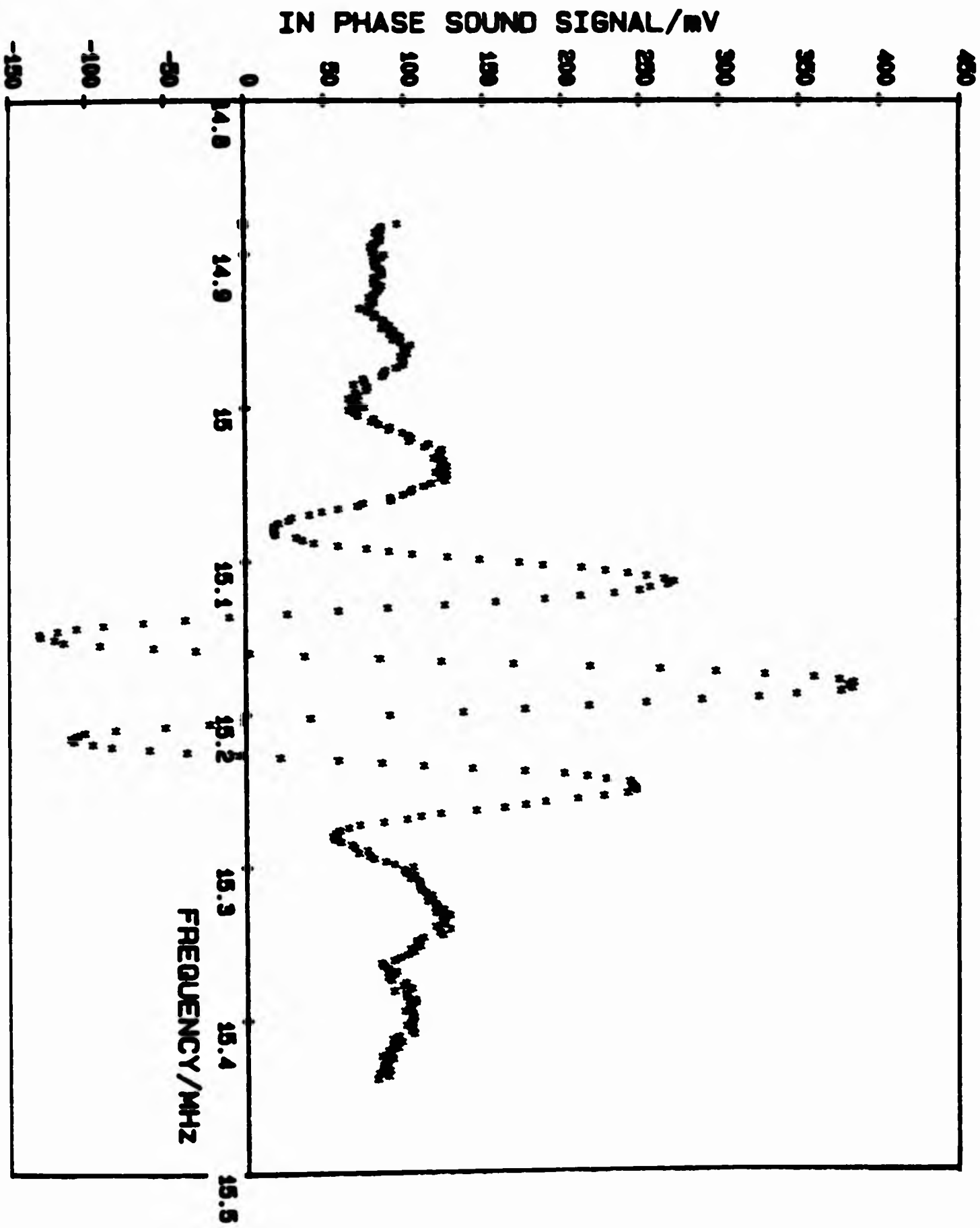

FIG 4.1 : Typical in phase sound signal frequency sweep, where the data was collected at 16.66 mK.

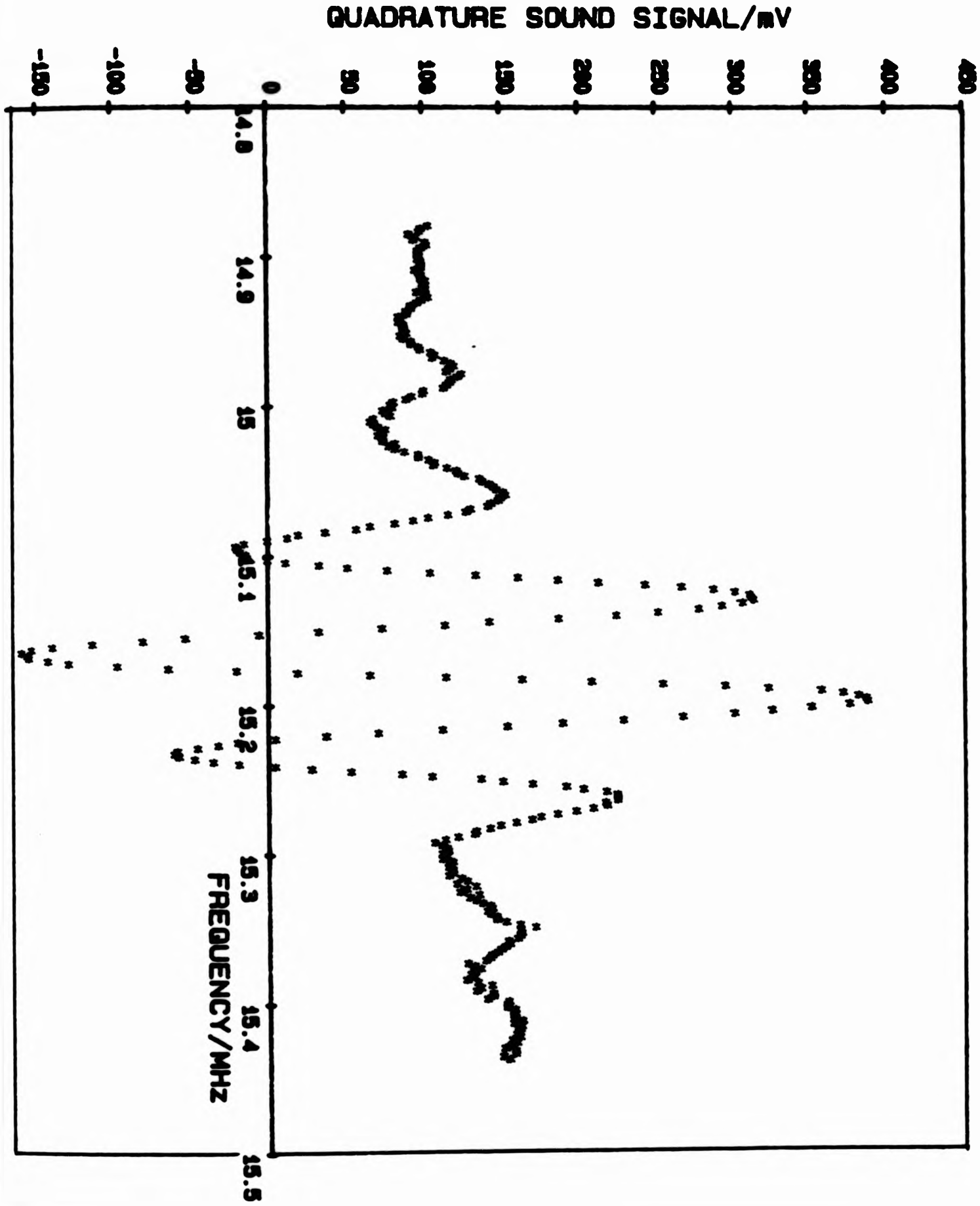

FIG 4.2 : Typical quadrature sound signal frequency sweep, where the data was collected at 16.66 mK.

4.3 Normal State Sound Data

Ordinary first sound at 15.15 MHz can be transmitted through normal state ^{3}He at 29 bar pressure down to temperatures of around 8 mK. Close to this temperature the relaxation time between collisions becomes too long for sound transmitted in the classical sense and the low temperature Fermi region is entered. In 1956 Landau expounded his model of a Fermi liquid for ^{3}He which introduced the interaction between atoms as a perturbation on the energy levels of a degenerate perfect gas governed by Fermi statistics (49). He introduced the concept of a quasiparticle, arising since the energy of a level is no longer a unique function for an atom but depends on the occupation numbers of all other levels, and the wave functions of the various levels will therefore no longer be true eigenfunctions. These excitations have a one to one correspondence to real particles. Starting from the Boltzmann equation for the distribution function of the quasiparticles, Landau derived the response of the distribution function to a periodic disturbance. In the limit $\omega\tau \ll 1$, where τ is the characteristic quasiparticle collision time, the disturbance was ordinary hydrodynamical sound. However, in the limit $\omega\tau \gg 1$ other wave solutions could be obtained, in particular a mode analogous to ordinary sound and referred to henceforth as "zero sound". Numerical calculations (50) show that the transition from first to zero sound occurs around $\omega\tau \approx 1.0$ and is characterised by a peak in the sound absorption and an increase in sound velocity.

Starting from the Boltzmann equation in the general form which has been solved by Khalatnikov and Abrikosov (51), Wölfle calculated expressions for the velocity and attenuation of first and zero sound in

^{3}He in terms of $\omega\tau$ and the Fermi liquid parameters (52). Wölfle then used these expressions together with data taken at 29.316 bar by Ketterson et al. (53) (who measured a fractional change in velocity of 20.24 MHz sound of $(c_o-c_1)/c_o = 6.3\times10^{-3}$ where c_o and c_1 are the zero and first sound velocities in the limits $\omega\tau = \infty$ and $\omega\tau = 0$ respectively) to show that Ketterson et al's data was fitted to a good approximation by

$$\omega\tau = \frac{0.63 \times 10^{-6}\omega}{T^2} \qquad (4.1)$$

$$c = c_1 \left\{ 1 + \frac{6.3 \times 10^{-3}}{(1+ (1/\omega\tau)^2)} \right\} \qquad (4.2)$$

$$\alpha = \frac{\omega}{c} \left\{ \frac{6.3 \times 10^{-3}\ \omega\tau}{(1 + (\omega\tau)^2)} \right\} \qquad (4.3)$$

where c and α are the velocity and attenuation of sound of frequency $\omega/2\pi$ in ^{3}He at temperature T (in mK).

The velocity and attenuation of 15.154 MHz sound transmitted through normal state ^{3}He below 20 mK have been calculated from these expressions and are shown as functions of temperature in Figures 4.3 and 4.4. A value for $c_1 = 400\ ms^{-1}$ was assumed with reference to Wheatley(12). The peak in attenuation of sound and the increase in sound velocity are apparent close to 8 mK.

These expressions found by Wölfle have been used in the analysis presented here of the normal state data. Equations 4.1-4.3 rely on Ketterson's temperature calibration which was based on a 29.316 bar T_c of approximately 2.55 mK and which is 3% down on the corresponding Manchester T_c. This difference was deemed small enough to justify an attempt to fit to the data measured here using these expressions for the velocity and attenuation.

The sound signals measured are expected to have the form

$$IP = IP\ (offset) + N_I(\omega) + B(\omega)\ e^{-\alpha d} \cos(\frac{\omega d}{c} + \Phi_1(\omega)) + C(\omega)\ e^{-3\alpha d} \cos(\frac{3\omega d}{c} + \Phi_3(\omega)) \quad (4.4)$$

$$Q = Q\ (offset) + N_Q(\omega) + B(\omega)\ e^{-\alpha d} \cos(\frac{\omega d}{c} + \Phi_1(\omega) - 1.59) + C(\omega)\ e^{-3\alpha d} \cos(\frac{3\omega d}{c} + \Phi_3(\omega) - 1.59) \quad (4.5)$$

where N_I, N_Q represent the nuisance signal contribution, and B and C represent the strengths of the contribution from the 1st and 3rd echos respectively at frequency $\omega/2\pi$ (for convenience B and C will be referred to as the amplitudes of the 1st and 3rd echo). d represents the spacing of the quartz crystals which is also the width of the helium channel and has a value of 2 mm. The attenuation α and velocity c are assumed to be the only variables which depend on the transmission of sound through the helium and therefore the only temperature dependent variables.

By fitting to the normal state sound data using equations 4.4 and 4.5 and values for the sound velocity and attenuation given by equations 4.2 and 4.3 values for N_I, N_Q, B, C, Φ_1 and Φ_3 could be found across a frequency range which encompassed the resonance of the system.

The IP(offset) and Q(offset) terms in equations 4.4 and 4.5 were found from the frequency sweeps in the manner described in section 4.2. Values for the amplitudes IP and Q were extracted from the frequency sweeps at 24 frequencies in the range 15.0 to 15.3 MHz and for the 13 temperatures at which sweeps were performed. By analysing the data at constant frequency N_I, N_Q, B, C, Φ_1 and Φ_3 were held constant and so could be found

by fitting the data at different temperatures. This was achieved by varying these coefficients and using the method of least squares to find the best fit. The fits typically had standard deviations of between 4 mV and 11 mV. Figures 4.5 and 4.6 show the fit obtained to the in phase and quadrature data at 15.154 MHz, which had a standard deviation of 10 mV. Values for the amplitudes B and C of the 1st and 3rd echos were found to within 0.5 mV and values for the phases Φ_1 and Φ_3 to within 0.01 radians i.e. a change of 0.5 mV or 0.01 radians in any of these parameters produced a noticeable increase in the standard deviation for the fit. This would suggest that although there were a relatively large number of fitting parameters involved the values obtained for them were fairly reliable. The estimated errors in these coefficients may be summarised by: N_I,N_Q(0.7-2.5%); B(0.2-1.5%); C(0.6-1.5%); Φ_1(0.2-1%); Φ_3(0.3%) where the errors are greater the further off resonance the frequency. Figures 4.7 and 4.8 show the measured in phase and quadrature data, adjusted for the offset in each case, at 15.14, 15.154 and 15.17 MHz to give an indication of the variation in signal over a relatively small frequency range around the resonance of the system.

Figures 4.9 to 4.13 show the values found for these fitting parameters. The in phase and quadrature nuisance signals have the form that might be expected from section 2.3.2 and the approximate $\pi/2$ phase shift between the two is apparent. The amplitude B and phase Φ_1 of the 1st echo show the behaviour expected for a system with a resonant frequency of approximately 15.15 MHz. A dip in amplitude close to resonance is apparent, although this is not too suprising since the individual quartz crystals displayed resonances matched to within about 15 kHz at 15.15 MHz and the signal amplitude measured reflects the combination of both of

these resonances in the experimental cell arrangement. The 1st echo would appear to be the dominant sound signal detected, with a contribution 2 - 3 times that of the 3rd echo. The variation in amplitude C and phase Φ_3 of the 3rd echo exhibit no clear frequency dependence. This may also be a reflection of the imperfectly matched crystal resonances, together with the effect of the secondary resonance peaks observed for the detector crystal in the system (see Figure 2.8). Either of these effects would be expected to have a greater influence on the sound signal which has been reflected twice and traversed the helium between the crystals three times (i.e. 3rd echo) than on the 1st echo signal. Any dispersion effects due to non-parallelism of the crystal faces would also be more apparent in the measurement of a 3rd echo, but these are expected to be very small because of the optically flat quartz annulus used as a spacer between the crystals.

In obtaining the above, Wölfle's fit to data measured by Ketterson et al. played an important part. The fact that the standard deviations for the fits descibed here are fairly small might indicate that this procedure was justified. In addition, by calculating α and c from equations 4.1 - 4.3 at a temperature of 2.63 mK together with the temperature independent variables N_I, N_Q, B, C, Φ_1, Φ_3, an in phase and quadrature frequency sweep could be simulated for this temperature. This was compared to a frequency sweep which had not been used in any of the fits, measured with the cell ^{3}He just in the normal state and the main ^{3}He bath still just in the superfluid state (a situation that was able to arise as a result of the temperature difference between the cell and main helium bath which is discussed in section 3.5). Figures 4.14 and 4.15 compare the measured and simulated data, the measured data having been adjusted for the offset in each case. The agreement between the two is good, providing further confidence in this method of fitting to the normal state sound data.

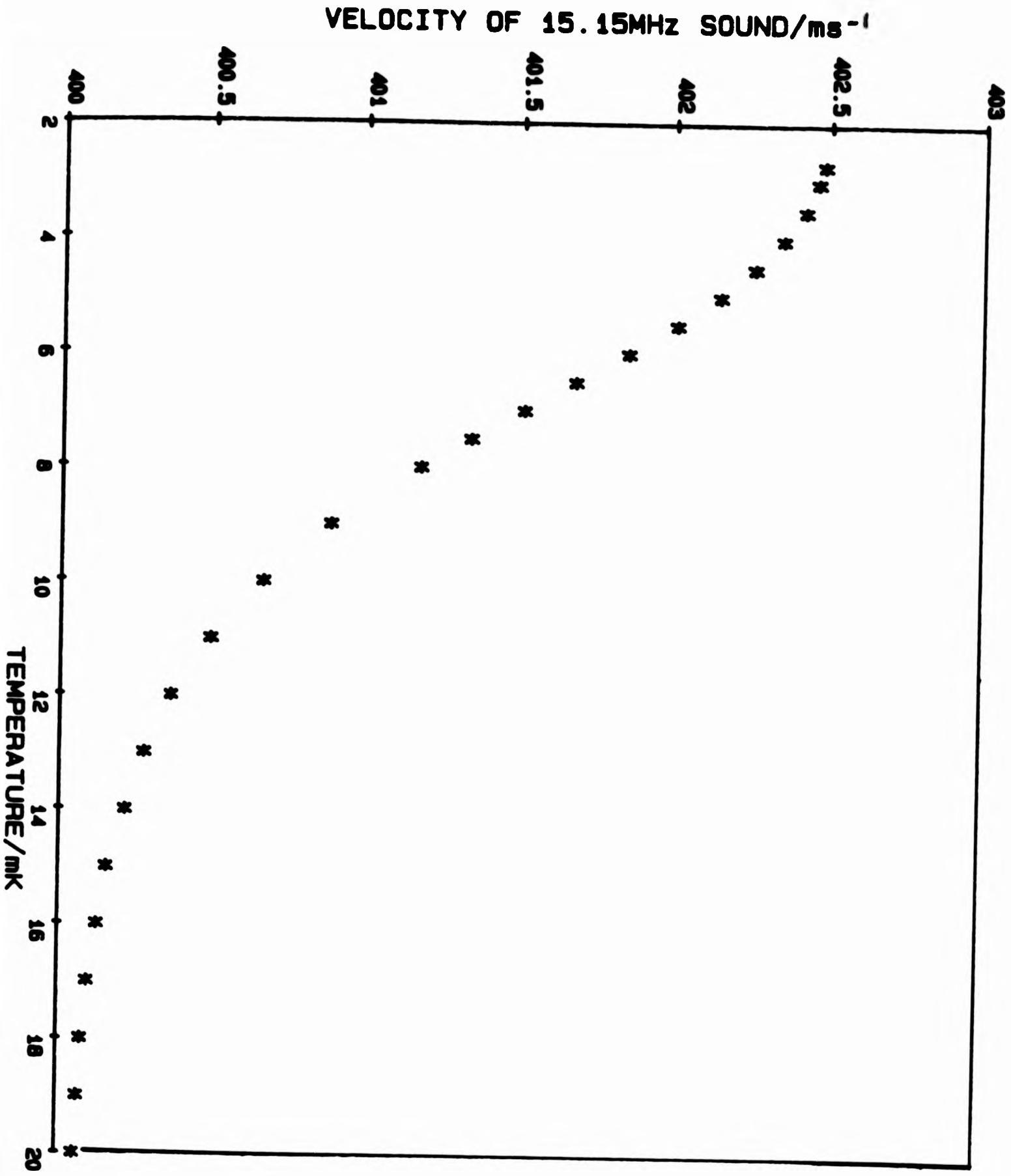

FIG 4.3 : Velocity of 15.15 MHz sound in normal state ^{3}He calculated from equations 4.1 and 4.2.

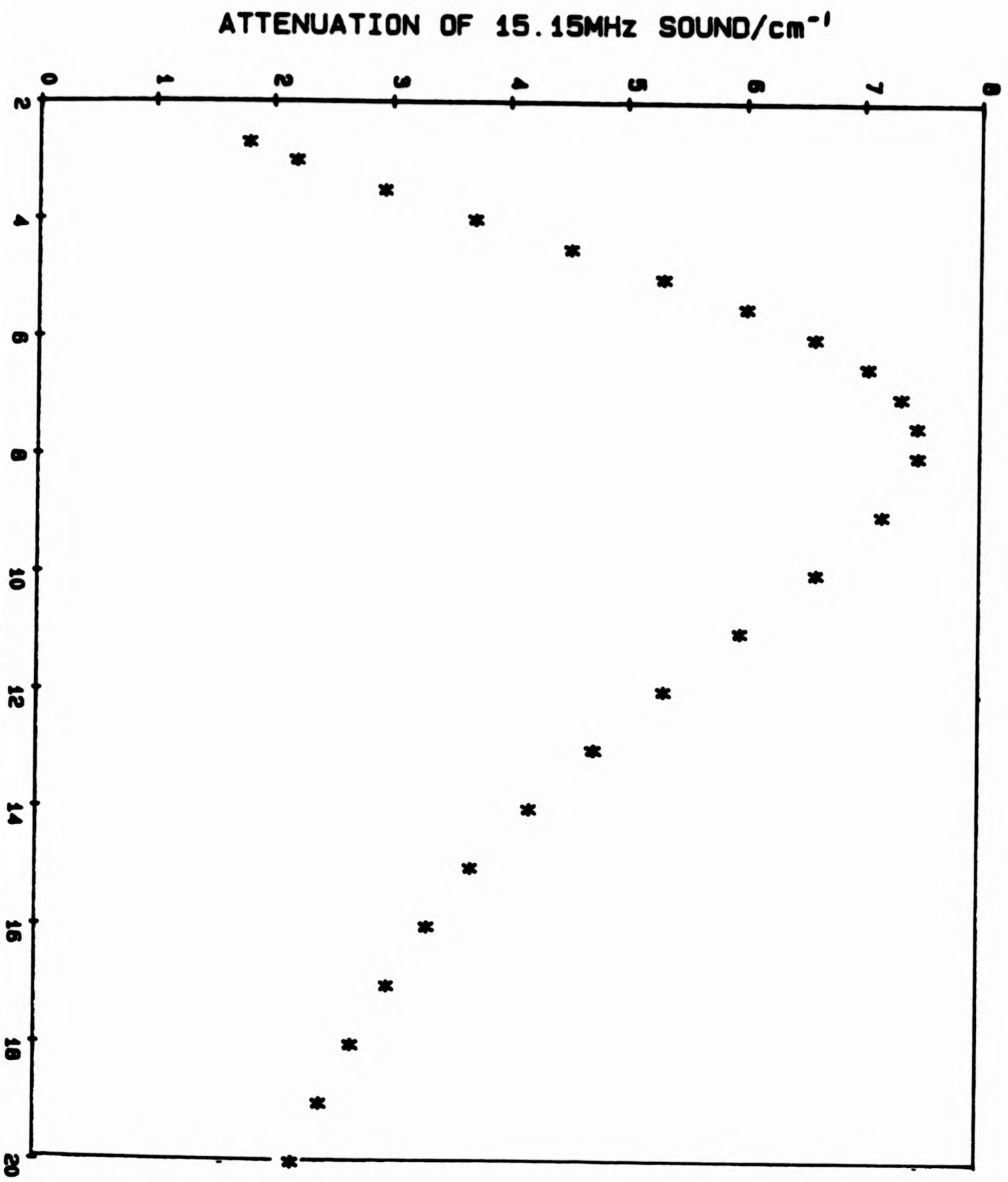

FIG 4.4 : Attenuation of 15.15 MHz sound in normal state ^{3}He calculated from equations 4.1 and 4.3.

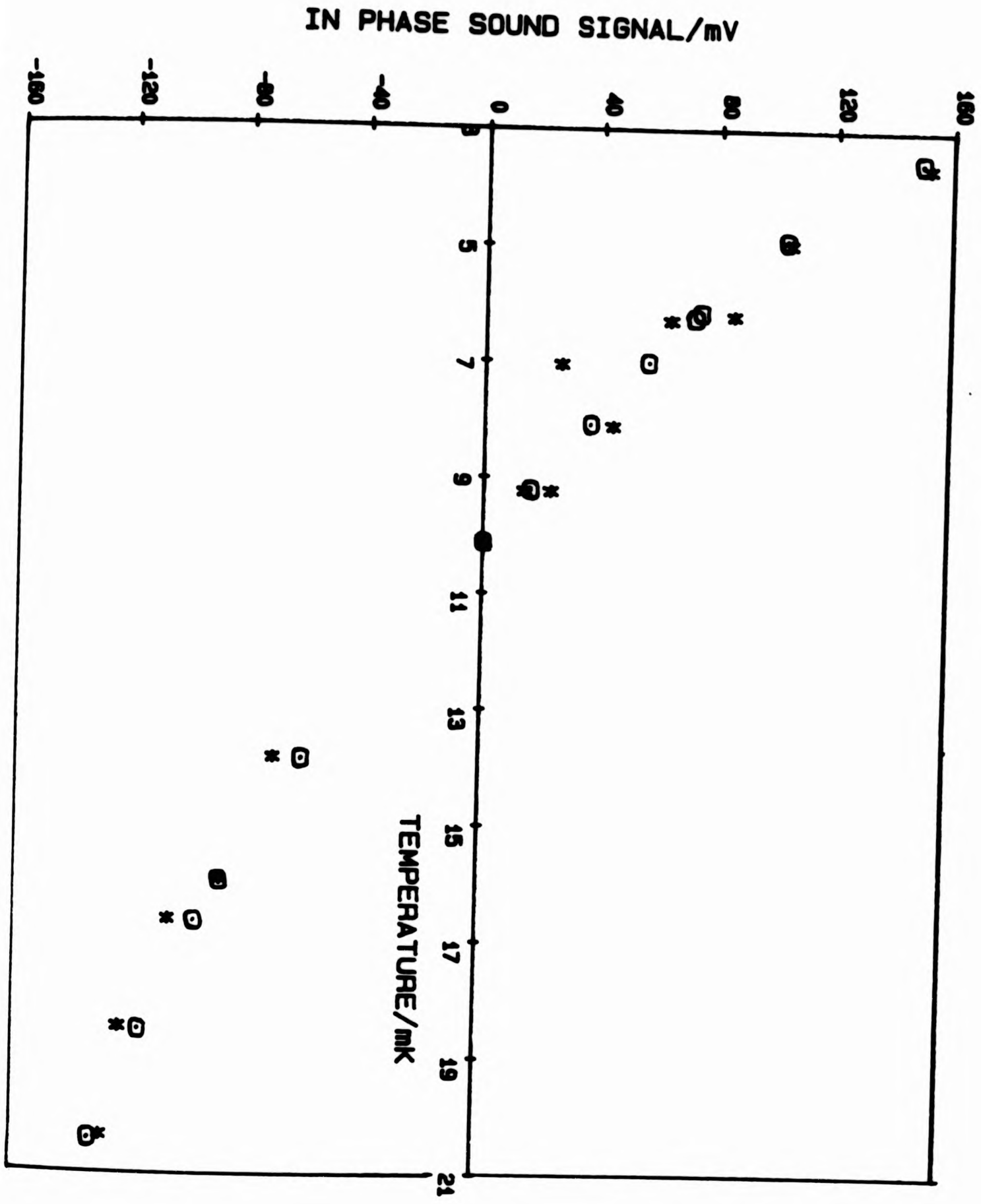

FIG 4.5 : Best fit to in phase normal state sound data at 15.154MHz. * measured data, ⊙ calculated data. Standard deviation for fit to in phase and quadrature data ≈ 10mV.

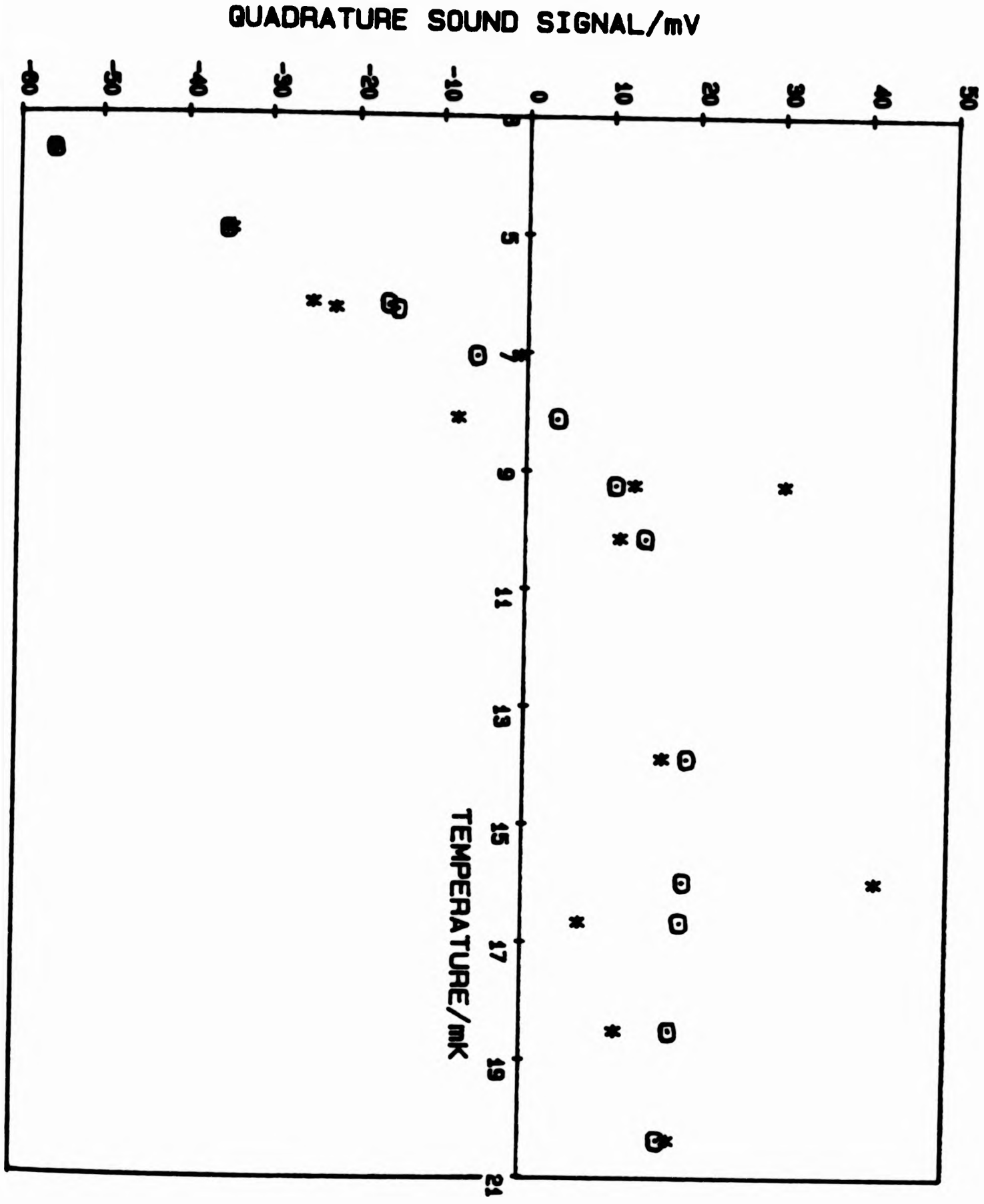

FIG 4.6 : Best fit to quadrature normal state sound data at 15.154MHz. * measured data, ⊙ calculated data. Standard deviation for fit to in phase and quadrature data ≈10mV.

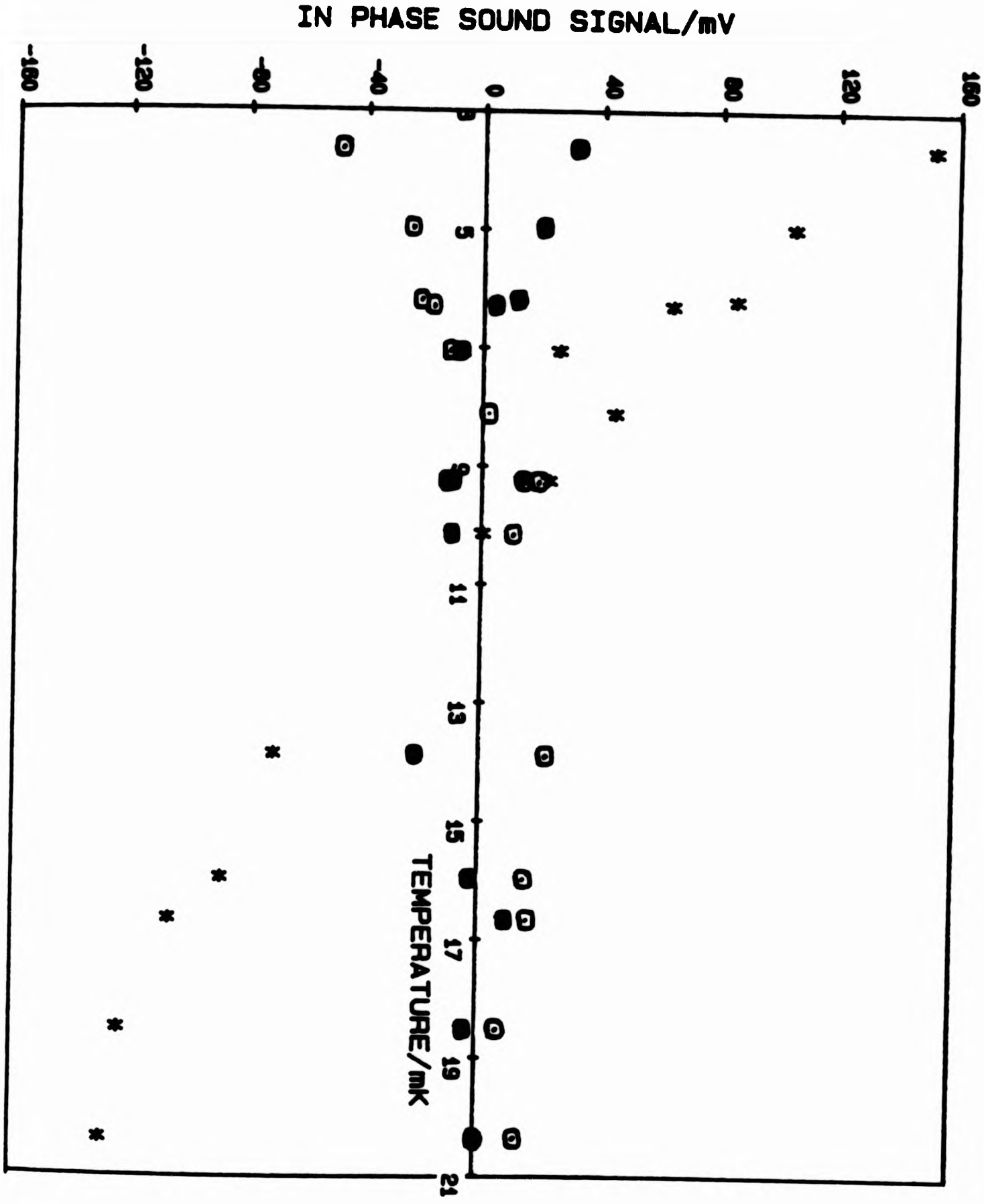

FIG 4.7 : Measured normal state sound data (in phase) at 15.14MHz (o) 15.154MHz (*) 15.17MHz (□) showing variation in signal over this small frequency range around the resonance of the system.

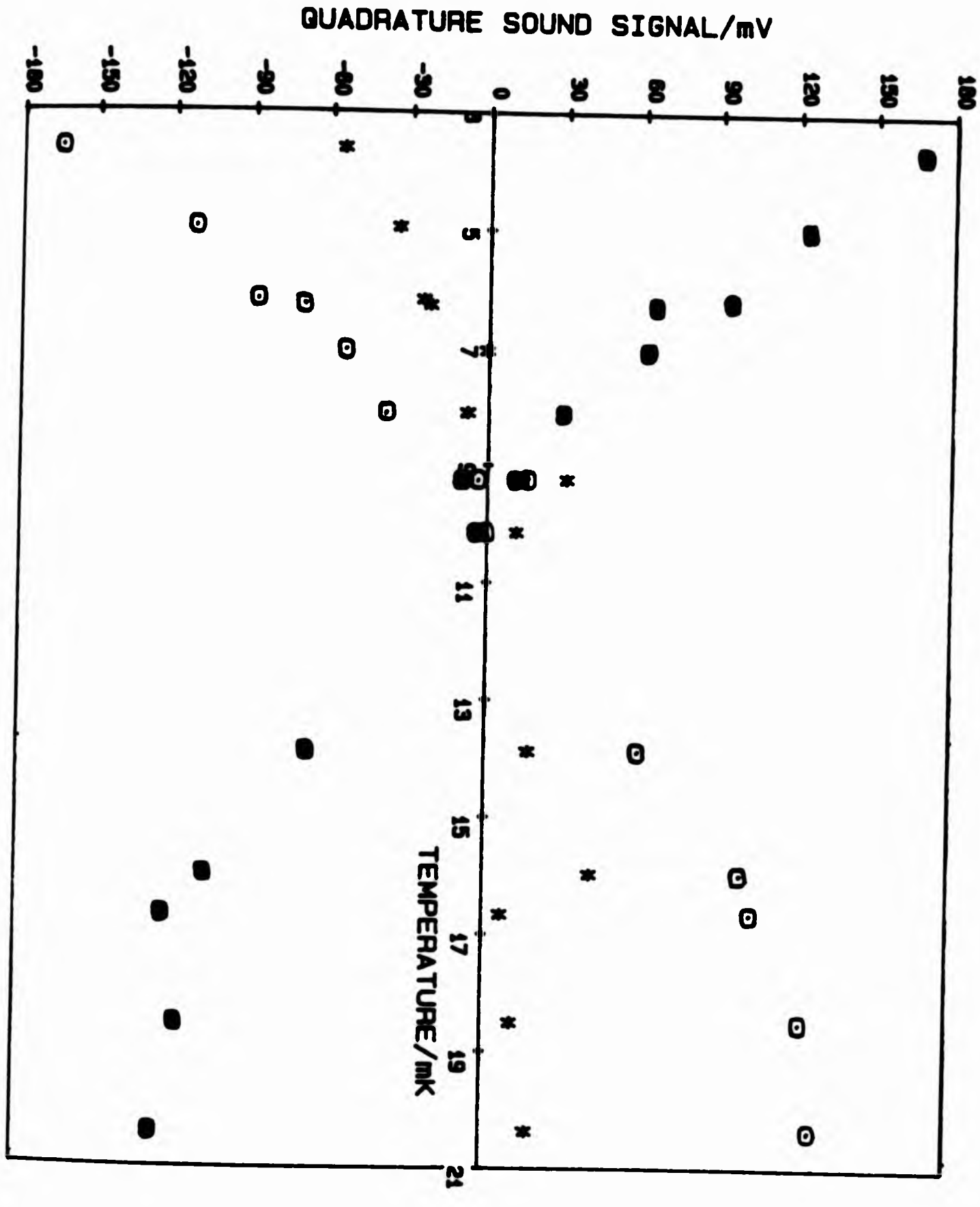

FIG 4.8 : Measured normal state sound data (quadrature) at 15.14MHz (o), 15.154MHz (x), 15.17MHz (o) showing variation in signal over this small frequency range around the resonance of the system.

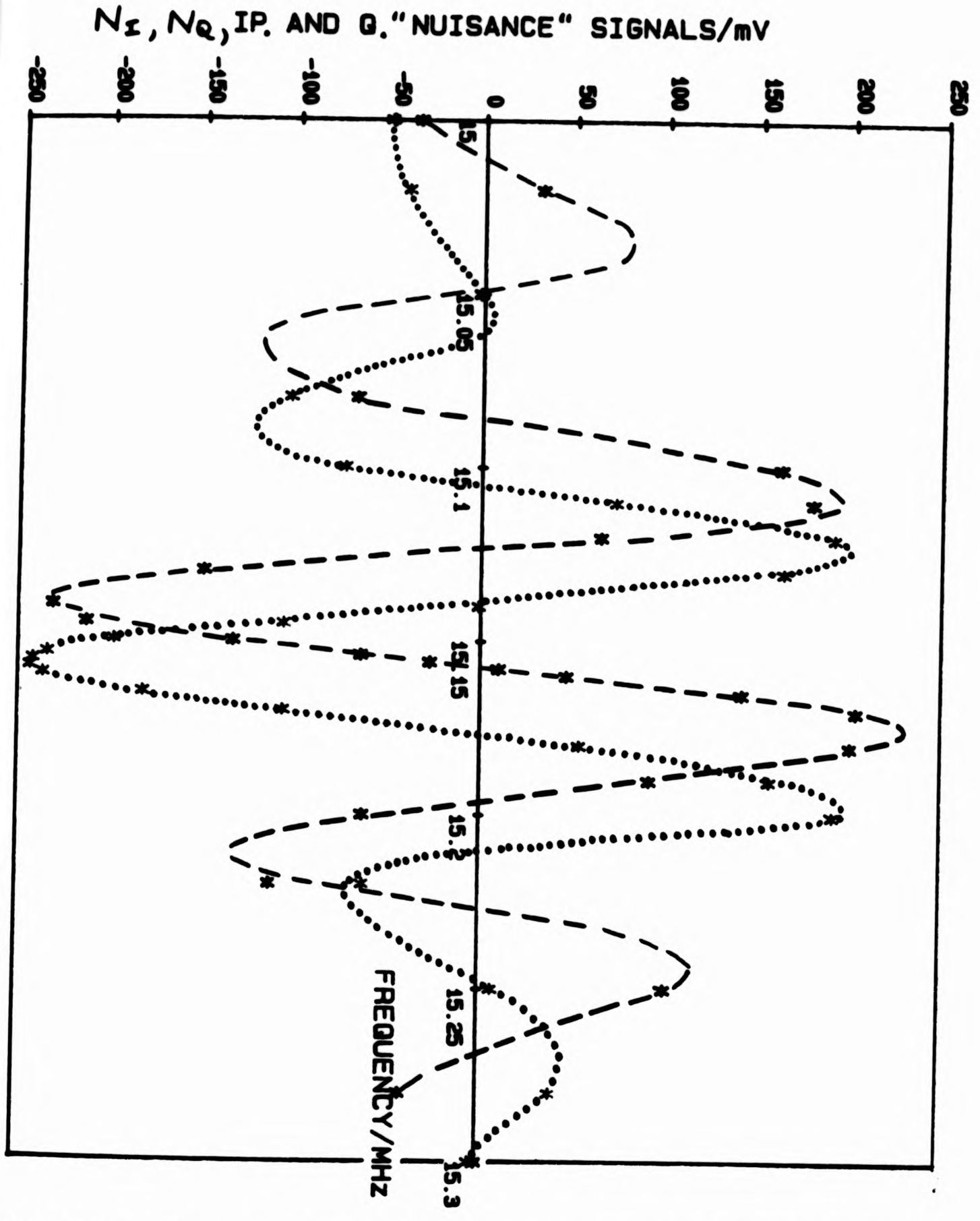

FIG 4.9 : The in phase and quadrature nuisance signals as a function of frequency. The dashed line acts as a guide to the eye for N_I and the dotted line acts as a guide to the eye for N_Q.

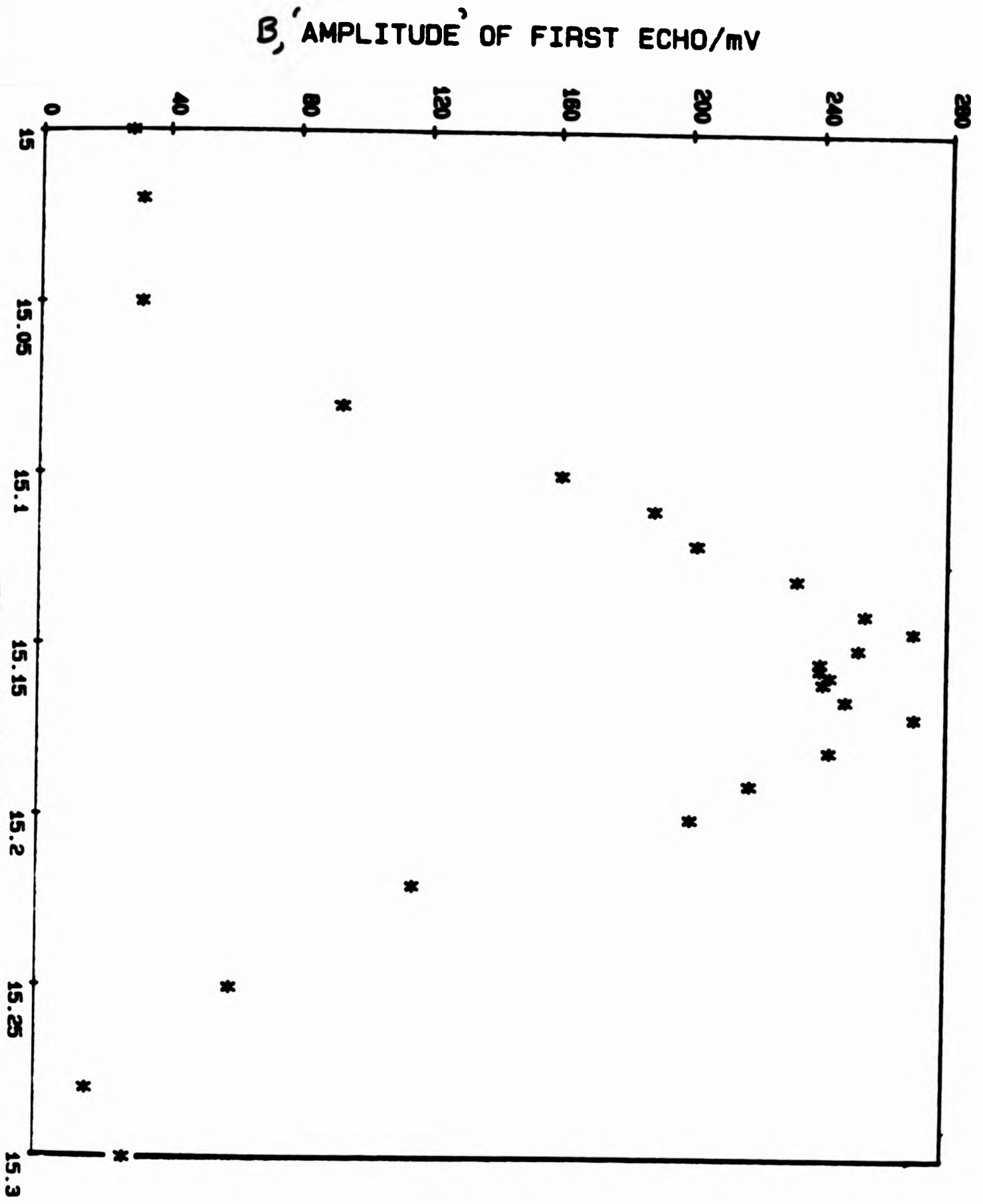

FIG 4.10 : The 'amplitude' B of the 1st. echo as a function of frequency.

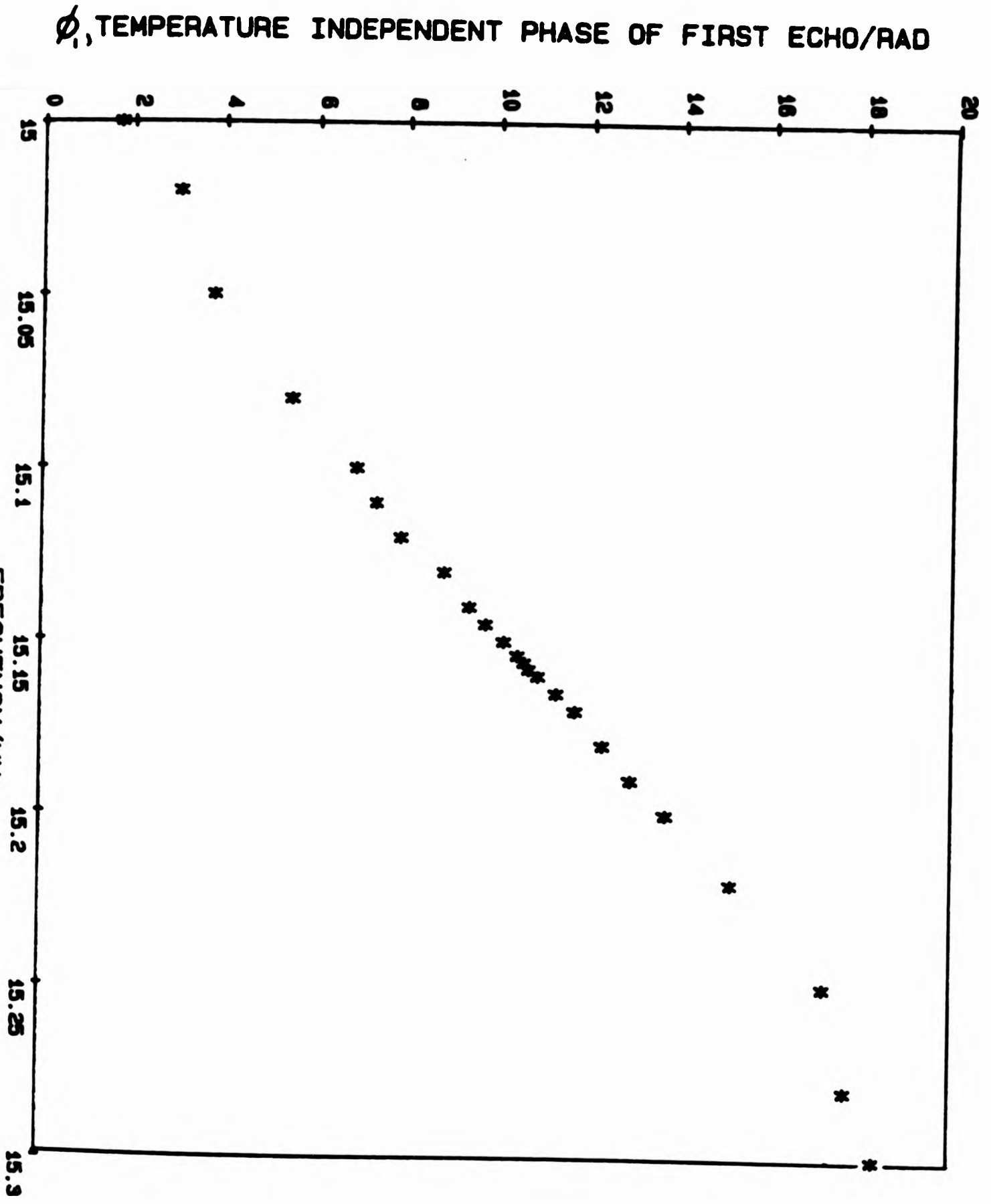

FIG 4.11 : The velocity-independent phase ϕ_1 of the 1st. echo as a function of frequency.

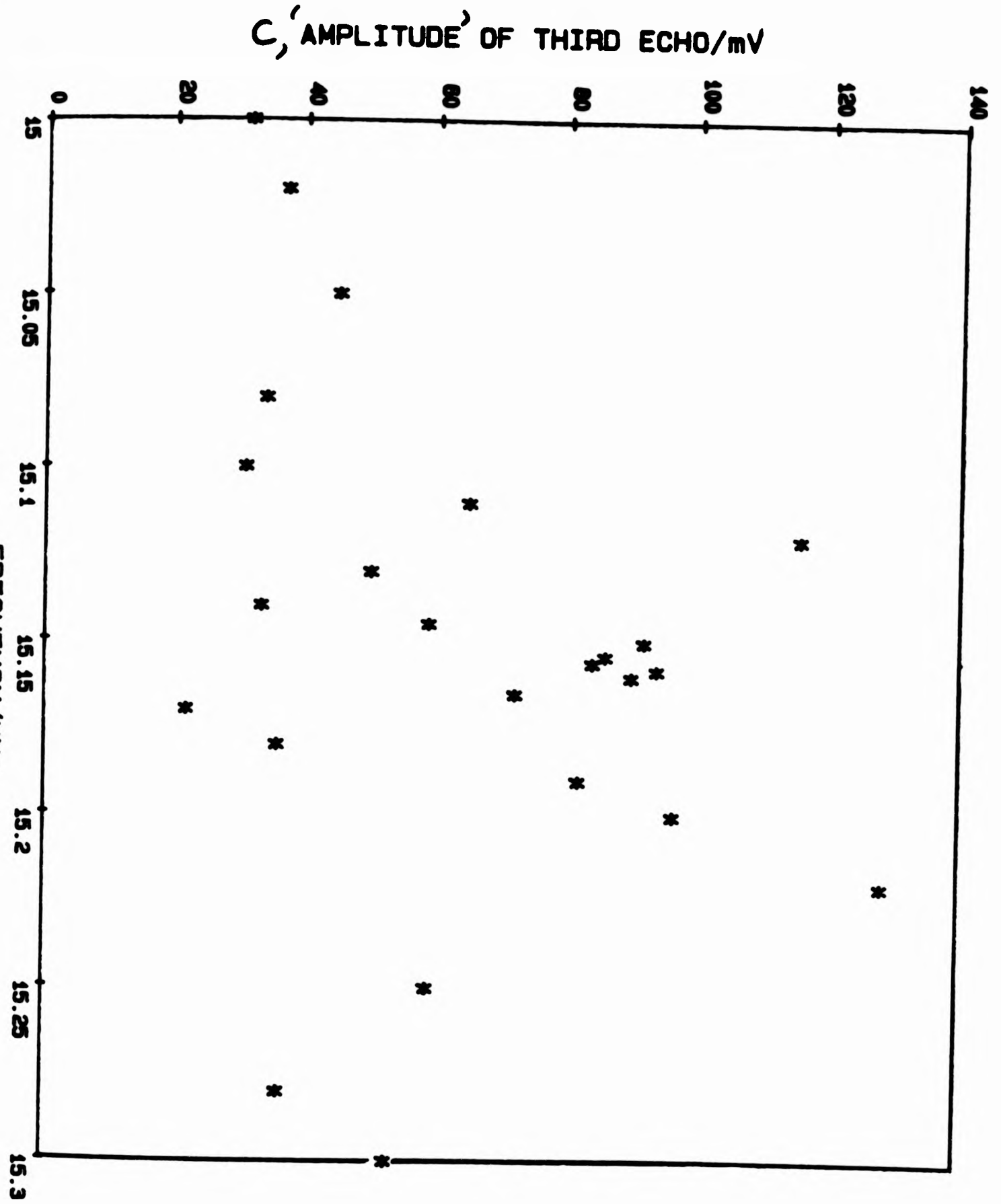

FIG 4.12 : The 'amplitude' C of the 3rd. echo as a function of frequency, showing no clear frequency dependence.

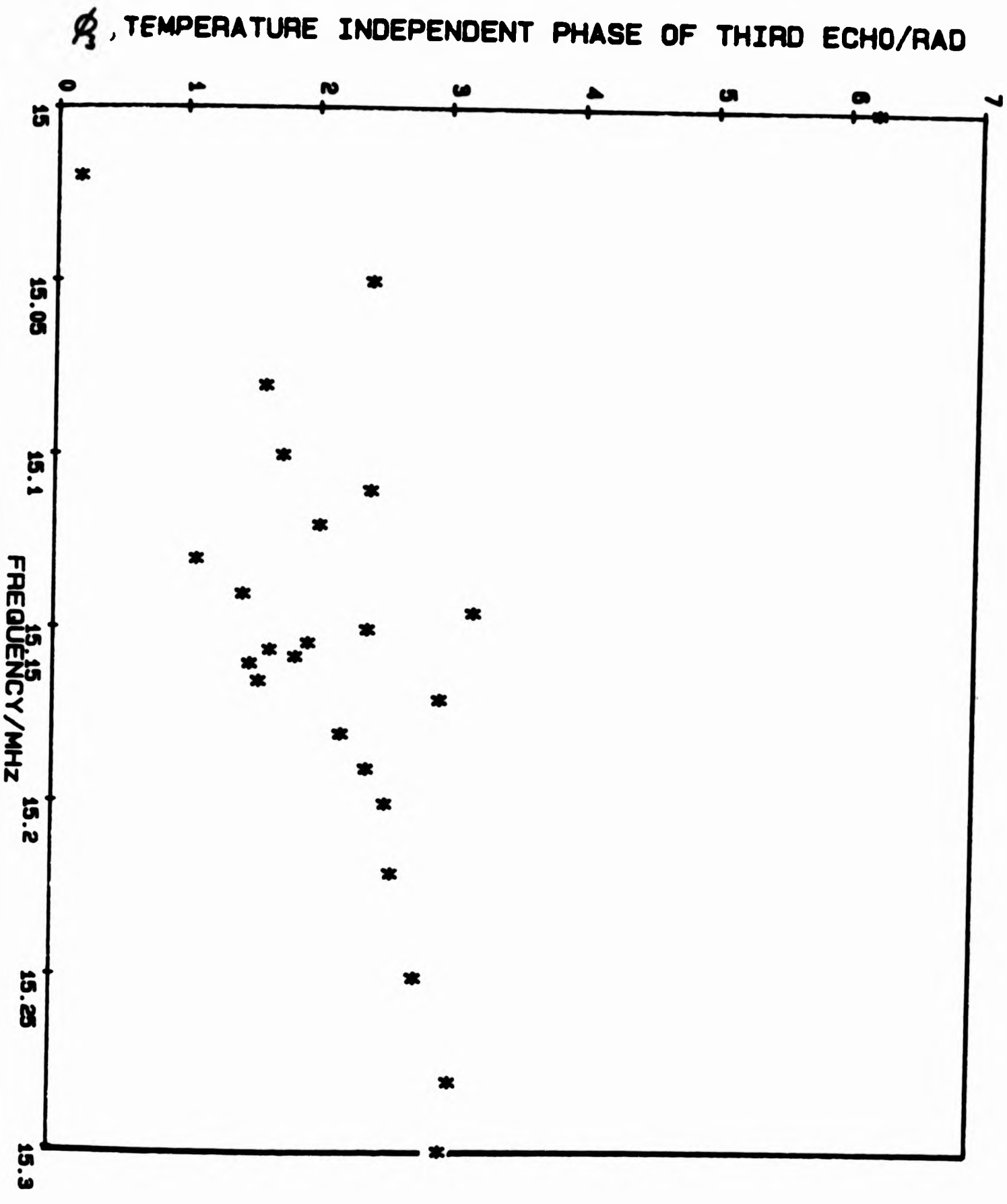

FIG 4.13 : The velocity-independent phase ϕ_3 (modulo 2π) of the 3rd. echo as a function of frequency, showing no clear frequency dependence.

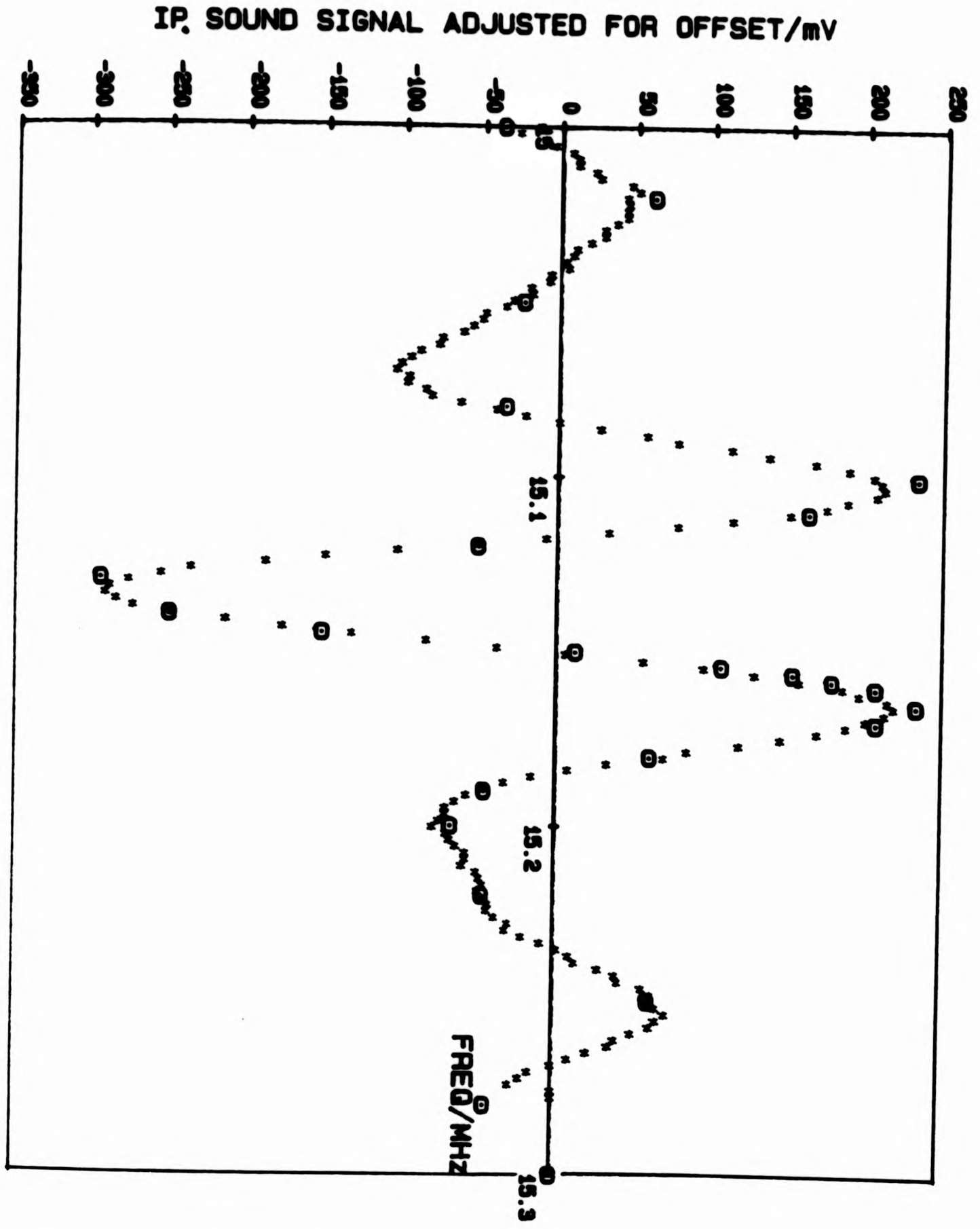

FIG 4.14 : Comparison of measured in phase data (x) and simulated in phase signal (o) as a function of sound frequency at T≈2.63mK.

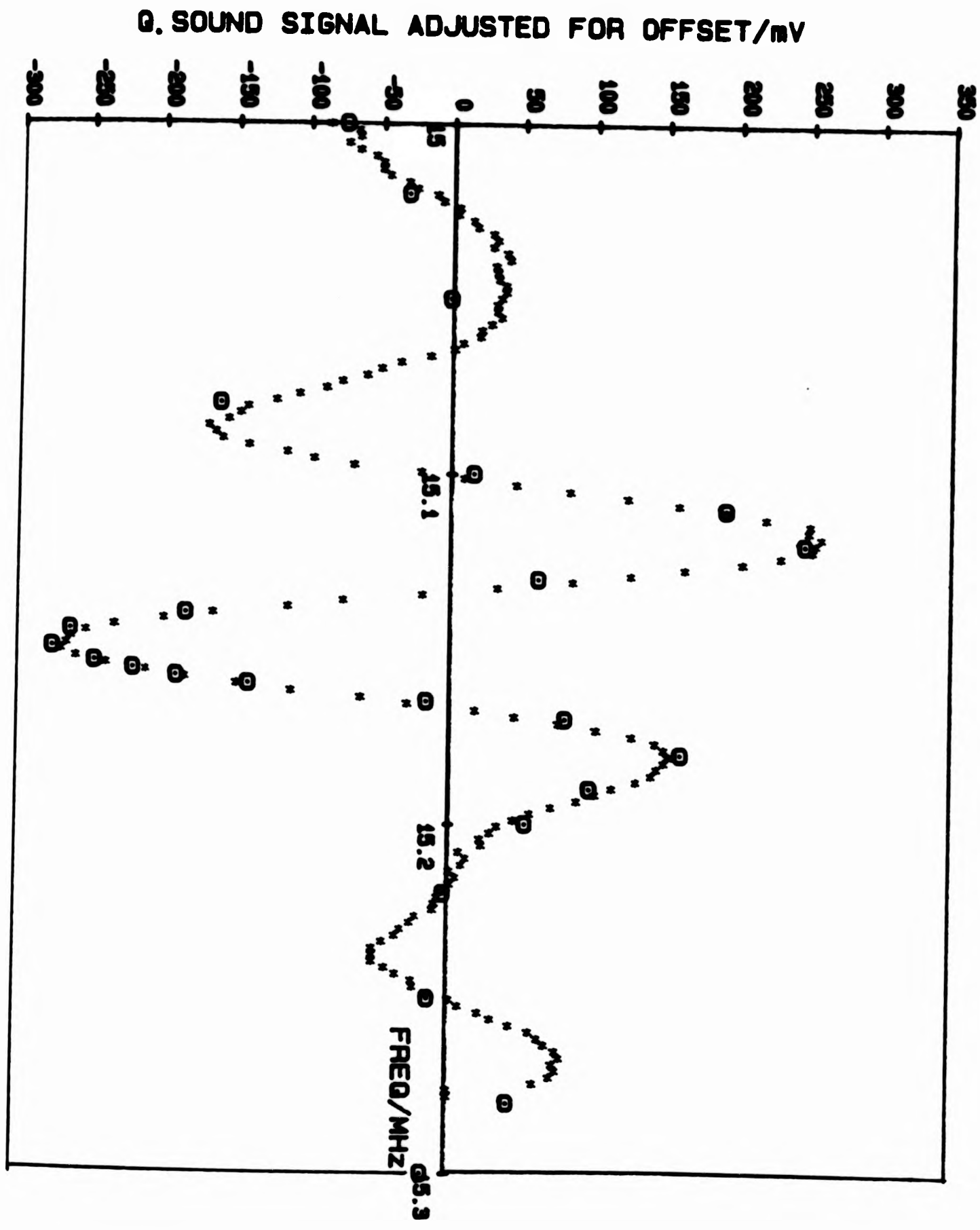

FIG 4.15 : Comparison of measured quadrature data (x) and simulated quadrature data (⊙) as a function of sound frequency at T ≈ 2.63mK.

4.4 Superfluid State Sound Data

In phase and quadrature records for the transmission of 15.154 MHz sound through the superfluid were gathered from two sources in order to increase the number of temperatures at which the sound velocity and attenuation could be found. Firstly, the signals at this frequency were extracted from the frequency sweeps. In addition, the transmission of 15.154 MHz sound through the helium was also detected using the sound settings described in section 2.3.2. Unfortunately, in spite of the Mu metal screening, there was a residual magnetic field experienced by the ^3He in the experimental cell. This may have been provided by the main solenoid magnet that was used to perform the nuclear demagnetisations. This residual field was found to have a component of about 1.04 G perpendicular to the plane of the helium slab and a component of about 0.11 G in the plane of the slab, measured at the cell with approximately 11% main solenoid field (≈ 8 kG) applied to the copper demagnetisation stage. The measurement and effect of this residual field on the superfluid will be discussed in greater detail in chapter 5. While making both kinds of measurement mentioned above the residual field perpendicular to the slab surfaces was compensated out by applying a steady opposing field with the experimental solenoid coil. Although the residual field in the plane of the slab was still present this would be expected to reinforce the uniform orbital texture.

The sweep measurements were made with the switchable attenuator of Figure 2.9 set to "31 dB" while the additional measurements made with a frequency of 15.154 MHz used a setting of "26 dB". In order to combine these data a comparison was made of the amplitude of the detected signal

for each of these attenuator settings. Figure 4.16 shows a plot of the amplitude of the in phase signal at 15.154 MHz, measured after passing from the cell and through the detection electronics, for "31 dB" attenuation of input signal against the corresponding signal measured for "26 dB" attenuation. A least squares line fit was performed to this data and is also shown on this figure. This corresponds to an actual difference of 5.4 dB between the two attenuator settings. The fact that this straight line does not pass through the origin is a manifestation of the offset voltage produced by the detection electronics. This has been assumed constant in fitting a line to these points which might explain some of the scatter.

Figures 4.17 and 4.18 show the records of in phase and quadrature data made up from these two sources. The data taken using "26 dB" attenuation has been adjusted by 5.4 dB and lies fairly closely on the same curves as the data taken using "31 dB" attenuation, providing some confidence in this adjustment.

The sound signal received after transmission through the superfluid might be expected to have a similar composition to that received from normal state ^3He. That is, the signal would be composed of contributions from the offset, the nuisance signal, the 1st sound echo and the 3rd sound echo in the form indicated by equations 4.4 and 4.5. For a frequency of 15.154 MHz values for N_I, N_Q, B, C, Φ_1 and Φ_3 have been found from fits to the normal state data. Using these values and by solving the equations for the in phase and corresponding quadrature sound signals in pairs values for the velocity and attenuation at each temperature could be deduced. These simultaneous equations have no analytic solution and therefore a Newton - Raphson iterative method was used to solve them.

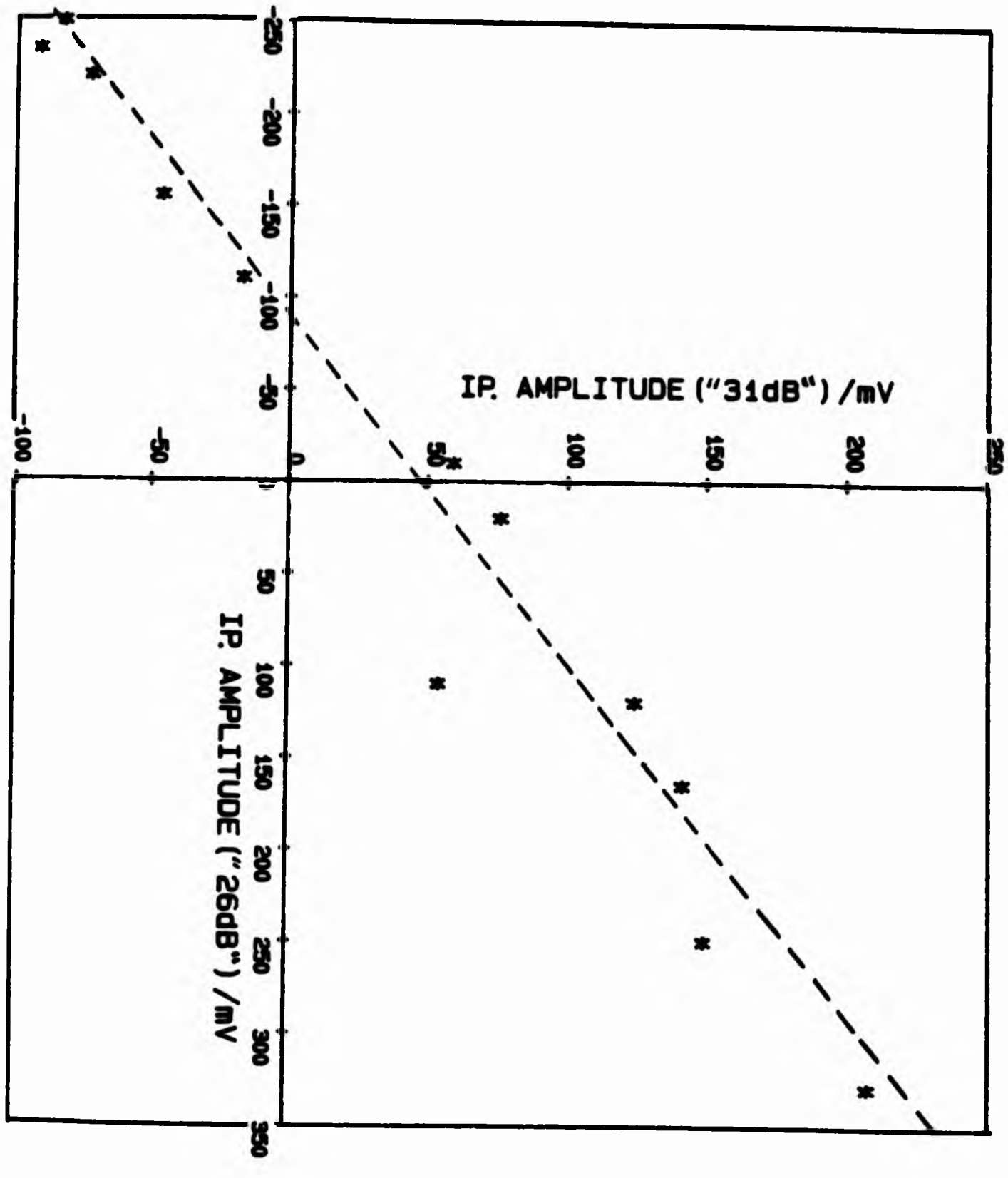

FIG 4.16 : Plot of in phase sound signal at 15.154MHz for '31 dB' attenuation on the input vs. corresponding signal with '26 dB' on the input. Least squares line fit to the data is shown as a dashed line.

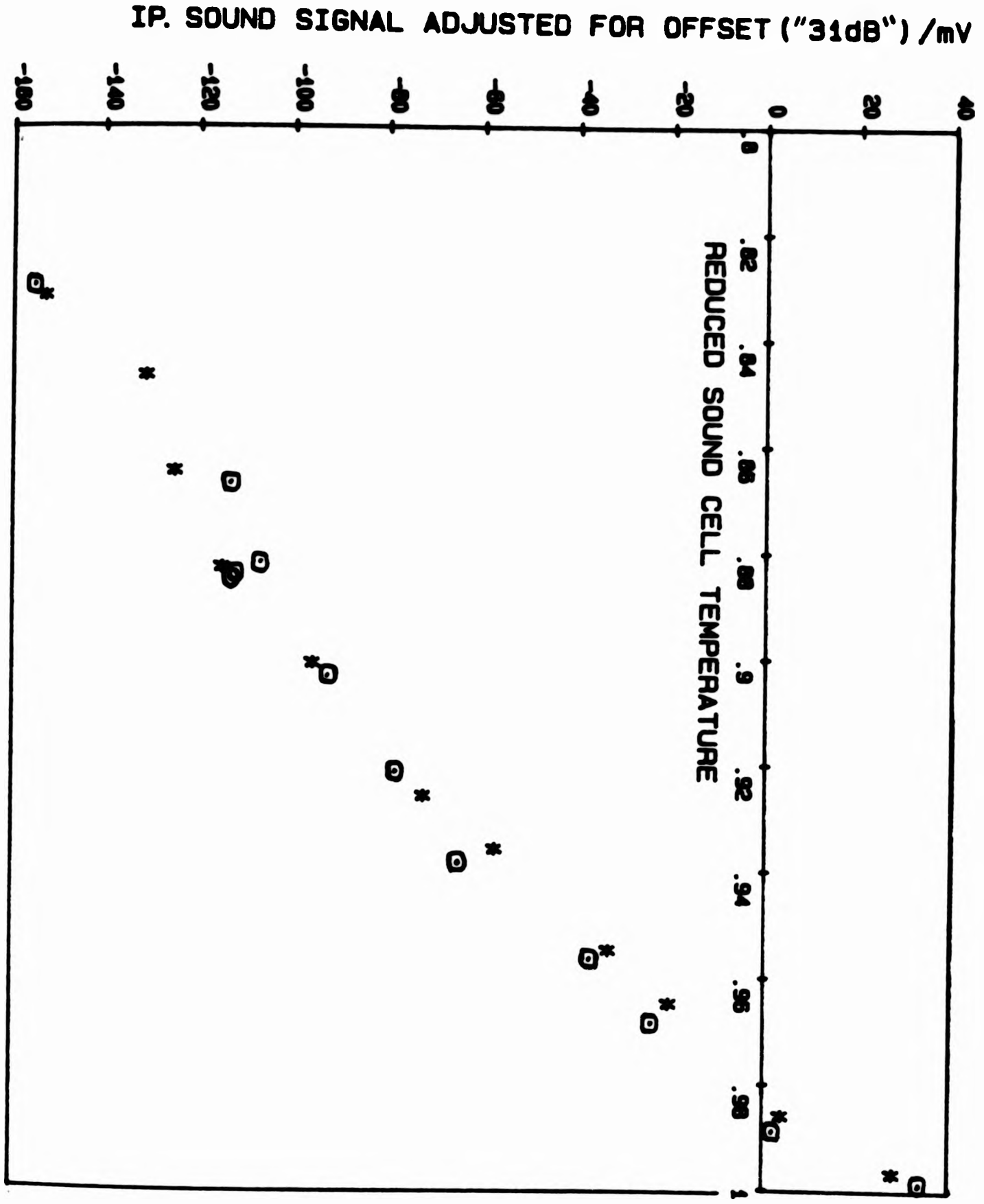

FIG 4.17 : 15.154MHz in phase sound record, with zero true vertical field & residual horizontal field (0.11G), across the A phase. * data taken using '31 dB' attenuation on signal input. ⊙ data taken using '26 dB' attenuation on signal input and adjusted by +5.4 dB.

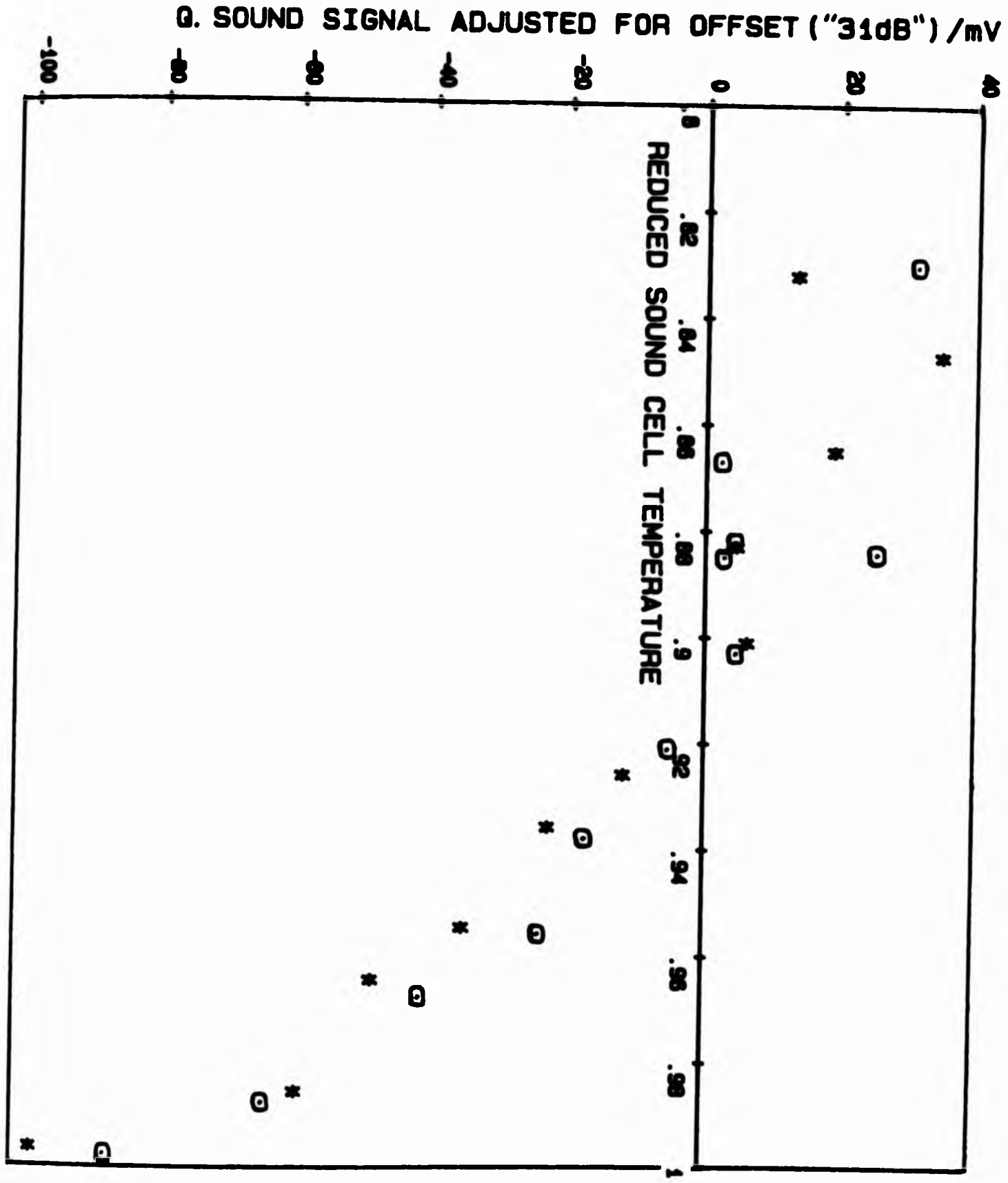

FIG 4.18 : 15.154MHz quadrature sound record, with zero true vertical field & residual horizontal field (0.11G), across the A phase. * data taken using '31 dB' attenuation on signal input. ⊙ data taken using '26 dB' attenuation on signal input and adjusted by +5.4 dB.

Appendix E contains further details about this procedure. In each case an initial guess was made for α and c by assuming zero contribution to the signal from the 3rd echo and solving the resulting equations analytically.

Values for the velocity and attenuation of 15.154 MHz sound transmitted through ^{3}He at 29.316 bar were found in this way at 23 temperatures in the A phase. Figure 4.19 shows a plot of the velocity for 2.18 mK to 10 mK where the normal state velocities are those calculated from equations 4.1 and 4.2. Figure 4.20 shows a plot for the attenuation below 3 mK. The unbroken line represents the attenuation found from equation 4.3 for 15.154 MHz sound in the normal state, while the broken line is an extrapolation of this made by assuming that the superfluid transition had not occurred.

A sudden change in slope of attenuation and a simultaneous sharp drop in velocity are observed at the transition, indicating the appearance of new excitation mechanisms in the superfluid phase. Paulson et al. (54) and Wheatley (12) have also seen this behaviour but in addition they have also observed a narrow peak in the sound absorption at a temperature just below T_c. Wölfle (55) and other authors (56) have described this in the framework of BCS theory as being caused by excitation of the pair condensate i.e. breaking of Cooper pairs followed by excitation of quasiparticle pairs and/or excitation of collective modes of the order parameter. These collective modes consist of vibrations of the internal structure of the order parameter, with frequencies of the order of the gap frequency. Different modes of oscillation are referred to, for example, as "clapping" and "flapping" modes. For the situation described here of sound transmission parallel to $\hat{\mathbf{z}}$ none of the collective modes could couple to

the sound. Also Wölfle calculates (assuming no quasiparticle collisions) that this peak in absorption will occur for $(\Delta_o(T)/\hbar\omega)^2$ between about 2 and 0, where $\Delta_o(T)$ is the maximum value of the energy gap and is given in terms of the mean value $\Delta(T)$ by $(3/2)^{1/2}\ \Delta(T)$.

In the Ginzburg-Landau region $\Delta(T)$ can be represented by

$$\Delta(T) = 3.06\ K^{-1}(k_B\ T_C)\ (1 - T/T_C)^{1/2} \qquad (4.6)$$

(3)

where K = 6/5 for weak coupling BCS theory. Including the trivial strong coupling effect correction which enhances $\Delta(T)$ by a factor of 1.3, then

$$\left[\frac{\Delta_o(T)}{\hbar\omega} \right]^2 = \frac{3/2 \times 3.06^2 \times (k_B\ T_C)^2(1 - T/T_C) \times 1.3^2}{6/5 \times (\hbar\omega)^2} \qquad (4.7)$$

Therefore $0 < (\Delta_o(T)/\hbar\omega)^2 < 2$ corresponds to $1 > T/T_C > 0.992$ for 15.154 MHz sound transmitted through ^{3}He-A at 29.316 bar, and it follows that any peak in the absorption would not have been detected by the measurements described here. In addition, if the effect of quasiparticle collisions is considered then it becomes apparent that at the frequencies and temperatures at which these measurements were taken the external field can neither induce pair breaking (apart from a small fraction of pairs with momenta in the direction of the gap axis) nor can it excite collective modes. This is described as the macroscopic regime(52).

How good are these values for the velocity and attenuation ? At a reduced temperature of 0.926 values were found for α and c of 1.15 cm^{-1} and 400.815 ms^{-1} respectively, using the method described above. These, together with the values for N_I, N_Q, B, C, Φ_1 and Φ_3, were used to simulate a frequency sweep. This was compared with the actual sweep measured,

adjusted for the offset. The agreement between measured and simulated data is shown in Figures 4.21 and 4.22 for both the in phase and quadrature signals. In each case the simulation was performed by assuming values of α and c constant and equal to those for 15.154 MHz sound across the frequency range 15.0 to 15.3 MHz. It can be seen that the agreement between measured and simulated data is good for the in phase signal but not as close for the quadrature signal. The reason for this is not known. The uncertainties in α and c were difficult to assess because α and c were frequency dependent and also because the errors in the coefficients N_I, N_Q, B, C, Φ_1 and Φ_3 increased with frequency away from the resonant frequency. For this reason the following procedure was adopted to provide a guide to the errors. The standard deviation was calculated for the fits shown in Figures 4.21 and 4.22 for the 10 frequency points nearest the resonant frequency i.e. at 10 points in the range 15.13 to 15.17 MHz. This was found to be about 4.5 mV. The attenuation and velocity were varied by a few percent in turn until a difference of $\pm$ 1 standard deviation was obtained for the fits. This was found to correspond to changes of $\pm$ 10% in α or $\pm$ 1% in c (i.e. about $\pm$ 2.5% in $e^{-\alpha d}$ or $\cos(\omega d/c+\Phi)$). However, it should be noted that not only did the errors vary with frequency but also with temperature (since at some temperatures the signals found after subtraction of the offset voltage were small so that any error in this offset would have a greater effect).

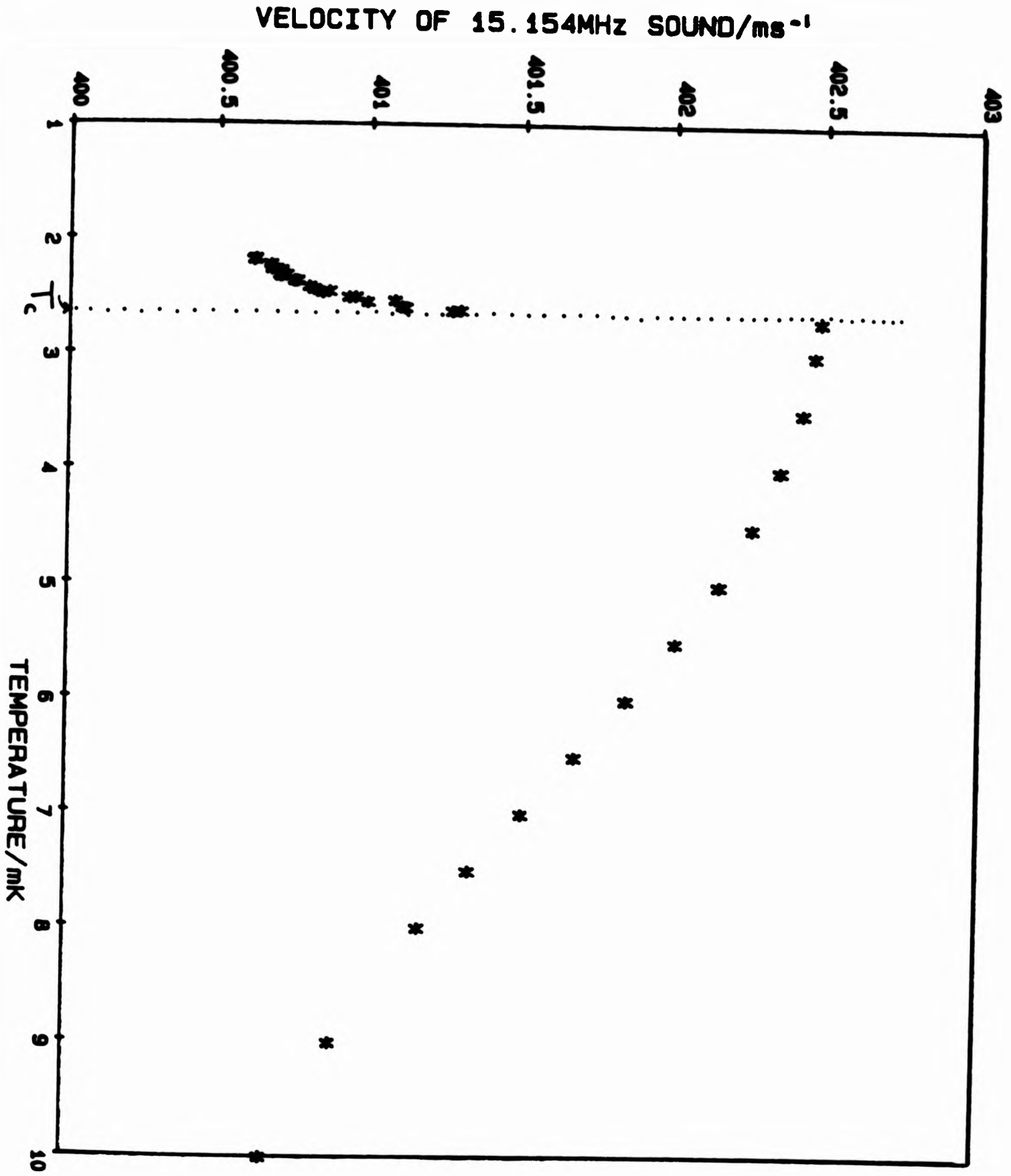

FIG 4.19 : Velocity of 15.154MHz sound in ^{3}He for 2.18mK to 10mK. The normal state velocities have been calculated from equations 4.1 and 4.2. A sharp drop in velocity is apparent at the transition.

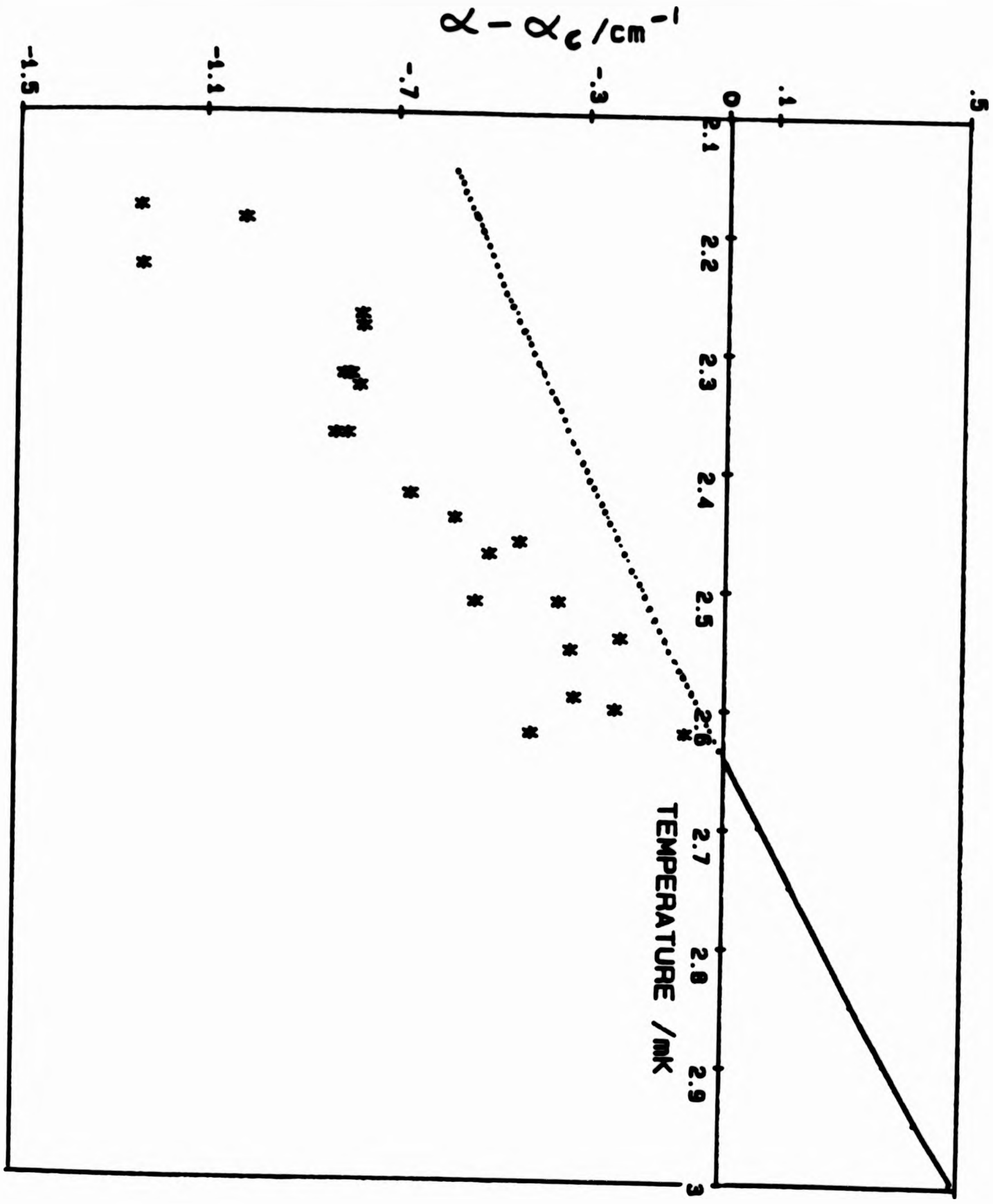

FIG 4.20 : Attenuation of 15.154MHz sound in ^{3}He below 3mK. The normal state attenuation (unbroken line) has been calculated from equations 4.1 and 4.3. The dotted line is an extrapolation of the normal state attenuation assuming no transition had occurred.

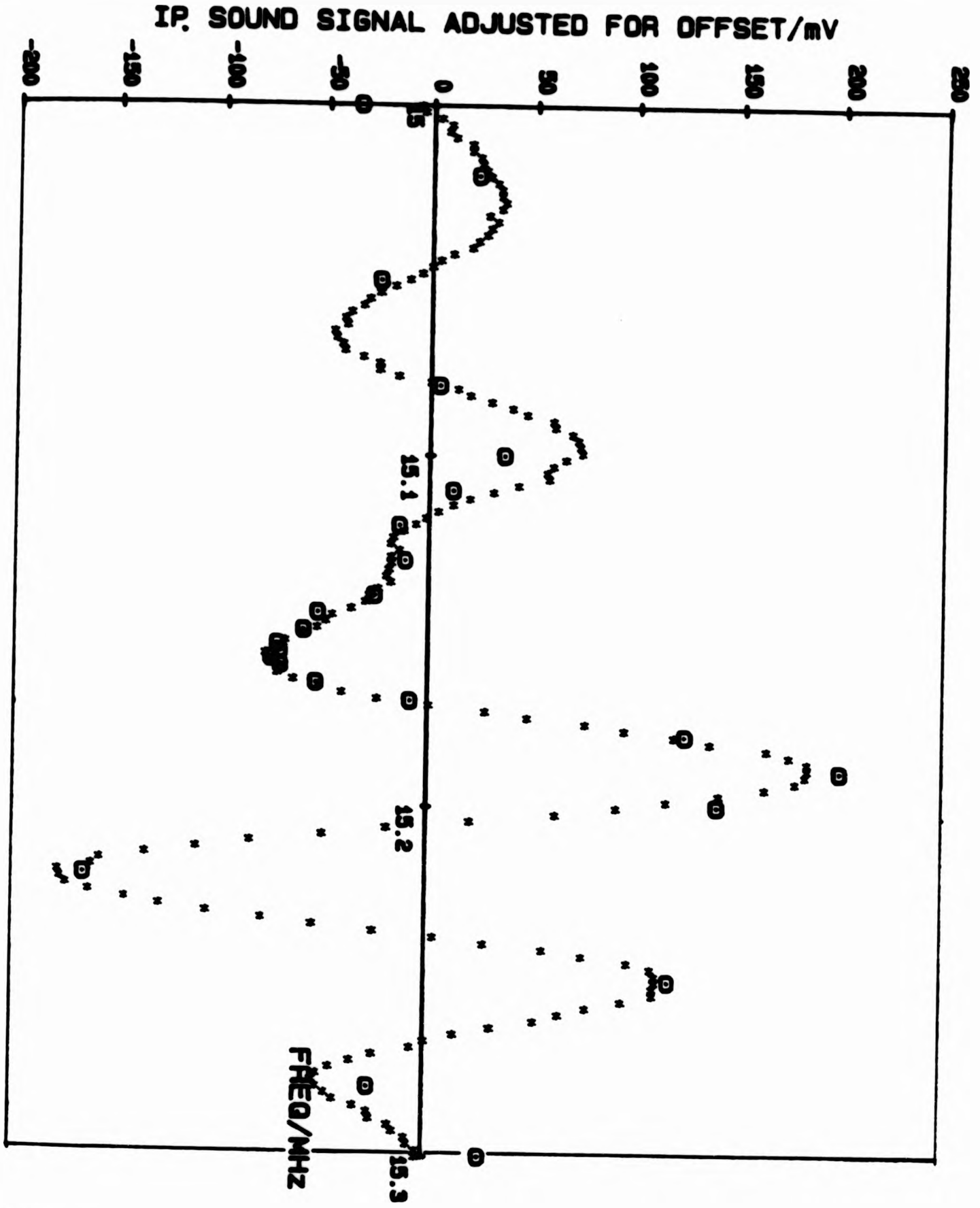

FIG 4.21 : Comparison of measured in phase data (*) and simulated in phase signal (o) as a function of sound frequency at T/T_c=0.926.

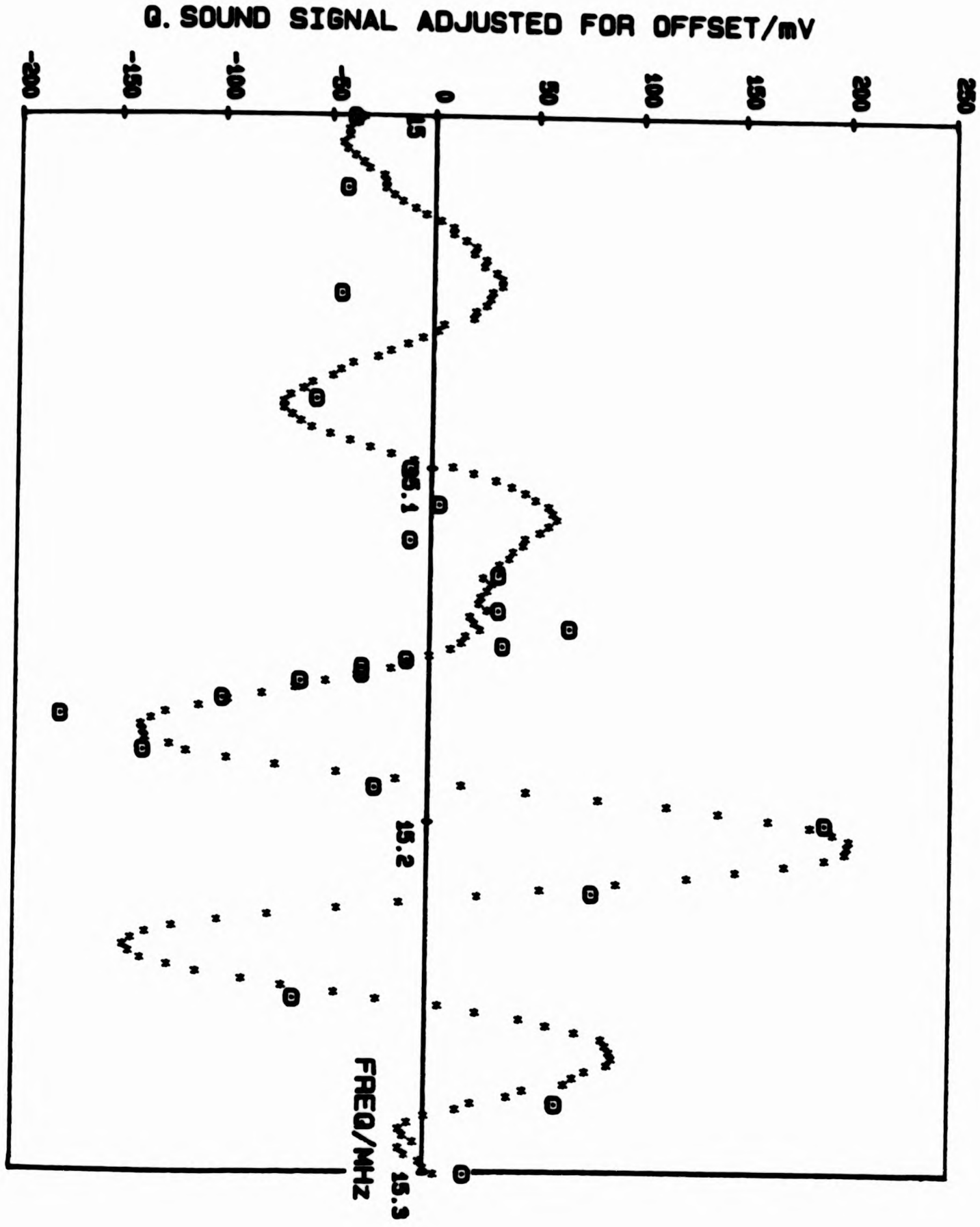

FIG 4.22 : Comparison of measured quadrature data (*) and simulated quadrature signal (©) as a function of sound frequency at T/T_c=0.926.

CHAPTER 5 : STATIC MAGNETIC FIELD INDUCED TEXTURAL CHANGES IN ^{3}He-A

5.1 Introduction

This chapter contains a discussion of static magnetic field induced textural changes in ^{3}He-A at 29.316 bar, determined using 15.154 MHz ultrasound as a probe.

Section 5.2 quantifies the residual magnetic field that was found to be present in the experimental region. Section 5.3 describes the measurements made of the Fréedericksz transition in ^{3}He-A and includes a comparison with the theoretical predictions. Section 5.4 discusses the determination of anisotropy coefficients, from the measurements described in 5.3, which characterise the attenuation and velocity of 15.154 MHz sound in terms of the angle made by the orbital vector $\hat{\mathbf{l}}$ with the direction of sound propagation. The determination of these coefficients also provided support for the underlying theory.

5.2 Residual Magnetic Fields

There was a residual magnetic field on the experimental sample of helium for zero applied magnetic field. This residual field appeared to possess a vertical and horizontal component, where the "vertical" direction is along the z axis perpendicular to the plane of the slab of ^{3}He-A, and therefore along the direction of sound propagation.

5.2.1 Residual Vertical Field

The residual vertical field had a magnitude greater than the critical field required to bring about a Fréedericksz transition (see section 1.3.2). When ramping on a vertical field in one direction two consecutive Fréedericksz transitions were observed on the sound signal (see Figure 5.1). By comparison, no transition was apparent when a vertical field was ramped on instead with opposing polarity (see Figure 5.2). The residual vertical field was given by the value of the applied field at a point midway between the two observed Fréedericksz transitions occurring at $H1_{applied} = H_{-f}$ and $H2_{applied} = H_{+f}$. Figure 5.1 shows how this field was estimated by $(H1_{applied} + H2_{applied})/2$. Figure 5.3 shows the residual vertical field plotted against reduced temperature showing no apparent dependence, and Figure 5.4 shows the residual vertical field plotted against the percentage of main (70 kG) solenoid field applied to the copper nuclear demagnetisation stage. There is not sufficient evidence to suggest the latter as the source of the residual field, although this is probable.

A mean value for the residual vertical field was found to be 1.04 G ± 3%

5.2.2 Residual Horizontal Field

Under the influence of the residual vertical field and with no applied magnetic fields the texture in the centre of the helium channel had already undergone a Fréedericksz transition. The effect of applying a horizontal field therefore was to produce a more uniform texture, with a corresponding response of the detected sound signal. By ramping on a

horizontal field in one direction using one of the sets of saddle coils and then repeating but with reversed field polarity one might expect any residual field directed along the axis to show up on a comparison of the detected sound signals. This comparison of sound signals was made for fields applied with both sets of saddle coils and is shown for the outer saddle pair in Figure 5.5 and the inner saddle pair in Figure 5.6.

There is evidence of a small residual field in the direction of field applied by the outer saddle coils. The magnitude of this was estimated by performing least squares line fits to the most responsive portions of the detected sound signals as indicated in Figure 5.5. The residual horizontal field suggested in this way was 0.11 G ± 10%. There was no measurable residual field in the direction of fields applied by the inner saddle coil pair i.e no field with magnitude ≥ 0.01 G could be detected.

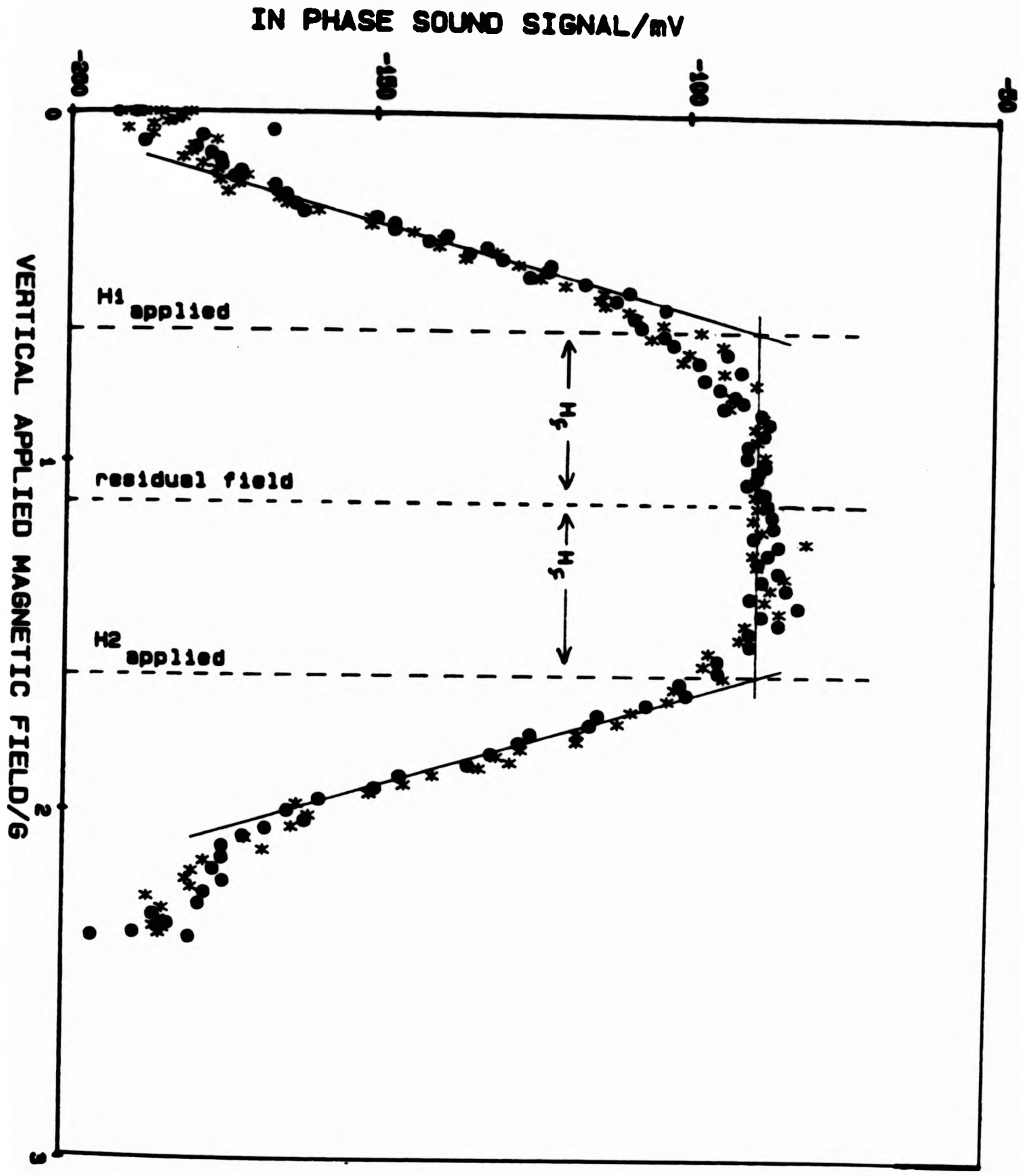

FIG 5.1 : In phase sound response as a function of vertical applied magnetic field for T/T_c =0.88. * field ramp up, ● field ramp down. Least squares line fits used in the determination of H_f are also shown. Residual vertical field =1.1G H_f =0.49G for this data.

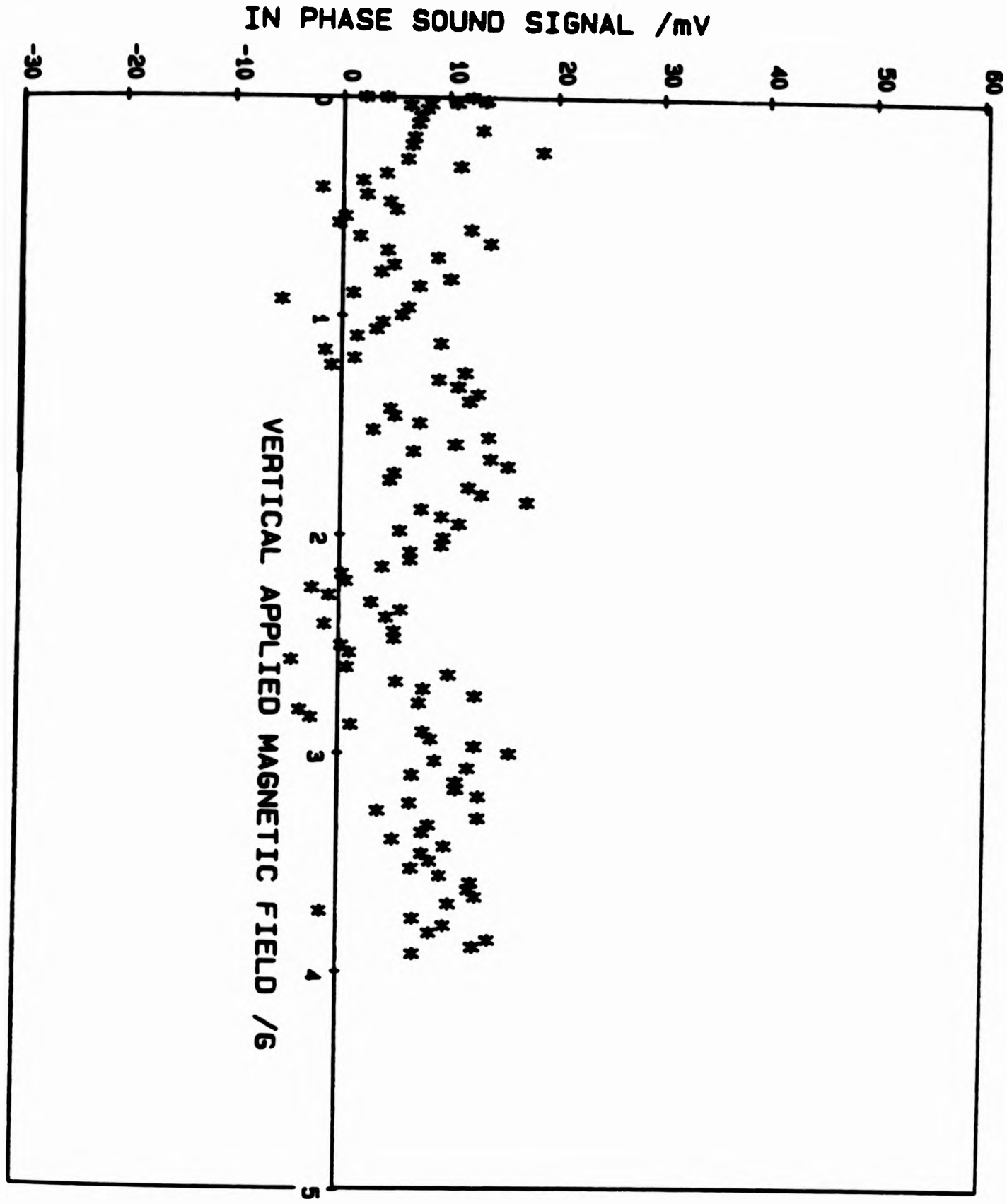

FIG 5.2 : In phase sound response as a function of applied magnetic field for field applied in opposing sense to that shown in Figure 5.1.

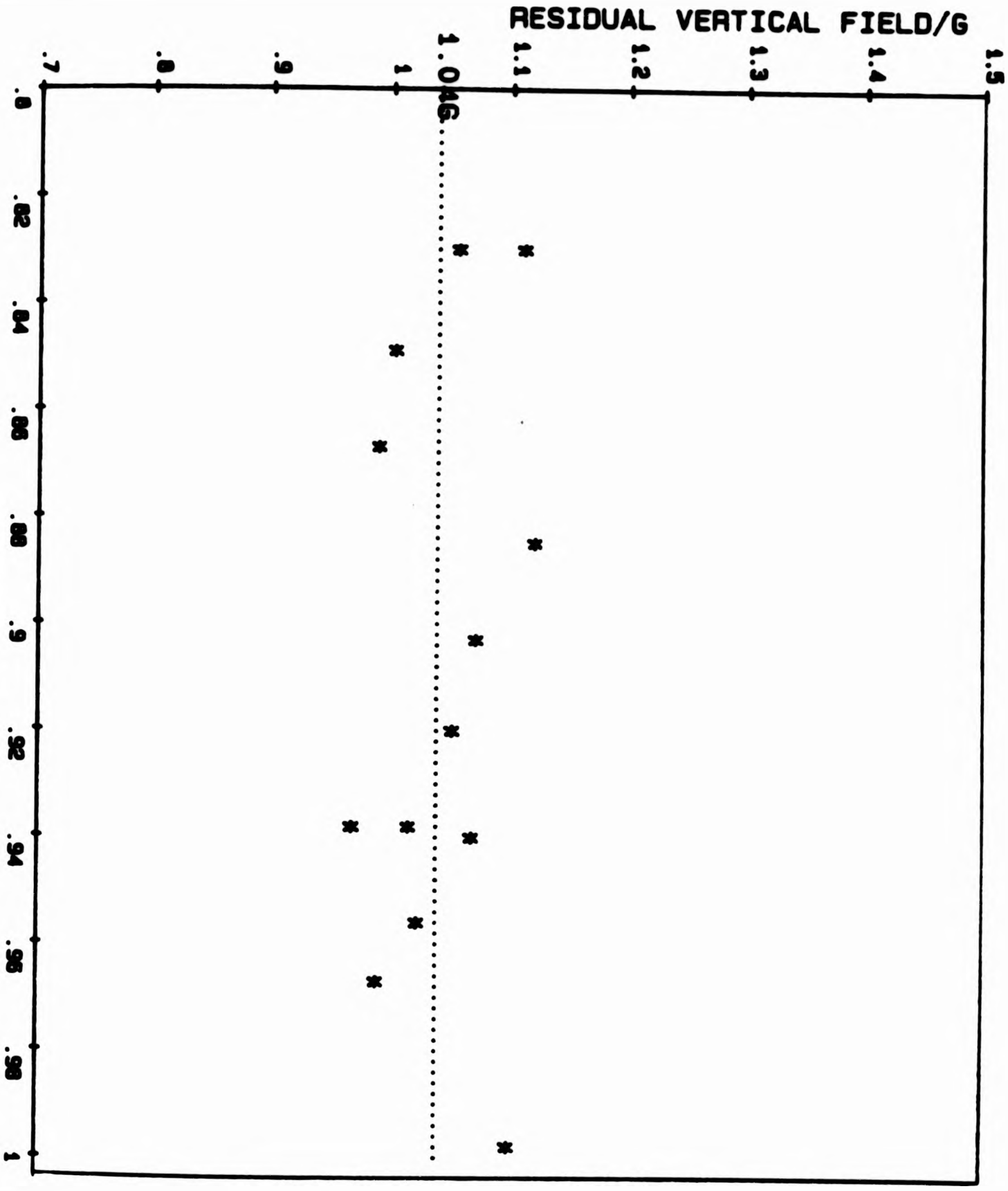

FIG 5.3 : Residual vertical field as a function of reduced temperature, showing no apparent dependence Dotted line represents mean value of H_{rv}=1.046

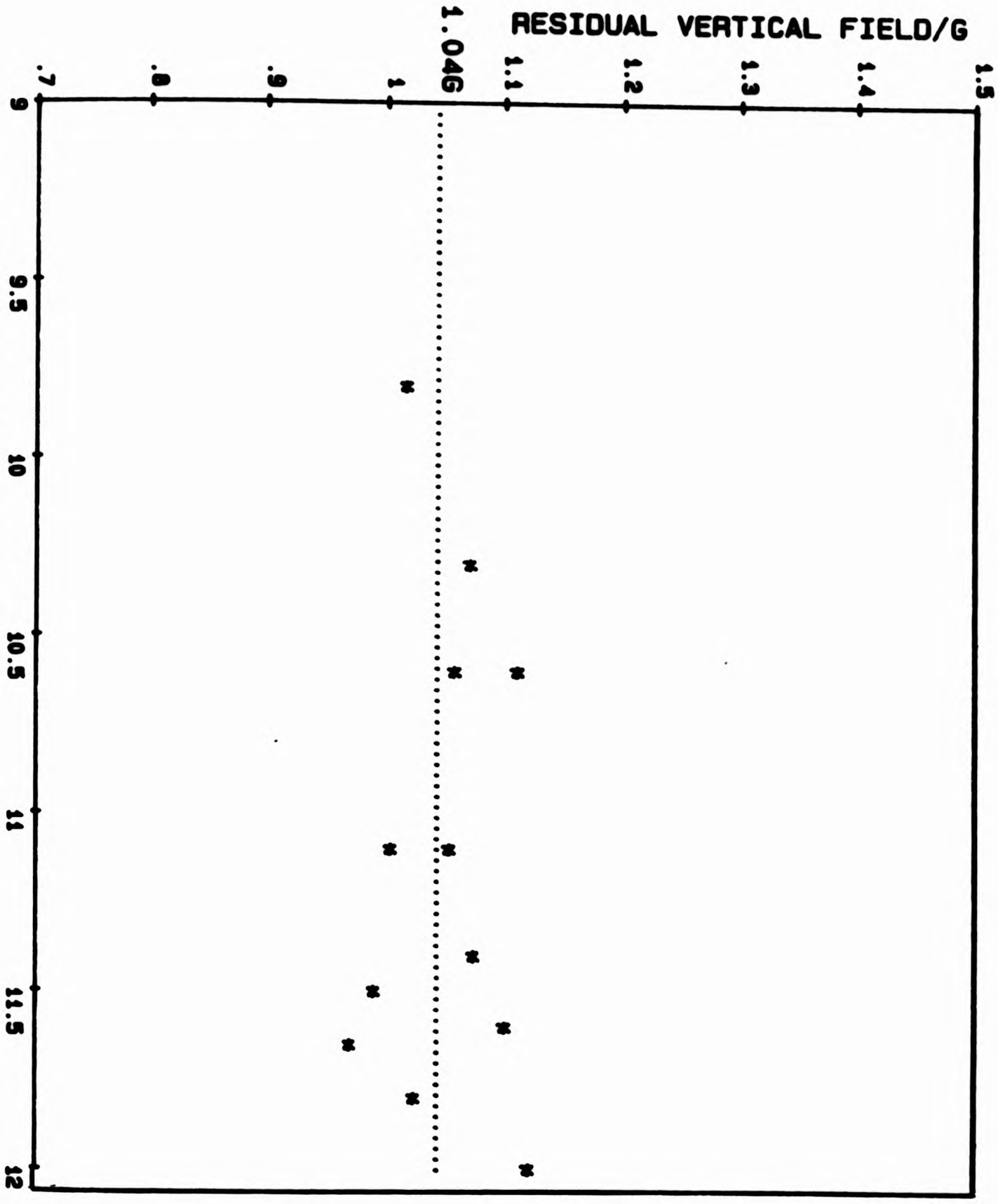

FIG 5.4 : Residual vertical field as a function of % main solenoid field applied to the nuclear demagnetisation stage. Dotted line represents mean value of H_{rv}=1.04G

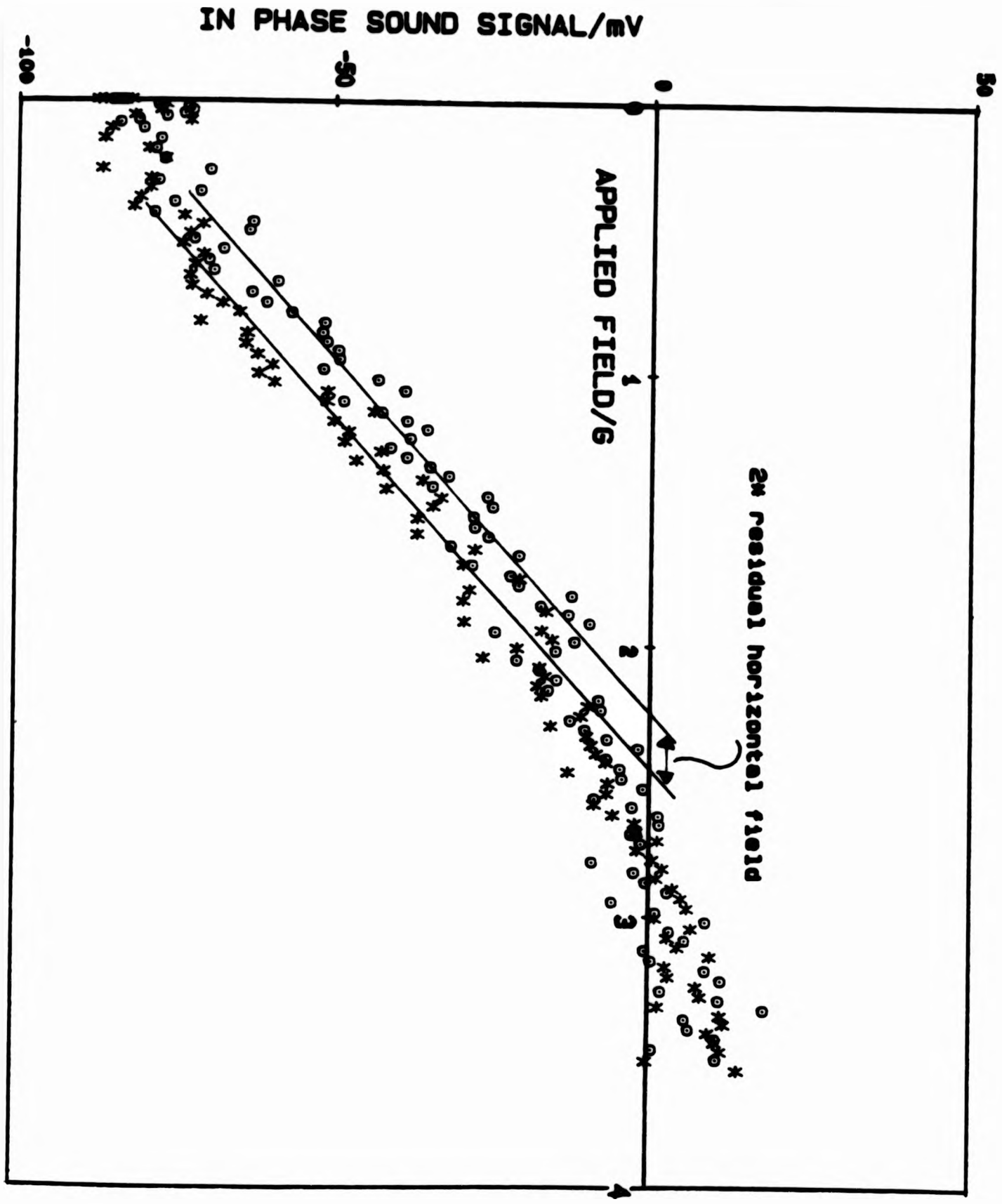

FIG 5.5 : In phase response as magnetic field was ramped on in outer saddle coils, first in one sense and then the other. Also shown are the least squares line fits used to deduce a value for the residual horizontal field of 0.11G±10% in this direction.

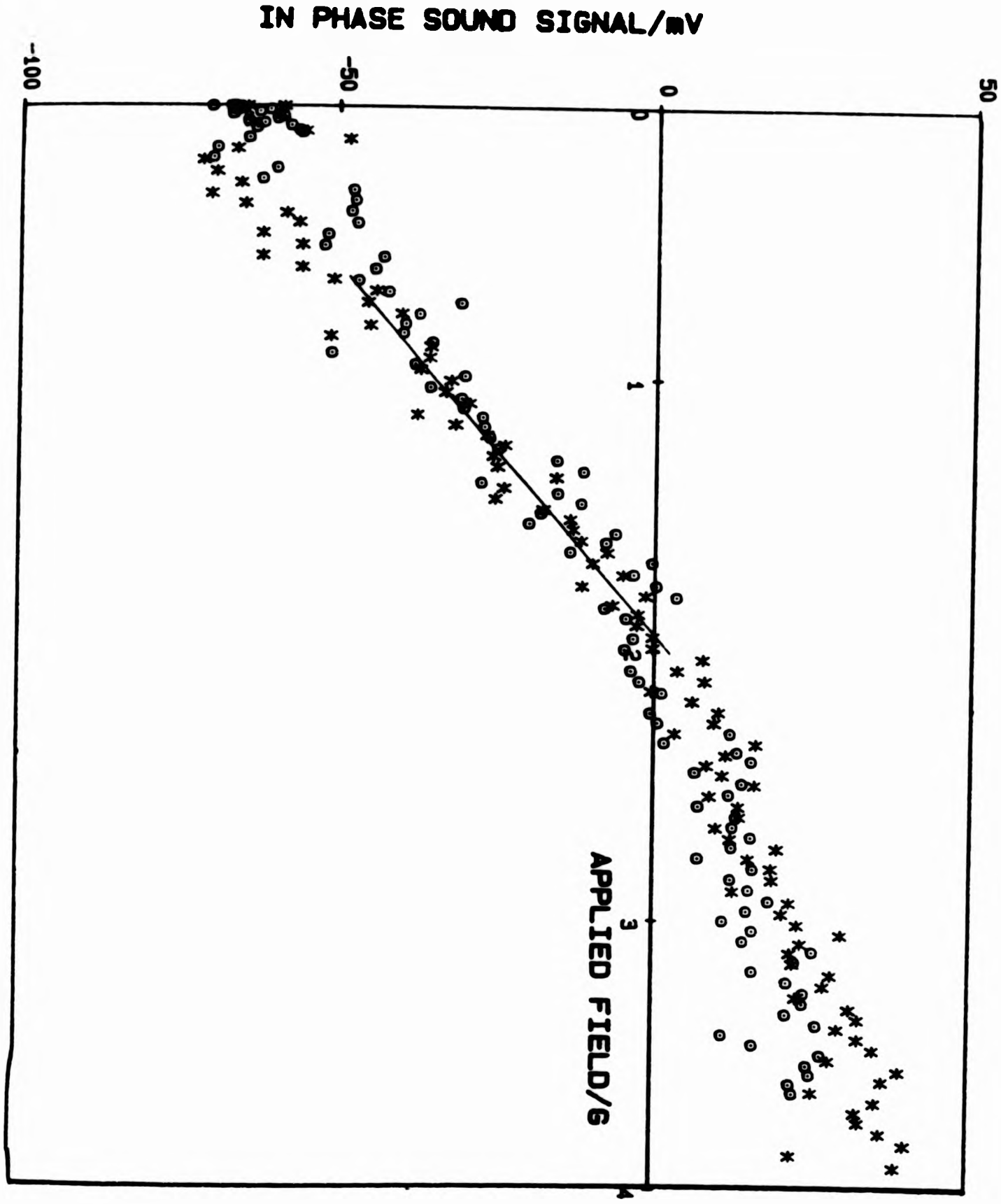

FIG 5.6 : In phase response as magnetic field was ramped on in inner saddle coils, first in one sense and then the other. Also shown is the least squares line fit used to deduce that there was no residual horizontal field in this direction.

5.3 The Fréedericksz Transition in ^{3}He-A

As described in chapter 1 the Fréedericksz transition in dipole-locked superfluid ^{3}He-A, contained between two parallel plane surfaces, is expected to consist of a sharp transition from a spatially uniform orbital texture to a more distorted texture, occurring at a well defined value of magnetic field H_f applied perpendicular to the surfaces.

5.3.1 Theory of Transition

The Fréedericksz transition was observed by studying the changes in received sound signal for pulses of 15.154 MHz sound transmitted through a 2 mm thick slab of ^{3}He-A. At the boundaries provided by the transmitter and receiver crystals $\hat{\mathbf{l}}$ was orientated parallel to the direction of sound propagation $\hat{\mathbf{q}}$ and thus the angle θ between $\hat{\mathbf{l}}$ and $\hat{\mathbf{q}}$ was zero. For a vertical magnetic field $>H_f$, θ at some distance away from the boundaries was finite, attaining a maximum value θ_o at the centre of the helium channel. The detected sound signal reflected an integration of the response across the 2 mm slab.

Consider a slab of ^{3}He-A of width d, as shown in Figure 5.7, with parallel plane boundaries at z = 0 and z = d and experiencing a field $\underline{H} = (-H_x, 0, H_z)$ where $H_x, H_z > 0$. The direction of sound propagation is along the z axis. Assuming $\hat{\mathbf{l}}$ distorts in the xz plane (an assumption that will be justified later in this section) then

$$\hat{\mathbf{l}} = (\sin\theta(z), 0, \cos\theta(z))$$

where $\theta(z)$ is the angle $\hat{\mathbf{l}}$ makes to the z axis and can be used to characterise the texture. The texture is assumed to vary only in the z direction and to be symmetric about z = d/2. For fields H of a few gauss

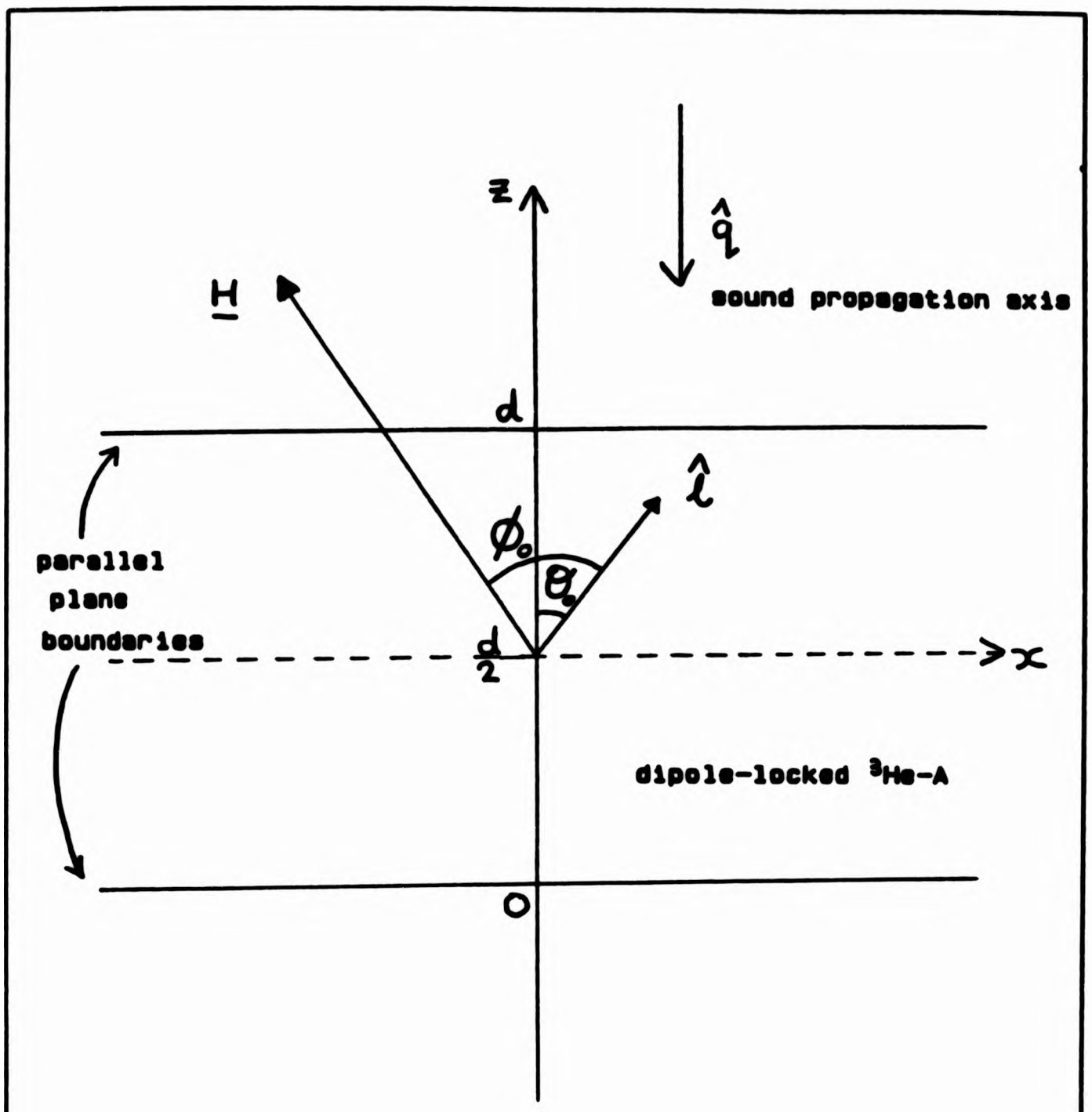

FIG 5.7 : Slab of ^{3}He-A considered in the theoretical calculations concerning the Fréedericksz transition. $\hat{l}$ is drawn at the centre of the slab so that $\theta(z)=\theta_0$ and $\phi(z)=\phi_0$.

the superfluid helium will be in the dipole-locked regime described in section 1.2, and the free energy density is given by (2)

$$f = \frac{1}{2} K_s (\text{div } \hat{\mathbf{n}})^2 + \frac{1}{2} K_b (\hat{\mathbf{n}} \times \text{curl}\hat{\mathbf{n}})^2 + \frac{1}{2} K_t (\hat{\mathbf{n}}.\text{curl}\hat{\mathbf{n}})^2 + \frac{1}{2} \Delta\chi (\hat{\mathbf{n}}.\underline{\mathbf{H}})^2 \quad (5.1)$$

where $\Delta\chi$ is the susceptibilty anisotropy and K_s, K_b, K_t are the dipole-locked splay, bend and twist bending energy coefficients (see section 1.2).

For the situation described above this becomes

$$f = \frac{1}{2} K_s \sin^2\theta(z)\, \theta'(z)^2 + \frac{1}{2} K_b \cos^2\theta(z)\, \theta'(z)^2 \quad (5.2)$$

$$+ \frac{1}{2} \Delta\chi \left(H_z^2 \cos^2\theta(z) + H_x^2 \sin^2\theta(z) - 2 H_x H_z \sin\theta(z) \cos\theta(z) \right)$$

The Euler-Lagrange equation for θ describes the equilibrium texture, and is given by

$$\frac{\partial f}{\partial \theta} - \frac{\partial}{\partial z}\left[\frac{\partial f}{\partial \theta'}\right] = 0 \quad (5.3)$$

i.e. $$\left(K_s \sin^2\theta + K_b \cos^2\theta \right) \theta'' =$$

$$-\sin 2\theta \left\{ \left(K_s - K_b \right) \frac{\theta'^2}{2} + \frac{\Delta\chi}{2} \left(H_z^2 - H_x^2 \right) \right\} - \Delta\chi H_x H_z \cos 2\theta \quad (5.4)$$

with the boundary conditions $\theta = 0$ at $z = 0$ and $z = d$.

In the following discussion Ginzburg-Landau values ($K_s = K_b$) of the bending energy coefficients have been assumed. Explicit calculation of K_s and K_b by Fetter(57) shows this to be a good approximation over the reduced temperature range 0.83 - 1.0.

In order to find an expression for the Fréedericksz transition field H_f consider the following. In the limit $H_x = 0$ and when $\theta(z)$ is

small equation 5.4 becomes

$$K_b\,\theta''(z) = -\Delta\chi\,H^2\,\theta(z) \tag{5.5}$$

with a finite solution $\theta = \theta_o \sin kz$ where $k^2 = \Delta\chi H^2/K_b$ only for

$$H_f = \frac{\pi}{d}\left[\frac{K_b}{\Delta\chi}\right]^{1/2} \tag{5.6}$$

For $H < H_f$ the only solution is the spatially uniform texture $\theta = 0$, but for $H > H_f$ the texture is distorted.

Comparison of this to the value for the threshold field calculated for a Fréedericksz transition in a nematic liquid crystal system(58) shows a similar result

$$H_{fn} = \frac{\pi}{d}\left[\frac{K}{\chi_\perp - \chi_\parallel}\right]^{1/2} \tag{5.7}$$

where K is the elastic constant appropriate to the system and $\chi_\parallel$, $\chi_\perp$ the magnetic susceptibilities for $\underline{H}$ parallel to and perpendicular to the director $\hat{n}$, respectively.

The distorted solution $\theta = \theta(z)$ can be found by solving equation 5.4. Including the effect of the residual horizontal field H_x (assumed constant), this equation can be integrated to give

$$K_b\,\theta'^2 = \frac{\Delta\chi}{2}\,(H_z^2 - H_x^2)\,(\cos 2\theta - \cos 2\theta_o) - \Delta\chi\,H_x\,H_z\,(\sin 2\theta - \sin 2\theta_o) \tag{5.8}$$

and thus

$$\int_0^{\theta_o}\left[\frac{\pi^2}{2}\,\frac{(H_z^2 - H_x^2)}{H_f^2}\,(\cos 2\theta - \cos 2\theta_o) - \pi^2\,\frac{H_x}{H_f}\,\frac{H_z}{H_f}\,(\sin 2\theta - \sin 2\theta_o)\right]^{-1/2} d\theta$$

$$= \int_0^{d/2}\frac{dz}{d} = \frac{1}{2} \tag{5.9}$$

This integral was solved numerically for H_z/H_f for different values of θ_o. The method used to perform this integration will be discussed in section 5.4.

Figure 5.8 shows how θ_o varies with H_z/H_f. For the situation where $H_x = 0$ it can be seen that as H_z increases through H_f, θ_o increases initially with infinite slope $\theta_o = 2\,(H_z/H_f - 1)^{1/2}$, and for $H_z \gg H_f$ θ_o tends asymptotically to $\pi/2$. For this situation the energy of the distorted texture is unaffected by rotation about the z axis and in the absence of a perturbation to break this degeneracy the plane into which the texture distorts is not well defined. The small residual horizontal field present in this experiment acts as a symmetry breaking perturbation forcing distortion of $\hat{\mathbf{l}}$ in the xz plane, with the additional effect of smearing out the sharp transition. This smearing out can be seen in Figure 5.8 when the effect of a small horizontal field component ($H_x/H_f = 0.216$) has been included. Superflow might also be expected to blurr out the transition because of the orientating effect this may have on $\hat{\mathbf{l}}$ (see section 1.2).

Figure 5.9 shows how Φ_o, the angle between $\hat{\mathbf{l}}$ and $\underline{H}$ at the centre of the slab, varies with H_z/H_f for both $H_x = 0$ and for the inclusion of a small horizontal field component ($H_x/H_f = 0.216$). For the latter, it can be seen that $\Phi_o = \pi/2$ in the limit $H_z/H_f = 0$, and Φ_o tends asymptotically to $\pi/2$ for $H_z \gg H_f$ in both cases as expected for dipole-locked ^{3}He-A.

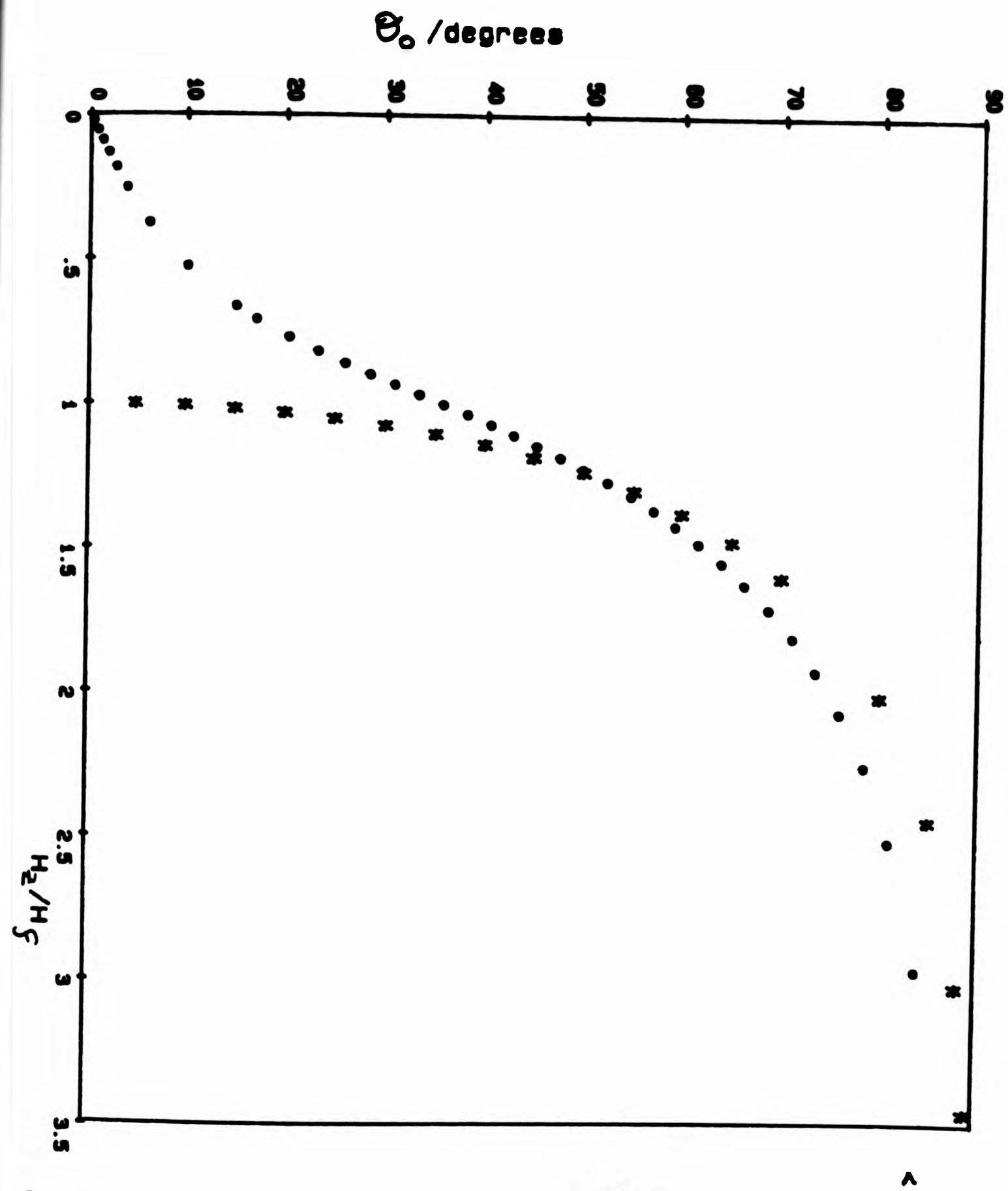

FIG 5.8 : Calculation of the angle θ_o, made between $\hat{\imath}$ and z at the centre of the slab, with increasing magnitude of field. * vertical field component only, • inclusion of small horizontal field component with H_x/H_ζ =0.216

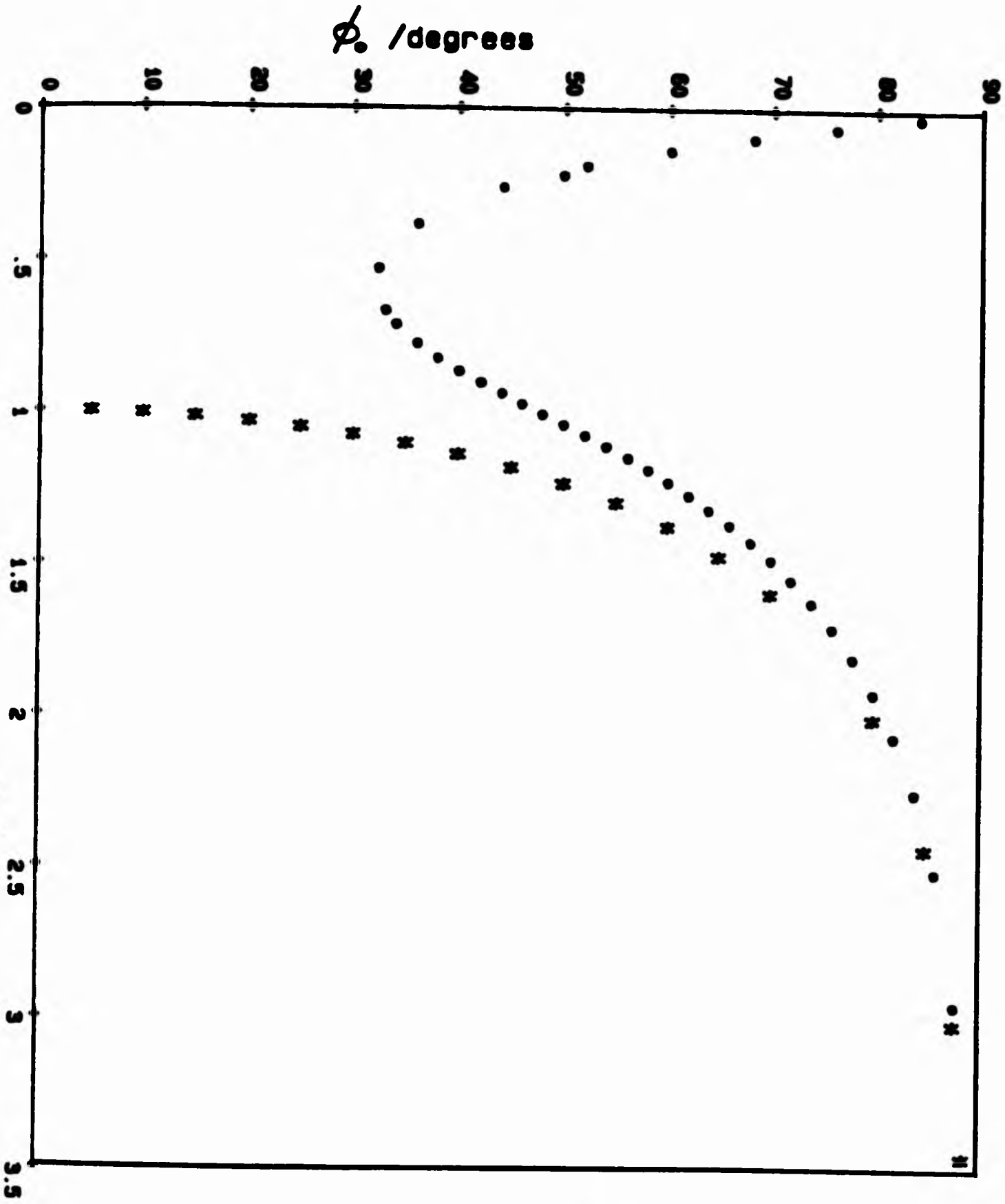

FIG 5.9 : Calculation of the angle ϕ_o, made between $\hat{\imath}$ and $\underline{H}$ at the centre of the slab, with increasing magnitude of field. * vertical field component only, • inclusion of small horizontal field component with H_x/H_ζ =0.216

5.3.2 Measurement of a Fréedericksz Transition

Measurements of the Fréedericksz transition were made at 10 temperatures in the A phase. In each case the measurement was made by detecting pulses of 15.154 MHz sound transmitted through the superfluid helium while a magnetic field was ramped on perpendicular to the slab in such a sense as to produce one Fréedericksz transition before the residual vertical field was compensated out and then another as the true vertical field was increased up to about $2.2H_f$. The response of both the in phase and quadrature detected sound signals to the static fields applied was measured at each temperature. The sound settings used were those described in section 2.3.2, with a detection electronics time constant of 1s. The data collection program listed in Appendix D was used to perform sound signal averaging and to record the sound and voltage ramp values.

The field ramp was provided by supplying a steady current ramp to the experimental solenoid coil. This was done using the Oxford Instruments voltage ramp together with the operational amplifier circuit described in section 2.4.4. A 1.9 kΩ potentiometer was included in this circuit to reduce the rate of increase/decrease of applied field to 0.065 G/min. This slow ramp rate was found to be necessary because of the orbital viscosity effect on the textural relaxation time (see section 1.3.1). Figure 5.1 shows the in phase response of the sound signal detected at a reduced temperature of 0.885 as the applied field was first increased and then decreased along the vertical direction at a rate of 0.065 G/min. It can be seen that the two sound signals are coincident within the noise, indicating that this was a reasonable value to choose for the ramp rate.

Figure 5.10 shows the response of the detected quadrature sound signal to a field applied in the vertical direction at the same reduced temperature. It is apparent that the variation in magnitude of the in phase signal is greater than that for the corresponding quadrature signal. This was true for all these Fréedericksz transition measurements, and for this reason the in phase signal records have been used to estimate values for the critical field H_f at each temperature.

All the Fréedericksz transitions observed were found to be rounded rather than sharp. The relatively large slab thickness was partly responsible for this as it resulted in weaker wall clamping of the uniform texture. The texture was therefore more easily disturbed by small influences other than the applied field perpendicualr to the slab. These influences included the presence of the residual magnetic field component of 0.11 G parallel to the slab surfaces (with H_x/H_f of order 0.2) and the supercurrent generated by the 0.2 nW heat input associated with the sound pulses. This 0.2 nW heat input was estimated to produce a superfluid flow with velocity $v_s \simeq 2\times10^{-6}$ ms^{-1} which was found to give an energy comparable to the susceptibility anisotropy energy in a magnetic field of around 0.03G. (Appendix F contains details of this calculation). However, for this situation involving counterflow v_s will increase rapidly as T_c is approached so that the influence of the flow on the $\hat{\mathbf{l}}$ texture might also be expected to increase. In fact the rounding out of the Fréedericksz transitions was not observed to become more severe near T_c suggesting that the effect of flow on the texture was relatively small. Another reason for this rounding might be that the geometry of the slab of ^{3}He, with an aspect ratio of approximately 5:1, was rather different to the slab of infinite lateral extent assumed by the theoretical calculation of 5.3.1.

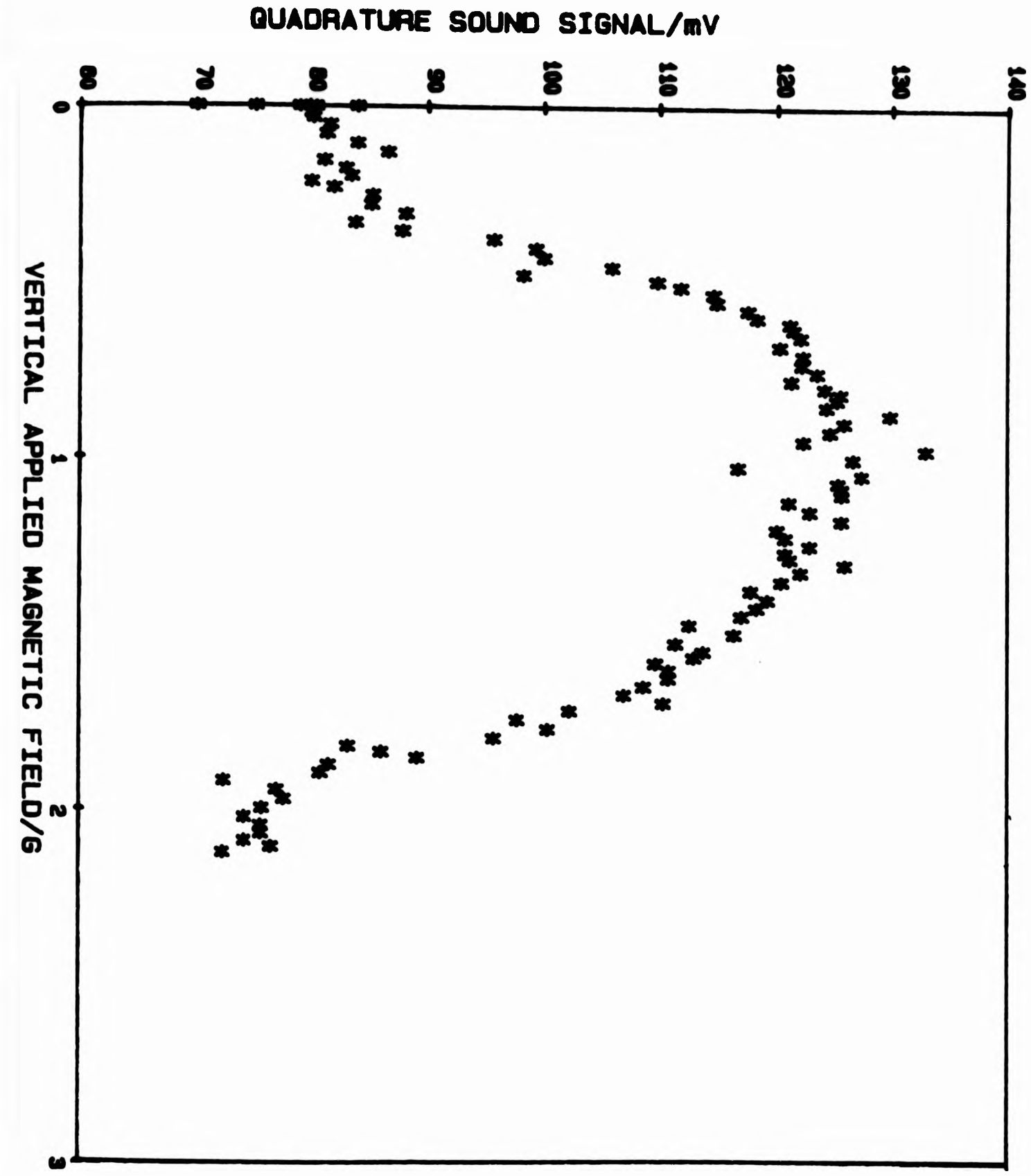

FIG 5.10 : Quadrature sound response as a function of vertical applied magnetic field for $T/T_c = 0.88$

The following method was employed to estimate values for H_f because of the rounding out of the transition. For each in phase sound measurement a least squares line fit was performed to the two steepest portions of the signal record, and another to the flatter portion of the signal record corresponding to small true vertical fields. The two points of intersection, occurring at applied fields of $H1_{applied}$ and $H2_{applied}$ indicated values for the critical Fréedericksz field which might have been observed if a sharp transition had taken place. By assuming that $H_{-f} = H_{+f}$ then a value for the residual field could be estimated as ($H1_{applied}$ + $H2_{applied}$)/2, and a value for the critical transition field H_f of ($H2_{applied}$ - $H1_{applied}$)/2. Figure 5.1 shows $H1_{applied}$ = 0.63 G, $H2_{applied}$ = 1.61 G and the residual vertical field = 1.12 G, providing a value for H_f = 0.49 G at this reduced temperature.

By performing these least squares line fits over different portions of the in phase sound record that still looked resonable the contribution made to the random error on H_f by this fitting procedure was estimated to be 2.5 %. Other contributions to the random error on H_f include the extraction of the value of applied field for each sound reading from the computer record of data. This error is expected to be less than 1%. There may also be a systematic error on H_f due to an estimated error of 3 % in the measurement of the solenoid field constant. Another contribution to the systematic error on H_f might be the conversion of voltages measured across a nominal 47 Ω resistor into currents flowing in the solenoid coil. The resistance of the 47 Ω wirewound resistor has been measured to better than 1%.

To summarise: the values of H_f measured have a random error of approximately 3% and a possible systematic error of around 3%.

5.3.3 Threshold Field for the Fréedericksz Transition

Values obtained for the threshold field for the Fréedericksz transition in ^{3}He-A are shown in Figure 5.11 and Table 2. Since $H_f \propto 1/d$ values for H_fd have actually been plotted. The error in the measurement of the slab thickness d is of order a few hundredths of a percent since this has been defined by the optically flat quartz spacer described in section 2.3.1. A variation of H_fd with reduced temperature is apparent, the threshold field decreasing as T_c is approached.

Figure 5.11 also shows two theoretical curves. These were calculated using equation 5.6 and taking expressions for Δx and K_b given by Leggett(3) and Cross(59) respectively.

Near T_c $\quad K_b \simeq 5/2\ \rho_{sII}\ (\hbar/2m)^2$ (5.10)

so that $\quad K_b \simeq 3/2\ \rho\ (\hbar/2m)^2\ (1-Y)/(1 + F_1^s/3)$ (5.11)

using an expression for ρ_{sII} given by Leggett, and where Y is the Yosida function and F_1^s one of the Fermi liquid parameters

Leggett also gives

$$\Delta x = x_N\ (1-Y)\ /\ (1 + F_0^a) \tag{5.12}$$

where the normal state susceptibility x_N may be written

$$x_N = 1/4\ \gamma^2\ \hbar^2\ (dn/d\epsilon)\ /\ (1 + F_0^a) \tag{5.13}$$

where γ is the gyromagnetic ratio of ^{3}He and $dn/d\epsilon$ is the density of states for a Fermi gas at the Fermi surface. For a gas of N particles (with momentum p_F at the Fermi surface) then $dn/d\epsilon = 3Nm/p_F^2$

Near T_c equation 5.6 therefore becomes

$$H_f = \frac{3\ \pi\ \rho\ \hbar^2\ \gamma}{4\ \sqrt{2}\ d\ m\ p_F\ x_N} \tag{5.14}$$

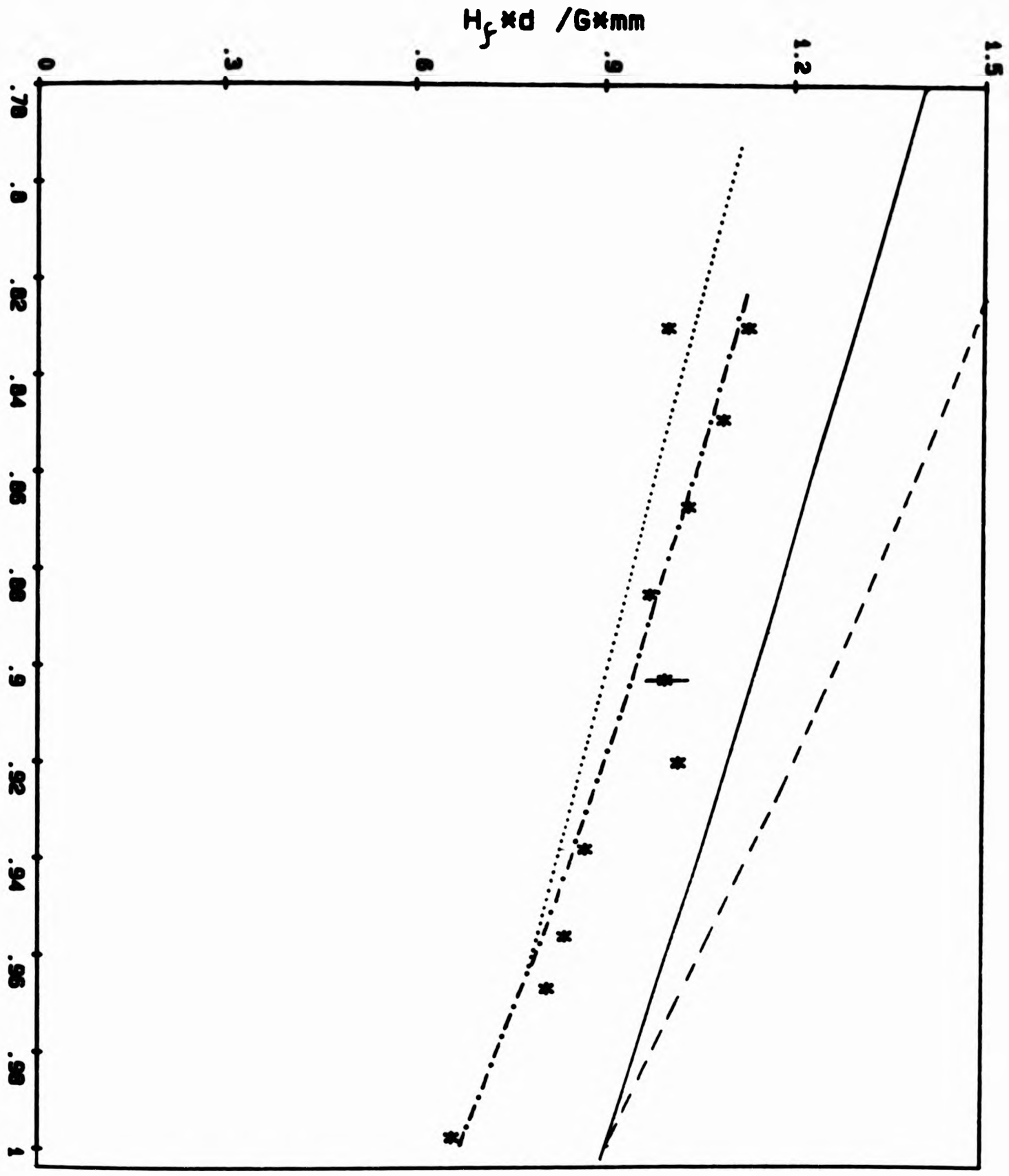

FIG 5.11 : The threshold field for the Fréedericksz transition. * : this data, dotted line : smoothed average of data taken by another worker (62), unbroken and dashed lines : theoretical curves, dash-dotted line : 25% scaling down of dashed theoretical curve.

Using the following data,

$\gamma = 2.0378\times10^{4}\ G^{-1}s^{-1}$ (12), $p_F = 9.27\times10^{-25}\ kgms^{-1}$ (12),

$m = 5.009\times10^{-27}\ kg$(12), $\rho = 115\ kgm^{-3}$(12), $x_N = 10.3\times10^{-6}$(12,60)

a calculated H_fd of around 0.90 Gmm was obtained near T_c.

Away from T_c $\quad K_b = 2\rho\hbar^2(\beta + 2\alpha/3 + \delta) / 8 m m^*$ (5.15)

a more complicated relationship, with expressions for β, α and δ given by Fetter(57). All other symbols have their usual meanings. The threshold field depends on the Fermi liquid parameters F_1^s, F_0^a and F_1^a and is also sensitive to strong coupling corrections to the energy gap. In calculating the theoretical curves shown in Figure 5.11 the following data has been used:- $F_1^s = 13.08(11)$, $F_0^a = -0.758(11,12)$, $F_1^a = -0.8(61)$.
The continuous theoretical curve was calculated for the energy gap predicted by the BCS theory and the dashed curve was obtained by applying an enhancement factor of 1.3 to the BCS gap as suggested by the specific heat dicontinuity measured by Greywall(11).

The experimental values of H_fd lie below the theoretical curves, but the temperature dependence predicted by theory does seem to be reflected. In addition to the approximate 3% random error on H_fd it should be noted that there is also a systematic uncertainty of around 3% in these values (see section 5.3.3). Measurements of the threshold field have also been made by S. G. Gould(62) using a torsional oscillator method for a ^{3}He-A slab thickness of 100 μm. These preliminary results also lie below the predicted curves, and a smoothed average of these data are shown as a dotted line on Figure 5.11.

There would appear to be a discrepancy between the calculated and measured values. This may reflect an uncertainty in the value taken for

x_N in drawing the calculated curves. This depends on the limiting value of C/x as T→0, where C is the Curie constant for liquid helium. x_N was measured by Ramm et al in 1970(60) with a quoted accuracy of 1%, and the values they obtained were found to agree with those measured by other workers to within about ±4%. Scaling both theoretical curves down by 25% produced better agreement with the experimental data, with a 25% scaling down of the dashed curve reflecting the observed temperature dependence of $H_f d$ more closely. This is shown as a dash-dotted line on Figure 5.11. Strong coupling effect corrections to the BCS theory (further to the trivial correction mentioned above) may need to be considered for a more reasonable theoretical prediction.

TABLE 2 : THRESHOLD FIELD FOR FRÉEDERICKSZ TRANSITION

T/T_C (±1%)	H_f d (/G mm) (±3%)
0.83	1.13
0.83	1.00
0.849	1.09
0.867	1.03
0.885	0.98
0.903	1.00
0.92	1.02
0.938	0.87
0.956	0.84
0.967	0.80
0.998	0.66

5.4 Anisotropy of Sound in Superfluid ^{3}He-A

As discussed in chapter 1, ultrasonic propagation in ^{3}He is of interest owing to a large anisotropy in the propagation. Thus the attenuation and the velocity of sound in ^{3}He-A can be characterised in terms of the angle made by the direction of sound propagation with the orbital vector $\hat{l}$. The remainder of this chapter is concerned with the determination of coefficients to describe this relationship. These have been found from sound records of the Fréedericksz transition measurements described in 5.3. The fact that these coefficients could be determined by fitting experimental data to theoretical expressions derived for the distorted $\hat{l}$ texture provides confidence in the theoretical predictions.

5.4.1 Evidence for Anisotropy of Attenuation and Velocity of Sound in ^{3}He-A

Many other workers(e.g. see 63,64) have noted changes in sound attenuation associated with the re-orientation of the $\hat{l}$ field by a magnetic field. The sound signal response to the Fréedericksz transition in ^{3}He-A illustrates this anisotropy. Values for the velocity and attenuation of 15.154 MHz sound were found by solving equations for the in phase and quadrature sound signals, measured at the same value of applied magnetic field, simultaneously using a Newton-Raphson iterative method. This process has already been described in section 4.4. It should be noted, however, that the angle made by $\hat{l}$ with the direction of sound propagation varied from 0° at the slab boundaries to a maximum at the centre of the slab, and therefore mean values for the attenuation and velocity

integrated over the 2 mm slab thickness were in fact deduced. Figures 5.12 and 5.13 show for the data of Figures 5.1 and 5.10 how α and c varied with increasing distortion of texture as the true vertical magnetic field was gradually increased from zero to approximately 2.2 H_f.

Similar measurements made in the superfluid B phase showed no dependence of signal amplitude on field direction, reflecting the sonic isotropy of ^{3}He-B.

5.4.2 Theoretical Representation of Sound Anisotropy

The velocity and attenuation of longitudinal zero sound in the normal state can be descibed by

$$c = c_1 + (c_0 - c_1) \mathrm{Re}\xi \qquad (5.16)$$

$$\alpha = - q (c_0 - c_1) \mathrm{Im}\xi / c_1 \qquad (5.17)$$

(52) where

$$\xi = \frac{1}{(1 + i/\omega\tau)} \qquad (5.18)$$

to a good approximation, and q represents the wave vector for the disturbance. All other symbols have the meanings explained in chapter 4. Equations 5.16 and 5.17 can also be used to describe propagation of sound in the superfluid state with

$$\xi = \frac{1 - \xi'}{1 + F_2^s \xi'/5} \qquad (5.19)$$

Sauls et al(61) have made a theoretical estimate for the Fermi liquid parameter $F_2^s \approx 0.5$ at melting pressure so that

$$\xi \approx 1 - (1 + F_2^s/5)\xi' \qquad (5.20)$$

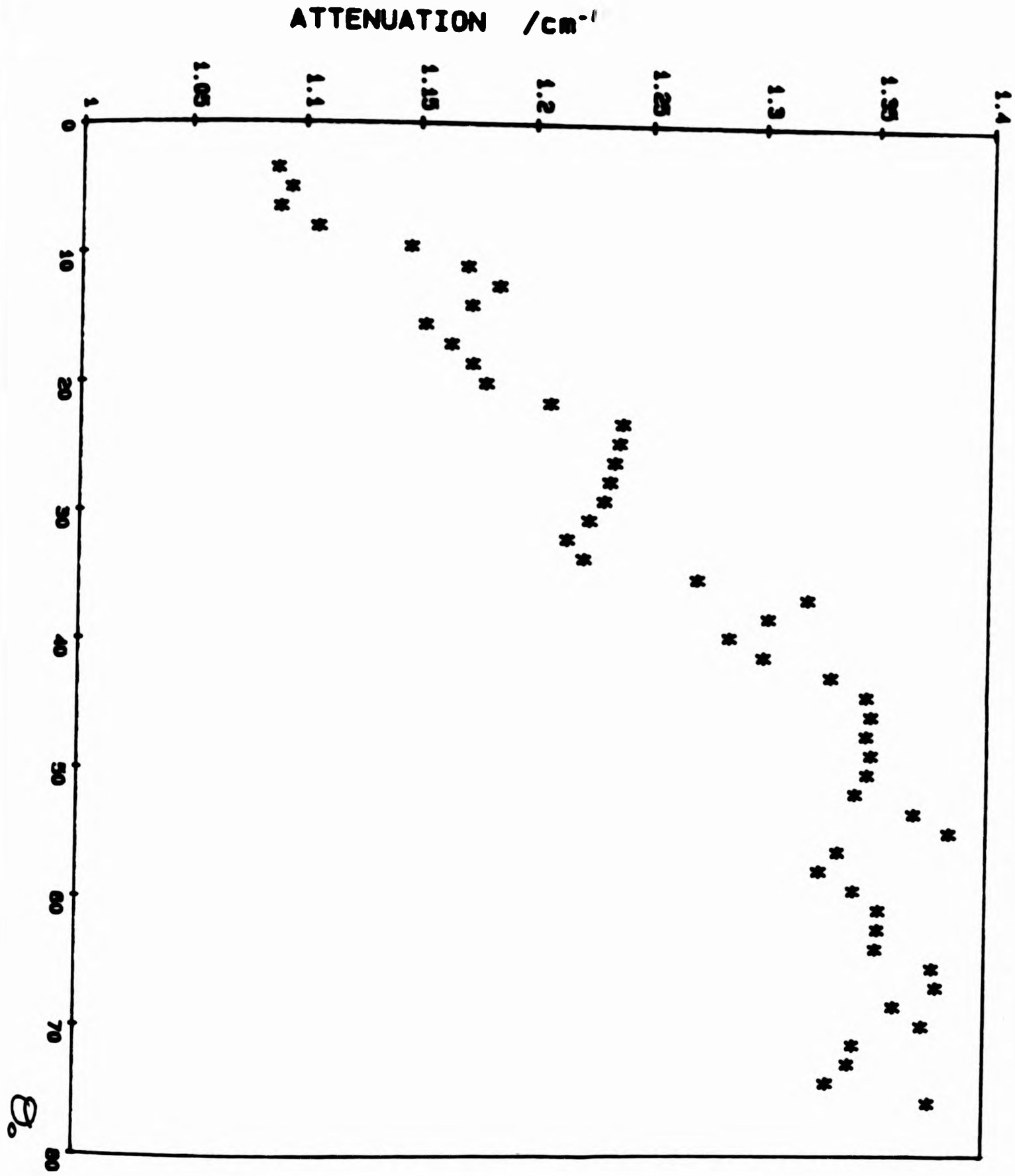

FIG 5.12 : Attenuation of 15.154MHz sound as a function of the angle made between $\hat{l}$ and z at the centre of the ^{3}He-A slab as the true vertical magnetic field was increased from 0 to $\approx 2.2\ H_f$. $(T/T_c = 0.88)$

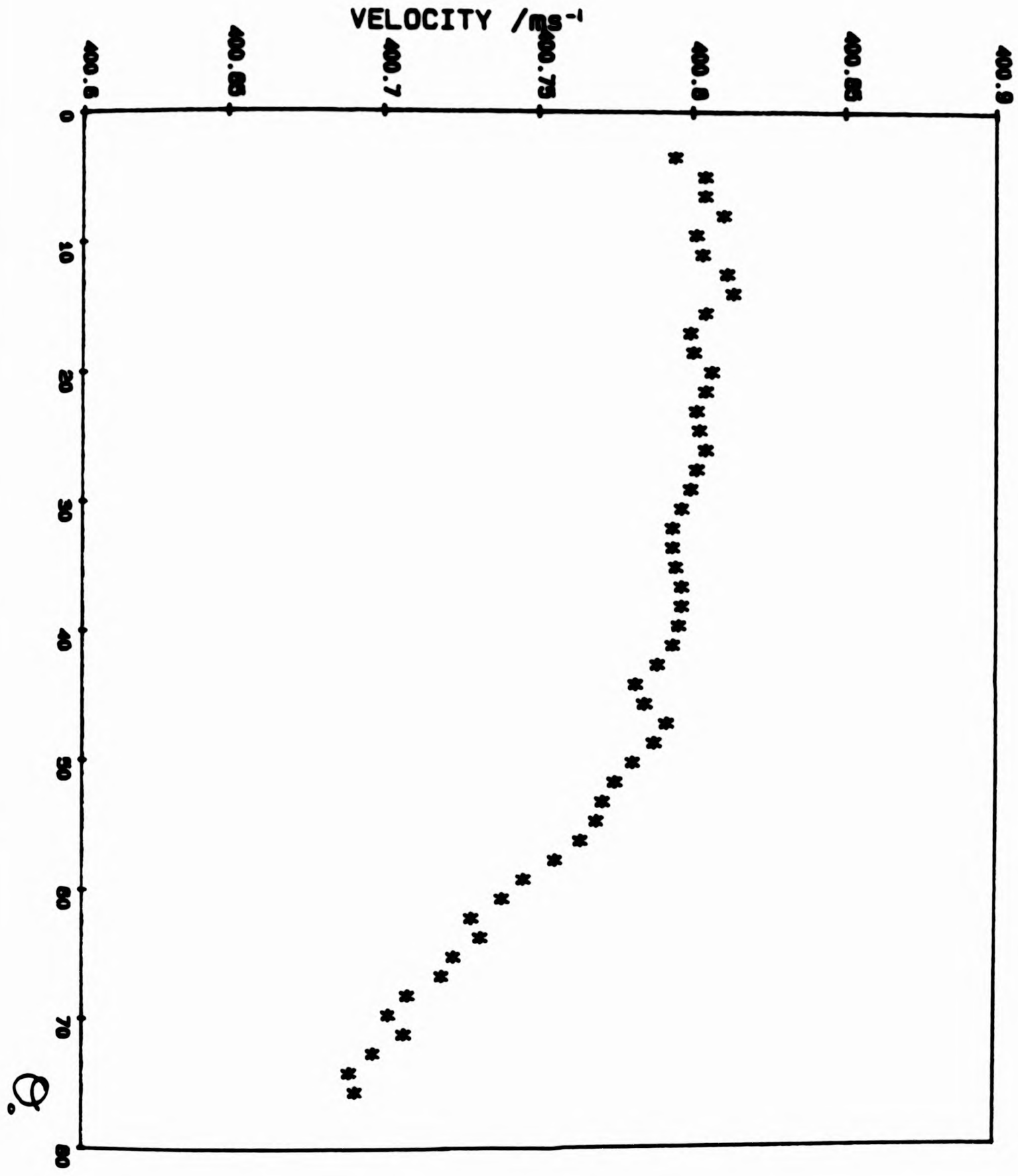

FIG 5.13 : Velocity of 15.154MHz sound as a function of the angle made between $\hat{l}$ and z at the centre of the ^{3}He-A slab as the true vertical magnetic field was increased from 0 to $\approx 2.2\ H_f$. $(T/T_c = 0.88)$

Writing $\varepsilon \equiv 1 - \varepsilon^o$

then for the superfluid A phase ε^o may be represented by

$$\varepsilon^o = \cos^4\theta\, \varepsilon_{\parallel}^o + 2 \sin^2\theta \cos^2\theta\, \varepsilon_c^o + \sin^4\theta\, \varepsilon_{\perp}^o \qquad (5.21)$$

where the exact form of the expressions for $\varepsilon_{\parallel}^o$, ε_c^o and $\varepsilon_{\perp}^o$ are given in reference 52, and θ describes the angle made by $\hat{\mathbf{l}}$ with $\hat{\mathbf{q}}$.

The anisotropy of the sound propagation properties is completely characterised by three independent functions. $\varepsilon_{\parallel}^o$ contains no contribution from the collective modes, ε_c^o contains some contribution from the flapping mode and $\varepsilon_{\perp}^o$ contains some contribution from the clapping mode. However at the temperatures at which measurements were taken (in the macroscopic regime) the incidence of pair breaking was low and no collective modes were excited (see section 4.4).

It is now possible to write the attenuation found from the detected sound signals (which has been integrated across the slab) in terms of these parameters :

$$\alpha_{meas} = \frac{1}{d} \int_o^d \alpha \, dz \qquad (5.22)$$

where α_{meas} is in dimensions of length^{-1}. This equation is true for the situation here of $2\pi/q$ ($= \lambda \approx 3\times10^{-5}$m) $\ll$ scale of spatial variation of the texture so that α is the local attenuation and a WKB approximation has been used.

From equation 5.17

$$\alpha_{meas} = \frac{1}{d} \int_o^d + q\ (c_o - c_1)\ Im\varepsilon^o \quad dz \qquad (5.23)$$

It is more convenient to write

$$\alpha_{meas} = \frac{2}{d} \int_o^{\theta_o} \frac{(A1\ \cos^4\theta + B1\ \sin^2\theta\ \cos^2\theta + C1\ \sin^4\theta)}{\theta'}\ d\theta \qquad (5.24)$$

where $A1 = q\ (c_o - c_1)\ Im\varepsilon^o_{\parallel} / c_1$ (5.25)

$B1 = 2q\ (c_o - c_1)\ Im\varepsilon^o_C / c_1$ (5.26)

$C1 = q\ (c_o - c_1)\ Im\varepsilon^o_{\perp} / c_1$ (5.27)

and these temperature and frequency dependent coefficients have dimensions of length^{-1}.

Similarly for the velocity:

$$(\ \omega d/c\ )_{meas} = \omega \int_o^d dz/c \qquad (5.28)$$

where $(\ \omega d/c\ )_{meas}$ is a dimensionless phase, and a WKB approximation has again been used.

$$\frac{\omega\ d}{c} = \frac{\omega\ d}{c_o} + \frac{\omega\ d}{c_o} \frac{(c_o - c_1)}{c_o}\ Re\varepsilon^o \qquad (5.29)$$

from equation 5.16, expanding by the binomial theorem for small $(c_o - c_1)/c_o$.

Since $(\ \omega d/c\ )_{meas} \equiv \beta_{meas} + 2n\pi$

and $\omega d/c_o \equiv \beta_o + 2n\pi$ where $0 < \beta_{meas}, \beta_o < 2\pi$

and n = 75, found by comparison with normal state velocities, then it is more convenient to write

$$\beta_{meas} = \frac{2}{d}\int_0^{\theta_o}\frac{(A2\cos^4\theta + B2\sin^2\theta\cos^2\theta + C2\sin^4\theta)}{\theta'}\,d\theta \qquad (5.30)$$

where $$A2 = \omega d\,(c_o - c_1)\,Re\varepsilon_{\parallel}^{o} / c_o^2 + \beta_o \qquad (5.31)$$

$$B2 = 2\omega d\,(c_o - c_1)\,Re\varepsilon_{C}^{o} / c_o^2 + \beta_o \qquad (5.32)$$

$$C2 = \omega d\,(c_o - c_1)\,Re\varepsilon_{\perp}^{o} / c_o^2 + \beta_o \qquad (5.33)$$

and these temperature and frequency dependent coefficients are dimensionless.

5.4.3 Determination of Anisotropy Coefficients A1,B1,C1,A2,B2,C2

These coefficients were determined by fitting velocities and attenuations found from the sound signal response to a Fréedericksz transition to equations of the form 5.24 and 5.30. Because of the presence of a residual vertical field of order $2H_f$, each "Fréedericksz transition measurement" consisted of two such transitions as H_z was swept from around $-2H_f$ to $+2H_f$.

Equations 5.24 and 5.30 can be rewritten as

$$\alpha_{meas} = A1\,AI + B1\,BI + C1\,CI \qquad (5.34)$$

$$\beta_{meas} = A2\,AI + B2\,BI + C2\,CI \qquad (5.35)$$

where AI, BI and CI represent the integrals

$$AI = 2\int_0^{\theta_o}\frac{\cos^4\theta}{X(\theta)}\,d\theta \qquad (5.36)$$

$$BI = 2\int_0^{\theta_o}\frac{\sin^2\theta\cos^2\theta}{X(\theta)}\,d\theta \qquad (5.37)$$

$$CI = 2\int_0^{\theta_o}\frac{\sin^4\theta}{X(\theta)}\,d\theta \qquad (5.38)$$

and

$$X(\theta) = \left[\frac{\pi^2}{2}\frac{(H_Z^2 - H_X^2)}{H_f^2}(\cos2\theta - \cos2\theta_o) - \pi^2\frac{H_X}{H_f}\frac{H_Z}{H_f}(\sin2\theta - \sin2\theta_o)\right]^{1/2} \qquad (5.39)$$

These integrals have a similar form to the integral in equation 5.9.

Equation 5.9 was solved to find values for H_z/H_f for particular values of Θ_o. These values were substituted into equations 5.36-5.38 which were then evaluated to give AI, BI and CI for each H_z/H_f. α_{meas} and β_{meas} were found from the in phase and quadrature sound data using a process of linear interpolation to obtain values at the same calculated H_z/H_fs. Fits were then performed, using equations 5.34 and 5.35, to determine the coefficients A1,B1,C1,A2,B2,C2.

Brief description of numerical methods employed

All four integrands diverge for $\Theta = \Theta_o$ so it was necessary to make the substitution

$$y = \sin^{1/2}(\Theta_o - \Theta)$$

thus rewriting equation 5.9, for example, as

$$\int_{\sin^{1/2}\Theta_o}^{0} \frac{2}{\cos(\Theta_o-\Theta)} \left[\pi^2 \left(\frac{\underline{H}_z^2}{H_f^2} - \frac{\underline{H}_x^2}{H_f^2}\right) \sin(\Theta+\Theta_o) + 2\pi^2 \frac{\underline{H}_x}{H_f}\frac{\underline{H}_z}{H_f} \cos(\Theta+\Theta_o)\right]^{-1/2} dy = 1/2 \qquad (5.40)$$

Simpson's rule was used to perform the integration, making an initial guess for H_z/H_f and then using a Newton-Raphson iterative method to converge to a value for H_z/H_f that satisfied the integral for a particular Θ_o. In practice it was found necessary to use an increasing number of Simpson steps for the integration as Θ_o increased towards $\pi/2$. Alternatively, equations 5.2-5.4 could be rewritten in terms of the variable Φ to give for equation 5.9

$$\frac{\pi H_z}{H_f d} = \int_{\Phi_{wall}}^{\Phi(z)} \frac{d\Phi}{\sin\Phi_o \left(1 - \sin^2\Phi/\sin^2\Phi_o\right)^{1/2}} \qquad (5.41)$$

where the integral in Φ can be expressed as elliptic integrals of the 1st kind, i.e. as

$$F(\arcsin(\sin\Phi(z)/\sin\Phi_o) \setminus \Phi_o) - F(\arcsin(\sin\Phi_{wall}/\sin\Phi_o) \setminus \Phi_o) \quad (5.42)$$

where Φ_o, the value of Φ at $z = d/2$, is evaluated by putting $z = d/2$ and $\Phi(z) = \Phi_o$ in equation 5.42. Therefore in this case the integral in Φ becomes $F(\pi/2 \setminus \Phi_o) - F(\arcsin(\sin\Phi_{wall}/\sin\Phi_o) \setminus \Phi_o)$ with $F(\pi/2 \setminus \Phi_o) = K$, the complete elliptic integral. The method of solution of these elliptic integrals has been documented by Abramowitz and Stegun(65). The integrals AI, BI and CI were executed using Simpson's rule. Appendix G contains a listing of the computer program used in performing the integrations.

Figure 5.14 shows how AI, BI and CI depend on H_z/H_f. The functional dependence was not found to vary significantly with temperature across the A phase, the temperature dependence being contained in H_f as it appears in the term H_x/H_f. H_f was taken as the value determined experimentally at each reduced temperature in the way described in section 5.3. For small H_z/H_f BI and CI = 0 and AI = 1 to a good approximation. This property was used to find A1 and A2 from α_{meas} and β_{meas} averaged over values found for $| H_z/H_f | < 0.12$.

In order to obtain the best values for B1,C1 and B2,C2 at each reduced temperature the sums of squares

$$Z1 = \sum_i \{ \alpha_i - \alpha(H_z/H_f, H_x/H_f, B1, C1) \}^2$$

$$Z2 = \sum_i \{ \beta_i - \beta(H_z/H_f, H_x/H_f, B2 ,C2) \}^2$$

were evaluated. Here the subscript i denotes the experimentally determined values for a particular H_z/H_f, and $\alpha(H_z/H_f,H_x/H_f,B1,C1)$ and $\beta(H_z/H_f,H_x/H_f,B2,C2)$ are the values calculated for particular values of

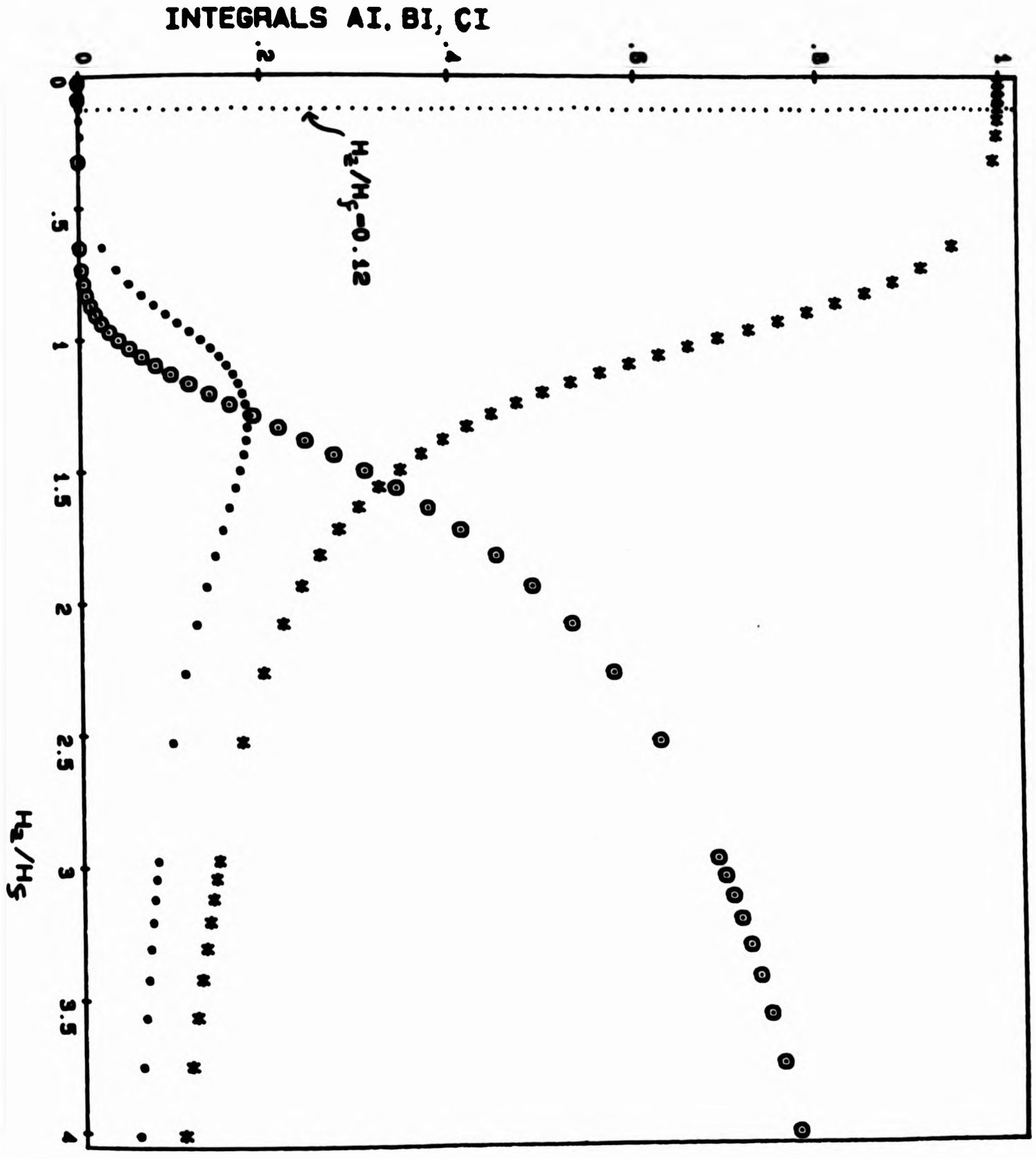

FIG 5.14 : Calculated integrals AI(*) BI(•) CI(⊙) as a function of vertical magnetic field. For H_z/H_c<.12 then AI=1, BI=CI=0 to a good approximation. (Figure drawn for H_x/H_c=0.195 for H_c measured at T/T_c=0.83).

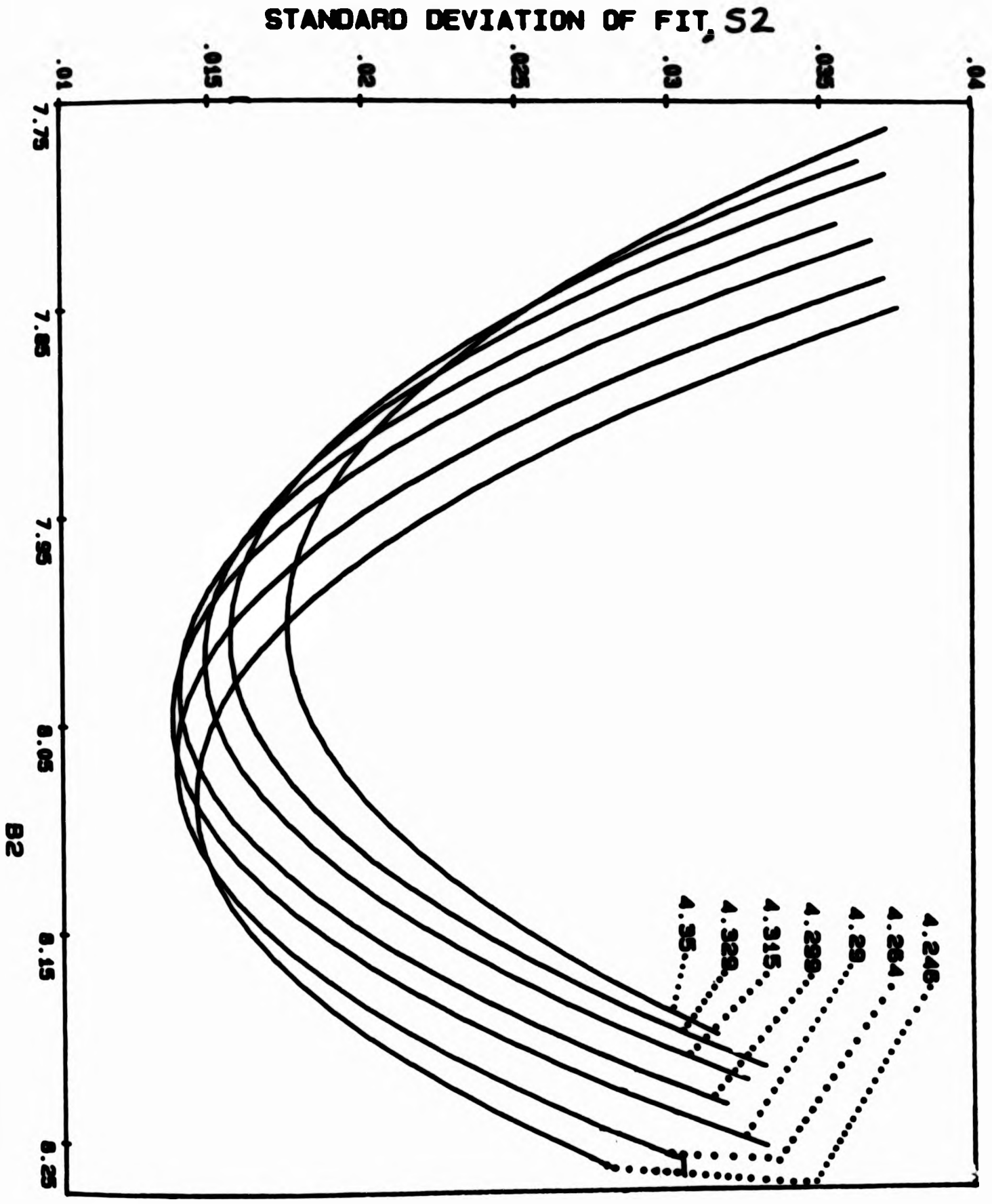

FIG 5.15 : S2 as a function of B2 for the values of C2 indicated, for the fits to the Fréederickaz data taken at a reduced temperature of 0.885. The best fit i.e. the minimum value for the standard deviation was obtained with B2=8.04 and C2=4.29

B1,C1,B2,C2,H_z/H_f and H_x/H_f by solving the integrals AI, BI and CI in the manner described above. The best values of B1,C1 and B2,C2 at any reduced temperature were taken to be those that minimised the standard deviations $S1 = (Z1/m-1)^{1/2}$ and $S2 = (Z2/m-1)^{1/2}$ where m was the number of data points. Figure 5.15 shows the variation of S2 with B2 and C2 for data taken at a reduced temperature of 0.885.

Figures 5.16-5.21 show the best fits obtained for the attenuation and phase records at reduced temperatures of 0.967, 0.885, and 0.830. There is some asymmetry about $H_z/H_f = 0$ apparent in the experimental values for α_{meas} and β_{meas}. Leggett(66) has suggested that ^{3}He-A might be ferromagnetic with a spontaneous magnetisation of order 10-20 mG in the bulk liquid. He predicts that this effect should be observable by examination of the orientation of the $\hat{l}$ vector which would be sensitive to the polarity of a small external field. Paulson et al(67) have detected a ferromagnetic magnetisation of around 3 mG using the transmission of 25 MHz ultrasound as a probe. It is not clear whether the asymmetry noted here could be due to this effect since the magnetic fields of order 1G experienced by the orbital texture may be too large to allow such small effects to be seen.

The coefficients A1,B1,C1 and A2,B2,C2 found from these best fits are shown in Figures 5.22 and 5.23. The precision of the fit enabled each of the attenuation coefficients B1 and C1 to be determined to within 0.005 cm^{-1} (i.e. around 0.3%), and each of the phase coefficients B2 and C2 to within 0.01 radians (i.e around 0.2%). A1 and A2 were found from the low field values of α and β in the manner described above and the estimated error in these coefficients was 2% for A1 and 0.3% for A2. Contributions

to the random error on B1,C1 and B2,C2 included the values used for the Fréedericksz threshold field H_f and the residual vertical field H_{rv}. These experimentally determined values had been previously found to have a random error of around 3% each, from the same source (see sections 5.2, 5.3). The main effect of errors in H_f and H_{rv} was in the evaluation of $(H_{applied}-H_{rv})/H_f$ which was necessary to align values for α and β found at different $H_{applied}$ with calculated values for H_z/H_f. The error in this term is expected to be less than 4.5% and was found to have a negligible effect on A1 and A2. In order to assess the effect of this error on the coefficients B1,C1,B2,C2 additional fits were performed to all data but with $H_f = H_f(meas) \pm 5\%$. This variation in H_f produced variations in the coefficients found for the best fits of 3%, 2.5%, 1% and 1/2% in B1, C1, B2 and C2 respectively. Another source of error in the determination of these anisotropy coefficients was errors in α and β. These have been estimated as 10% in α and 1% in β (see section 4.4) and were found to be the dominant contribution to errors in the sound anisotropy coefficients, providing errors with a maximum of about 10% (in A1), 20% (in B1), 10% (in C1), 1% (in A2), 2% (in B2) and 1% (in C2). (Although these values for the errors should be taken as a rough guide only). The standard deviation for each fit was found to be rather sensitive to small changes in the fitting coefficients. To illustrate this, Figures 5.24 and 5.25 show simulated curves for α and β at a reduced temperature of 0.83 indicating the effect that a 5% increase in each coefficient in turn had on the simulations.

Values for the real and imaginary parts of ε^o were evaluated using equations 5.25-5.27 and 5.31-5.33 and c_0, c_1 from section 4.3. These values are given in Table 3 and shown in Figures 5.26 and 5.27. The dotted line in Figure 5.27 represents $Im\varepsilon^o$ for the normal state, evaluated using

equation 5.18. The behaviour of $Im\epsilon_{\parallel}^{o}$, $Im\epsilon_{C}^{o}$, $Im\epsilon_{\perp}^{o}$, $Re\epsilon_{\parallel}^{o}$, $Re\epsilon_{C}^{o}$ and $Re\epsilon_{\perp}^{o}$ at temperatures just below T_C has been predicted by Wölfle. He defines a function $x(\Delta_o/\hbar\omega) = 2/5\ \epsilon^o k_B T/\hbar\omega$, and the behaviour of Imx and Rex (in the collisionless limit) are shown in Figures 5.28 and 5.29. He predicts a broad peak in $Im\epsilon_{C}^{o}$ and a sharper, narrower peak in $Im\epsilon_{\perp}^{o}$. These have been seen by Paulson et al(63) and correspond to the sharp peak in sound absorption they observed (see section 4.4). Corresponding features are predicted in $Re\epsilon_{C}^{o}$ and $Re\epsilon_{\perp}^{o}$. However, for the frequency of sound and pressure of ^{3}He-A used in this experiment these features would be contained in the reduced temperature range 0.992-1.0, as discussed in section 4.4. The $Im\epsilon^o$ coefficients determined here do appear to reflect the tailing off effect with decreasing temperature observed by Paulson et al. at 15 MHz and with a ^{3}He-A pressure of 33.5 bar. They did not determine the phase coefficients. Also the $Re\epsilon^o$ and $Im\epsilon^o$ coefficients measured have the order of magnitude that might be expected from Wölfle's predictions (with $x \simeq 1.4\epsilon^o$ for 15.154 MHz sound).

Finally, the fact that the experimental data could be fitted to theoretically derived expressions in this way supports the theoretical predictions about the distorted texture discussed in this work.

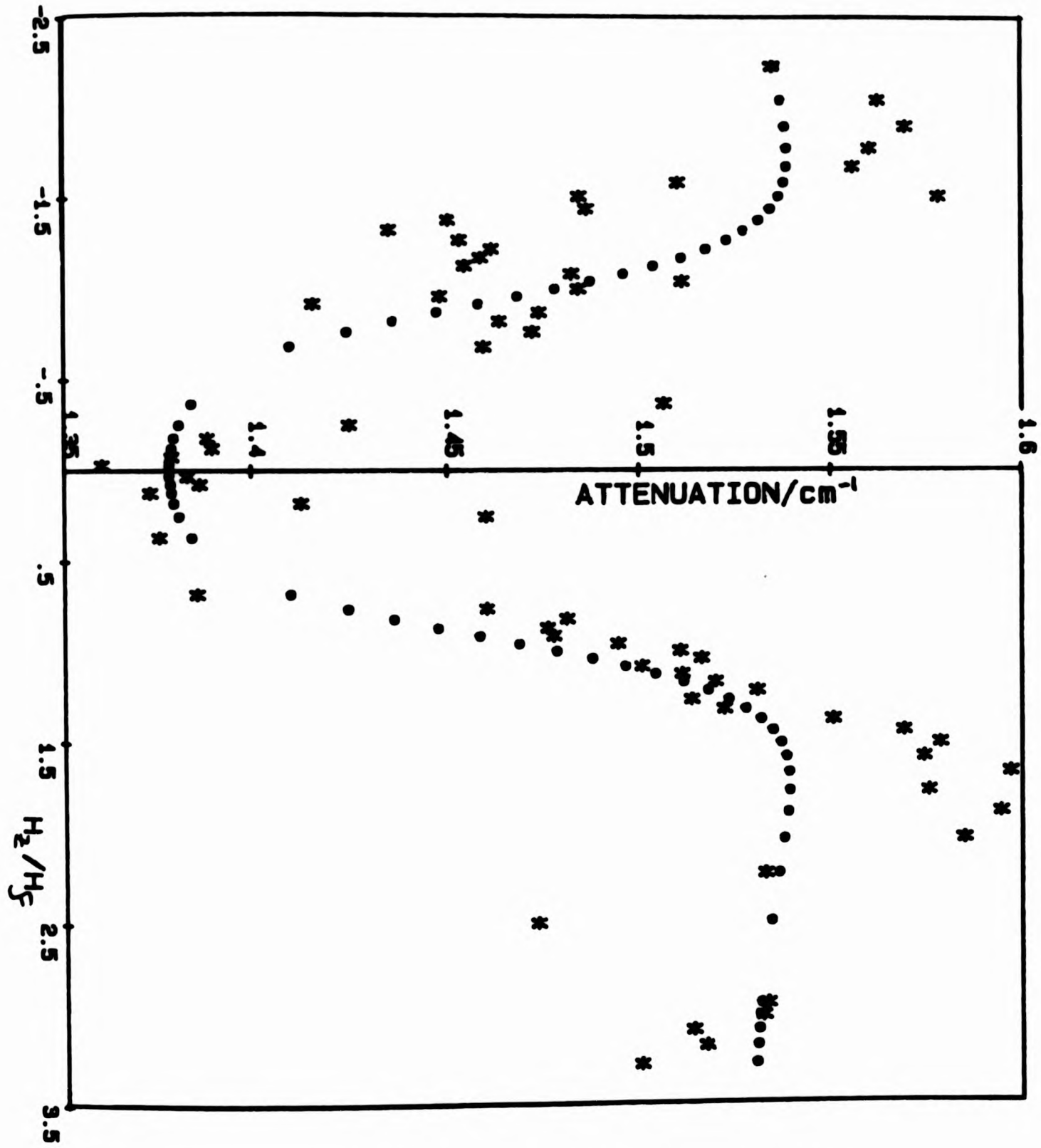

FIG 5.16 : Attenuation of 15.154MHz sound as a function of true vertical field for T/T_c =0.967

* measured α_j ● α calculated for the best fit to the data (S1=0.040)

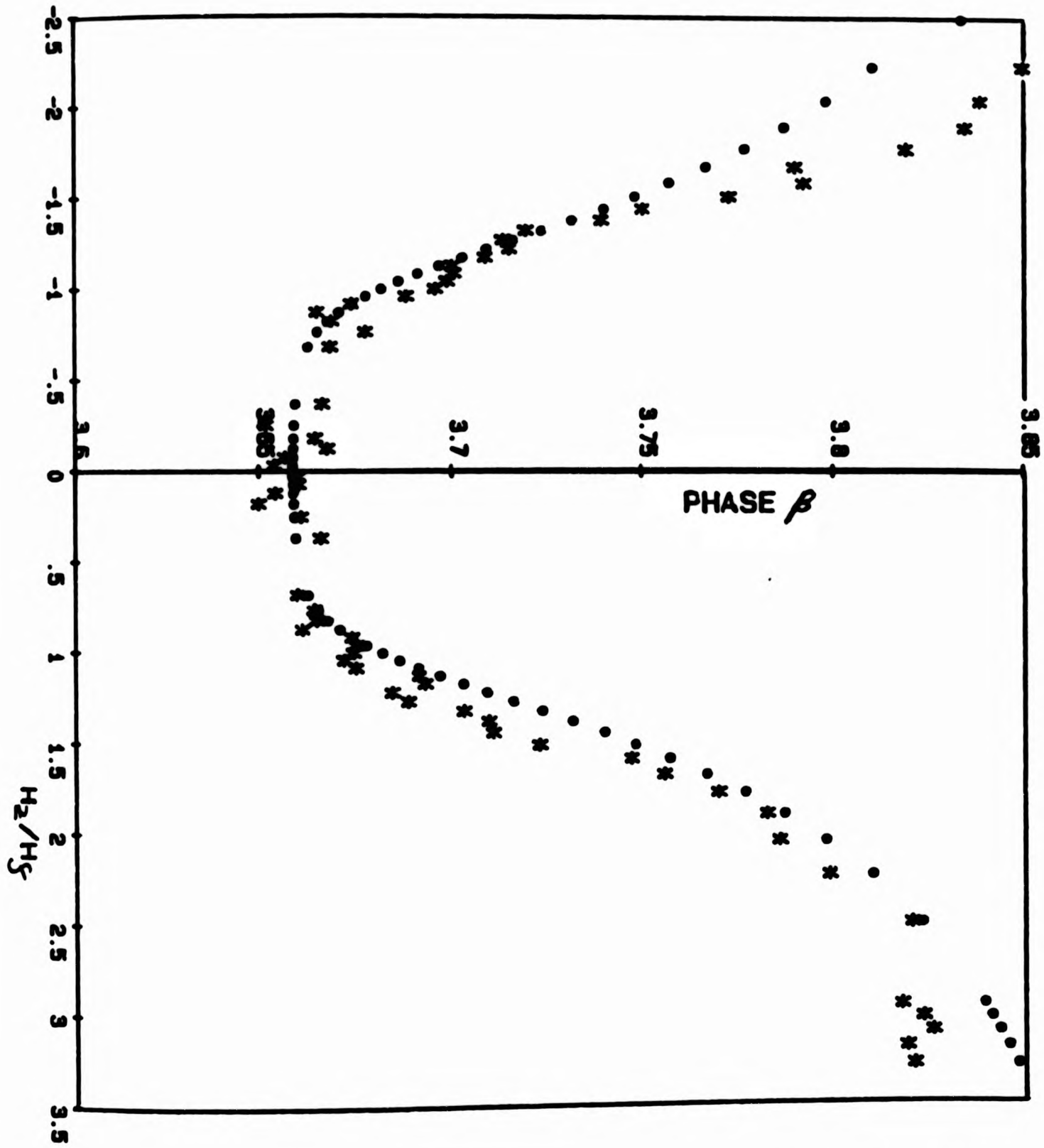

FIG 5.17 : Velocity dependent phase as a function of true vertical field for T/T_c=0.967. * measured β, • β calculated for the best fit to the data (S2=.017)

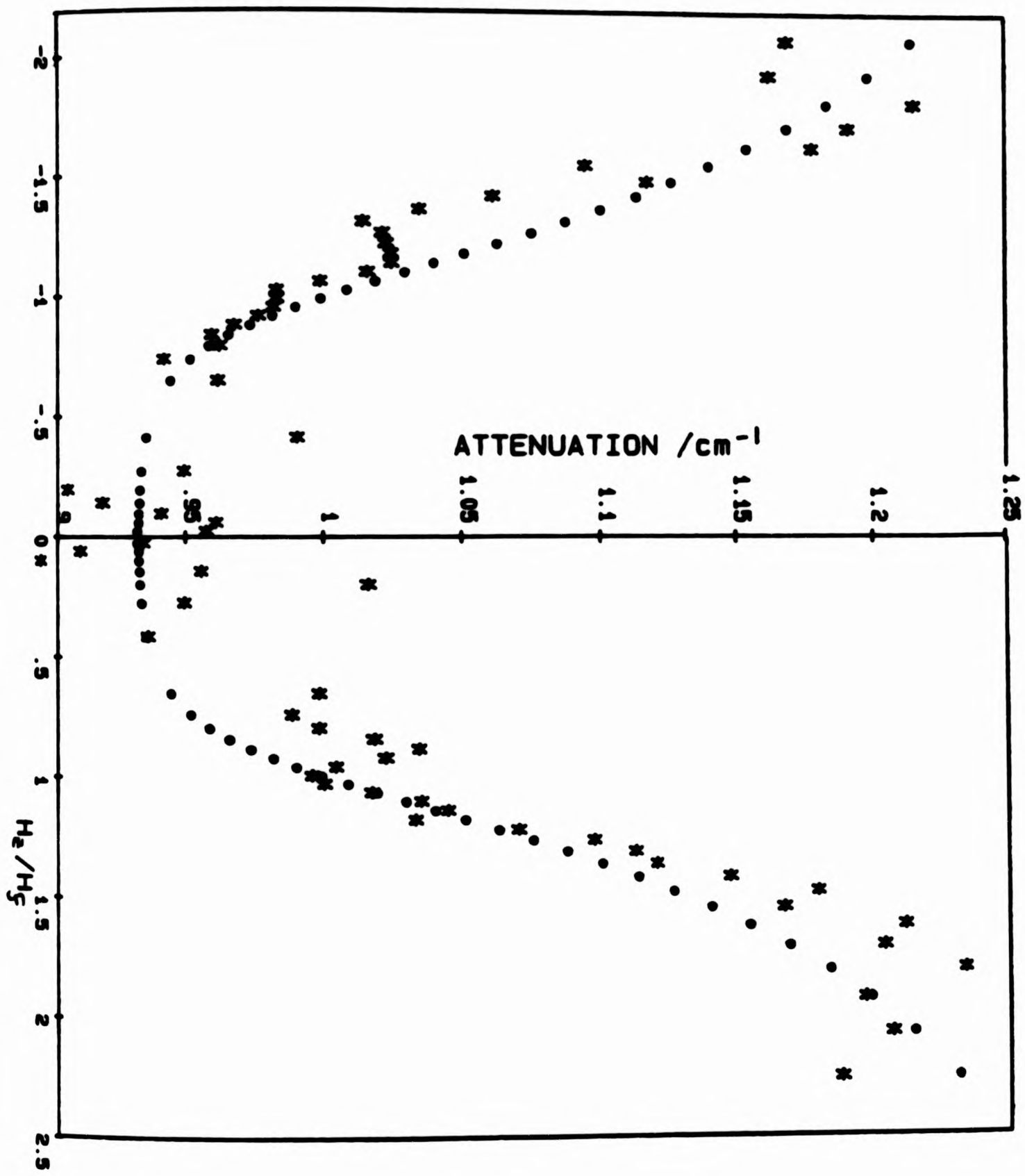

FIG 5.18 : Attenuation of 15.154MHz sound as a function of true vertical field for T/T_c=0.885

* measured α_j ● α calculated for the best fit to the data (S1=0.034)

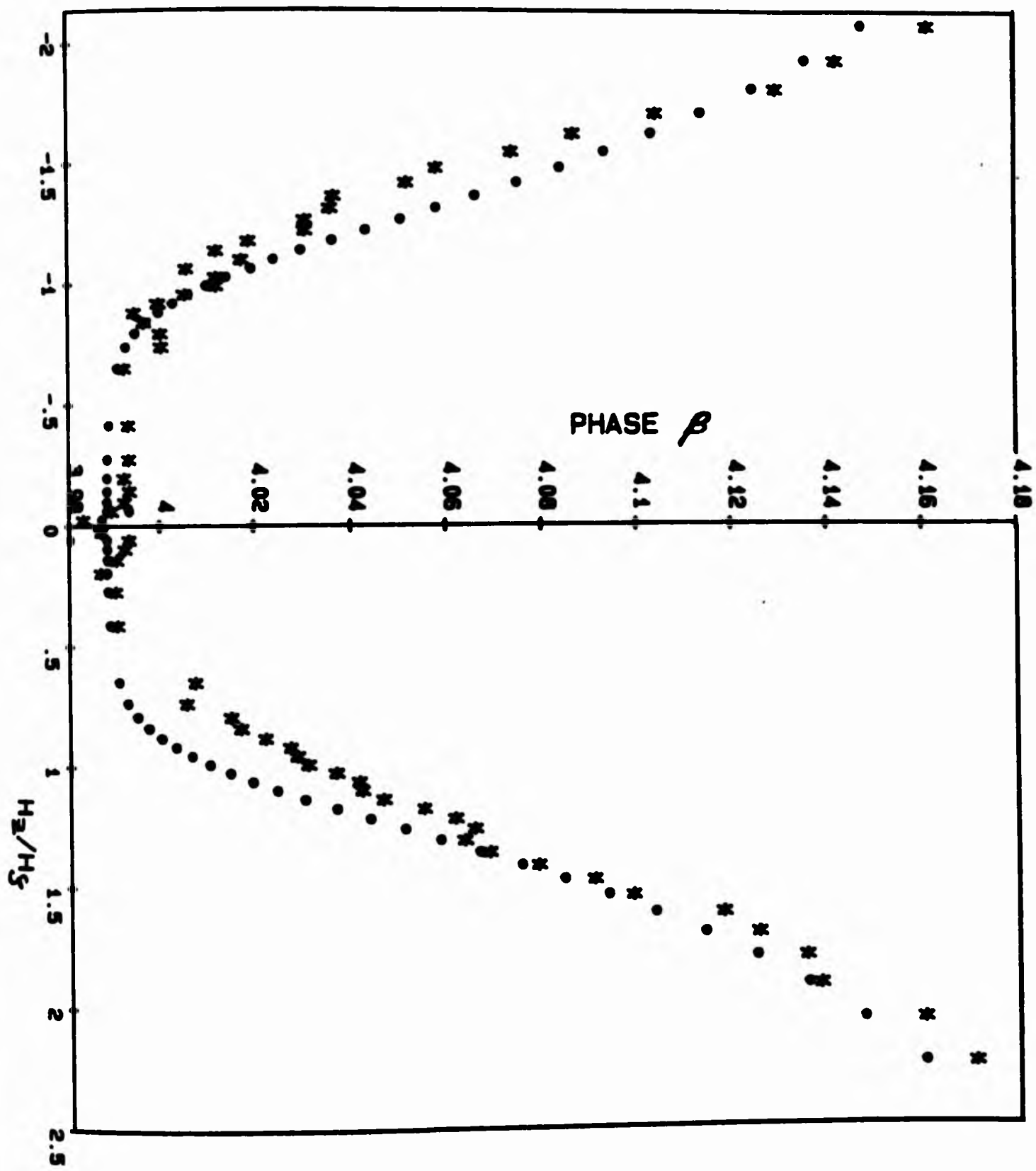

FIG 5.19 : Velocity dependent phase as a function of true vertical field for T/T_c=0.885. * measured β, • β calculated for the best fit to the data (S2=0.014)

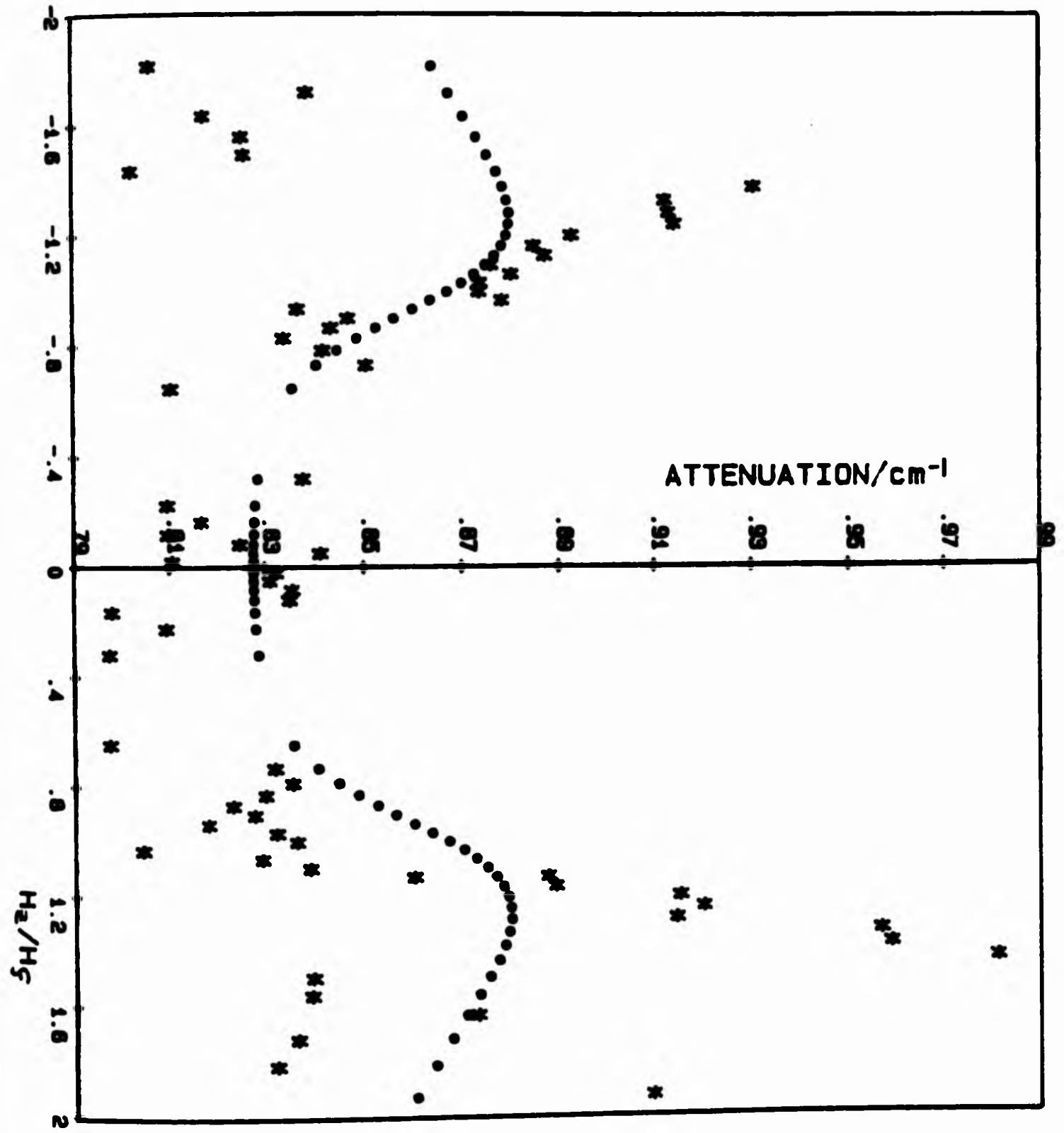

FIG 5.20 : Attenuation of 15.154MHz sound as a function of true vertical field for T/T_c=0.83

* measured α, ● α calculated for the best fit to the data (S1=0.035)

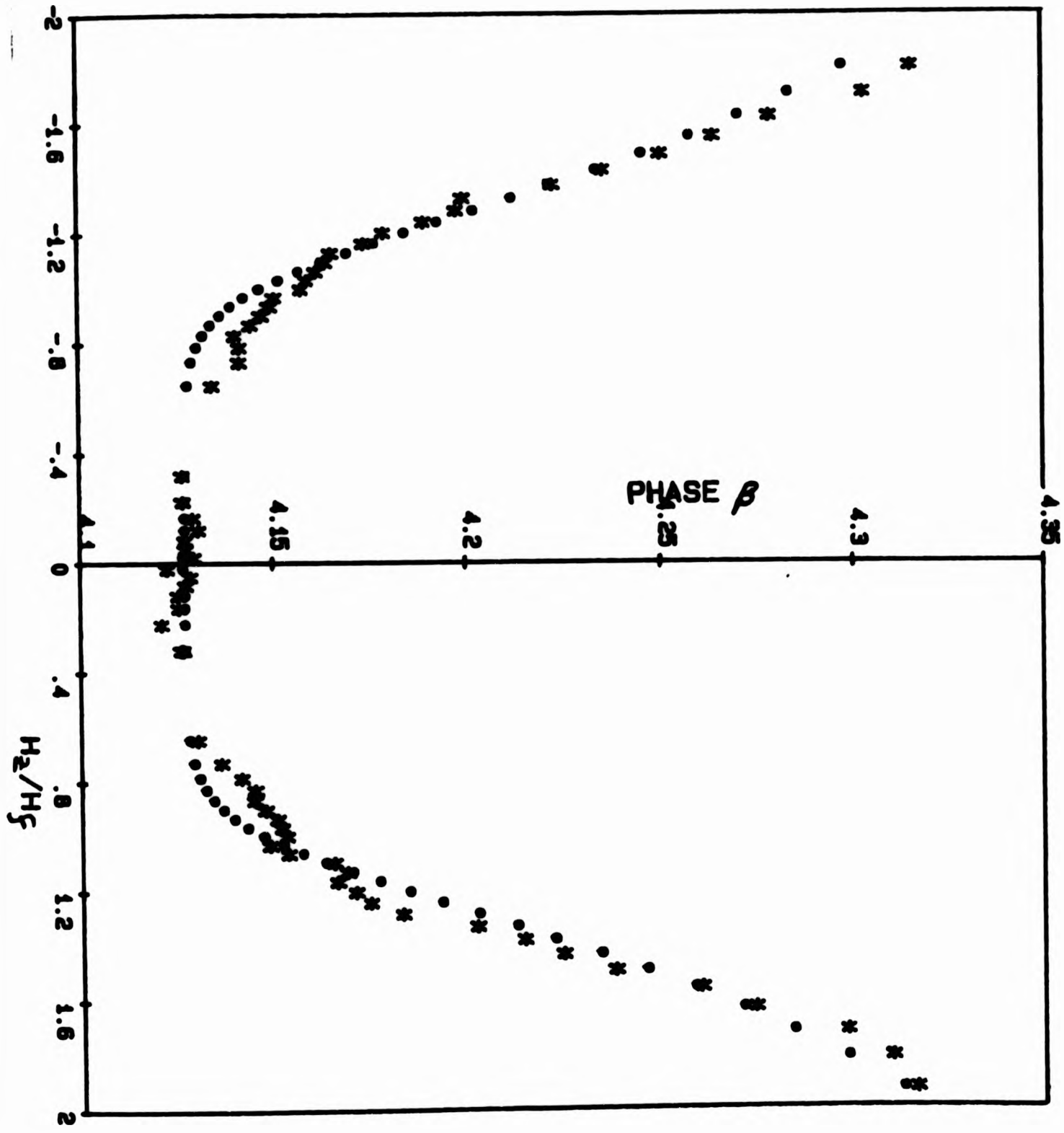

FIG 5.21 : Velocity dependent phase as a function of true vertical field for T/T_c=0.83, * measured β, • β calculated for the best fit to the data (S2=0.008)

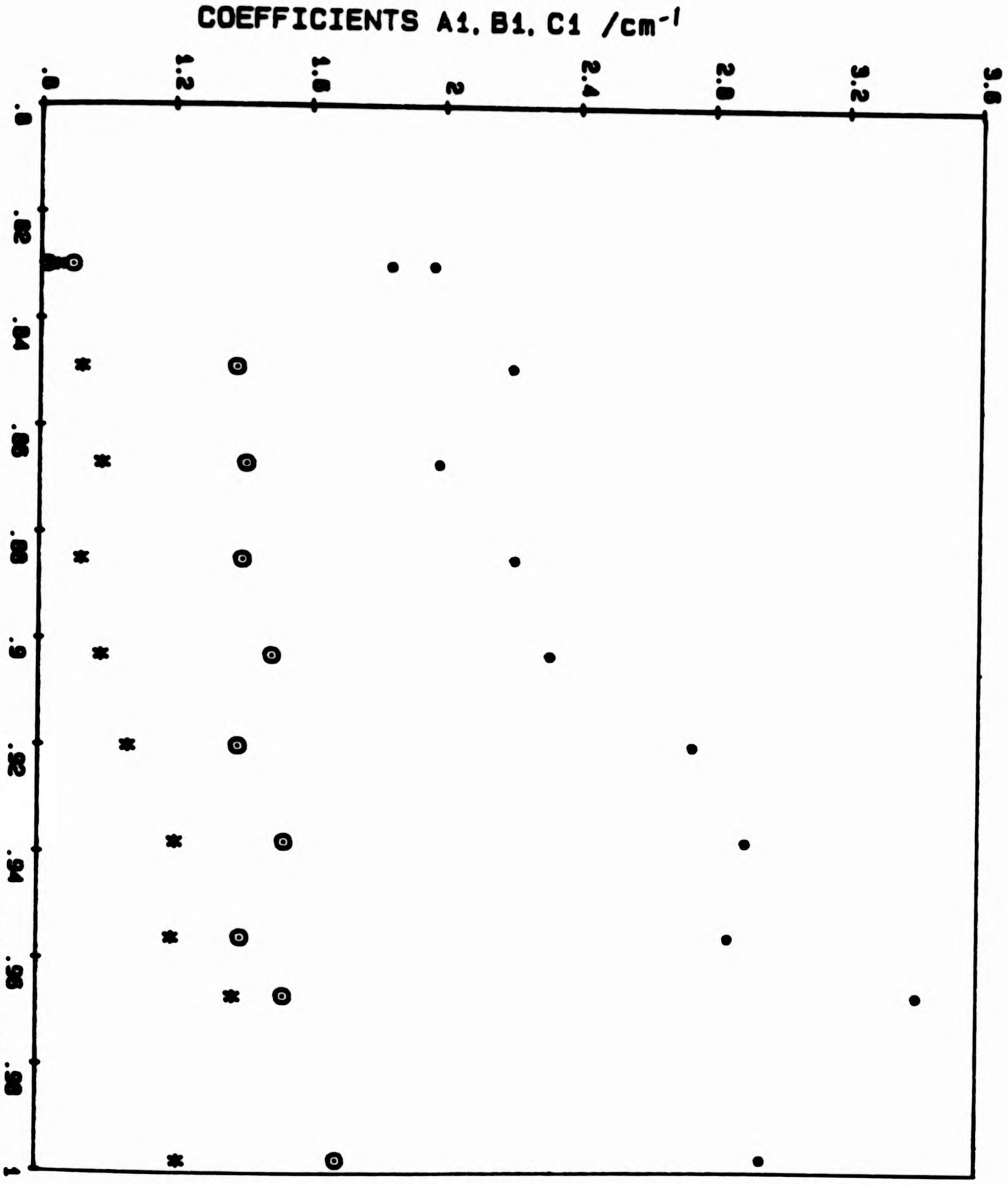

FIG 5.22 : Anisotropic sound attenuation coefficients

* represents A1, • represents B1, ⊙ represents C1

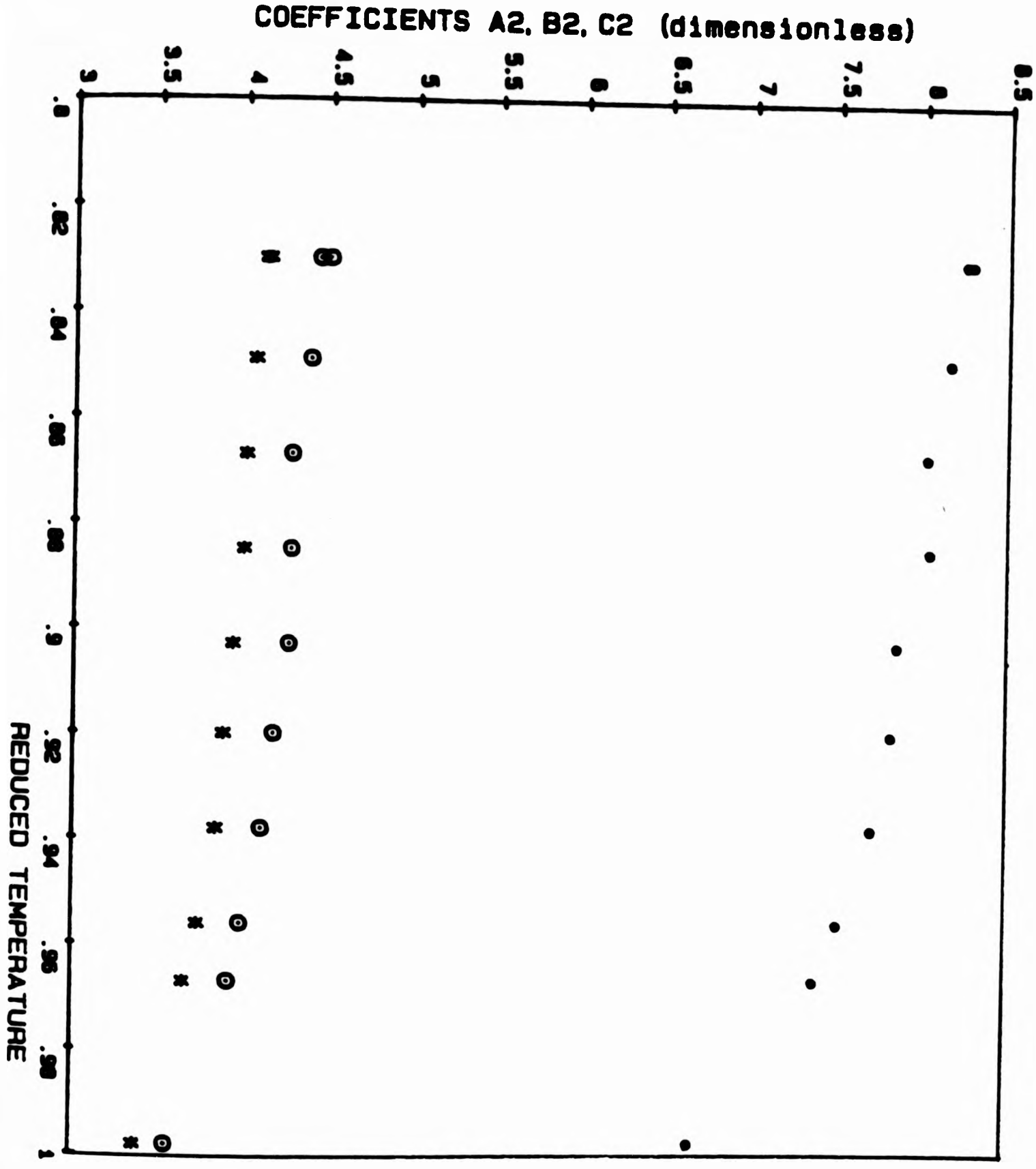

FIG 5.23 : Anisotropic sound velocity coefficients

* represents A2, • represents B2, ⊙ represents C2

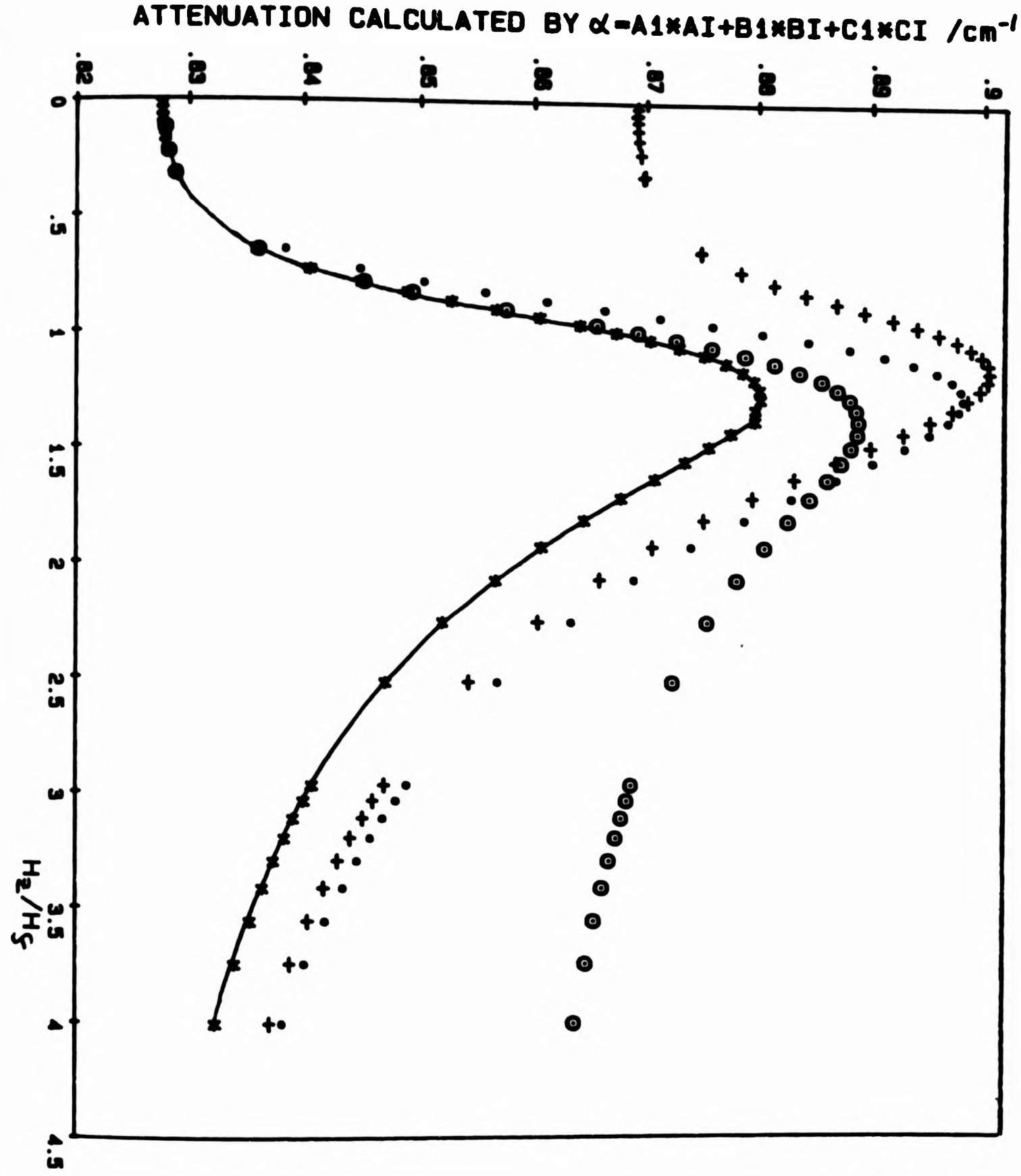

FIG 5.24 : Calculated attenuation. * represents α for values of coefficients for best fit to data at T/T_c=.83 Other curves show effect that a 5% increase in each coefficient in turn has on simulations. (5% increase in A1 (+) B1 (•) C1 (◎). (Solid line acts as a guide to the eye).

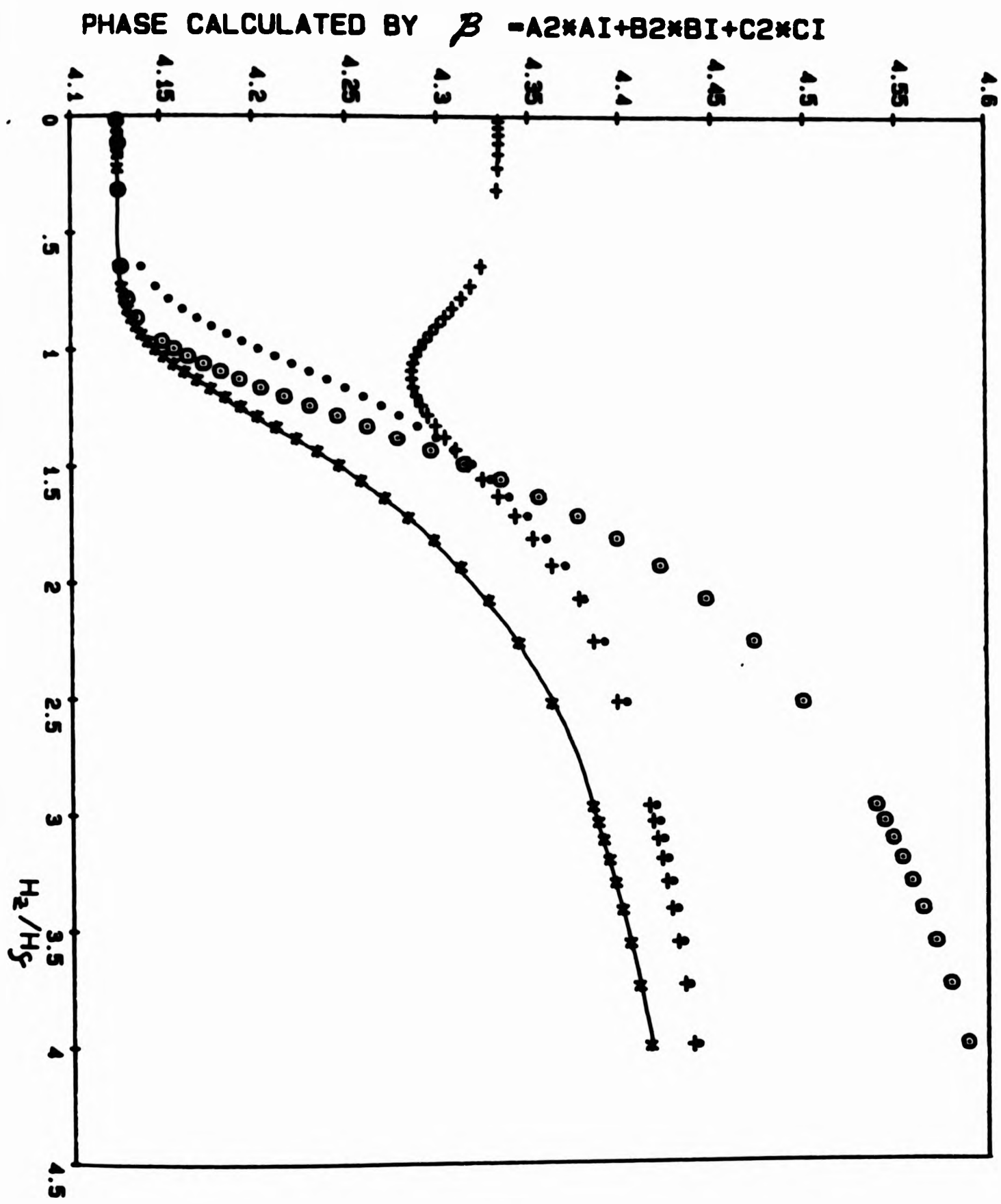

FIG 5.25 : Calculated phase β. * represents β for values of coefficients for best fit to data at $T/T_c = .83$ Other curves show effect that a 5% increase in each coefficient in turn has on simulations. (5% increase in A2(+) B2(•) C2(⊙)). (Solid line acts as a guide to the eye).

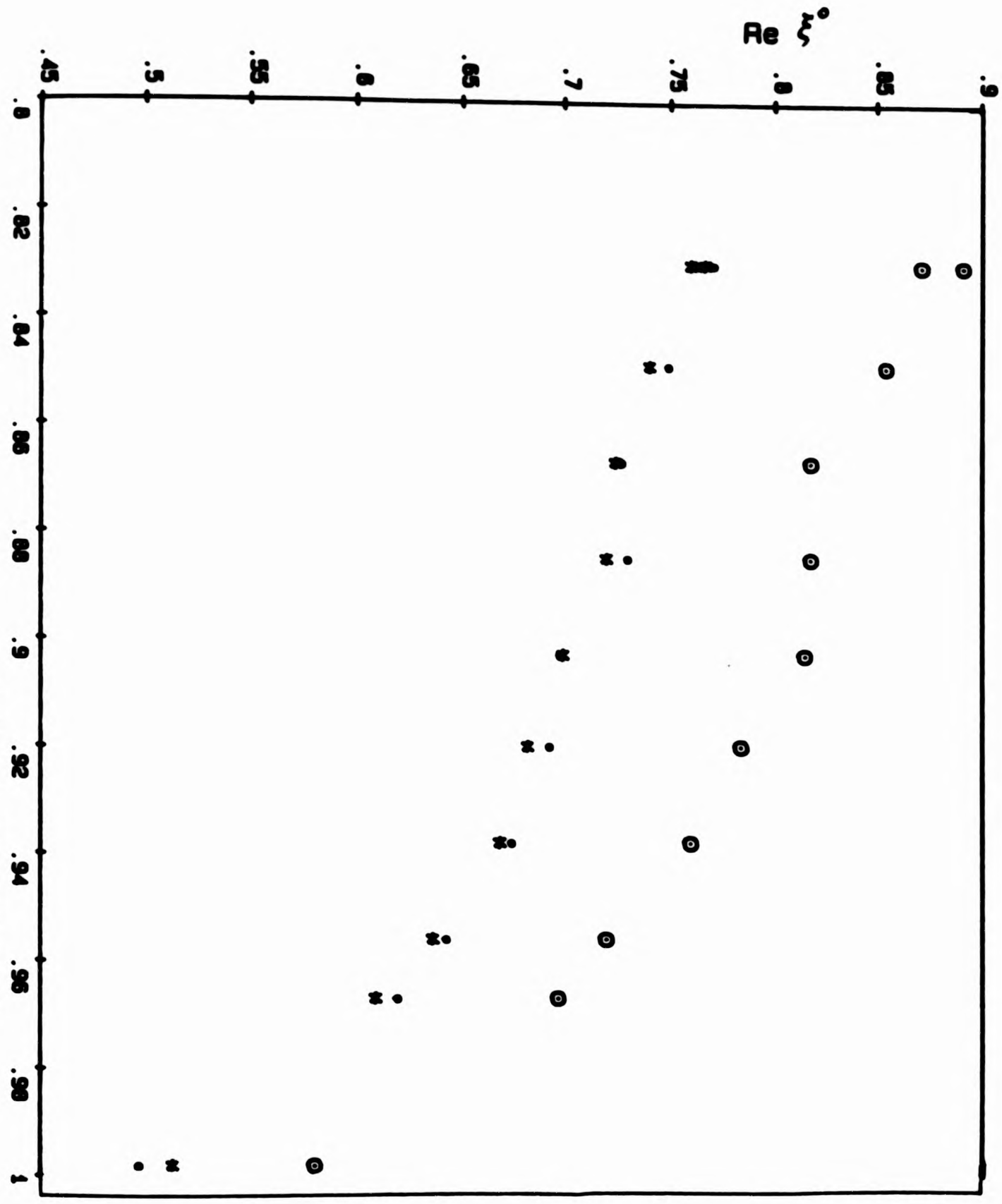

FIG 5.26 : Real parts of ξ° . * represents $Re\xi^{\circ}_{//}$, • represents $Re\xi^{\circ}_{c}$, ⊙ represents $Re\xi^{\circ}_{\perp}$

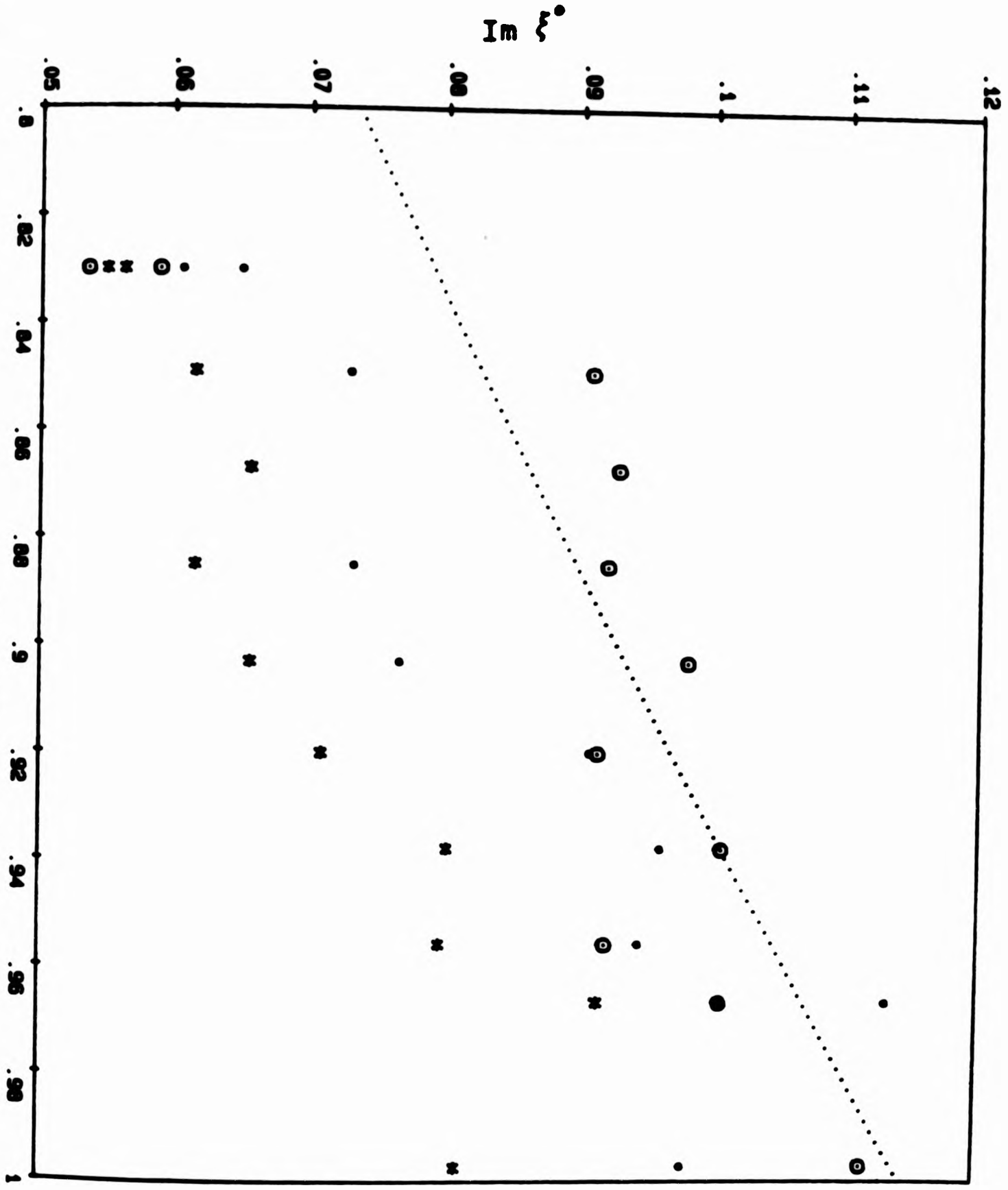

FIG 5.27 : Imaginary parts of ξ° . × represents $\mathrm{Im}\,\xi^\circ_{//}$, • represents $\mathrm{Im}\,\xi^\circ_c$, ⊙ represents $\mathrm{Im}\,\xi^\circ_\perp$ .The dotted line represents $\mathrm{Im}\,\xi^\circ$ extrapolated from the normal state, assuming no superfluid transition had occurred

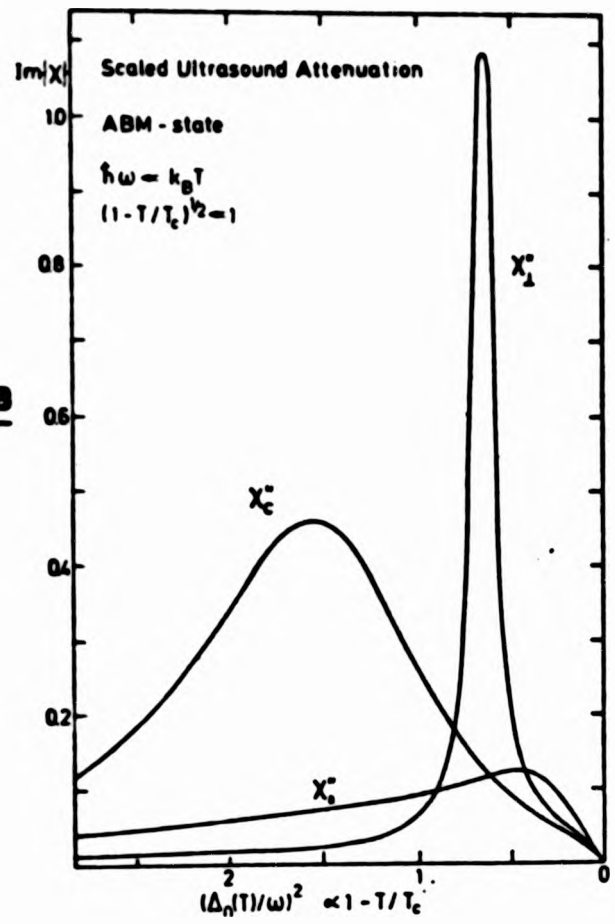

FIG 5.28

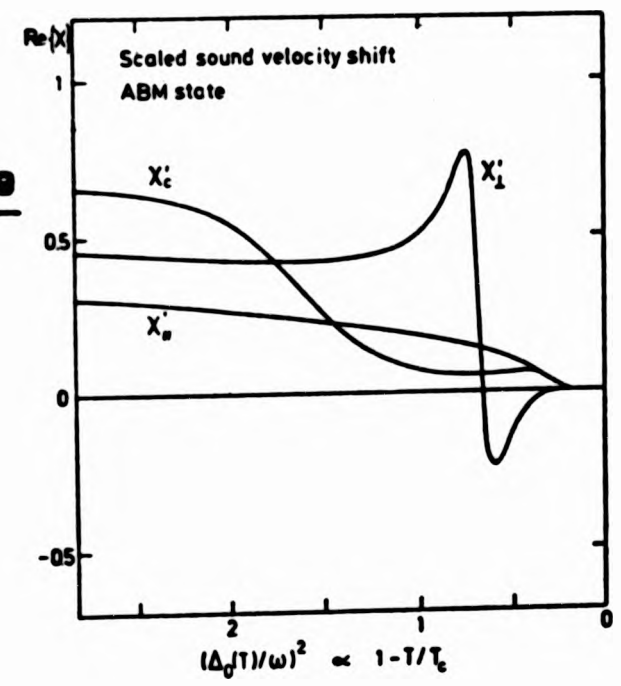

FIG 5.29

FIGS 5.28 & 5.29 : Sound anisotropy components ImX and ReX near the transition (in the collisionless limit), as calculated by Wölfle (52)

TABLE 3 : SOUND ANISOTROPY COEFFICIENTS

T/T_c (±1%)	$Im\varepsilon_{\parallel}^{o}$ /cm^{-1} (±10%)	$Im\varepsilon_{c}^{o}$ /cm^{-1} (±20%)	$Im\varepsilon_{\perp}^{o}$ /cm^{-1} (±10%)	$Re\varepsilon_{\parallel}^{o}$ (±1%)	$Re\varepsilon_{c}^{o}$ (±2%)	$Re\varepsilon_{\perp}^{o}$ (±1%)
.83	.056	.061	.059	.76	.76	.87
.83	.055	.065	.054	.77	.77	.89
.849	.062	.073	.091	.74	.75	.85
.867	.066	.066	.093	.72	.73	.82
.885	.062	.073	.092	.72	.73	.82
.903	.066	.077	.098	.70	.70	.81
.920	.071	.091	.092	.68	.69	.78
.938	.080	.096	.101	.67	.68	.76
.956	.080	.095	.092	.64	.64	.72
.967	.092	.113	.101	.61	.62	.70
.998	.081	.098	.112	.51	.50	.58

CHAPTER 6 : PRECESSING MAGNETIC FIELD INDUCED TEXTURAL CHANGES IN ^{3}He-A

6.1 Introduction

This chapter contains a discussion of the textural changes that have been predicted for a slab of ^{3}He-A of thickness d experiencing a precessing magnetic field. Attempts to observe these experimentally are also described.

Section 6.2 describes the solutions obtained to the equation of motion of $\hat{l}$ for this experimental arrangement and indicates how the inertia associated with an intrinsic angular momentum might be observed. Section 6.3 discusses the experimental procedure employed in attempts to see the predicted textures, and suggests why these attempts were unsuccessful.

6.2 Theoretical Predictions

6.2.1 Solution of Equation of Motion of $\hat{l}$

Consider the situation shown in Figure 6.1. A magnetic field $\underline{H}$ was allowed to precess with frequency ω_o at an angle $\pi/4$ about the z axis, where the z axis is perpendicular to the surfaces of a slab of ^{3}He-A with thickness d and infinite lateral extent. Θ, Φ are the polar angles of $\hat{l}$ measured in a frame rotating with the field, the field being in the xz

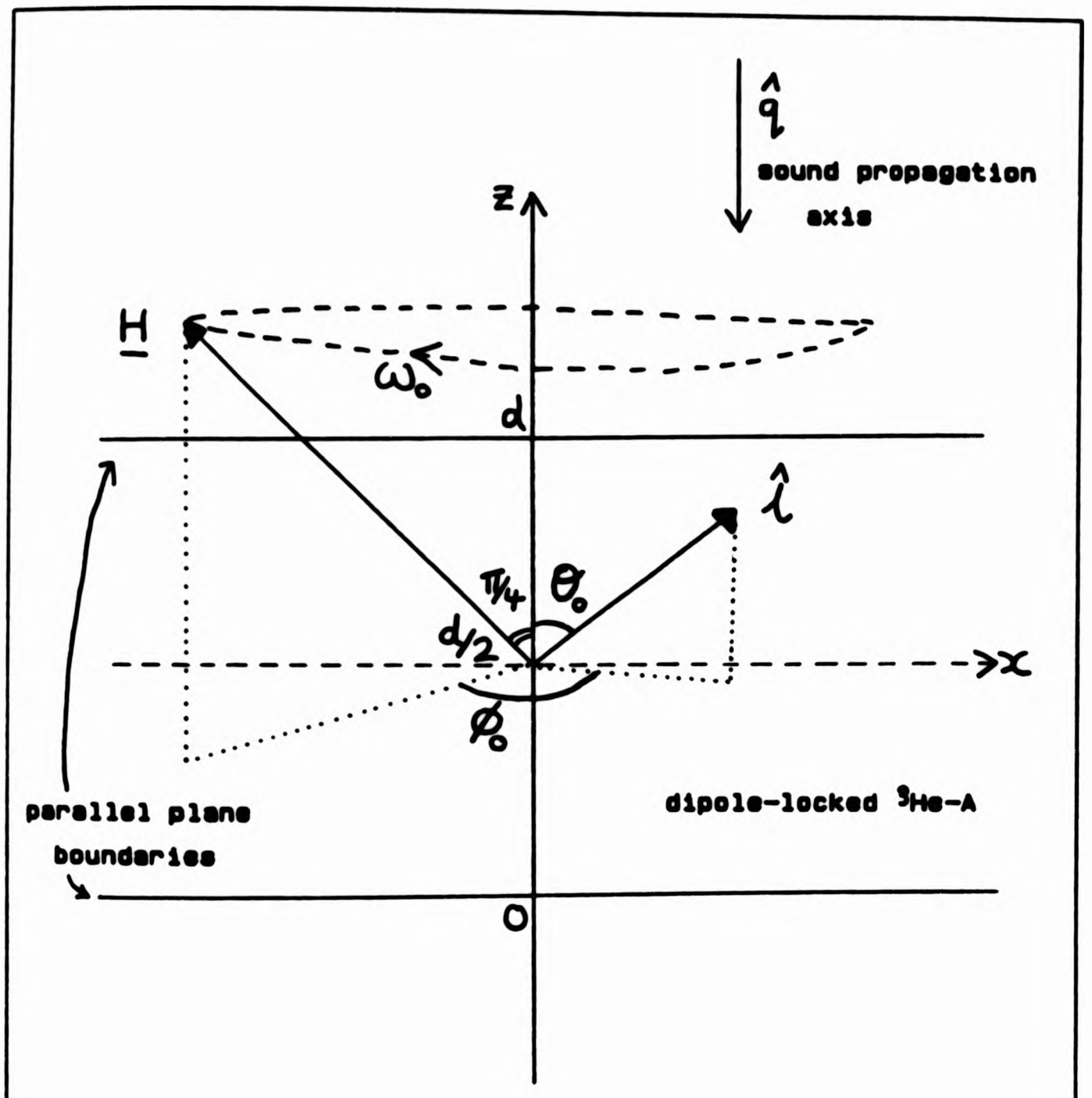

FIG 6.1 : Slab of ^{3}He-A considered in the solution of the equation of motion of $\hat{l}$ when a magnetic field $\underline{H}$ is caused to precess at frequency ω_o at $\pi/4$ about the z axis. $\hat{l}$ is drawn at the centre of the slab so that $\theta(z) = \theta_o$ and $\phi(z) = \phi_o$.

plane in this frame. It was assumed that H ≪ 30 G so that the dipole-locked regime could be considered. For an intrinsic angular momentum density·(2C - C_o) $\hat{\ell}$ the equation of motion of $\hat{\ell}$ is given by

$$\mu \frac{\partial \hat{\ell}}{\partial t} - (2C - C_o)\, \hat{\ell} \times \frac{\partial \hat{\ell}}{\partial t} - \Delta\chi \{\hat{\ell} \times (\hat{\ell} \times \underline{H})\} (\hat{\ell}.\underline{H}) = \hat{\ell} \times [\hat{\ell} \times \frac{\delta f}{\delta \hat{\ell}}] \qquad (6.1)$$

(see section 1.3)

where [$\delta f/\delta \hat{\ell}$] represents the variational derivative of the free energy density. Writing the free energy density explicitly for the situation shown in Figure 6.1 in the absence of flow

$$\hat{\ell} \times [\hat{\ell} \times \delta f/\delta \hat{\ell}] = K_s \underline{A} + (K_t - K_s)\, \underline{B} - [2(K_t - K_s) + C_o]\, \underline{C} + (K_b - K_s)\, \underline{D} \qquad (6.2)$$

where K_s, K_b and K_t are the bending energy coefficients, and

$$\underline{A} \equiv [\, \nabla^2 \hat{\ell} - (\hat{\ell}.\nabla^2 \hat{\ell})\, \hat{\ell}\,] \qquad (6.3)$$

$$\underline{B} \equiv \hat{\ell} \times \nabla(\, \hat{\ell}.\mathrm{curl}\hat{\ell}\,) \qquad (6.4)$$

$$\underline{C} \equiv (\, \hat{\ell}.\mathrm{curl}\hat{\ell}\,)\, \hat{\ell} \times (\hat{\ell}.\nabla)\, \hat{\ell} \qquad (6.5)$$

$$\underline{D} \equiv \{\, \nabla_i[\ell_i\, (\hat{\ell}.\nabla)\, \hat{\ell}] - \hat{\ell}\, \ell_i \ell_j \ell_k \nabla_i \nabla_j \ell_k - \nabla \ell_i\, (\hat{\ell}.\nabla)\, \ell_i + \hat{\ell}\, [(\hat{\ell}.\nabla)\, \ell_i]^2\} \qquad (6.6)$$

(see reference 68)

To solve the equation of motion (equation 6.1) it was found necessary to write the equation in the form $d\hat{\ell}/dt$ = sum of time independent terms. This could be done by evaluating

$$1/\alpha * (\text{equation 6.1}) + \beta/\alpha * \hat{\ell} \times (\text{equation 6.1})$$

where α and β were defined as the dimensionless coefficients

$\alpha = \Delta\chi\, H^2/\, \mu\omega_o$ and $\beta = (2C - C_o)/\mu$

The equation of motion of $\hat{\ell}$ then became

$$(1+\beta^2)\frac{d\hat{\ell}}{d(\omega_o t)} = [\alpha\{(\hat{\ell}.\hat{h})\hat{\ell} - \hat{h}\} - \alpha\beta(\hat{\ell}\times\hat{h})](\hat{\ell}.\hat{h}) + \frac{1}{\mu\omega_o}\hat{\ell}\times[\hat{\ell}\times\frac{\delta f}{\delta\hat{\ell}}] - \frac{\beta}{\mu\omega_o}\hat{\ell}\times[\frac{\delta f}{\delta\hat{\ell}}] \quad (6.7)$$

where $\hat{h} = \underline{H} / H$.

Equation 6.7 was solved numerically using an 'n' space point approximation for the slab (where typically n = 5). The sole assumption about the nature of motion of $\hat{\ell}$ was of spatial variation only in the z direction. The evolution of $\hat{\ell}$ with time at n points across the slab was simulated, together with values for θ and ϕ at each space and time point. The main points of the calculation are as follows:

Each term in the expression for $[\ \delta f/\delta\hat{\ell}\ ]$ was evaluated explicitly in spatial derivatives with respect to z. Near T_c the Ginzburg-Landau values $K_b = K_s = K_t = 5C_o\hbar/4m$ for dipole-locked ^{3}He-A were assumed. This simplified the term in $\underline{C}$ and the terms in $\underline{B}$ and $\underline{D}$ vanished from $\hat{\ell}\times[\hat{\ell}\times\delta f/\delta\hat{\ell}]$ altogether, leaving for the last two terms in equation 6.7 a sum of expressions of the form

$$[K_s(1/\alpha+\beta/\alpha\ \hat{\ell}\times)\underline{A}]_i = K_s/\alpha\ [\ell_i''(1-\ell_j^2) - \ell_i\ell_j\ell_j'' - \ell_i\ell_k\ell_k'' + \beta\ell_j\ell_k'' - \beta\ell_k\ell_j''] \quad (6.8)$$

$$[C_o(1/\alpha+\beta/\alpha\ \hat{\ell}\times)\underline{C}]_i = C_o/\alpha\ (\ell_i\ell_j' - \ell_j\ell_i')\ [\ell_k(\ell_j\ell_k' - \ell_k\ell_j') - \beta\ell_k\ell_i'] \quad (6.9)$$

A three point finite difference approximation was used to evaluate the spatial derivatives. The form of this approximation arises from a Taylor series expansion

$$\frac{\partial f_o}{\partial z} = \frac{(f_1 - f_{-1})}{2k} + O(k^2) \quad (6.10)$$

$$\frac{\partial^2 f_o}{\partial z^2} = \frac{(f_1 - 2f_o + f_{-1})}{k^2} + O(k^2) \quad (6.11)$$

where $f_r = \ell_i(z_r)$ and $z_r = z_o + rk$ for r = 0,1,2...

The actual algorithm used for the integration was

$$\hat{\ell}_i(t + \delta t) = \hat{\ell}_i(t) + \delta t \, (\partial \hat{\ell}_i / \partial t)_t \qquad (6.12)$$

and since $\hat{\ell}$ must remain a unit vector the normalisation $\hat{\ell}_i \rightarrow \hat{\ell}_i / (\hat{\ell}_x^2 + \hat{\ell}_y^2 + \hat{\ell}_k^2)^{1/2}$ was performed after each time step throughout the calculation. At the boundaries, z = 0 and z = d, $\hat{\ell}$ was held fixed with $\hat{\ell}_z = 1$ and $\hat{\ell}_x = \hat{\ell}_y = 0$ (see section 1.2). Therefore the two extreme spatial steps were fixed during the calculation with $\theta = 0$.

A suitable time step for the integration was calculated within the simulation program using

$$\delta(\omega t) = 1/S \, (k/d)^2 \, \Omega \qquad (6.13)$$

where k is the space step and Ω the dimensionless coefficient $\omega_o \mu d^2 / K_b$. S was adjusted until stable accurate integrations were obtained.

6.2.2 Simulation Results

Before solving the equation of motion of $\hat{\ell}$ it was expected that a precessing magnetic field would cause $\hat{\ell}$ to precess about the same axis at the same rate. However it was found that equation 6.1 did not have this precessing solution for $\hat{\ell}$ in bulk ^{3}He-A. Instead in the presence of such a rotating field the polar angle of $\hat{\ell}$ measured in the stationary xy plane did not change and θ varied periodically with frequency ω_o as the field rotated.

However, if the liquid were contained between two parallel planes as shown in Figure 6.1 then the boundary conditions on $\hat{\ell}$ together with the $\hat{\ell}$ bending energy were found to suppress the oscillatory solution for small field rotation rates. In this case a solution with $\hat{\ell}$ precessing at the

field rotation frequency ω_o about the field rotation axis (z) was found, with θ and ϕ constant with time. As ω_o was gradually increased with the field magnitude kept constant there came a point when $\hat{\mathbf{l}}$ was no longer able to precess at ω_o and had to occasionally slip a revolution. This slip was characterised by a rapid jump up and then down in the angle θ as the precessing field $\underline{H}$ passed by $\hat{\mathbf{l}}$, and this motion occurred with frequency ω ($<\omega_o$). If ω_o was increased still further the solution tended to that found in the bulk liquid with no precession of $\hat{\mathbf{l}}$ and θ varying periodically at frequency ω_o.

This behaviour was predicted to occur even in the absence of inertia. The inclusion of the inertial term in the simulations was found to cause the transition between the precessional and oscillatory solutions to occur at different values of ω_o for positive and negative rotations.

Figure 6.2 illustrates the two types of motion that were predicted to occur. This figure has been drawn for θ, ϕ at the centre of the slab, and the subscripts + and - refer to the two directions of field rotation. For this field rotation frequency ω_o, corresponding to $\Omega = 10.7$ and with inertia given by $\beta = 0.02$ (i.e. inertial term 2% of dissipative term) and magnetic field by $H/H_f = 3.6$ (where H_f is the Fréedericksz transition field), then positive rotation produced the precessing solution with time independent values of θ and ϕ, whereas negative rotation produced the oscillatory solution with periodic motion of θ associated with the 2π phase slips of ϕ. This figure illustrates that the inclusion of 2% inertia has caused the transition between types of solution to occur at different values of ω_o for opposing field rotation directions. However, at a larger field rotation rate corresponding to $\Omega = 11.6$, but for the same inertia

and magnetic field, then both directions of rotation produced the oscillatory solution. This is shown in Figure 6.3, where Θ, Φ are measured at the centre of the slab. It is apparent that the inclusion of the inertial term has caused a significant difference in the frequencies ω_+ and ω_- of the periodic motion of Θ obtained for opposing senses of field rotation.

The splitting in the transition, illustrated in Figure 6.2, suggested this as a sensitive method for detecting any inertia associated with an intrinsic angular momentum density. Also for small ω_o, when the precessional solution was obtained for field rotation in either sense, any inertia associated with the motion of $\hat{\mathbf{n}}$ would be apparent as a difference in the angle Θ between Θ_+ for positive rotation and Θ_- for negative rotation. Figure 6.4 illustrates the effect that the inclusion of an inertial term ($\beta = 0.02$) in the simulations had on both types of solution. $H/H_f = 3.6$ for this figure. For small ω_o, when the precessional solution was obtained, the values of Θ in the centre of the slab have been drawn showing distinct values Θ_+ and Θ_- for field precession in opposing senses. For larger ω_o, when the oscillatory solution was obtained, the frequencies of the periodic motion of Θ have been drawn indicating distinct values ω_+ and ω_- for both directions of field rotation. This figure also shows the increase in ω towards its limiting value of ω_o as the field rotation frequency was increased. The simulations performed suggested that it should be possible to detect values of β as small as 10^{-3} (i.e. 0.1%).

Figure 6.5 shows the phase boundary between precessional and oscillatory behaviour as a function of the magnitude of a magnetic field H/H_f precessing at $\pi/4$ about the z axis. The inertial term has been

neglected (i.e. $\beta = 0$) for this figure. It is apparent that as the magnetic field was reduced in magnitude the frequency of field rotation at which the transition occurred became very large. Figure 6.6 shows the phase boundary for a magnetic field with magnitude $H/H_f = 5.2$ as a function of the angle at which the field was caused to precess about the z axis. Again the inertial term has been neglected for this figure. It can be seen that as the angle was increased towards $\pi/2$ the frequency ω_o at which the transition occurred became very large.

In drawing Figures 6.2-6.6 the simulations were performed using 5 space steps.

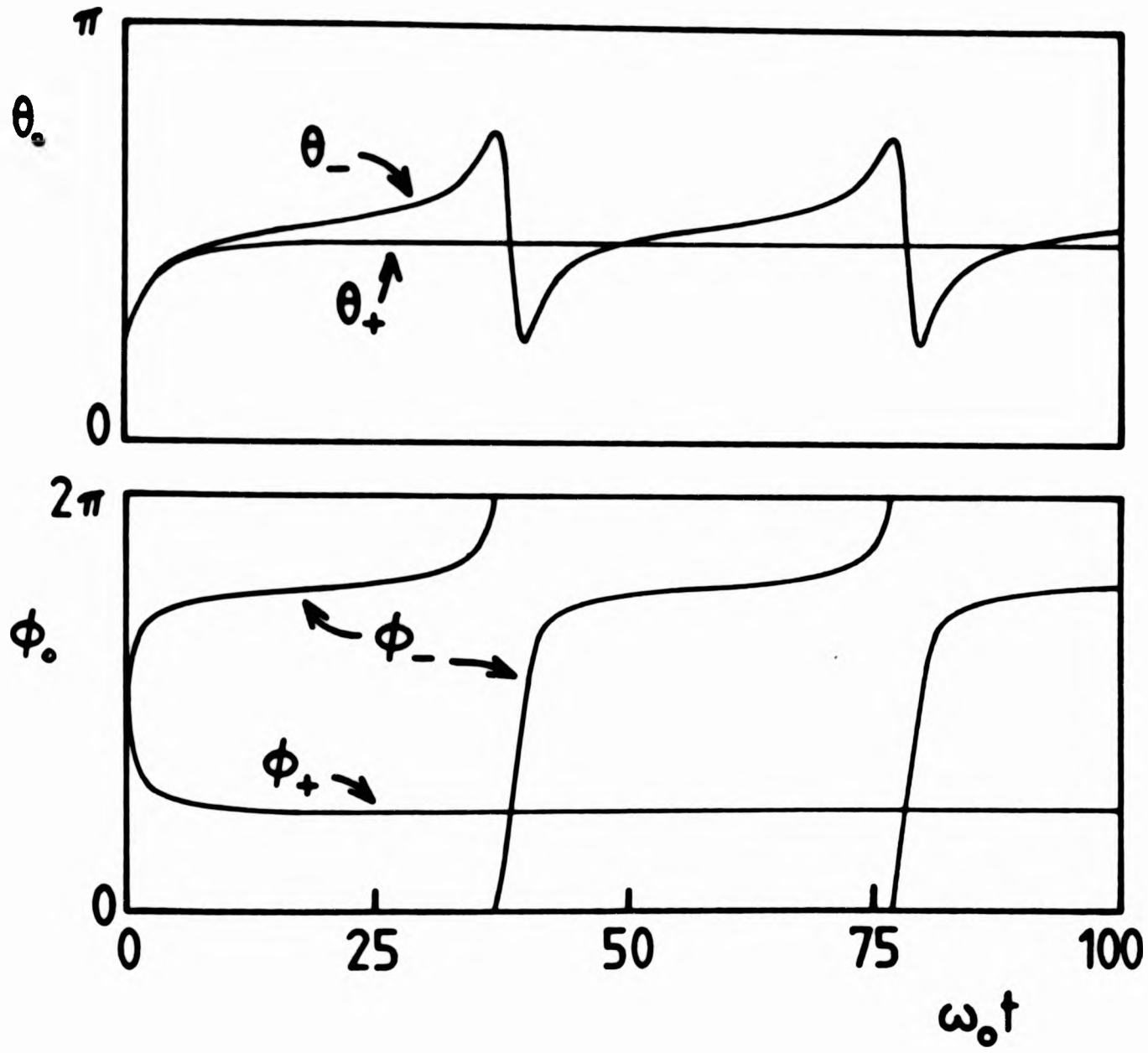

FIG 6.2 : Two types of motion of $\hat{l}.\Omega$=10.7, β=0.02, H/H_f =3.6 (ϕ_0 modulo 2π is plotted). Positive rotation of field produces the precessing solution negative rotation produces the oscillatory solution.

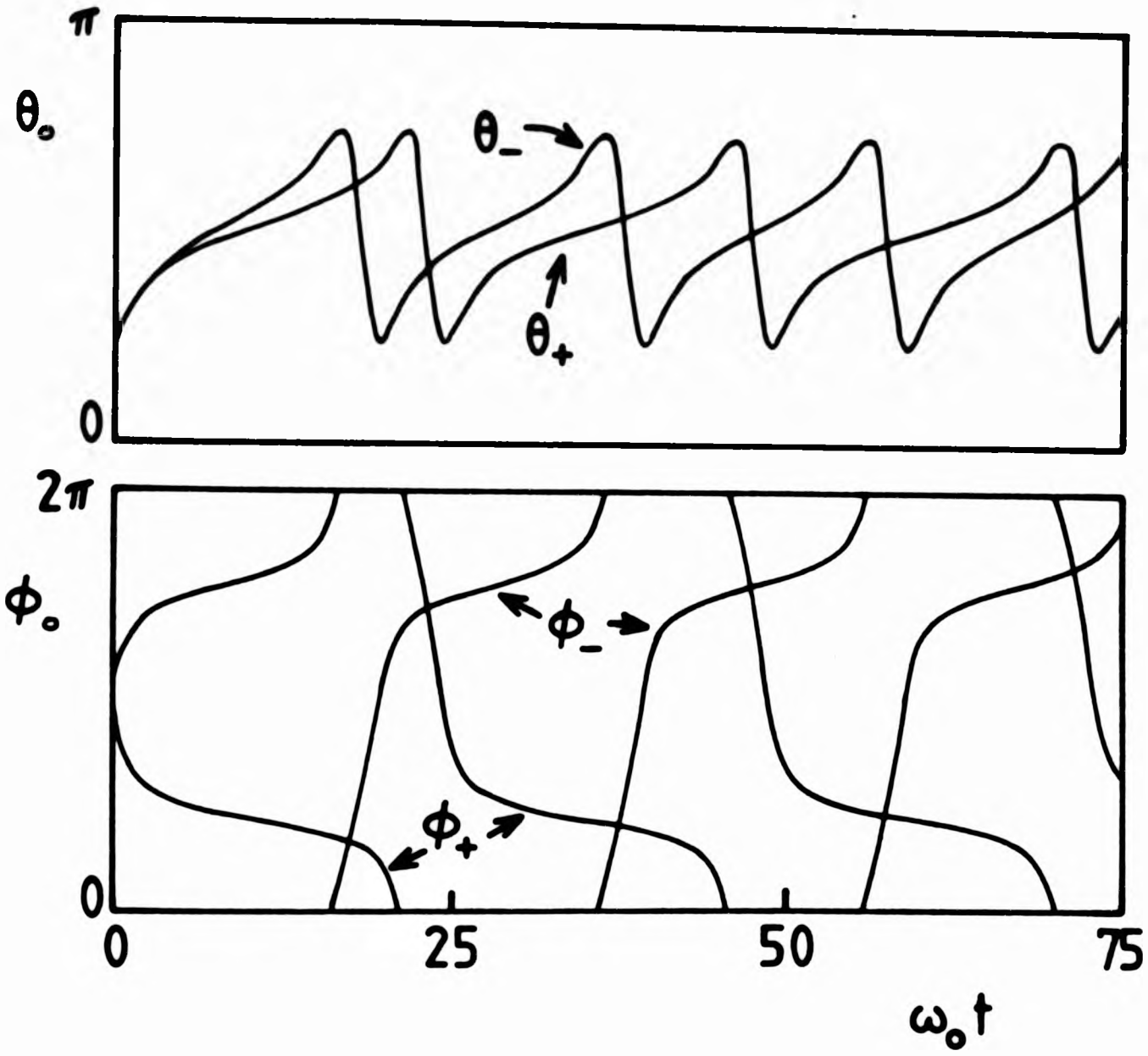

FIG 6.3 : Oscillatory solution for motion of $\hat{l}$ for both directions of field rotation. Ω=11.6, β=0.02, H/H_f =3.6 (ϕ_0 modulo 2π is plotted).

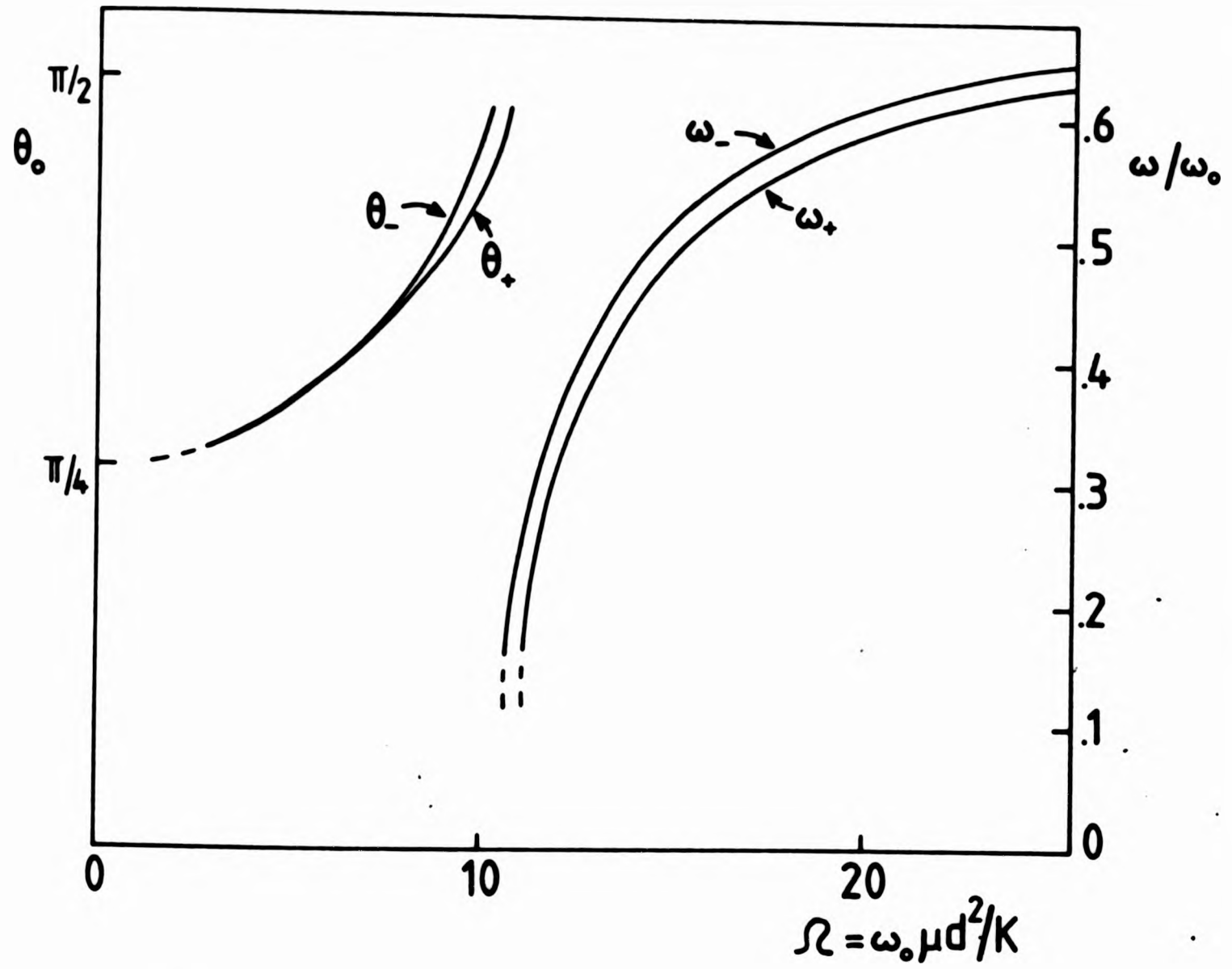

FIG 6.4 : The effect of inclusion of 2% inertia on both types of solution for motion of $\hat{l}$. β =0.02, H/H_f =3.6

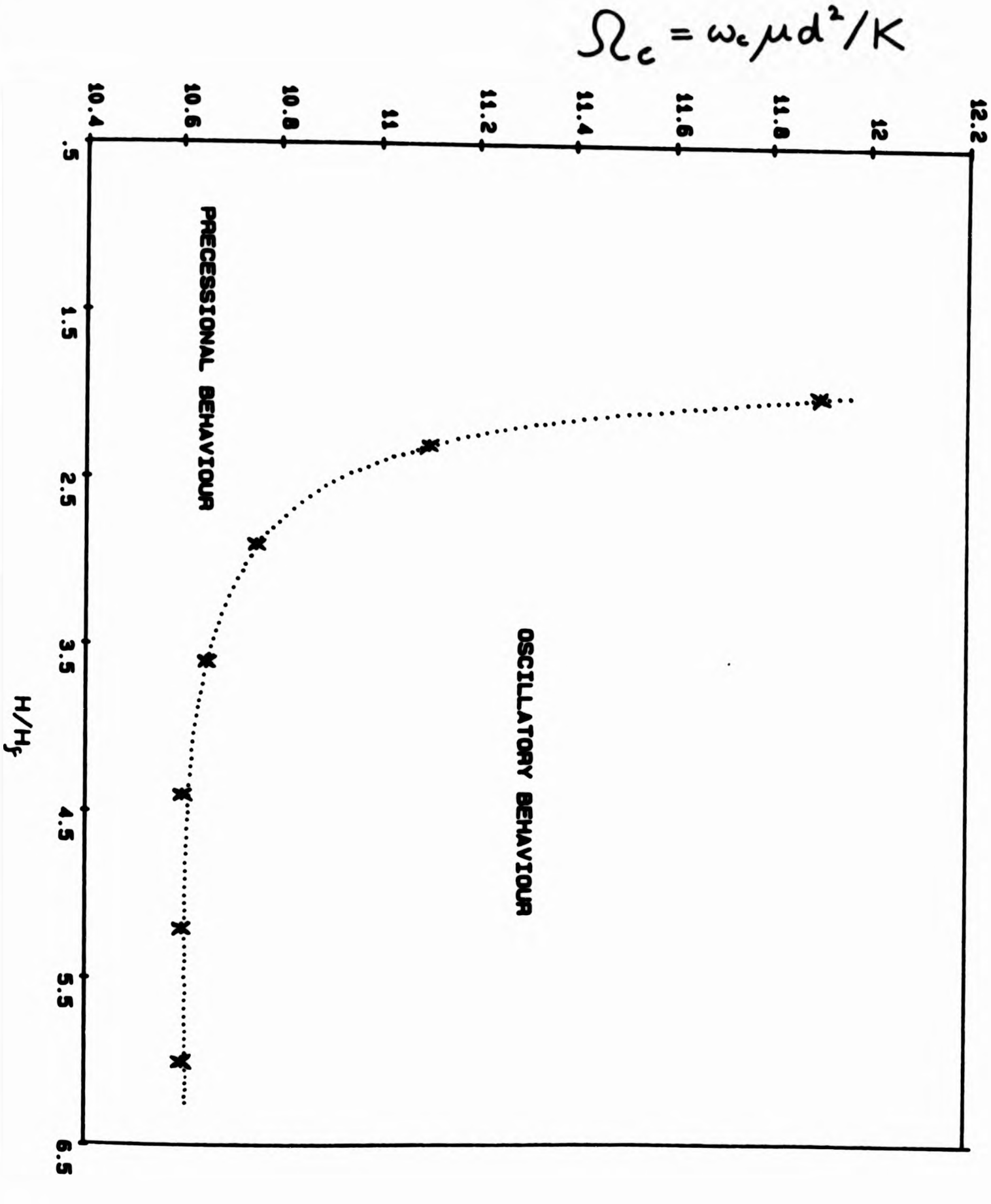

FIG 6.5 : Phase boundary between precessional and oscillatory behaviour of $\hat{l}$ as a function of the magnitude of a magnetic field precessing at $\pi/4$ about the z axis. Calculated points (*). Dotted line acts as a guide to the eye.

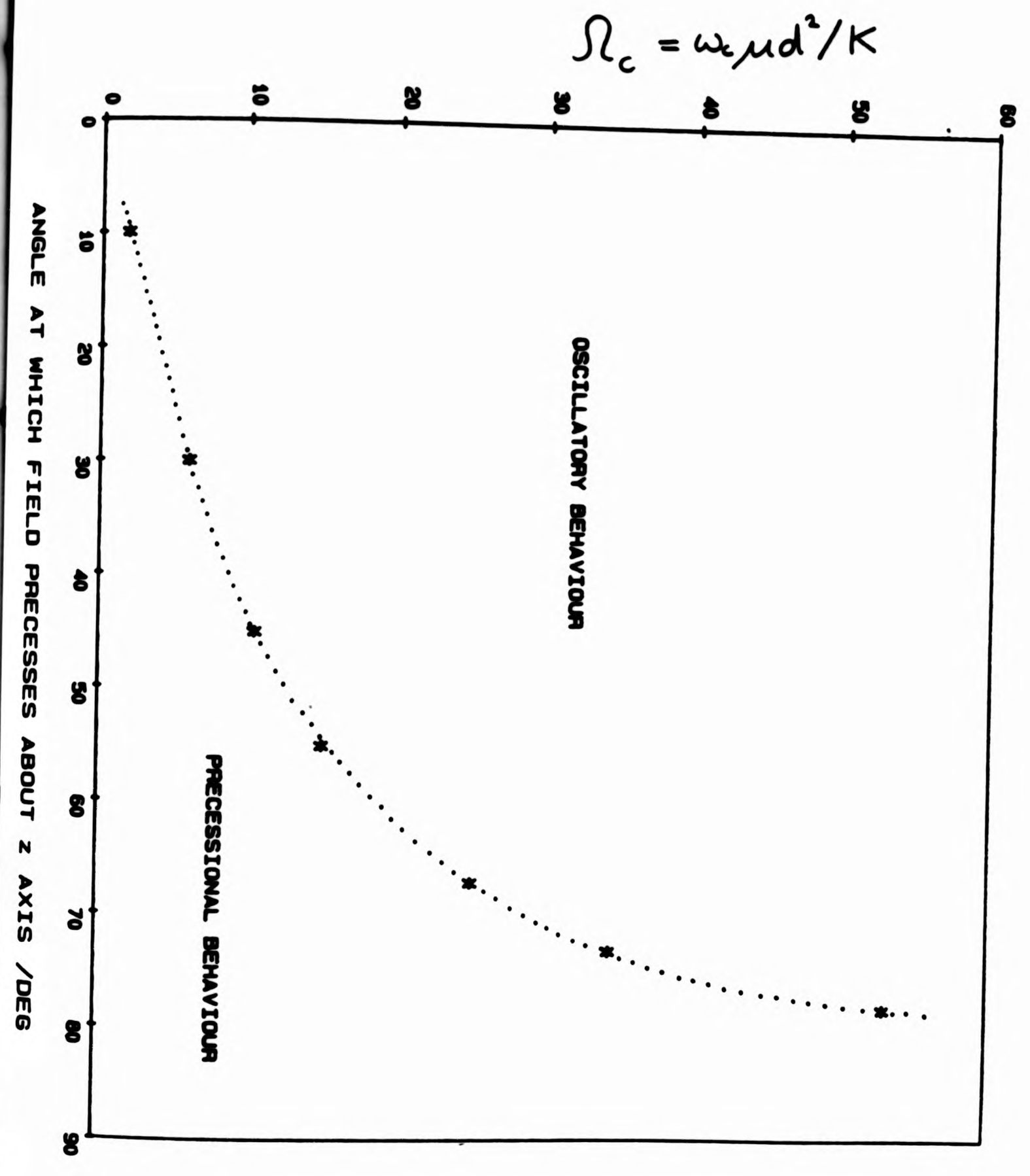

FIG 6.6 : Phase boundary between precessional and oscillatory behaviour of $\hat{l}$ as a function of the angle at which a field H/H_f =5.2 was caused to precess about the z axis. Calculated points (*). Dotted line acts as a guide to the eye.

6.3 Experimental

6.3.1 Experimental Procedure

It is apparent from the preceding section that a transition should occur in the behaviour of $\hat{\mathbf{r}}$ as the frequency ω_o of a precessing magnetic field is increased from zero. By detecting this transition for field precession in opposing senses the inertia associated with an intrinsic angular momentum density should manifest itself as a difference in ω_o for the transition in each case.

A magnetic field precessing about the vertical was set up as follows. The experimental solenoid coil was fed with a steady current using the current ramp source of section 2.4.4 to produce a steady vertical field (the residual vertical field having first been compensated out). Each set of saddle coils was fed with a sinusoidal current of similar magnitude, and frequency ω_o, but $\pi/2$ out of phase with respect to each other. This was achieved using the 2 channel oscillator and operational amplifier circuit of section 2.4.4. By suitable choice of relative magnitudes of the solenoid and saddle coil currents a field could be set up rotating at any angle about the vertical.

15.154 MHz sound was transmitted through the liquid helium using the settings described in section 2.3.2, and with a detection electronics time constant of 1s. The data collection program of Appendix D was used to store some of the data records. Both the in phase and quadrature sound signals were monitored.

In order to look for the predicted transition in behaviour of $\hat{\mathbf{l}}$ it was necessary to estimate the magnitude of field and frequency of field rotation at which the transition should occur for a slab of thickness d = 2mm. Figure 6.5 was used to give Ω_c (= $\omega_c \mu d^2/K_b$, the value at the transition) for different values of H/H_f when the field was rotated at $\pi/4$ about the z axis. For H/H_f = 5.2, for example, the transition in the behaviour of $\hat{\mathbf{l}}$ was predicted to occur for $\Omega_c = \omega_c \mu d^2/K_b$ = 10.6. For $(1 - T/T_c)$ = 0.1 and p = 29.3 bar then $\mu \approx 1.8\times10^{-8}$ $Nm^{-2}s$(10). Also in the Ginzburg-Landau limit $K_b = (\hbar/2m)^2$ 5/2 $\rho_{s\parallel}$ where $\rho_{s\parallel} \approx 3.5$ kgm^{-3} at $(1 - T/T_c)$ = 0.1(10). This suggested a field rotation frequency of about 20 mHz for the transition. Similarly, for H/H_f = 2.0 the transition was predicted to occur at a field rotation frequency of about 25 mHz. These values for ω_o at the transition were approximate only and were taken as a guide to the order of magnitude of ω_o required.

The 2 channel oscillator was capable of delivering sine waves with frequencies as small as 2 mHz. However, the amplitude control only allowed the voltages from either channel to be set to within about 2% of the desired values. Therefore a sine wave synthesizer was built that was capable of producing sine waves at lower frequencies if necessary, and with amplitudes that could be set more accurately. This synthesizer created each sine wave digitally and used presettable counters to enable a phase difference of any magnitude to be set up between the two signals. Figure 6.7 shows a block diagram of the circuit that was designed and built for this purpose. Unfortunately, noise problems prevented its use in this experiment.

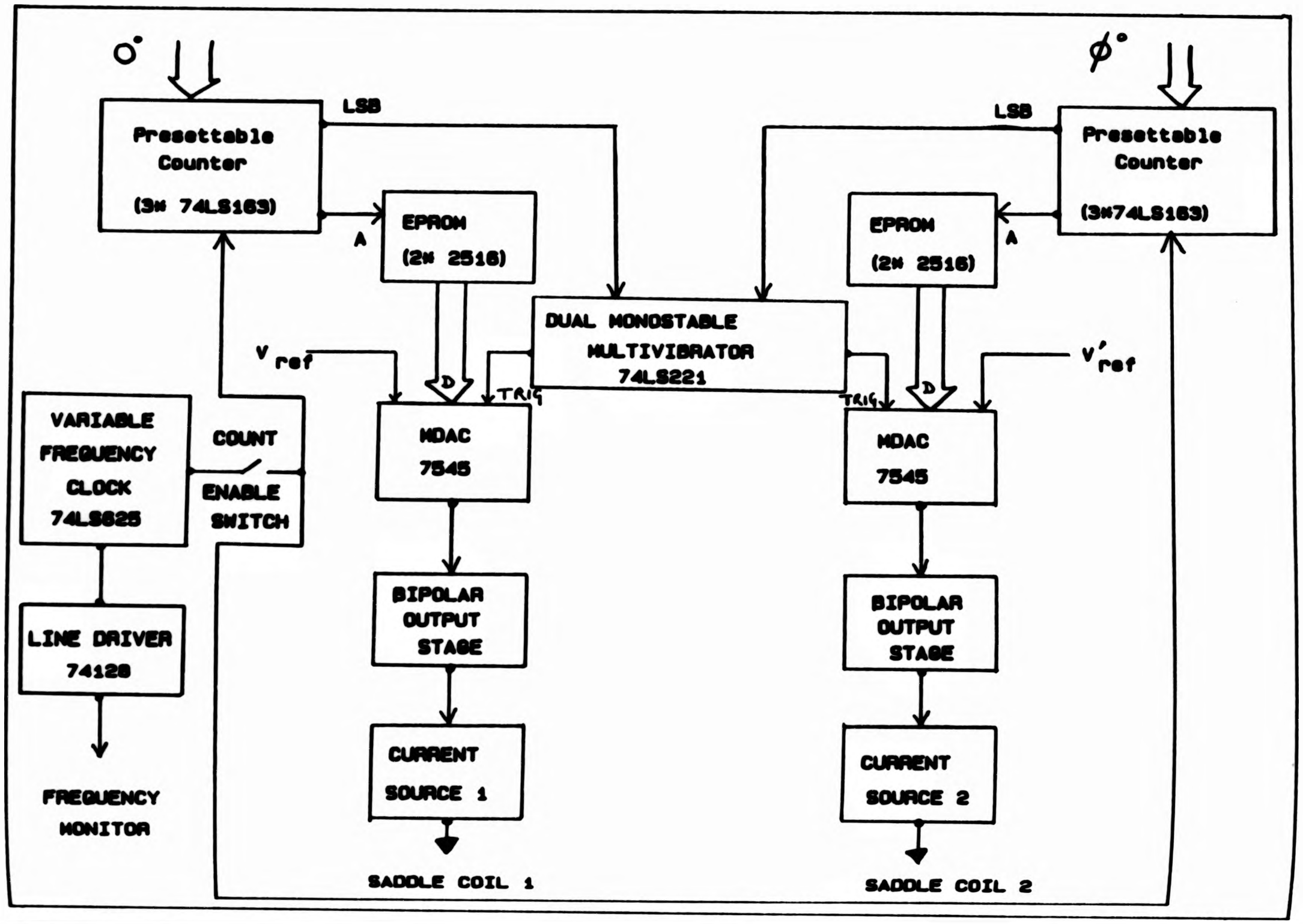

FIG 6.7: SADDLE COILS POWER SUPPLY

6.3.2 Experimental Results

No evidence of a transition in the behaviour of $\hat{\mathbf{l}}$ was observed and therefore it was not possible to look for inertia associated with an intrinsic angular momentum.

In attempts to set up the textures described above magnetic fields with magnitudes ranging from $H/H_f \approx 1$ to $H/H_f \approx 6$ were rotated about the z axis at angles in the range $\pi/4$ to $\pi/2$. In each case the sound signal response of the in phase and quadrature signals were similar. Two features were apparent: firstly, wobbles on the sound signal periodic with the field precession frequency, and secondly, a steady "lying down" of the $\hat{\mathbf{l}}$ texture as the field rotation frequency was increased.

The latter effect can be seen clearly in Figure 6.8 which shows a portion of chart recorder record displaying the in phase sound signal detected with a field of $H/H_f \approx 5.1$ precessing at 78° about the z axis. For the range of field rotation frequencies 2 mHz to 40 mHz then it is apparent from Figure 6.6 that the predicted behaviour of $\hat{\mathbf{l}}$ was precessional. As the field rotation frequency was increased from 2 mHz to 40 mHz the sound signal became progressively more negative. Reference to Figure 5.1, for example, shows that this corresponds to a more distorted texture i.e. an increase in the angle θ_o between $\hat{\mathbf{l}}$ and $\hat{\mathbf{q}}$ at the centre of the slab. The size of the sound signal corresponding to the uniform texture at this temperature is also shown in Figure 6.8.

Figure 6.9 illustrates the periodic wobbles observed on the detected sound signal for a field $H/H_f \approx 4.8$ precessing at $\pi/4$ about the z

axis. The range of field rotation frequencies 2 mHz to 50 mHz employed should have encompassed the transition in behaviour of $\hat{\mathbf{r}}$. The periodic wobbles can be seen most clearly for a field rotation frequency of 2 mHz, and may be due to an asymmetry in the rotating field caused by an unequal magnitude of field directed along each saddle coil axis. This could arise from several sources. Firstly, the sine waves that were fed to each saddle coil pair had amplitudes that were generally matched to within 2%, but the field constant determined for each pair had a possible error of 3%, resulting in an uncertainty of around 3.5% in the matching of amplitudes. Secondly, the residual horizontal field, estimated to be 0.11 G in the direction of fields applied by the outer saddle pair, was not compensated out for these measurements. This would cause a mismatch in the maximum field directed along each saddle coil axis of around 4% for the field magnitude of Figure 6.9. Smaller effects include the fact that the field axis of the inner pair was aligned to be at 90° to the axis of the outer pair with an uncertainty of about 0.5°, and that the 90° phase difference between the two sine waves was set up with an estimated error of around 0.5° using the 2 channel oscillator.

A wobble of a few percent in the angle which $\underline{\mathbf{H}}$ makes locally with the z axis might be expected to produce a corresponding wobble in the angle θ, made between $\hat{\mathbf{r}}$ and the z axis (and therefore $\hat{\mathbf{q}}$). Figure 5.8 would indicate that a 4% wobble in θ_o could be associated with a change in H/H_f of about 0.13, and by reference to Figure 5.1 for example, this might be expected to correspond to a change in sound signal of order ± 10 mV. It should be noted that this is a very rough estimate. In fact the amplitude of the wobbles observed on the in phase signal of Figure 6.9 for a field rotation frequency of 2 mHz was about ± 15 mV.

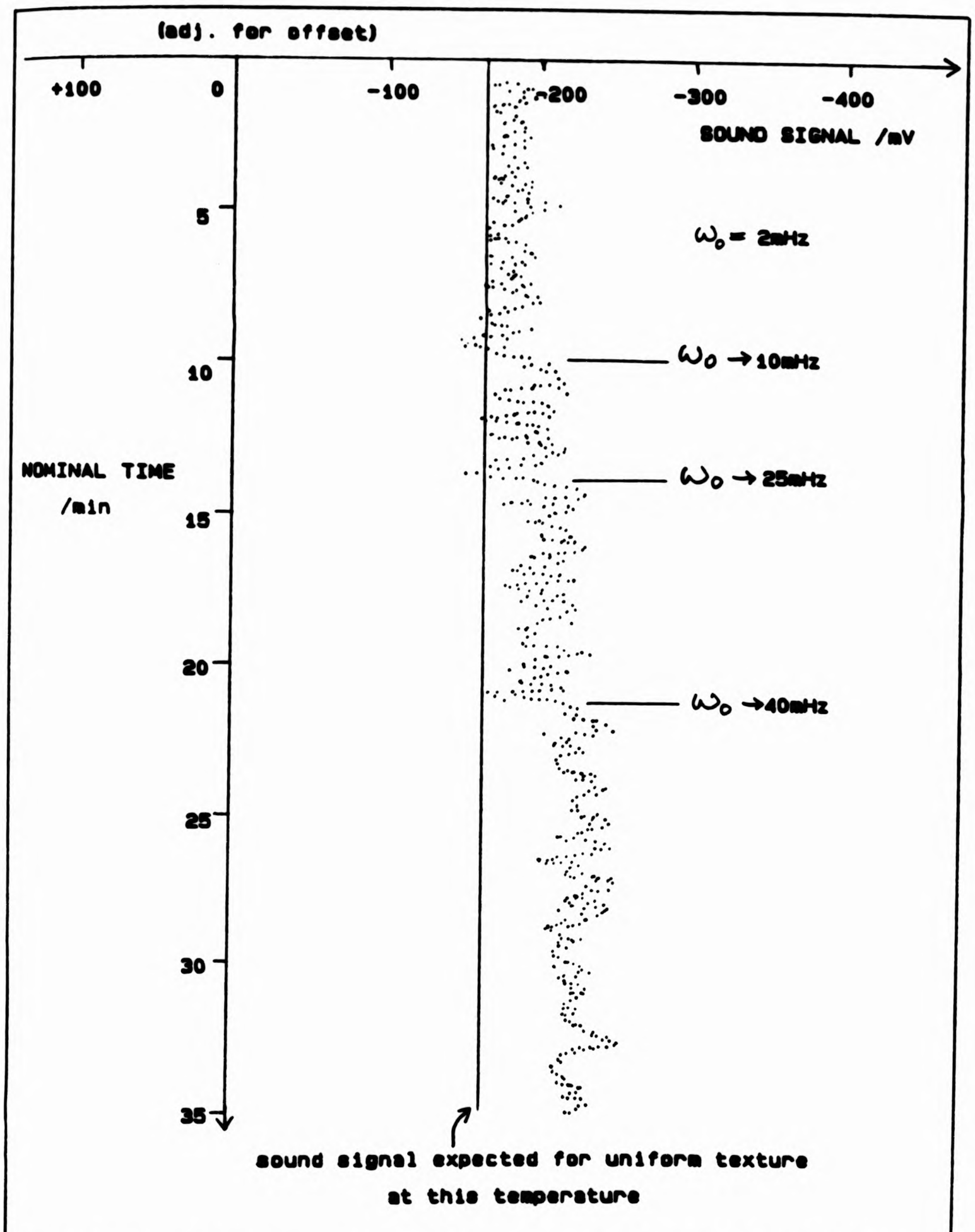

FIG 6.8 : Portion of chart recorder record displaying in phase sound signal detected at $T/T_c = 0.89$ with a field of $H/H_f \approx 5.1$ precessing at 78° about the z axis as the field rotation frequency ω_0 was increased from 2 mHz to 40 mHz.

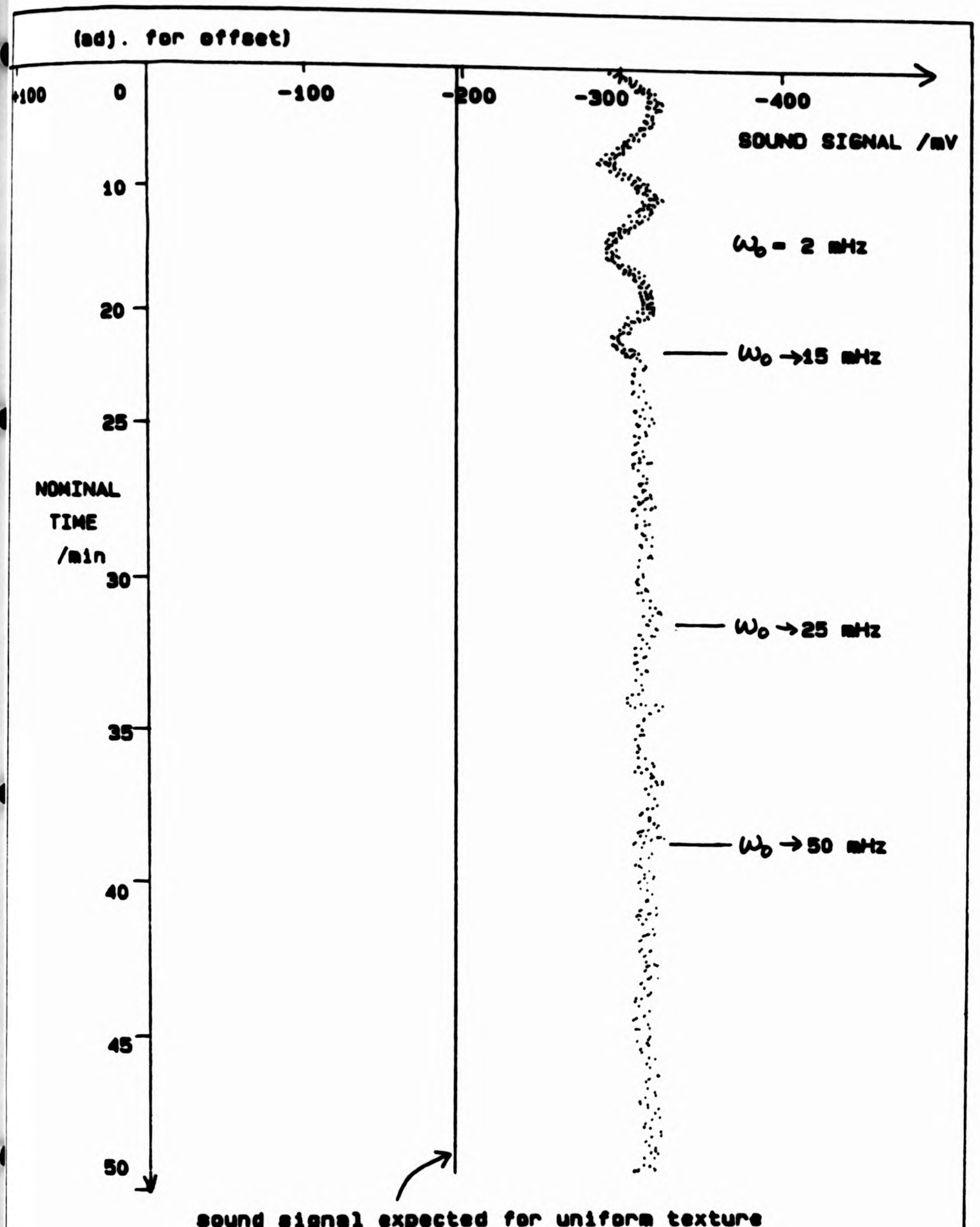

FIG 6.9 : Portion of chart recorder record displaying in phase sound signal detected at T/T_c =0.87 with a field of $H/H_s \approx 4.8$ precessing at 45° about the z axis. Periodic wobbles are apparent on signal for ω_0=2 mHz.

There are several reasons why attempts to set up the motion of $\hat{\mathbf{l}}$ predicted here were unsuccessful. Firstly, the magnetic field was not rotated smoothly about the z axis but wobbled by several percent, as mentioned above. Perhaps more importantly, the calcualtions discussed here have assumed a ^{3}He-A slab of infinite lateral extent whereas the slab used in this experiment had an aspect ratio of only about 5:1 (spatial constraints prevented this being larger). Therefore the effect of the curved boundaries may not be negligible, possibly resulting in very different behaviour of $\hat{\mathbf{l}}$. Also the presence of flow has not been taken into account in these calculations although there was evidence of superflow with $v_s \approx 2\times10^{-6}$ ms^{-1} for this experimental arrangement resulting from a 0.2 nW heat leak to the liquid helium (see Appendix F). Finally, the fields set up by the saddle coils were not completely homogeneous across the lateral extent of the cell but varied by 3-5% from their values at the centre of the cell as can be seen in Figures 2.17 and 2.19.

CHAPTER 7 : SUMMARY

The experimental and theoretical work described in the previous chapters has yielded various significant results. These are summarised as follows, where an indication of some possible improvements has also been given.

The transition that has been predicted in the behaviour of the angular momentum $\hat{\mathbf{l}}$ for ^{3}He-A contained between two parallel planes provides a sensitive method for detecting the inertia characteristic of an intrinsic angular momentum density. This transition from precessional to oscillatory motion of $\hat{\mathbf{l}}$ as the frequency of a magnetic field precessing about the z axis is increased was not observed in attempts to set up the textures described here and therefore it was not possible to look for this inertia. Possible reasons for this include the fact that the slab of ^{3}He-A was not infinite in lateral extent as assumed by the calculations so that the influence of the side walls on the $\hat{\mathbf{l}}$ texture may need to be considered. Also the magnetic field was not precessed smoothly about the z axis due to a mismatch in magnitude of field produced by each saddle coil along its axis. Nevertheless, this proposed method for detecting the inertia is still good and a measurement of this inertia would be invaluable in the controversial arguments concerning the relative contributions of the inertial and dissipative terms to the equation of motion of $\hat{\mathbf{l}}$.

The Fréedericksz transition has been observed for the first time in ^{3}He-A, and the temperature dependence of the threshold field has been measured at 29.316 bar. This reflects the temperature dependence

predicted by theory, where the trivial correction for strong coupling effects in ^{3}He-A has been made (i.e. an enhancement factor of 1.3 has been applied to the energy gap predicted by BCS theory). The experimental data which agree broadly with that measured by another worker (at a similar time) lie below the calculated curve. Further strong coupling effect corrections to the BCS energy gap may be required for a better theoretical representation.

Sound anisotropy coefficients have been determined, describing the velocity and attenuation of 15.154 MHz sound in ^{3}He-A at 29.316 bar in terms of the angle made between the $\hat{l}$ vector and the direction of sound propagation. These coefficients were found by fitting values for the velocity and attenuation, calculated using the theoretical predictions about the distorted $\hat{l}$ texture presented in this work, to experimentally determined values. The fact that this procedure could be employed provided confidence in this theory. The anisotropy coefficients were found to have the order of magnitude predicted by another worker.

No dependence of sound signal amplitude on applied magnetic field was observed for sound transmission through ^{3}He-B, reflecting the sonic isotropy of this superfluid phase.

Two major improvements could be made to reduce the errors in the velocities and attenuations measured, and hence in the sound anisotropy coefficients determined. Firstly, if the 'nuisance' signal could be eliminated by connection of crystal earths at the cell this would enable an integration window for the detection electronics to be chosen such that the '1st echo' only were detected. cw sound measurements might then also be

possible. Secondly, if the temperature drift of the electronic components of the detection electronics (shown in Figure 2.11) were eliminated by the use of heat sinks this would eliminate the 'offset' voltage (or if still present, it would be constant with time). Together, these improvements could reduce the contributions to the detected sound signal so that equation 4.4 for example might become

$$IP = B'(\omega)\, e^{-\alpha d} \cos(\omega d/c + \Phi_1'(\omega)) \qquad (7.1)$$

thus considerably reducing the number of parameters involved in the determination of α and c (see chapter 4).

In order to improve the aspect ratio of the ^{3}He-A slab for the same 2 mm plane spacing the cell and coil system would need to be rotated through $\pi/2$ so that the plane slab surfaces would become parallel to the cryostat insert axis of symmetry. This is necessary because spatial constraints prevent the increase of the slab diameter in its present configuration, and would involve a re-design of the experimental components. It is also recommended that the magnetic shielding of the cell be improved so that any residual fields are reduced to a more acceptable level (i.e. $H_{residual} \ll H_f$).

By choosing an earlier period after the input of the transmitter pulse over which to integrate the detected sound signal the amplitude of sound pulses input to the cell could be reduced for a similar magnitude of signal detected. This would reduce the heat leak to the cell helium and thus reduce the incidence of flow in the cell. In addition, the temperature difference ΔT between the cell and main bath helium would be reduced.

All the measurements discussed in this thesis have been performed on an $\hat{\mathbf{l}}$ texture formed by cooling into the A phase with the residual vertical field compensated out and with a large ($\approx 10\ H_f$) horizontal field applied to encourage formation of the uniform texture. On cooling into the A phase with no applied fields, i.e. under the influence of the residual field, the texture formed responded in a similar manner to that described in chapter 5, although there was some evidence that the Fréedericksz transition threshold field was slightly depressed. However, on warming into the A phase from the B phase, with no applied fields, a very different $\hat{\mathbf{l}}$ texture appeared to have been formed. Its in phase and quadrature sound response to an applied vertical field are shown in Figures 7.1 and 7.2 for a reduced temperature of 0.85. It can be seen that most of the signal response occurs in the quadrature signal. A comparison with Figures 5.1 and 5.10 illustrates how different the response of this texture is from that investigated in the preceding chapters.

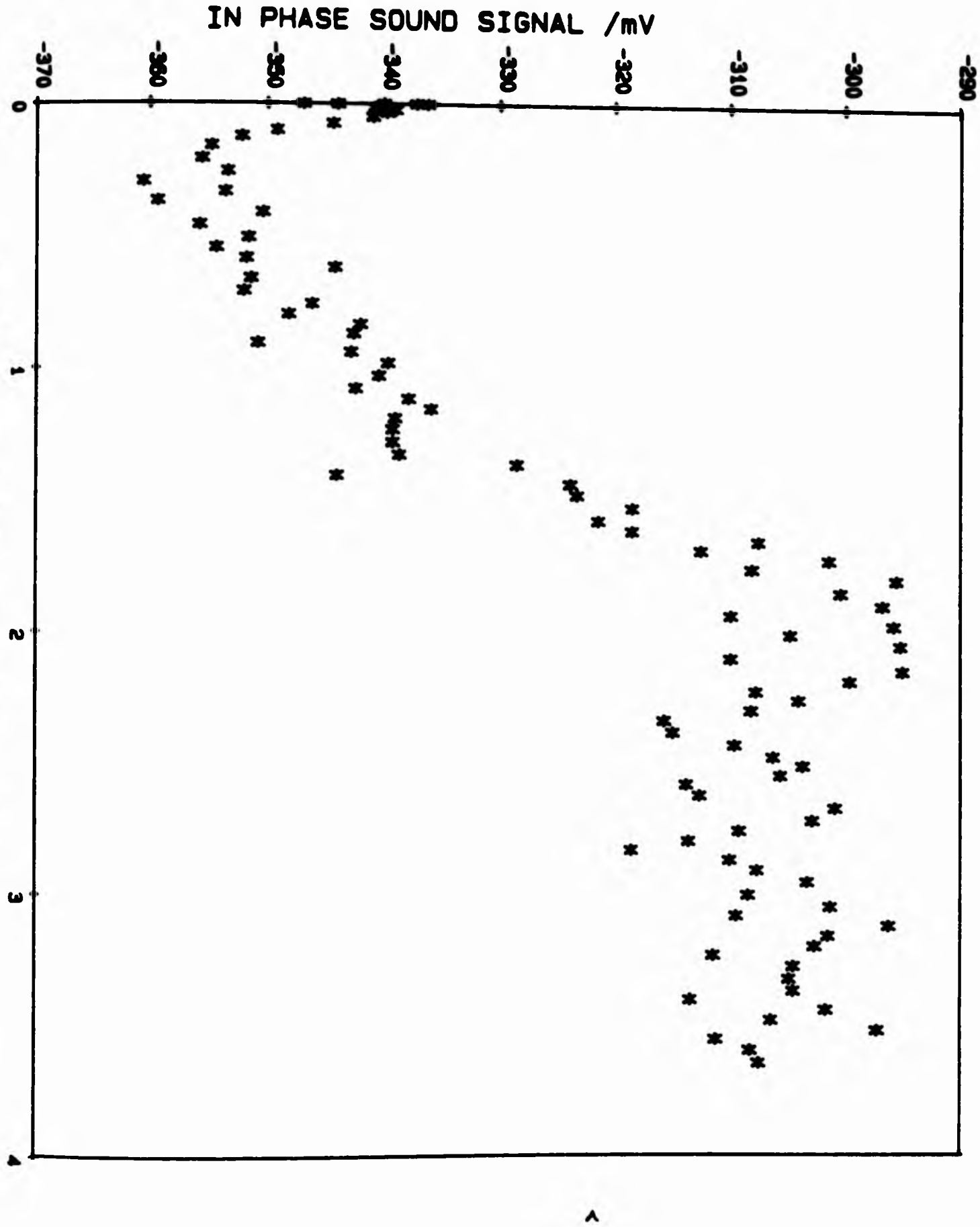

FIG 7.1 : In phase response of $\hat{l}$ texture (formed when warming from B to A phase) to 15.154MHz sound as a function of applied vertical field at $T/T_c = 0.85$. (Note that there is a residual vertical field $\approx 1G$).

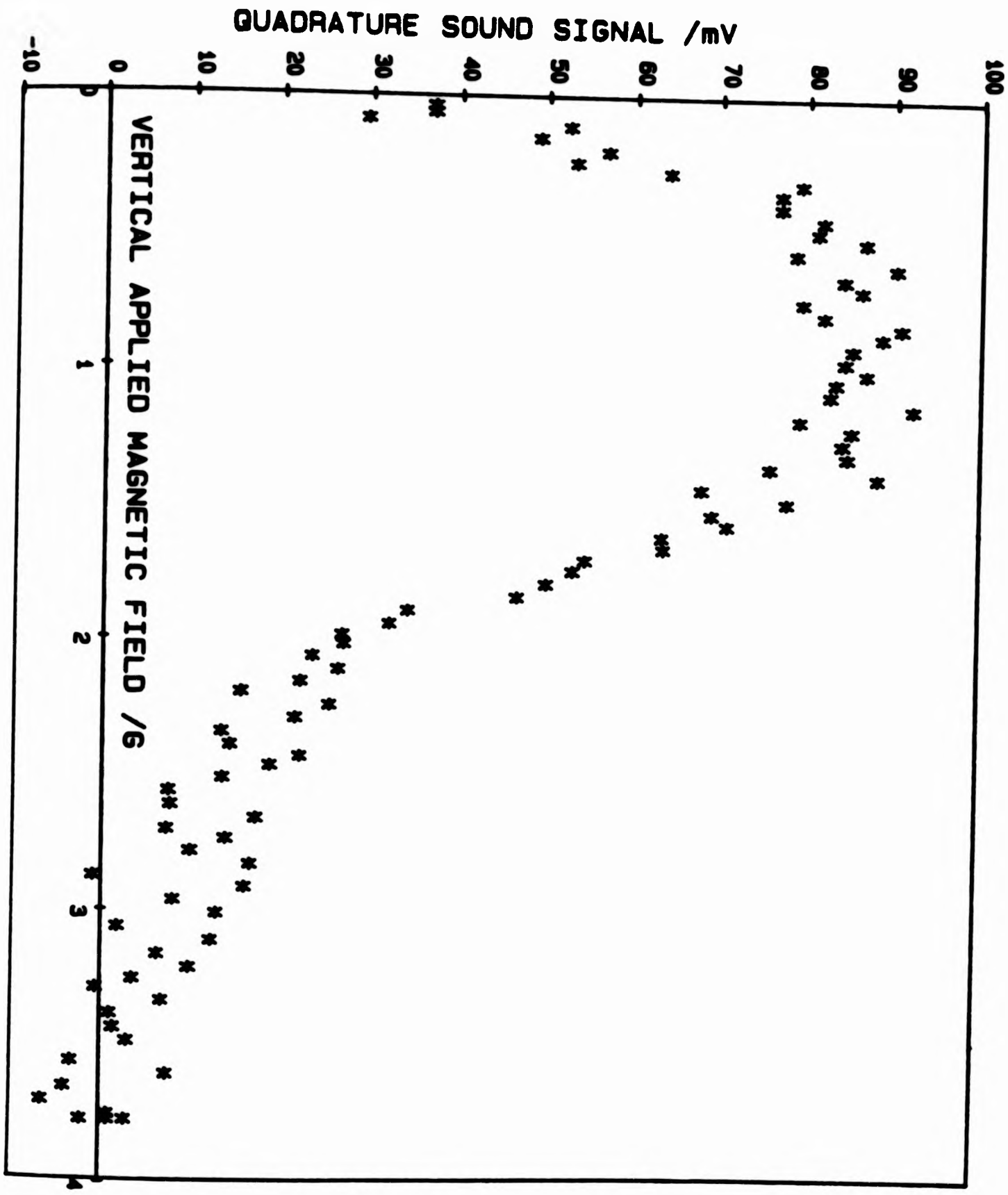

FIG 7.2 : Quadrature response of $\hat{l}$ texture (formed when warming from B to A phase) to 15.154MHz sound as a function of applied vertical field at $T/T_c = 0.85$. (Note that there is a residual vertical field $\approx 1G$).

REFERENCES

1. Alvesalo,T.A., Haavasoja,T., Manninen,M.T., Soinne,A.T., Phys. Rev. Lett. 44 1076 (1980)

2. Brinkman,W.F., Cross,M.C., in: Progress in Low Temperature Physics, Vol VIIA, ed. D.F.Brewer, (North-Holland,Amsterdam, 1978) p.105

3. Leggett,A.J., Rev. Mod. Phys. 47 331 (1975)

4. Ambegaoker,V., de Gennes,P.G., Rainer,D., Phys. Rev. A9 2676 (1974)

5. Anderson,P.W., Morel,P., Phys. Rev. 123 1911 (1961)

6. Cross,M.C., J. Low Temp. Phys. 26 165 (1977)

7. Paulson,D.N.,Krusius,M.,Wheatley,J.C., Phys. Rev. Lett. 36 1322 (1976)

8. Liu,M., Physica 109 & 110B 1615 (1982)

9. Hall,H.E., Hook,J.R., in: Progress in Low Temperature Physics, Vol IX, ed. D.F.Brewer, (North-Holland,Amsterdam, 1986) p.143

10. Wheatley,J.C., in: Progress in Low Temperature Physics, Vol VIIA, ed. D.F.Brewer, (North-Holland,Amsterdam, 1978) p.1

11. Greywall,D.S., March 1985 Preprint

12. Wheatley,J.C., Rev. Mod. Phys. 47 415 (1975)

13. Fréedericksz,V., Repiewa,A., Z. Physik 42 532 (1927)

14. Carless,D.C., Ph.D. thesis, Manchester University, 1981

15. Mitchell,R., Ph.D. thesis, Manchester University, 1984

16. Eastop,A.D., Diploma report, Manchester University, 1983

17. Vacuumschmelze GMBH, 6450 Hanau, W. Germany, also Boll, Soft Magnetic Materials, (Heyden) p.286

18. Emerson & Cumming (U.K.) Ltd., Colville Rd., Acton, London

19. Roark,R.J., Formulas for stress and strain, (McGraw-Hill, 1965)

20. Gooch & Housego, Cornhill, Ilminster, Somerset

21. R.S. Components Ltd., P.O. Box 12, Stockport, U.K.

22. Cooner coax, U.S.A.

23. Matec, Inc., 60 Montebello Rd., Warwick, U.S.A.

24. Hewlett-Packard Co., P.O. Box 301, Loveland, Colarado 80537, U.S.A.

25. Hatfield Instruments Ltd., Plymouth, England

12. Wheatley,J.C., Rev. Mod. Phys. 47 415 (1975)

13. Fréedericksz,V., Repiewa,A., Z. Physik 42 532 (1927)

14. Carless,D.C., Ph.D. thesis, Manchester University, 1981

15. Mitchell,R., Ph.D. thesis, Manchester University, 1984

16. Eastop,A.D., Diploma report, Manchester University, 1983

17. Vacuumschmelze GMBH, 6450 Hanau, W. Germany, also Boll, Soft Magnetic Materials, (Heyden) p.286

18. Emerson & Cumming (U.K.) Ltd., Colville Rd., Acton, London

19. Roark,R.J., Formulas for stress and strain, (McGraw-Hill, 1965)

20. Gooch & Housego, Cornhill, Ilminster, Somerset

21. R.S. Components Ltd., P.O. Box 12, Stockport, U.K.

22. Cooner coax, U.S.A.

23. Matec, Inc., 60 Montebello Rd., Warwick, U.S.A.

24. Hewlett-Packard Co., P.O. Box 301, Loveland, Colarado 80537, U.S.A.

25. Hatfield Instruments Ltd., Plymouth, England

26. Avantek, Inc., 3175 Bowers Ave., Santa Clara, California 95051, U.S.A.

27. Leeds & Northrup Ltd., Wharfdale Rd., Tysley, Birmingham, England

28. Hitachi Denshi (U.K.) Ltd., Video House, 55 Manor Rd., Leeds, U.K.

29. Supercon, Inc., 9 Erie Drive, Natick, Mass. 01760, U.S.A.

30. Niomax; IMI (Kynoch) Ltd., New Metals Div., P.O. Box 216, Birmingham

31. Edwards high vacuum, Manor Royal, Crawley, West Sussex, England

32. Vespel SP22, Du Pont (U.K.) Ltd., 18 Breams buildings, Fetter Lane, London

33. Oxford Instruments Ltd., Osney Mead, Oxford, England

34. Feedback variable phase generator VPG 608, Electroplan, P.O. Box 19, Orchard Rd., Royston, Herts., England

35. Harlyn Automation Ltd., Centronic House, King Henry's Dr., New Addington, Croyden, England

36. Nascom Microcomputers, 92 Broad St., Chesham, Buckinghamshire, England

37. Built by Peter Alexander

38. Anderson,A.C., Temperature 4 773 (1972)

39. Brookdeal Electronics Ltd., Doncastle Rd., Bracknell, Berks., England

40. Cryogenic Consultants Ltd., Metrostore Building, 231 The Vale, London

41. Lounasmaa,O.V., Experimental Principles and Methods Below 1K, (Academic Press) 1974

42. Greywall,D.S., Busch,P.A., J. Low Temp. Phys. 46 451 (1981)

43. General Radio Company, Concord, Massachusetts, U.S.A.

44. Instruments for Technology OY,AB, P.O.Box 38, 02211 Espoo 21, Finland

45. Greywall,D.S., Phys. Rev. B27 2747 (1983)

46. Ahonen,A.I.,Krusius,M.,Paalanen,M.A., J. Low Temp. Phys. 25 421 (1976)

47. Mitchell,R., Eastop,A.D., Faraj,E., Hook,J.R., J. Low Temp. Phys. 64 43 (1986)

48. Alvesalo,T.A., Haavesoja,T., Manninen,M.T., J. Low Temp. Phys. 45 373 (1981)

49. Landau,L.D., Zh. Eksp. Teor. Fiz. 30 1058 (1956) (English Translation, SOVIET Phys.- JETP 3 920 (1957))

50. Wilks,J., Properties of Liquid and Solid Helium, (Clarendon Press, Oxford) 1967

51. Abrikosov,A.A., Khalatnikov,I.M., Rep. Progr. Phys. 22 329 (1959)

52. Wölfle,P. in: Progress in Low Temperature Physics, Vol VIIA, ed. D.F.Brewer, (North-Holland,Amsterdam, 1978) p.191

53. Ketterson,J.B., Roach,P.R., Abraham,B.M., Roach,P.D., in: Quantum Statistics and the Many-Body Problem, eds. Trickey,S.B., Kirk,W.P., Dufty,J.W., (Plenum, New York, 1975)

54. Paulson,D.N., Kleinberg,R.L., Wheatley,J.C., J. Low Temp. Phys. 23 725 (1976)

55. Wölfle,P., Phys. Rev. Lett. 30 1169 (1973)

56. Ebisawa,H., Maki,K., Progr. Theor. Phys. 51 337 (1974)

57. Fetter,A.L., Phys. Rev. B20 303 (1979)

58. de Gennes,P.G., The Physics of Liquid Crystals, (Clarendon Press, Oxford) 1974

59. Cross,M.C., J. Low Temp. Phys. 21 525 (1975)

60. Ramm,H., Pedroni,P., Thompson,J.R., Meyer,H., J. Low Temp. Phys. 2 539 (1970)

61. Sauls,J.A., Serene,J.W., Phys. Rev. B24 183 (1981)

62. Hook,J.R., Eastop,A.D., Faraj,E., Gould,S.G., Hall,H.E. J. Low Temp. Phys. (to be published) 1986, or Gould,S.G., Ph.D. thesis

63. Paulson,D.N.,Krusius,M.,Wheatley,J.C., J. Low Temp. Phys. 26 73 (1977)

64. Lawson,D.T., Bozler,H.M., Lee,D.M., in: QSMBP p.19 (see 53)

65. Abramowitz,M., Stegun,J.A., Handbook of Mathematical Functions, (Dover, New York, 1965)

66. Leggett,A.J., Nature 270 585 (1977)

67. Paulson,D.N., Wheatley,J.C., Phys. Rev. Lett. 40 557 (1978)

68. Hook,J.R., Hall,H.E., J. Phys. C: Solid State Phys. 12 783 (1979)

62. Hook,J.R., Eastop,A.D., Faraj,E., Gould,S.G., Hall,H.E. J. Low Temp. Phys. (to be published) 1986, or Gould,S.G., Ph.D. thesis

63. Paulson,D.N.,Krusius,M.,Wheatley,J.C., J. Low Temp. Phys. 26 73 (1977)

64. Lawson,D.T., Bozler,H.M., Lee,D.M., in: QSMBP p.19 (see 53)

65. Abramowitz,M., Stegun,J.A., Handbook of Mathematical Functions, (Dover, New York, 1965)

66. Leggett,A.J., Nature 270 585 (1977)

67. Paulson,D.N., Wheatley,J.C., Phys. Rev. Lett. 40 557 (1978)

68. Hook,J.R., Hall,H.E., J. Phys. C: Solid State Phys. 12 783 (1979)

Appendix A : Magnetic Field Calculations for Saddle Coil Design

A calculation was executed to find the x component of the field off-axis in both the x and y directions for a "bent rectangular" set of saddle coils (see Figure 2.13 and section 2.4.3). These expressions were used in the design of the saddle coils discussed in section 2.4 in an attempt to minimise the variation in off-axis field, with respect to the field produced at the centre by the coils.

A.1 x Component of field off-axis in x the direction i.e. $B_x(x)$

a) Curved sections

Figure A.1 shows a sketch of the situation considered, where $B_x(x)$ at the point P is to be determined.

For the arc with $x > 0$ and $z = 0$:

$$Q = (R\cos\theta,\ R\sin\theta,\ 0)$$

$$P = (x,\ 0,\ d)$$

$$\underline{\delta\ell} = R\,\delta\theta\,(-\sin\theta,\ \cos\theta,\ 0)$$

$$\underline{r} = \underline{QP} = (x - R\cos\theta,\ -R\sin\theta,\ d)$$

Using the Biot-Savart law which states that

$$\underline{\delta B} = \frac{\mu_0\, i}{4\pi r^2}\ \underline{\delta\ell} \times \underline{r} \qquad (A.1)$$

for the x component only:

$$B = B_o(i,\ d,\ x) = \frac{\mu_0 i\ Rd}{4\pi}\int_{-\Phi}^{\Phi} \frac{\cos\theta\ d\theta}{(x^2 - 2\,x\,R\cos\theta + R^2 + d^2)^{3/2}} \qquad (A.2)$$

where 2Φ is the angle subtended by the arc of the windings at the centre.

For the arc with $x < 0$ and $z = 0$, $B = -B_o(-i,\ d,\ -x)$

For the arc with $x > 0$ and $z = 2d$, $B = B_o(-i, -d, x)$

For the arc with $x < 0$ and $z = 2d$, $B = -B_o(i, -d, -x)$

Using the binomial expansion up to powers in x^2 and integrating, gives the field from all 4 circular arcs at the point P as

$$B_C = \frac{\mu_o\, i\, R\, d}{\pi\,(R^2+d^2)^{3/2}} \sin\Phi \left[2 - \frac{3x^2}{(R^2+d^2)^2}(R^2 + d^2 - 5R^2 + 5R^2\sin^2\Phi/3)\right] \qquad (A.3)$$

b) Vertical Sections

Figure A.2 shows a sketch of the situation considered.

At $z = d$ i.e. in the vertical centre:

$$P = (x, 0, d)$$

$$\underline{\delta\ell} = (0, 0, \delta z)$$

$$Q = (R\cos\Phi, R\sin\Phi, z)$$

$$\underline{r} = \underline{QP} = (x - R\cos\Phi, -R\sin\Phi, d - z)$$

Using the Biot-Savart law for the x component due to section i) only gives

$$B = B_o(i, x, d) = \frac{\mu_o\, i}{4\pi} R \sin\Phi \int_o^{2d} \frac{dz}{(x^2 + R^2 - 2x\,R\cos\Phi + (d-z)^2)^{3/2}} \qquad (A.4)$$

For section ii) $B = B_o(-i, x, d)$ and $\Phi = -\Phi$

For section iii) $B = B_o(i, -x, d)$

For section iv) $B = B_o(-i, -x, d)$ and $\Phi = -\Phi$

Using the binomial expansion up to powers in x^2 and integrating, gives the field from all 4 vertical sections at the point P as

$$B_V = \frac{2\mu_o iRd\sin\Phi}{\pi R^2(R^2+d^2)^{1/2}} \left[1 - x^2\left(1 - \frac{4\cos^2\Phi}{R} + \left(\frac{R^2+d^2 - 7R^2\cos^2\Phi - 4d^2\cos^2\Phi}{2(R^2 + d^2)^2}\right)\right)\right] \qquad (A.5)$$

Thus if $B_X(x) = B_X(0) + \delta B_X(x)$ the field at the centre of the coil system can be identified as

$$B_x(0) = \frac{2\,\mu_o\, i\, R\, d \sin\Phi\, (2\,R^2 + d^2)}{\pi\, R^2\, (R^2 + d^2)^{3/2}} \qquad (A.6)$$

and $\delta B_x(x)/B_x(0)$ gives a measure of the deviation of the field from this value at a point x off-axis.

A.2 x Component of field off-axis in the y direction i.e. $B_x(y)$

$B_x(y) = B_x(0) + \delta B_x(y)$ was calculated in a similar manner.

For the design of coils with this "bent rectangular" shape an attempt was made to minimise both $\delta B_x(x)/B_x(0)$ and $\delta B_x(y)/B_x(0)$, as far as spatial limitations would allow, so that the coil system would produce magnetic fields that were as homogeneous as possible. A computer program was used to minimise these expressions in the design of the inner and outer saddle coil pairs. Best values of R = 1.27 cm, d = 1.9 cm and Φ = 61° were found for the inner saddle coils, and R = 1.42 cm, d = 1.9 cm and Φ = 59° for the outer saddle coils.

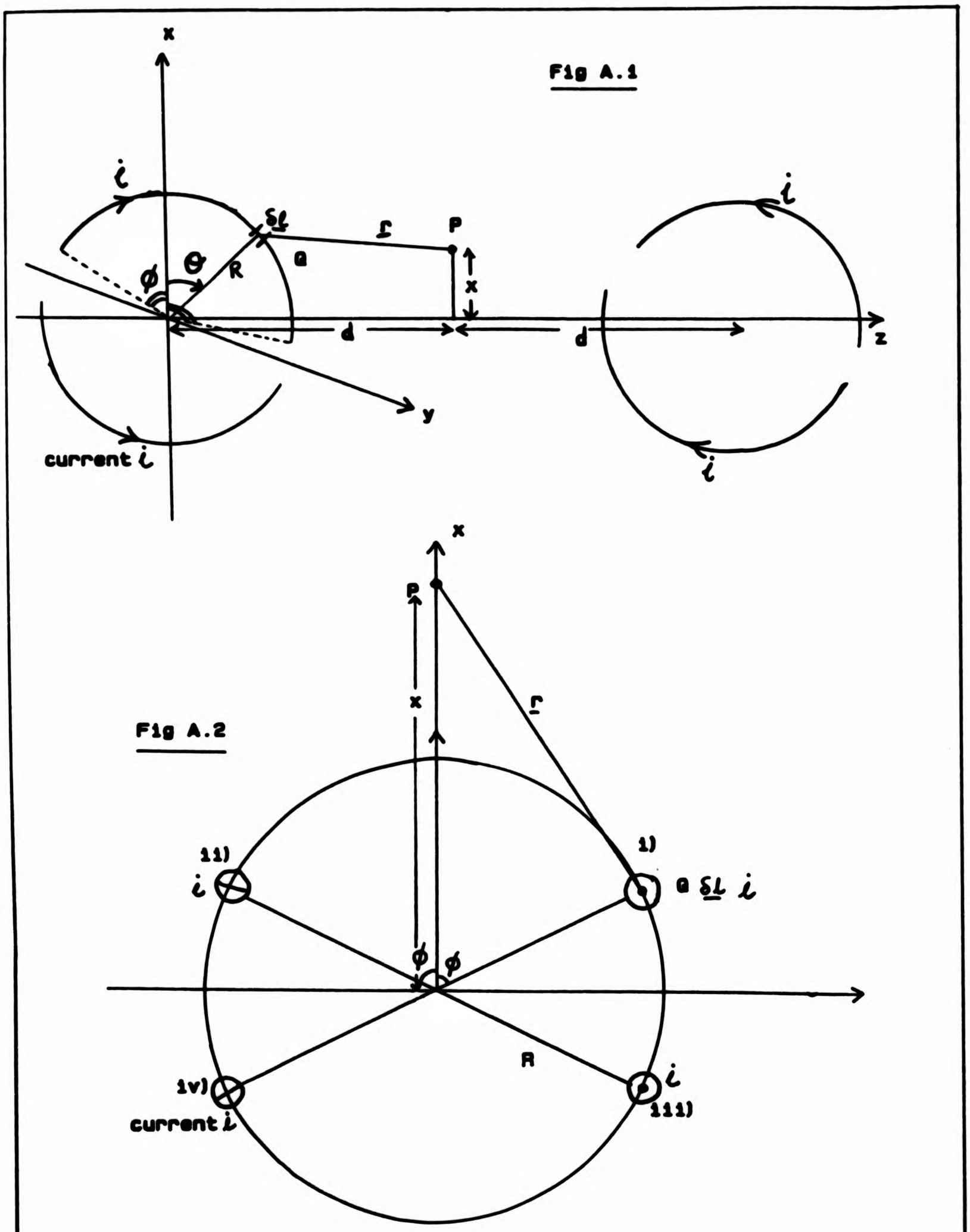

FIG A.1&A.2 : Sketch showing curved & vertical sections respectively of "bent rectangular" saddle coil

Appendix B : Estimation of Heat Input to Cell by Conduction Along Matrix of Magnet Coil Wires

The system may be schematically represented as shown in Figure B.1 (see section 2.4). It has been assumed that $T_{coils} \approx T_{mc}$, i.e. that the magnetic coils were at approximately the same temperature as the dilution refridgerator mixing chamber, since the copper matrix of the wires provided an effective thermal short.

The coil system was separated from the cell flange by 3 vespel SP22 bolts and washers. The dimensions of the thermal path through the vespel have been taken as that of the thin annular washer to give an upper limit on the estimate of the conductive heat leak, $\dot{Q}$, to the platform.

The thermal conductivity of vespel SP22 $\simeq \alpha T^2$, where $\alpha = 17\times10^{-4}$ $Wm^{-1}K^{-3}$ in the low millikelvin temperature range (Locatelli,M., Arnaud,D., Rotin,M., Cryogenics June 1976 p.374).

$\dot{Q}$ was estimated by

$$\int_0^{\ell} \dot{Q}\, dx = 3\, \alpha\, A \int_{T_{plat}}^{T_{mc}} T^2\, dT \qquad (B.1)$$

This provided a value of approximately 0.2 nW for the conductive heat leak to the cell flange on which the magnetic field coils were bolted. In fact, evidence of a rather small heat leak to the ^3He bath (see section 2.2) would suggest this figure to be high.

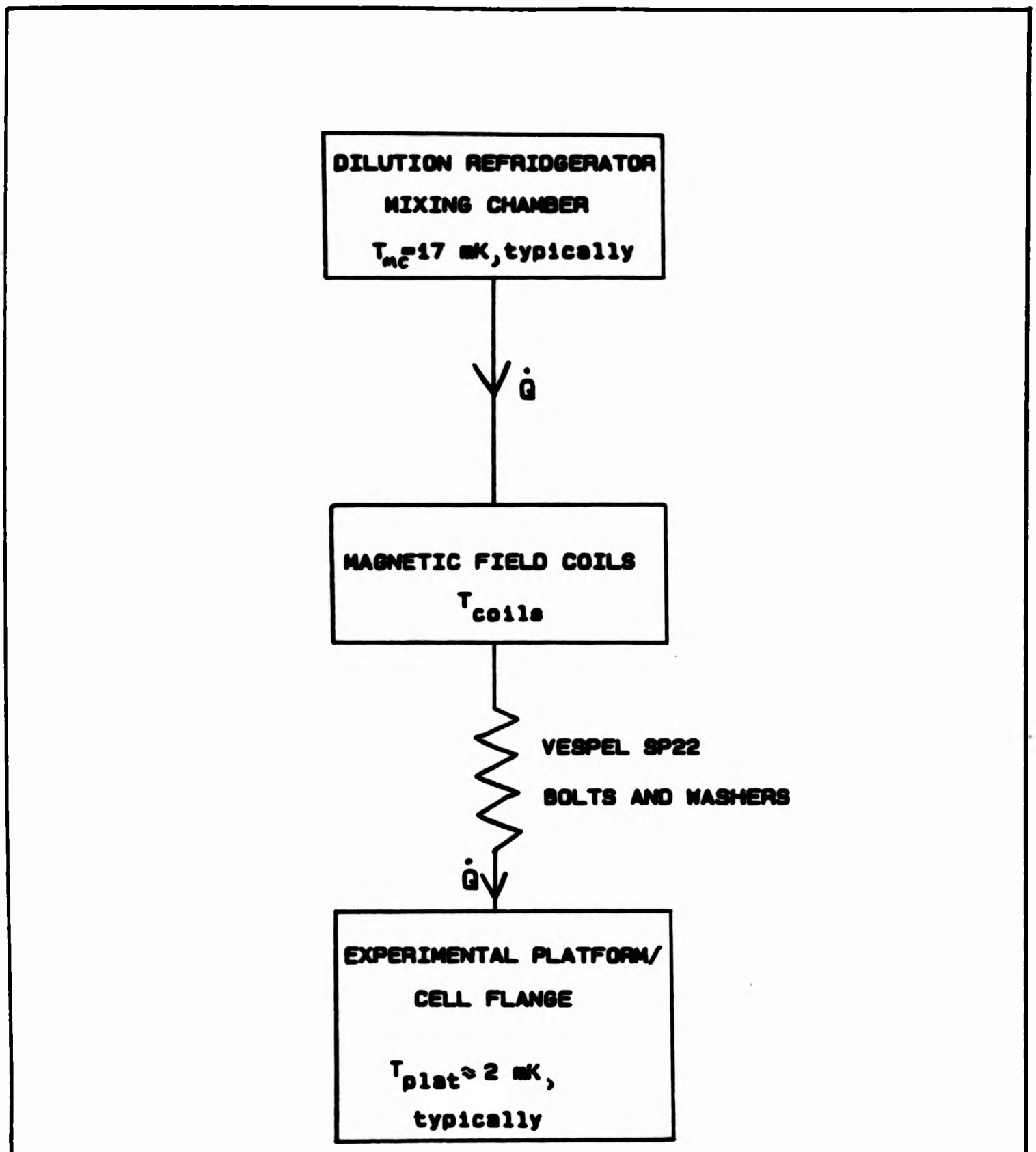

FIG 8.1 : Schematic representation of thermal link between magnetic field coils and experimental platform

Appendix C : Calculation of Magnetic Shielding Provided by Mu Metal Shield

Reference 17 contains the following details about "Mu metal" shielding capabilities:

A magnetostatic shielding factor, S, may be defined as $S = H_o/H_i$, where H_o is the field outside the screen and H_i is the field inside the screen. Assuming the fields involved are small (i.e a few Gauss) and there is no iron core present, then for a long hollow cylinder with wall thickness d and diameter D

$$S_j = \mu\, d \,/\, D \qquad (B.1)$$

where S_j represents the shielding effect of the cylinder jacket and μ is the relative permeability which is about 70 000 for the "Cryoperm 10/4.2" used for the shield.

The shielding factor S may also be written

$$1/S = 1/S_{op} + 1/S_j \qquad (B.2)$$

where S_{op} represents the effect of the opening on the shielding. Reference 17 gives values for S_{op} vs. x/ℓ at a distance x from the open end of a hollow cylinder with length ℓ. For a shield of length 5.7 cm and with x = 2.5 cm (i.e. the cylindrical shield used in this experiment, where x corresponds to the position occupied by the cell ^{3}He) then $S_{op} = 350$. For the same shield, with diameter D = 3.87 cm and thickness d = 1 mm, then $S_j = 1800$ from equation B.1. Thus the shielding factor S for this shield was estimated to be about 300, using equation B.2.

Figures for the main solenoid field profile in the experimental region, where it has been nulled out to a large extent, were provided by Cryogenic Consultants Ltd.(40). These suggested a residual vertical field of order 1.8 G in the cell region (which was off the solenoid coil axis by a few cm), provided by the main solenoid at 11% of a total 70 000 G field. The earth's magnetic field, with magnitude ≤1G, was also present. Therefore it was believed that the Mu metal shield would reduce these fields to about 10 mG at the cell. No figures exist for the solenoid field profiles in the x, y directions. The addition of Mu metal ends to the shield would have improved its shielding properties, but practically this was not possible. A residual field of 10 mG at the cell seemed reasonably acceptable as this represented only 1-2% of an applied experimental field of 0.5-1 G.

APPENDIX D : DATA COLLECTION PROGRAM

```
1 REM PROGRAM TO COLLECT DATA FROM 3 CHANNELS
2 REM OF THE "HARLYN DVM"
3 REM SOUND SIGNAL RECORDED ON CHANNEL 0
4 REM FACILITY TO AVERAGE THIS OVER N READINGS
5 REM N INPUT VIA KEYBOARD DURING DATA COLLECTION
7 REM INITIALISATION AND START CLOCK
10 DIM C$(4),S(5,152),R(5)
20 D=7:L=5:CN=0:CT=0:AV=0:AL=1:A1=1:CL=1:C1=1
30 IA=1:TR=-1:GOSUB 10000
60 GOSUB 12000
70 GOSUB 12700
90 REM READ SOUND FROM CHANNEL 0
100 CH$="COR3T":GOSUB 12300
110 R(0)=VAL(B$):R(4)=0:R(5)=0:CN=CN+1
130 IF CN<>CL*AL+1 THEN 200
135 REM READ FIELD VOLTAGES FROM CHANNELS 1&2
140 CH$="C1R3T":GOSUB 12300
150 R(4)=VAL(B$)
160 CH$="C2T":GOSUB 12300
170 R(5)=VAL(B$)
180 CN=1:CT=1
190 REM CLOCK TIME BCD TO DECIMAL CONVERSION
200 BCD=SC2:GOSUB 12200
210 R(1)=DEC
220 BCD=MN:GOSUB 12200
230 R(2)=DEC
235 IF TR=-1 THEN 250
240 IF R(2)<>0 THEN 500
250 BCD=H:GOSUB 12200
260 R(3)=DEC:TR=0
400 REM AVERAGE CHANNEL 0 AS REQUESTED
410 REM AND STORE ARRAY ON CASSETTE
500 GOSUB 12400
510 REM SCREEN PRINTOUT OF CURRENT VALUES
525 CLS
530 SCREEN1,1
532 PRINT"R(0)  R(1)  R(2)  R(3)  R(4)  R(5)";
533 PRINT"  AV  IA"
535 PRINTR(0);"  ";R(1);"  ";R(2);"  ";R(3);
536 PRINT"  ";R(4);"  ";R(5);"  ";AV;"  ;IA
540 GOSUB 12800
550 GOSUB 12100
560 GOTO 100
999 END
1000 REM SUBROUTINES
10000 REM INITIALISATION
10010 OUT 11,128:OUT 11,147:OUT 12,INP(12)
10020 OUT 8,0:OUT 9,0:OUT 11,131:OUT 11,0
10030 OUT 11,143:OUT 11,15:OUT 11,144
10040 RFD=0
10050 RETURN
10100 REM TAKE CONTROL;ATN=TRUE
10110 X=INP(10):IF X AND 2 THEN 10130
10120 GOTO 10150
10130 X=INP(8):IF X AND 16 THEN 10150
```

```
10140 GOTO 10130
10150 OUT 11,12
10160 RETURN
10200 REM UNTALK
10210 D1=95:GOSUB 10500
10220 OUT 11,10
10230 RETURN
10300 REM UNLISTEN
10310 D1=63:GOSUB 10500
10320 OUT 11,9
10330 RETURN
10400 REM NASCOM TO TALK TO ADDRESS=D
10401 REM CONFIGURE NASCOM TALKER;D LISTENER
10402 REM THEN GOTO STANDBY; ATN=FALSE
10410 GOSUB 10100
10420 GOSUB 10200
10430 OUT 11,138:GOSUB 10300
10450 D1=D+32:GOSUB 10500
10460 OUT 11,11
10470 RETURN
10500 REM NASCOM TALK OUT ONE BYTE=D1
10510 X=INP(8):IF X AND 16 THEN 10530
10520 GOTO 10510
10530 OUT 15,D1
10540 RETURN
10600 REM NASCOM TALK OUT STRING=D$
10610 LN=LEN(D$)
10620 FOR I=1 TO LN-1
10630 D1=ASC(MID$(D$,I,1)):GOSUB 10500
10640 NEXT I
10650 D1=ASC(RIGHT$(D$,1))
10660 OUT 11,8:GOSUB 10500
10670 RETURN
10700 REM NASCOM TO LISTEN TO ADDRESS=D
10701 REM CONFIGURE NASCOM LISTENER;D TALKER
10702 REM THEN GOTO STANDBY; ATN=FALSE
10710 GOSUB 10100
10720 GOSUB 10200
10730 D1=D+64:GOSUB 10500
10740 GOSUB 10300
10750 OUT 11,137:OUT 11,11
10760 RETURN
10800 REM NASCOM LISTEN IN ONE BYTE=B
10810 OUT 11,RFD:X=INP(8):IF X AND 32 THEN 10840
10830 GOTO 10820
10840 EOI=X AND 8 :RFD=2:B=INP(15)
10860 RETURN
10900 REM NASCOM LISTEN IN L CHARACTER STRING=B$
10910 B$="":GOSUB 10800
10930 B$=B$+CHR$(B)
10940 IF EOI OR LEN(B$)=L GOTO 10960
10950 GOTO 10920
10960 RETURN
11000 REM IS SRQ=TRUE? (SERVICE REQUEST)
11010 X=INP(11):IF X AND 4 THEN 11030
11020 GOTO 11010
11030 SRQ=X AND 4
11040 RETURN
```

```
12000 REM CLOCK ROUTINES
12001 REM START CLOCK
12010 INPUT"BCD TIME.FORMAT----HRS--/--/85";CK$
12020 C$(1)=MID$(CK$,1,2):C$(2)=MID$(CK$,3,2)
12040 C$(3)=MID$(CK$,8,2):C$(4)=MID$(CK$,11,2)
12060 DY=VAL(C$(3)):MN=VAL(C$(2)):H=VAL(C$(1))
12070 OUT 39,VAL(C$(4)):OUT38,DY:OUT36,H:OUT35,MN:OUT53,0
12100 REM READ CLOCK IN BCD
12110 SC1=INP(33):IF SC1>1 THEN 12110
12120 SC2=INP(34)
12130 MN=INP(35):IF MN<>0 THEN RETURN
12140 H=INP(36):IF H<>0 THEN RETURN
12150 DY=INP(39)
12160 RETURN
12200 REM CONVERT BCD TO DECIMAL
12210 DEC=BCD AND 15
12220 FOR I=16 TO 32 STEP 16
12230 IF BCD AND I THEN DEC=DEC+I/16*10
12240 NEXT I
12250 IF BCD AND 64 THEN DEC=DEC+40
12260 RETURN
12300 REM READ CHANNEL=CH$
12320 GOSUB 10400:D$=CH$:GOSUB 10600
12330 FOR I=1 TO 55:NEXT I
12340 GOSUB 10700
12350 GOSUB 10900
12360 RETURN
12400 REM DATA AVERAGED THEN ARRAYED
12402 REM THEN STORED ON CASSETTE
12410 AV=AV+1:IF CT=0 THEN 12445
12425 FOR I=1 TO 5
12430 S(I,IA)=R(I)
12435 NEXT I
12440 IA=IA+1:CT=0
12445 FOR I=0 TO 3
12450 S(I,IA)=S(I,IA)+R(I)
12455 NEXT I
12460 IF AV<AL THEN RETURN
12465 FOR I=0 TO 3
12470 S(I,IA)=S(I,IA)/AL
12480 IF AL<>A1 OR CL<>C1 THEN CN=A1*C1
12490 AV=0:AL=A1:IA=IA+1:CL=C1:IF IA<=150 THEN RETURN
12520 IA=1
12530 CSAVE*S
12540 FOR I=0 TO 5
12550 FOR J=1 TO 150
12560 S(I,J)=0
12570 NEXT J
12580 NEXT I
12590 RETURN
12700 REM USR(0) ROUTINE:SCAN KEYBOARD
12710 DOKE3200,25311:DOKE3202,312:DOKE3204,18351
12720 DOKE3206,10927:DOKE3208,-8179:POKE3210,233
12740 DOKE4100,3200
12800 K$="":U=USR(0):K$=CHR$(U):IF ASC(K$)=00 GOTO 12850
12840 INPUT"NO. PTS AVERAGED OVER(SOUND)";A1
12845 INPUT"NO. AVS BEFORE CH1,2 READ";C1
12850 RETURN
```

Appendix E : Newton-Raphson Iterative Method used to Find α and c in ^{3}He-A

To find the velocity and attenuation of 15.154 MHz sound in superfluid ^{3}He-A it was necessary to solve equations of the form :

$$f(x,y) = -IP + N_I + B\, y \cos(x + \Phi_1) + C\, y^3 \cos(3x + \Phi_3) = 0 \qquad (E.1)$$

$$g(x,y) = -Q + N_Q + B\, y \cos(x + \Phi_1 - 1.59) + C\, y^3 \cos(3x + \Phi_3 - 1.59) = 0 \qquad (E.2)$$

where $y = e^{-\alpha d}$, $x = \omega d/c - 2n\pi$ and all other symbols have the meanings discussed in section 4.3. By solving the above pair of equations simultaneously at different temperatures values for α and c across the A phase could be deduced. These equations have no analytic solution and therefore a Newton-Raphson iterative method was used.

Generalising for two functions of variables x and y i.e. $f(x,y) = 0$ and $g(x,y) = 0$ then

$$df = \left(\partial f/\partial x\right) dx + \left(\partial f/\partial y\right) dy \qquad (E.3)$$

$$dg = \left(\partial g/\partial x\right) dx + \left(\partial g/\partial y\right) dy \qquad (E.4)$$

By making an initial guess for x and y values for f and g could be found from equations E.1 and E.2 and hence increments dx and dy by solving $f+df = 0$ and $g+dg = 0$ simultaneously.

$$\text{to give} \quad dx = \frac{-\left(f\,(\partial g/\partial y) - g\,(\partial f/\partial y)\right)}{\left((\partial f/\partial x)(\partial g/\partial y) - (\partial g/\partial x)(\partial f/\partial y)\right)} \qquad (E.5)$$

$$\text{and} \quad dy = \frac{-\left(f\,(\partial g/\partial x) - g\,(\partial f/\partial x)\right)}{\left((\partial g/\partial x)(\partial f/\partial y) - (\partial f/\partial x)(\partial g/\partial y)\right)} \qquad (E.6)$$

Using these new values for $x = x+dx$ and $y = y+dy$ and repeating the process gives a rapidly converging solution.

For these sound equations an initial guess was made for x and y by assuming zero contribution to the signal from the 3rd echo (i.e C=0) and solving the resulting equations analytically.

APPENDIX F : ESTIMATION OF FLOW PRODUCED BY 0.2nW HEAT INPUT TO ^{3}HE-A

Pulses of ultrasound input to the cell using the settings described in section 2.3.2 were estimated to produce a heat input of 0.2 nW (±50%) (see section 3.5). It might be expected that this heat input would set up counterflow in the horizontal plane. An order of magnitude estimate for the velocity of the superfluid flow produced was made as follows.

If $\dot{Q}$ is input by the sound pulses over a total area A then the heat flow $\dot{q}$ through the helium in a radial direction away from the centre of the slab and at a distance r from the centre may be represented by

$$\dot{q}\ 2\pi\ r\ d = \dot{Q}\ \pi\ r^2\ /\ A \qquad (F.1)$$

or $$\dot{q} = \dot{Q}\ r\ /\ 2\ d\ A \qquad (F.2)$$

The heat flow is given by

$$\dot{q} = s\ v_n\ T \qquad (F.3)$$

where s is the entropy per unit volume and v_n the normal fluid velocity. For the experimental arrangement described here $A \approx (10^{-2})^2\ \pi/4 \approx 10^{-4}$ m^2, d = 2 mm and $0 < r < 10.7$ mm. Near T_c the entropy per mole is given by $C_n(T_c)$ to a good approximation, and $C_n(T_c)/RT_c \approx 4.4$ K^{-1}mole^{-1} at 29 bar (47). For a molar volume of around 26 cm^3 at 29 bar then from equations F.2 and F.3 $v_n \approx 2\times10^{-7}$ ms^{-1} (for r = 4 mm).

For counterflow

$$\rho_s\ v_s + \rho_n\ v_n = 0 \qquad (F.4)$$

with $\rho_s/\rho_n \approx (1 - T/T_c)$ so that for $(1 - T/T_c) = 0.1$ then $v_s \approx 2\times10^{-6}$ ms^{-1}.

From section 1.2 it can be seen that a flow velocity of 2×10^{-6} ms^{-1} will give an energy comparable to the susceptibility anisotropy energy in a field of around 0.03 G.

It should also be noted that there is a critical superfluid flow velocity at which a second order transition in the $\hat{l}$ texture (similar to a Fréedericksz transition) may occur. This can be represented in the dipole-locked limit near T_c by

$$v_{sc} = \sqrt{5}\,\pi\,\hbar\,/\,4\,m\,d \qquad (F.5)$$

(see reference 9).

For a plane spacing d of 2 mm $v_{sc} = 2\times10^{-5}$ ms^{-1}, a factor of 10 greater than the superfluid flow velocity estimated above at $(1 - T/T_c) = 0.1$. However, as T_c is approached v_s will increase rapidly so that this critical superfluid flow velocity may be exceeded (but see section 5.3.2).

APPENDIX G : PROG

FOR D

```
C       FINDS HZ/
C       AND FINDS
C
        SUBROUTI
        COMMON SO
        J=0
        K=0
        PI=3.141
        IC=1
        A=PI*PI*
        B=PI*A/2.
        DO 1 I=4,
        PO=PI*FL
        C=AK(PO)
        D=2.02/S
        Z=C*C+H
        IF(Z.LT.
        J=1
        IM=I
    1   CONTIN
        IN=INT(
        DO 3 II=
        PO=PI*(
        AG=(PO-
        CALL S
        IF(K.E
        CALL A
        IC=IC+1
    2   K=0
    3   CONTI
        DO 5 I=
        PO=PI
        C=AK(
        A=CH/
        AG=(
        CALL
        IF(K
        CALL
        IC=I
    4   K=0
    5   CONT
        IC=I
        RETU
        END
C
C       FIN
C
        SUB
        DIM
```

APPENDIX G : PROGRAM SUBROUTINES USED TO PERFORM INTEGRATIONS ACROSS SLAB FOR DISTORTED $\hat{i}$ TEXTURE (see section 5.4.3)

```
C       FINDS HZ/HF FOR DIFFERENT THETA-0
C       AND FINDS INTEGRALS AI,BI,CI
C
        SUBROUTINE THETA(HX,CH,IC)
        COMMON SOP(2,120),SOQ(2,120),HZ(60),TO(60),AI(60),BI(60),CI(60)
        J=0
        K=0
        PI=3.14159265
        IC=1
        A=PI*PI*HX*HX/8.
        B=PI*A/2.
        DO 1 I=4,88,2
        PO=PI*FLOAT(I)/180.
        C=AK(PO)
        D=2.02/SIN(PO)
        Z=C*C+HX*PI*D
        IF(Z.LT.0.OR.J.EQ.1)GOTO1
        J=1
        IM=I
    1   CONTINUE
        IN=INT((88.-FLOAT(IM))/8.)
        DO 3 II=1,IN
        PO=PI*(92.-FLOAT(II)*8.)/180.
        AG=(PO-B)/(1.-A)
        CALL SEEKAL(AG,PO,K,AN,S,HX)
        IF(K.EQ.1)GOTO2
        CALL ATTEN(AN,S,IC,PO,HX)
        IC=IC+1
    2   K=0
    3   CONTINUE
        DO 5 I=IM,88,2
        PO=PI*FLOAT(I)/180.
        C=AK(PO)
        A=CH/SIN(PO)
        AG=(C-SQRT(C*C+PI*HX*A))/A
        CALL SEEKAL(AG,PO,K,AN,S,HX)
        IF(K.EQ.1)GOTO4
        CALL ATTEN(AN,S,IC,PO,HX)
        IC=IC+1
    4   K=0
    5   CONTINUE
        IC=IC-1
        RETURN
        END
C
C       FINDS INTEGRALS AI,BI,CI ACROSS CHANNEL FOR DIFFERENT HZ/HF
C
        SUBROUTINE ATTEN(A,S,IC,PO,HX)
        DIMENSION F(21),G(21)
```

```
      COMMON SOP(2,120),SOQ(2,120),HZ(60),TO(60),AI(60),BI(60),CI(60)
      DATA N,PI/21,3.14159625/
      TAN(X)=SIN(X)/COS(X)
      TO(IC)=PO-A
      HZ(IC)=-HX/TAN(A)
      RH=SQRT(HZ(IC)*HZ(IC)+HX*HX)
      SA=SIN(A)
      CA=SQRT(1.-SA*SA)
      H=SQRT(S-SA)/FLOAT(N-1)
      DO 1 I=1,N
      Y=FLOAT(I-1)*H
      SP=S-Y*Y
      CP=SQRT(1.-SP*SP)
      CT=CP*CA+SP*SA
      ST=SP*CA-CP*SA
      B=CT*CT/(CP*SQRT(S+SP))
      F(I)=B*CT*CT
      G(I)=B*ST*ST
    1 CONTINUE
      CALL INTEG(N,H,F,SUM)
      AI(IC)=4.*SUM/(PI*RH)
      CALL INTEG(N,H,G,SUM)
      BI(IC)=4.*SUM/(PI*RH)
      CI(IC)=1.-2.*BI(IC)-AI(IC)
      RETURN
      END
C
C     PERFORMS INTEGRATIONS USING SIMPSONS RULE
C
      SUBROUTINE INTEG(N,H,F,SUM)
      DIMENSION F(21)
      K=N/2
      SUM=F(1)+4.*F(2)+F(N)
      DO 1 I=2,K
      SUM=SUM+2.*F(2*I-1)+4.*F(2*I)
    1 CONTINUE
      SUM=SUM*H/3.
      RETURN
      END
C
C     USES NEWTON-RAPHSON TO FIND ALPHA GIVEN PHIO
C
      SUBROUTINE SEEKAL(AG,PO,K,AN,S,HX)
C
      SUBROUTINE SEEKAL(AG,PO,K,AN,S,HX)
      ASIN(X)=ATAN(X/SQRT(1-X*X))
      PI=3.14159625
      AO=AG
      NC=1
      S=SIN(PO)
    1 SA=SIN(AO)
      A=PI*HX/(2.*SA)
      IF(ABS(SA/S).LE.1.AND.NC.LE.5)GOTO2
      K=1
      RETURN
    2 PH=ASIN(SA/S)
      G=AK(PO)-EF(PH,PO)+A
      H=1./SQRT(S*S-SA*SA)+A*SQRT(1.-SA*SA)/SA
      AN=AO+G/H
      IF(ABS((AN-AO)/AO).LT.2E-5)RETURN
```

```
      NC=NC+1
      AO=AN
      GOTO 1
      END
C
C     CALCULATES COMPLETE ELLIPTIC INTEGRAL
C
      FUNCTION AK(AL)
      CN=COS(AL)
      PRO=1
      SN=2./(1+CN)-1.
      PRO=PRO*(1.+SN)
      CN=SQRT(1.-SN*SN)
      IF(SN.GT.1E-2)GOTO1
      AK=3.14159625*PRO/2.
      RETURN
      END
C
C     CALCULATES ELLIPTIC INTEGRAL F(PHI.ALPHA)
C
      FUNCTION EF(PH.AL)
      TAN(X)=SIN(X)/COS(X)
      ASIN(X)=ATAN(X/SQRT(1.-X*X))
      PI=3.14159625
      PRO=1.
      IF(AL.GT.PI/4.)GOTO6
      CN=COS(AL)
      PN=PH
      SN=2./(1.+CN)-1.
      PRO=PRO*(1.+SN)/2.
      PNR=PN
    2 IF(PNR.LT.PI)GOTO3
      PNR=PN-PI
      GOTO 2
    3 DP=ATAN(CN*TAN(PNR))
      CN=SQRT(1.-SN*SN)
    4 IF(ABS(PN-DP).LT.PI/2.)GOTO5
      DP=DP+PI
      GOTO 4
    5 PN=PN+DP
      IF(SN.GT.1E-2)GOTO1
      EF=PN*PRO
      RETURN
    6 S=SIN(AL)
      SN=S
      PN=PH
    7 CN=2./(1.+SN)-1.
      PN=PN/2.+ASIN(SN*SIN(PN))/2.
      SN=SQRT(1.-CN*CN)
      PRO=PRO*SN
      IF(CN.GT.1E-2)GOTO7
      EF=SQRT(PRO/S)*ALOG(TAN(PI/4.+PN/2.))
      RETURN
      END
```